



Quasithermalization of fermions in a quadrupole potential and evaporative cooling of 40K to quantum degeneracy

Mihail Rabinovic

► To cite this version:

Mihail Rabinovic. Quasithermalization of fermions in a quadrupole potential and evaporative cooling of 40K to quantum degeneracy. Physics [physics]. Université Paris sciences et lettres, 2017. English. NNT : 2017PSLEE019 . tel-01628803

HAL Id: tel-01628803

<https://theses.hal.science/tel-01628803>

Submitted on 4 Nov 2017

HAL is a multi-disciplinary open access archive for the deposit and dissemination of scientific research documents, whether they are published or not. The documents may come from teaching and research institutions in France or abroad, or from public or private research centers.

L'archive ouverte pluridisciplinaire **HAL**, est destinée au dépôt et à la diffusion de documents scientifiques de niveau recherche, publiés ou non, émanant des établissements d'enseignement et de recherche français ou étrangers, des laboratoires publics ou privés.

THÈSE DE DOCTORAT
de l'Université de recherche
Paris Sciences et Lettres –
PSL Research University

préparée à
l'École Normale Supérieure

**Quasithermalization
of Fermions in a
Quadrupole Potential
and
Evaporative Cooling of ^{40}K
to Quantum Degeneracy**

*Quasithermalization de fermions dans
un Potentiel Quadrupolaire et re-
froidissement évaporatif
d'un gaz de ^{40}K jusqu'à la
dégénérescence Quantique*

par **Mihail Rabinovic**

École doctorale n°564
Physique en Île-de-France
Spécialité: Physique
Soutenue le 11.05.2017

Composition du Jury :

M J.T.M. Walraven
Universiteit van Amsterdam
Président du jury

Mme Isabelle Bouchoule
CNRS – Institut d'Optique
Rapporteuse

M Stefan Kuhr
University of Strathclyde
Rapporteur

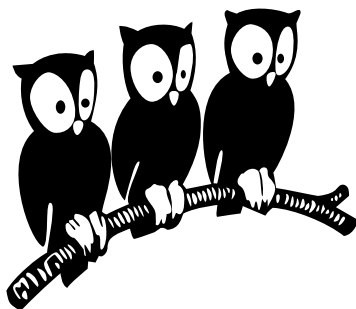
M Frédéric Chevy
École Normale Supérieure
Directeur de thèse

M Christophe Salomon
CNRS - LKB
Co-Directeur de thèse

Mme Patricia Vignolo
Université Nice Sophia Antipolis
Membre du Jury

M Carlos Lobo
University of Southampton
Membre du Jury

LABORATOIRE KASTLER BROSSEL
ÉCOLE NORMALE SUPÉRIEURE



PhD Thesis

Quasithermalization of Fermions
in a Quadrupole Potential

and

Evaporative Cooling of ^{40}K
to Quantum Degeneracy

by

Mihail Rabinovic

Paris, May 11th 2017

Director: Prof. Dr. Frédéric Chevy
Co-Director: Dr. Christophe Salomon

Dedicated to

the mechanical workshop of the LKB, in particular

Mathieu Sardin and Jules Aimé Silembo

and

the electronic technicians

Toufik El Atmani and Lionel Perennes

Abstract

In this thesis we investigate experimentally the physics of ultra-cold fermions on an apparatus designed to create a cold fermionic mixture consisting of ^6Li and ^{40}K . After a short description of the experimental apparatus and of a few technical particularities implemented during my PhD, for example the light-induced atomic desorption in the 2D-MOT by UV-light, we focus on two main observations of the fermionic nature of the gas.

The first part describes the quasithermalization of ^6Li in a magnetic quadrupole potential. Even though collisions are absent in a spin-polarized fermionic gas below a given temperature, the statistical ensemble undergoes energy redistribution after an excitation within the linear potential. We present an extensive experimental study as well as a comprehensive theoretical analysis of this phenomenon. Moreover, the studied Hamiltonian can be canonically mapped onto a system of massless, harmonically trapped particles and the previously developed results are re-interpreted in order to describe this experimentally inaccessible system. A further development of the realized experiment allows even for the implementation of non-Abelian spin-orbit coupling in a gas of non-interacting fermions.

In the second part, we describe the evaporative cooling of ^{40}K to quantum degeneracy. Through different evaporative cooling stages we reach with a final number of $1.5 \cdot 10^5$ atoms in the ground-state a temperature of 62 nK, which corresponds to 17 % of the Fermi temperature.

Résumé

Dans cette thèse, nous avons étudié expérimentalement les propriétés physiques des fermions ultra-froids grâce à une machine conçue pour refroidir un mélange fermionique de ^6Li et ^{40}K . Après une courte description concernant la construction de l'expérience et quelques améliorations que j'ai implémentées pendant ma thèse (telles que la désorption atomique par lumière ultraviolette dans le 2D-MOT), l'exposé se concentre sur deux observations principales de l'origine fermionique des gaz de potassium et de lithium.

La première partie présente la quasithermalization du ^6Li dans un potentiel quadrupolaire, créé par un piège magnétique. Malgré l'absence de collisions dans un gaz fermionique polarisé en dessous d'une température donnée, nous observons une redistribution d'énergie dans l'ensemble statistique après une excitation dans le piège linéaire. Une étude expérimentale détaillée ainsi qu'une analyse théorique du phénomène sont présentées. De plus, une transformation canonique de l'hamiltonien du système permet la description de particules sans masses dans un piège harmonique. Les résultats expérimentaux du système réel (gaz ^6Li dans un potentiel quadrupolaire) sont donc réinterprétés pour décrire ces particules non massiques, difficiles à observer. Un développement supplémentaire de notre système expérimental permet également la réalisation d'un couplage spin-orbite non-abélien dans le gaz fermionique sans interactions.

Dans la deuxième partie, on décrit la réalisation d'un gaz dégénéré de ^{40}K à l'aide du refroidissement évaporatif. Une succession d'étapes d'évaporation, utilisant différentes technologies de piégeage, nous permet d'obtenir $1.5 \cdot 10^5$ atomes dans l'état fondamental à une température de 62 nK, température équivalente à 17 % de la température de Fermi.

Contents

List of Figures	xiii
List of Tables	xvii
1 Introduction	1
2 Experimental Setup	9
2.1 Main Experimental Sequence	10
2.2 Vacuum Chamber and Atomic Sources	12
2.2.1 Lithium oven and Zeeman slower	13
2.2.2 Potassium 2D-MOT	14
2.3 Optical System	16
2.4 Common MOT	20
2.5 Gray Molasses Cooling	20
2.5.1 Motivation and main idea	21
2.5.2 Experimental realization	22
2.6 Magnetic Trapping	25
2.6.1 Trappable ground states of ^6Li and ^{40}K	26
2.6.2 Optical pumping	28
2.6.3 Spin-composition test	28
2.6.4 Transport	30
2.7 Absorption Imaging	31
2.7.1 Technical realization	33
2.7.2 Calibration of the magnification	35
2.7.3 Image analysis and temperature measurement	36
2.8 Computer System	36
2.9 Summary of the Sequence	37
3 Quasithermalization of Non-Interacting Particles in a Quadrupole Trap	43
3.1 First Experimental Observations	44
3.2 Experimental Concept	46
3.3 Analytical Calculation of the Time Evolution of the Momentum	48

3.3.1	Analytical prediction of the steady state	50
3.4	Experimental Study of the Momentum Transfer	51
3.4.1	Magnetic kick	52
3.4.2	Experimental sequence	54
3.4.3	Experimental results	56
3.4.4	Realistic kick estimation	60
3.5	Conclusion	64
4	Quantum Simulation in the Quadrupole Potential - SOC in a Non-Interacting Gas	67
4.1	Simulation of Massless Harmonically Trapped Non-Interacting Particles	67
4.2	Spin-Orbit Coupling	69
4.3	Realization of Non-Abelian Spin-Orbit-Coupling	71
4.3.1	ODT potential	71
4.3.2	Potential created by four Ioffe bars	72
4.3.3	SOC-Hamiltonian through canonical mapping	73
4.4	Ground State of a SOC System	74
4.4.1	Density distribution	77
4.5	Conclusion	79
5	Pathway to Quantum Degenerate ^{40}K	81
5.1	Setup Around the Science Cell	82
5.2	Majorana Losses and Plugged Quadrupole Trap	84
5.3	Evaporative Cooling of ^{40}K	87
5.3.1	Principle of evaporative cooling	87
5.3.2	RF evaporation in a magnetic trap	90
5.3.3	Loading a single beam ODT from a quadrupole trap	93
5.3.4	Evaporative cooling in an ODT	95
	Spin-flip and mixture preparation	97
	Evaporation sequence overview	98
5.4	Magnetic Field Effects	100
5.4.1	Precise measurement of the bias field	100
5.4.2	Role of magnetic curvature	101
5.4.3	Feshbach resonances	103
5.5	Degenerate Fermi Gas in a Harmonic Trapping Potential	107
5.5.1	Fermi-Dirac distribution	107
5.5.2	At zero temperature - The Fermi energy	108
5.5.3	Comparison of Fermi and Gaussian profiles	110
5.5.4	Evaluation of the experimental results	110
5.6	Conclusion	114
6	Summary and Outlook	115

A	Lattice Laser Setup	117
A.1	A Lattice Laser for ^{40}K in Presence of ^6Li	117
A.2	An Example of a MOPA System	119
B	Notes on AOM Drivers	123
C	New TA Support Design	127
D	Optocoupling of Signals	141
D.1	TTL Signal Optocoupling	141
D.2	Analog Signal Optocoupler	145
E	UV-LED Driver	149
F	Microcontroller Based Security System	155
G	50Hz Mains Synchronization Device	161
H	Time-of-Flight Expansions	165
H.1	Free Expansion during TOF	165
H.1.1	TOF evolution from a harmonic trapping potential	165
H.2	TOF Evolution in Presence of a Magnetic Curvature	167
H.2.1	Case of Boltzmann distribution	168
H.2.2	Case of Fermi distribution	169
I	Supplemental Calculations for Chapter 3	171
I.1	Scalar Product from Eq. (3.11)	171
I.2	Properties of the Liouville Operator	172
I.3	Vanishing Intergral Terms in Eq. (3.12)	173
I.4	Properties of the Momentum Redistribution Matrix θ_{ij} from Eq. (3.16)	174
I.5	The Virial Theorem	175
I.6	Approximation of the Potential Energy in Eq. (3.45)	176
J	Fermi-Temperature of the SOC System in Sec. 4.3	177
	Bibliography	181
	Acknowledgements	201

List of Figures

1.1	Periodic table of cooled and trapped elements	3
1.2	BEC-BCS crossover on a Feshbach resonance	5
2.1	Cross section of the FerMix experiment	11
2.2	CAD-design of the FerMix vacuum assembly (from [111])	13
2.3	Magenetic field evolution in the Zeeman slower (from [108])	14
2.4	Schematic setup of the ^{40}K 2D-MOT	15
2.5	Fluorescence signal during MOT loading: Influence of LIAD	16
2.6	2D-MOT pressure and MOT loading rate for ^{40}K	17
2.7	Optical setup for ^6Li D ₂ -line transitions	18
2.8	Optical setup for ^{40}K D ₂ -line transitions	19
2.9	Illustration of the gray-molasses cooling scheme (from [137])	22
2.10	Detuning dependency of the gray molasses (from [111])	23
2.11	Gray molasses setup	24
2.12	Coil geometry in anti-Helmholtz configuration	26
2.13	Zeeman splitting of the hyperfine ground states of ^6Li and ^{40}K	27
2.14	Magnetic trappability as a function of optical pumping intensity	29
2.15	Spin composition analysis for ^{40}K	30
2.16	Principle of magnetic transport	31
2.17	Illustration of $\sigma_+ + \sigma_-$ imaging at high magnetic fields	32
2.18	Imaging in double shutter mode	34
2.19	Calibration of imaging magnification by free fall	35
2.20	Scheme of the computer control of the experiment	37
2.21	Parameters of the experimental sequence from MOT-loading to the magnetic trapping in the MOT chamber	39
3.1	Illustration of the symmetries in the quadrupole potential	44
3.2	Absence of cross-thermalization in a quadrupole trap (from [111])	45
3.3	Concept of the "kick" experiment	47
3.4	Simulation of the momentum evolution after a kick	51
3.5	Trap displacement by the push coil	52
3.6	Illustration of the magnetic kick procedure	53
3.7	Experimental sequence for the kick measurements	54

3.8	Switching dynamics of the kick performing coils	55
3.9	Effect of eddy currents on the kick performance	56
3.10	Cloud oscillation after performing a kick in x -direction	57
3.11	Momentum transfer measurements for x -kicks	58
3.12	Momentum transfer measurements for z -kicks	59
3.13	Corrected kick transfer factors α'_{Zz} and α'_{Xx}	64
4.1	Aharonov-Bohm experiment in a non-Abelian vector field	70
4.2	Magnetic field derivation for a setup of four Ioffe bars	72
4.3	Eigenenergy branches of the SOC-system	75
4.4	Characterization of the ring structure of the lower SOC energy branch	76
4.5	Contrast of the energy ring-minimum in a SOC system	78
5.1	Detailed setup around the science chamber	82
5.2	Lifetime and heating rate of ^{40}K in a quadrupole trap	85
5.3	Potential of a plugged quadrupole trap	86
5.4	Illustration of the evaporation process	88
5.5	RF transition in magnetically trapped ^{40}K	92
5.6	Characterization of the RF-evaporation in the magnetic trap	92
5.7	Loading an ODT from the magnetic trap	94
5.8	Characterization of the ODT evaporation	96
5.9	Spin manipulation of ^{40}K	97
5.10	Evaporation sequence overview	99
5.11	RF-spectroscopy for precise bias measurement	100
5.12	Curvature compensation experiment	102
5.13	s -wave Feshbach resonance in the $-9/2, -7/2$ mixture	104
5.14	d -wave Feshbach resonances in the $+9/2, +7/2$ mixture	106
5.15	1D-Fermi profiles for different T/T_F values	109
5.16	Gaussian-fit benchmark for ultra-low temperature Fermi distributions	111
5.17	Measurement of trap frequencies in the ODT	112
5.18	Image and analysis of a degenerate ^{40}K cloud	113
A.1	2D-lattice illustration	117
A.2	Choice for the lattice wavelength	119
A.3	Optical setup of the 808 nm MOPA laser system	120
A.4	TA performance for variable currents and chip temperature	121
B.1	AOM driver setup	124
B.2	Adapter for Crystal Technology AOMs	125
C.1	Dimensions and design of a C-mount TA chip	127
C.2	Thorlabs parts used in the TA setup	129
C.3	DT12/M and LM05XY/M adapter	131

C.4	TA support: base unit CAD part 1/3	132
C.5	TA support: base unit CAD part 2/3	133
C.6	TA support: base unit CAD part 3/3	134
C.7	TA support: chip holder base plate CAD	135
C.8	TA support: chip holder CAD	136
C.9	TA support: Side element	137
C.10	TA support: front / back and top cover	138
C.11	TA support: complete assembly	139
D.1	Basic TTL optocoupling circuit	142
D.2	Optocoupling circuit using HCPL-2201 (from [236])	143
D.3	Response of the HCPL-2201 at 1 MHz	143
D.4	Optocoupling circuit using HCPL-7721 (from [237])	144
D.5	Optocoupling circuit to drive an IGBT	144
D.6	Analog optocoupling circuit (from [241])	146
D.7	Performance of the analog optocoupling circuit	146
D.8	Rescaling circuit for voltages in the range of 0 V to 10 V	147
E.1	UV-LED driver circuit	150
E.2	MCU pinout in the UV-LED driver	153
F.1	Mini security system - circuit parts	156
F.2	Main security loop	158
F.3	Menu function of the security system	160
G.1	50Hz mains synchronization circuit	162
G.2	50Hz mains synchronization box - regulation part	163
J.1	Population of the lower SOC energy branch at $T = 0$	179
J.2	Fermi-temperature characterization of the lower SOC energy branch	180

List of Tables

2.1	Temperatures and atom numbers in the MOT chamber	41
5.1	Technical characteristics of laser and magnetic coils around the science cell . .	83
5.2	Scaling of various quantities for a power law potential (from [205])	89

Introduction

Since Max Planck’s prediction of the quantized nature of energy [1], representing the birth of quantum physics, and the soon to follow discoveries like the photo effect by Albert Einstein [2] or the first spectroscopic observation by Niels Bohr on hydrogen [3], we know that classical physics is only a large scale limit of the underlying quantum world. The subsequent formulation of the mathematical equations describing the time evolution of quantum particles through wave-equations by Erwin Schrödinger [4] and the complementary introduction of quantum operators by Werner Heisenberg [5] and Paul Dirac [6, 7] opened up not only a new domain of physics, but also changed the approach in this field of research. While in classical physics most discoveries and their mathematical description were based on foregone experimental observations, the early extensive formulation of quantum mechanical models allowed the prediction of many phenomena far earlier than their eventual experimental realization. A well known example is the phase transition to condensation of Bosons at a given density below a threshold temperature, an effect known as Bose-Einstein condensation. Predicted in works by Albert Einstein [8] and Satyendranath Bose [9], it was experimentally realized more than 70 years later in the domain of ultra cold gases [10–12].

Soon, the explored systems became more sophisticated and their mathematical description within the quantum mechanical formalism more elaborate, which gave rise to problems unsolvable by numerical methods. A prominent example are Mott insulators, which should be conducting materials according to their electron band structure, but rather show insulating properties in a given temperature range [13]. In solid-state physics, these systems are described and explained by the Hubbard model [14], whose mathematical treatment, either analytically or numerically, is still challenging. The complexity of the solution scales with the involved particle number and becomes, even with today’s computational resources, unsolvable on a reasonable timescale. Based on the several challenges of the evolving quantum world, Richard Feynman stated his often cited claim, that a simulation of physics and of nature in general should be done by quantum simulators, rather than classical tools or mathematical engines (like computers) [15].

About 20 years later, the cold atom community approached Feynman’s idea by simulating the transition from the superfluid phase (equivalent to a perfectly conducting medium) to a Mott insulator in a Bose-Einstein condensate of ^{87}Rb [16]. In the following, we will recap the development in the field of ultra cold gases before presenting a short outline of the thesis manuscript.

Quantum gases ...

The modern research domain of quantum gases originated from the branch of spectroscopy of atoms and molecules. The early absorption and fluorescence experiments showed a discrete spectrum, which is based on the internal energy level- and spin structure of the atoms. The study of the spectra confirmed the angular momentum quantization, which states that every (elementary) particle owns either an integer (therefore called *Bosons*) or a half integer (named *Fermions*) spin, expressed in multiples of Planck's constant \hbar .

The parallel advances in laser technology provided narrowband coherent light sources at the wavelength of the previously studied atomic transitions. Lasers paved the way for a variety of explorations concerning the atom-light interaction [70]. By addressing distinct transitions of the atoms, the quantum model of the atoms level structure was confirmed further [71]. The demand for a longer timescale for the manipulation and observation of coherence phenomena required additional cooling and even trapping of the atoms. The revolutionary inventions of the optical molasses [72], the MOT (**M**agneto **O**ptical **T**rap) [73], and distinct sub-Doppler cooling techniques [74] (events, which are marking the beginning of the era of quantum gas experiments) allowed to reach a temperature range of 10 μ K to 300 μ K with typical sample sizes of around few 10^6 atoms, depending on the utilized species. The alkaline elements play a special role throughout this historical development, since they have only a single electron in their outer shell. Being "hydrogen-like", their clear ground-state level structure allows for the usage of narrow-band laser sources in the visible to the near infrared spectrum in order to realize the afore-mentioned cooling schemes. Moreover, the cooling attempt changed the viewpoint from a single atom physics to the description of a statistical ensemble. Here the distinction of quantum mechanics and classical physics manifests on a many-body level.

In a simplified picture and in absence of collisions, the transition to a quantum-statistically dominated regime takes place as soon as the inter-particle spacing d (which can be approximated through the spatial ensemble density $n \sim d^{-3}$) becomes smaller than the de-Broglie wavelength λ_{dB} . The latter describes the wave nature of the particles and is calculated by

$$\lambda_{dB} = \sqrt{2\pi\hbar^2/mk_B T} ,$$

with the Boltzmann constant k_B , m the mass of the particle and T the ensemble temperature. The previous statement about the transition to the quantum regime is essentially contained in the increase of the phase-space density (*PSD*), a dimensionless quantity calculated as

$$PSD = n_0 \lambda_{dB}^3 .$$

By entering the quantum regime with an ensemble of atoms, the statistical difference between Bosons and Fermions becomes drastically evident. While Bosons tend to accumulate in the lowest energy state (the common ground state), Fermions occupy successively the lowest energy states due to Pauli blocking (see embedded illustration in fig. 1.1): Bosons undergo a phase transition to a Bose-Einstein condensate (starting at a $PSD > 2.612$), while for Fermions in absence of interactions no phase transition occurs. The latter rather follows a smooth transition from classical to quantum behavior. For a spin-polarized Fermi-ensemble at zero temperature, the energy levels get filled one by one up to the Fermi-energy E_F , which is dependent on the trap configuration and notably also on the total atom number.

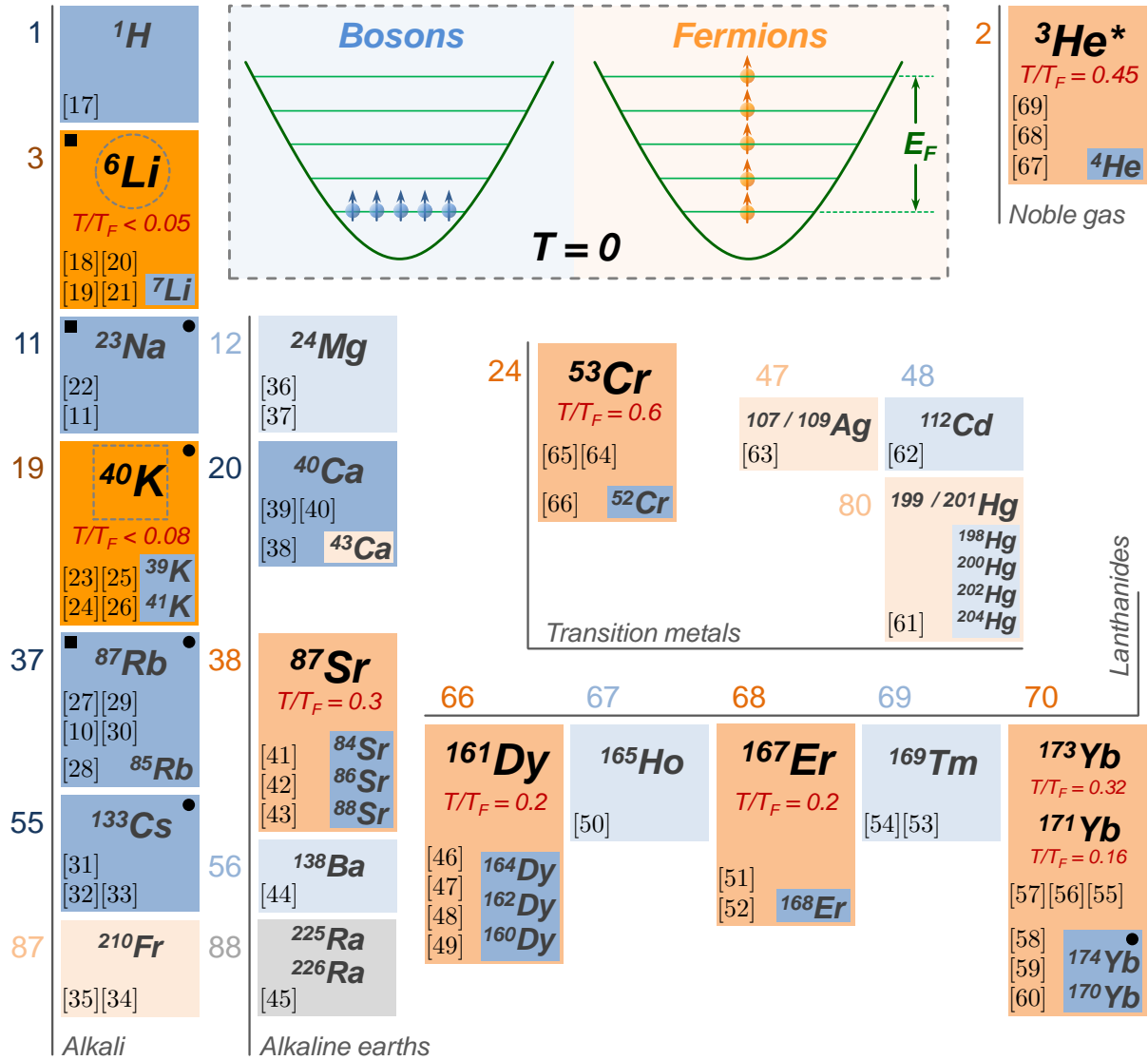


Figure 1.1: Periodic table of cooled and trapped (neutral) atoms until today (status March 2017). Orange colors denote Fermions, while blue colors mark bosonic isotopes. Darker tones denote the achievement of BEC or a degenerate Fermi-gas correspondingly. For the latter the best achieved T/T_F -ratio is mentioned. Black squares and circles mark the mixture of the current element with fermionic ^4K or ^6Li correspondingly. The embedded figure demonstrates the different behavior of trapped non-interacting Bosons and Fermions at absolute zero temperature: While Bosons condense by occupying a common ground state, only one Fermion per energy level is allowed.

However, solely through laser cooling as described above, it is not possible to reach the low temperatures which are necessary in order to observe the transition to the degenerate quantum regime in an ensemble. The breakthrough to ultra low temperatures of the order of a few hundred nK is achieved by subsequent evaporative cooling of the gas. Evaporation is based on the removal of the ensemble's most energetic particles and its ensuing rethermalization to a lower temperature through collisions [75, 76]. In this way, the first Bose-Einstein condensates (*BEC*) were achieved in three groups¹ at about the same time in the year 1995. Using similar cooling techniques as for Bosons, the first degenerate Fermi-gas was produced few years later in the group of Deborah S. Jin [23] (using ^{40}K as fermionic species). Since then, a great variety of elements have been cooled down to the quantum degenerate regime (see fig. 1.1).

Of course these states of matter can, in principle, be generated by cooling down any sample of molecules or atoms without resorting to ultra-cold gas experiments. In reality however, many-body collisions would lead to the formation of liquids and solids before a sufficiently high PSD is reached. The dilute gases created in ultra high vacuum experiments have comparably low densities ($n \sim 10^{14} \text{ cm}^{-3}$ [77]) and inter-particle interactions are usually weak. In turn, the time-scale for reaching a solid or liquid phase through three-body collisions is much larger than the time required for the cooling mechanisms (based on elastic two-body collisions) to achieve quantum degeneracy.

The additional possibility to trap the atoms by far-detuned laser beams enabled the creation of different potential arrangements in lattice-forms [78], which are nowadays a major tool of many experimental setups. As indicated previously, this turned the field of ultra-cold gases from the simple study of the newly reached quantum phases, to simulating condensed matter physics [79, 80]. Taking now into account the role of interactions, which might range from simple isotropic contact interactions to long-range dipolar interactions, enriches the variety of observed features [81]. Recent progress in the field of dipolar interactions in BECs was reported in [48], where a sudden emergence of a triangular lattice structure due to the long range interactions was observed.

... Experiments with Fermions ...

Cold atom experiments with Fermions are more challenging in terms of cooling efficiency, in particular regarding the evaporative cooling step, which relies on the continuous rethermalization of the gas through interactions. Due to Pauli-blocking, *s*-wave interactions are forbidden for spin-polarized Fermi gases. Therefore, either an equilibrated spin mixture is necessary (like in [23] for ^{40}K , in [82] using ^6Li and in [55] for ^{173}Yb) or a bosonic buffer coolant has to be added. For the latter case, there is a vast range of experiments using either the bosonic isotope of the same element or a well studied Boson of a different element, like ^{87}Rb or ^{23}Na (see fig. 1.1). Remarkably, a recently realized degenerate Fermi gas of ^{167}Er in [51] exploited the strong magnetic dipole-interactions between the spin-polarized Fermions to reach quantum degeneracy.

The degree of quantum degeneracy of a Fermi-gas is expressed in terms of the Fermi-temperature. The latter is deduced from the previously mentioned Fermi energy via $T_F = E_F/k_B$, with the Boltzmann constant k_B . Since every energy state can be occupied by different spin states, but only by one of each kind, the Fermi temperature is calculated for each spin constituent

¹In the groupe of Eric A. Cornell [10] it was achieved in ^{87}Rb , by Wolfgang Ketterle [11] in ^{23}Na and by Randall G. Hulet [12] in an attractive gas of ^7Li .

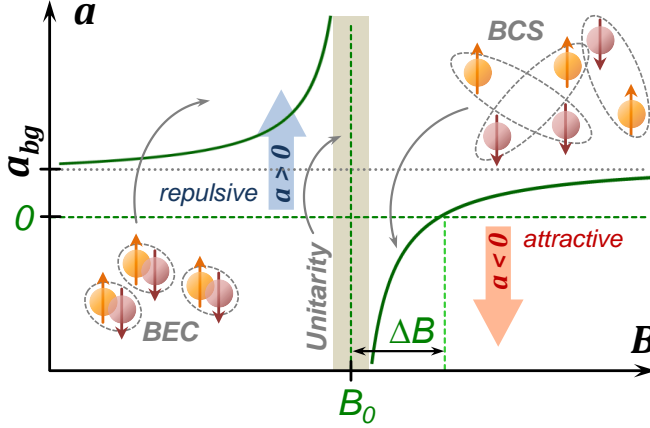


Figure 1.2

Illustration of the BEC-BCS crossover on a Feshbach resonance. A s -wave Feshbach resonance allows to tune the interparticle scattering length a of an optically trapped two-spin state mixture by changing the bias field B . The resonance is characterized through the position B , the width ΔB at zero-crossing and the background scattering length a_{bg} . For an ensemble below $T/T_F \sim 0.2$ a continuous superfluid transition from the BEC to the BCS limit is observed, even at the strongly interacting unitary regime [86].

and can differ, e.g. in the case of an imbalance in atom number per spin state. Expressing the overall temperature of the gas in terms of the Fermi temperature (i.e. by the ratio T/T_F) illustrates how densely the states below E_F are occupied². We emphasize again that, different from Bose-Einstein condensation, there is no phase-transition for a spin-polarized fermionic gas in absence of interactions. However, as will be shown later on, a noticeable deviation from the classical Boltzmann distribution takes place when $T/T_F < 0.3$, revealing the quantum-statistical behavior.

Nowadays, The most important and widely used tool in cold atom experiments with Fermions are Feshbach resonances [85]. At a Feshbach resonance the colliding atoms couple to a molecular bound state, which results in an increase of the elastic scattering length and therefore stronger interactions within the ensemble. The energy level of the molecular bound state with respect to the relative energy of the colliding atoms can be tuned, for example by changing the magnetic bias field. This affects the Zeeman shifts and therefore the relative internal energy splitting of the colliding partners, provided that they constitute to different spin states. In summary, a Feshbach resonances allows for a full control over the scattering length of an optically trapped two-state spin-mixture, by simply changing the magnetic field. This includes the strongly interacting case as well as the absence of interaction (zero-crossing - see fig. 1.2).

In the fermionic case, the magnetic sweep to the resonance position is not necessary accompanied by high losses and heating of the gas, in contrast to Feshbach resonances in bosonic gases. It is suggested to observe pair formation throughout the entire region of a s -wave Feshbach resonance for fermionic spin mixtures in the zero-temperature limit. By sweeping through the resonance to positive, but weak scattering lengths, a formation of strongly bound molecules should occur[87]. Being sufficiently cold, the resulting molecules constitute Bosons and therefore a BEC of molecules should be observed. Similarly, a sweep through the resonance towards small, but negative scattering lengths implies the formation of Cooper-pairs, which are long-range correlations between two Fermions described by the Bardeen-Cooper-Schrieffer (*BCS*) theory. The latter is an approach of describing superconductivity [88], the transition to zero electrical resistance of particular materials cooled below a given threshold temperature. The analogous effect in liquids and quantum gases is called superfluidity. The emergence of superfluidity in

²A number of proposals, like in [83] and [84], suggest the indirect observation of Pauli-blocking through reduced photon absorption by energetically low lying states.

strongly correlated systems can be observed for molecular BECs as well as for BCS pairs. A direct consequence of a "flow-without-resistance" is the formation of quantized vortex structures in a stirred superfluid cloud. In [86] the appearance of vortices was presented for the entire range of the Feshbach resonance, therefore underlining the theory of a smooth crossover from BEC-to BCS-type superfluids [89]. The unique point of divergent scattering length at the position of the Feshbach resonance is of particular interest, since the only relevant energy scale of the gas is given by the Fermi energy in this regime. Arriving at a profound understanding of the cross-over physics might get us closer to the understanding and production of high-temperature (even room-temperature) superconductors [90].

A recent approach in Fermi-gas experiments is the implementation of single-atom imaging techniques in a lattice structure [91–94], adapted from previous bosonic experiments [95]. It is called quantum-gas microscopes, due to the installation of high-resolution objectives for fluorescence-imaging near the experimental glass cell.

... including two species

Apart from the simple fact that experiments of two Fermionic species enable to cross-check the observations against species-specific parameters, e.g. Feshbach-resonance properties, the composite system promises interesting features: A possible inter-species Feshbach resonance would allow the formation of heteronuclear bosonic molecules with an electric dipole moment. In turn, the study of weakly bound trimers is proposed in [96]. So far, experiments including two different fermionic species are utilizing the only two fermionic alkaline isotopes, ^6Li and ^{40}K . To our knowledge, six groups worldwide have constructed experimental machines to address these two Fermions simultaneously.

- The experiment at MPQ (Munich) reached as one of the first groups the double degenerate regime in 2008, using RF-evaporation on ^{87}Rb , which in turn sympathetically cooled down ^6Li and ^{40}K [20]. Even triple degeneracy with a small BEC of ^{87}Rb was achieved in the magnetic QUIC-trap. After the implementation of an optical dipole trap, the group reported on the first creation of heteronuclear bosonic molecules in [97] at a previously determined Feshbach resonance.
- The experiment at the University of Amsterdam (Netherlands) was one of the first to present a quantitative approach to study and characterize the interspecies Feshbach resonances between ^6Li and ^{40}K . In [98] they determine with high precision the width of the large Feshbach resonance at $B_0 = 114.4\text{ G}$ to be $\Delta B = 1.5\text{ G}$.
- The experiment at MIT (United states) used ^6Li and ^{40}K in conjunction with the bosonic isotope ^{41}K to reach triple degeneracy, again using a Boson as an efficient coolant during evaporation. In the same publication [24], the group reports on the observation of various Feshbach resonances in the two possible types of Bose-Fermi mixtures in this system. While initially being a triple-species machine, the group studies nowadays ground state molecules of ^{23}Na and ^{40}K [22].
- The experiment at the IQOQI in Innsbruck (Austria) was the first one to study Feshbach resonances in the fermionic mixture of ^6Li and ^{40}K [99]. The same experiment reached later

on in 2010 the simultaneous double degeneracy of both species. The particularity of the experiment published in [100] is the direct evaporative cooling of the two fermionic clouds in a (crossed) optical dipole trap loaded from the MOT. The cloud is neither transported to a separated UHV region, nor another Bosonic element as coolant is being used. Moreover, any step of pure magnetic trapping is avoided. This group also investigated in [101] the strongly interacting regime on the interspecies Feshbach resonance and reported in [102] the first observation of atom-dimer interactions (between ^{40}K and ^6Li - ^{40}K dimers, created on the BEC-side of the resonance).

- In Shanghai (China) an experimental apparatus was recently constructed, whose design and cooling sequence is very similar to ours. The experiment can prepare both fermionic species. Currently, the group switched from ^{40}K to the bosonic isotope ^{41}K and created the first double species superfluid of ^6Li bound molecules and ^{41}K BEC, proving the existence of the superfluid phase by creating vortex lattices by stirring the clouds [103].

Our experiment in Paris (France) was initially designed to study the two Fermions in different dimensions: The heavier ^{40}K would have been confined in a 2D- or 1D-lattice in presence of a free ^6Li gas. While the latter case provides a system similar to the ones studying Anderson localization [104, 105], the 2D-system is suitable to study long-range multilayer interactions mediated by the free gas [106].

Outline of this thesis

This thesis presents studies performed on the double-fermionic species ultra-cold gas experiment in the group of Prof. Dr. Frédéric Chevy and Dr. Christophe Salomon at the Laboratoire Kastler Brossel in the period of April 2013 until January 2017. The FerMix (**F**ermionic **M**ixture) experiment is designed to cool and trap ^6Li and ^{40}K atoms simultaneously. In this work, we continued paving the way towards the realization of a double-degenerate two-species Fermi-gas. The two major results, which were obtained during that time, are the observation of the ensemble dynamics of non-interacting particles in a non-separable potential (the quadrupole potential) and the cooling of ^{40}K to quantum degeneracy. The main text of the thesis is split into four chapters:

Chapter 2 The FerMix Experiment

We first introduce the experimental setup and its key features. Given that the vacuum system, the dual-species MOT and the magnetic transport were set up by previous PhD-generations [107], we focus mostly on the improvements of the existing setup. This includes the implementation of LIAD (**L**ight-**I**nduced **A**tom **D**esorption) for the ^{40}K 2D-MOT, the study of the simultaneous gray-molasses cooling of ^6Li and ^{40}K and the optimization of optical pumping. We also discuss in greater detail the absorption imaging technique and its implementation.

Chapter 3 Quasithermalization of non-interacting particles in a quadrupole trap

In this chapter, we will discuss one of the main results of this thesis: The energy redistribution after a momentum kick within a non-interacting gas of spin-polarized ^6Li in a non-separable

trapping potential. Pauli-exclusion forbids interactions through collisions in this scenario. Nevertheless, we observe a partial energy redistribution after an excitation within the symmetry plane of the studied quadrupole potential. We develop a comprehensive theoretical model for the excited trapped gas and verify the results experimentally.

Chapter 4 Quantum simulation in the quadrupole potential - SOC in a non-interacting gas

The absence of an interaction term in the single-particle Hamiltonian of the previously studied system allows for a canonical mapping, which exchanges the role of momentum and position coordinates. Owing to the form of the quadrupole potential, we establish an analogy to a system of harmonically trapped massless particles (i.e. Weyl particles), opening up the possibility of simulating their dynamics in a cold gas experiment. In turn, the results of chapter 3 can be reinterpreted for this system. Further developing the idea of canonical mapping in a non-interacting gas of Fermions, we propose a realization of non-Abelian spin-orbit coupling and estimate the experimental parameters for an implementation for ^6Li .

Chapter 5 Pathway to quantum degenerate ^{40}K

In the last chapter, we present the process of evaporative cooling of ^{40}K to quantum degeneracy. We reach a temperature of 62 nK with a sample of $1.5 \cdot 10^5$ atoms in the absolute ground state, which corresponds to $T/T_F = 0.16$ in terms of the Fermi-temperature. We discuss the analytical methods for evaluating the density profiles as well as the differences emerging in the density profiles at lower temperatures between the classical- and quantum mechanical regime. We also briefly address the characterization of a few Feshbach resonances in ^{40}K and the compensation of magnetic curvature.

Technical notes and supplementary calculations are attached at the end of the manuscript in the form of **Appendix A – J**. The appendix is divided in three major parts,

Optical notes In appendix **A** we discuss the lattice laser, the purpose of which is to confine ^{40}K in two-dimensional planes. It serves as a general example of a MOPA-laser system. Appendix **B** shows the radio-frequency installation we are using to drive the acousto-optical modulators in our experiment. Finally, in appendix **C** we present a new mechanical design to support tapered amplifier chips, which allows for precise optical alignment of the collimation lenses at the in- and output side of the chip.

Electrical notes We test several optocoupling circuits, for digital as well as for analog signals (appendix **D**), and three different applications of micro-controllers: a high-power LED-driver (appendix **E**), a versatile security system (appendix **F**) and a 50 Hz mains detection/synchronization device (appendix **G**).

Supplementary calculations In order to provide additional information outside of the main text, the reader will find the calculations concerning time-of-flight expansions (appendix **H**) and some supplementary calculations for chapter 3 (appendix **I**) as well as chapter 4 (appendix **J**) in the three last appendix sections.

The FerMix Experiment

This chapter is dedicated to the description of the experimental apparatus and the preparation procedure to obtain a cold sample of ^6Li - and ^{40}K -atoms. The construction of the experiment started in September 2007 [108]. Few ensuing generations of PhD-students accomplished the basic setup of the main machine [109–112], which led to some milestones like the photoassociative creation of ^6Li - ^{40}K molecules [113] or the gray D_1 molasses [114]. During my thesis I continued with the implementation of evaporative cooling techniques in the science chamber to realize a quantum degenerate Fermi-mixture (see chapter 5). In turn, some details of the cooling and trapping procedures of the atomic clouds were modified during the past four years. Although the main starting procedure remained principally unchanged, it was optimized to its best performance. The current chapter recaps the main experimental steps and is structured as follows:

- **Section 2.1** discusses the overall experimental sequence to give an overview of all applied procedures towards the creation of an ultra cold dual-species gas. One part of the used techniques will be characterized in the following section, while the second part beyond the MOT-chamber will be discussed in chapter 5.
- **Section 2.2** characterizes the two atomic sources of our experiment, i.e. the ^6Li Zeeman slower and the ^{40}K 2D-MOT.
- **Section 2.3** describes the used atomic cooling transitions and the optical setup to generate the necessary detuning frequencies.
- **Section 2.4** summarizes briefly the particular setup of the dual-species MOT and the key performance numbers.
- **Section 2.5** presents the gray-molasses cooling, which was first implemented in our experiment.
- **Section 2.6** provides the basics of magnetic trapping. This will be of particular importance later on for the chapter 3, where we will discuss the quasi-thermalization in a quadrupole trap.
- **Section 2.7** explains the techniques behind the detection of the atoms by light absorption.

- **Section 2.8** summarizes briefly the computer control of the experiment. The associated topic of optocoupling can be found in appendix D.

2.1 Main Experimental Sequence

Figure 2.1 shows a modeled and simplified cross section of the FerMix (**F**ermionic **m**ixture) experiment, including the main experimental techniques.

The experiment starts from two (hot) sources: The Lithium (*Li*) oven on the left hand side of the picture and the heated glass cell of the two-dimensional magneto-optical trap (*2D-MOT*) of Potassium (*K*) on the bottom. For both atomic sources, ^6Li - and ^{40}K , we use a pre-cooling stage before loading the common magneto-optical trap (*MOT*):

- Hot ^6Li atoms get decelerated in the Zeeman slower *ZS* [115]. A motorized shutter *S* allows to block the hot atomic beam after the MOT loading phase, in order to avoid collisions of the hot stream with the atomic cloud during the further cooling processes.
- ^{40}K atoms are captured and pre-cooled in the 2D-MOT[116].

After the common MOT-phase and a 4 ms short compressed MOT-phase (*CMOT*), the gray molasses technique is applied for both species simultaneously. This allows to reach temperatures of $\sim 50\text{ }\mu\text{K}$ for ^6Li and up to $12\text{ }\mu\text{K}$ for ^{40}K . Subsequently, the atoms are optically pumped into their magnetically trappable hyperfine states and captured in a quadrupole potential created by the MOT-coils (*C_{MOT}*).

Both clouds are then magnetically transported to the ultra-high-vacuum ($\sim 10^{-13}$ mbar) science cell (*SC*). The transport¹ incorporates a 90° elbow, which allows for full optical access around the science cell. Similarly to the initial magnetic trap in the MOT-chamber, the atoms are again re-captured in a high-gradient quadrupole trap created by the inner-pair of coils (*C_{IC}*) around the science cell. To avoid Majorana losses, the magnetic zero of the trap is plugged by a repulsive (blue-detuned) laser (*Verdi-laser* at 532 nm).

For precise control of the bias field, two pairs of coils are placed around the science cell (a pair of *inner coils* - *C_{IC}* and *outer coils* - *C_{OC}*). The design of the coils allows for a perfect canceling of the magnetic curvature at high bias-fields (up to ~ 500 G) using both pairs simultaneously.

Once in the science cell, the cloud is further cooled down by evaporation. By driving radio-frequency hyperfine transitions, hot atoms are removed from the magnetic trap. Once a sufficiently high phase-space density (*PSD*) is reached, the cloud is transferred into an optical dipole trap (*ODT*).

Since ^6Li possesses only one magnetically trappable low-field seeker state, it cannot be cooled down alone by evaporation in a magnetic trap: in our case, ^{40}K has to serve as a collision partner. Therefore, the strategy is roughly the following:

- The RF-evaporation is performed on ^{40}K , which cools down the ^6Li -cloud sympathetically. At this stage a sufficiently higher number of ^{40}K atoms is required to cool down a smaller sample of ^6Li .

¹The transport coil color-code in fig. 2.1 is chosen similar to the one in [111], where the transport sequence and technique is described in great detail.

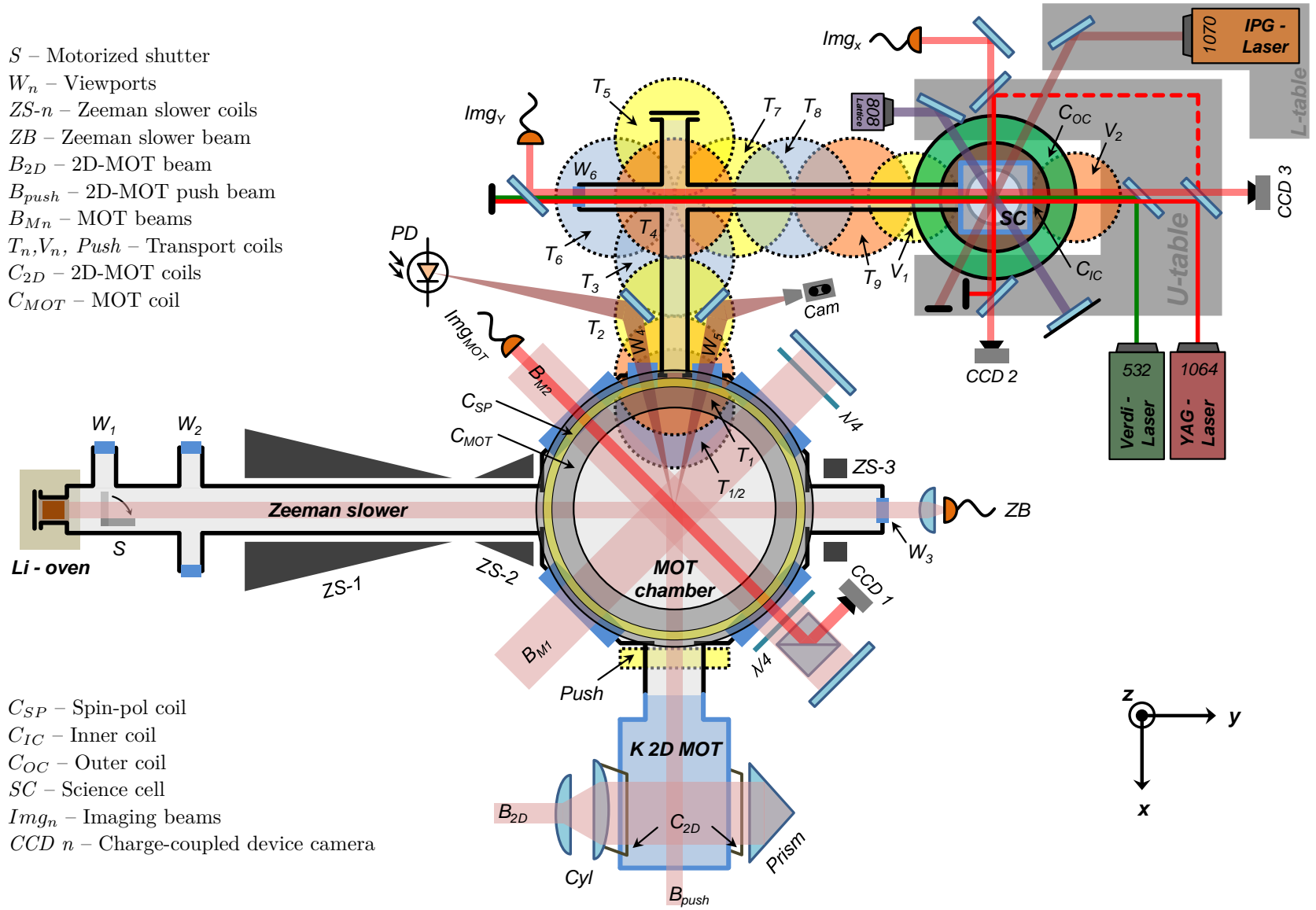


Figure 2.1: Schematic cross section of the FerMix-machine and its main experimental setups.

- After loading both clouds in the ODT, we can take advantage of the broad Feshbach resonance of ^6Li to cool down sympathetically the remaining (smaller) amount of ^{40}K .

Depending on the PSD, either a single mode 10 W (*YAG-laser*, Mephisto-MOPA at 1064 nm) laser is used or a multimode 300 W (*IPG-laser* at 1070 nm) laser. So far, only $1 \cdot 10^5$ lithium atoms were loaded into the 10 W single-beam ODT at 60 μK , without any ^{40}K atoms left after RF-evaporation. The loading into the high-power IPG-ODT is in preparation at this moment.

The YAG-Laser is also used (in different alignment realizations) as a crossed ODT to increase the trap depth at the loading stage, or to increase the collision rate at later stages of optical evaporation stages. In a crossed dipole trap, we cooled down ^{40}K to degeneracy (in absence of ^6Li throughout the whole cooling process), reaching a temperature of $T/T_F \approx 0.2$, where T_F is the Fermi-temperature of the atomic sample in the given harmonic trap.

For the purpose to study the fermionic mixture in two dimensions, a 2D-lattice-laser at 800 nm was build (appendix A). It should confine ^{40}K atoms in standing-wave "sheets" (quasi 2D-traps), while ^6Li would mediate the interactions between distinct 2D-potassium traps[106, 117–119].

2.2 Vacuum Chamber and Atomic Sources

For the observation of fermions in the deeply quantum degenerate regime, it is required to cool down the sample to a few hundred nK. The low temperatures are reached by forced evaporative cooling in either magnetic or optical traps. At this stage, collisions with background gases lead to losses from the trap and might heat up the trapped sample. The competition between background collisions and the time required for evaporative cooling (elastic collisions) might ultimately limit the attainable low temperature. Therefore, a ultra-high vacuum (*UHV*) chamber is required for any cold gases experiment. Figure 2.2 shows a 3D-CAD drawing of the experimental setup with a few length-annotations, to give an impression of the dimensions of the experimental apparatus.

Obviously, in the source regions the background pressure is higher ($\sim 10^{-8}$ mbar). Since the sources need to be heated up either to 80 $^\circ\text{C}$ for the ^{40}K -2D-MOT glass cell or to a few hundred $^\circ\text{C}$ in case of the ^6Li -oven to provide a sufficient atomic flux. Therefore, the 2D-MOT and the Li-Zeeman slower are separated from the MOT-chamber by differential pumping stages². Another ion-pump (20 L/s) near the Li-oven and a following up ion-pump separated from each other by two additional pumping stages in front of the Zeeman slower assure the low pressure stability up to $\sim 10^{-8}$ mbar. A 40 L/s ion-pump attached to the MOT-chamber and two smaller pumps (20 L/s) at the source entrances maintain a pressure of 10^{-10} mbar in the MOT chamber [108]. A differential pumping tube between the transport and the MOT-chamber, two ion-pumps at the elbow of the transport and near the science cell and a special Titanium-Zirconium-Vanadium getter alloy developped at CERN [110] sustain a background pressure of 10^{-12} mbar.

A good indicator of the vacuum quality is the lifetime of a trapped atomic sample. In our case, the life-time of ^{40}K in the MOT-chamber is about 4 s in a magnetic trap of 150 G/cm at a sample temperature of $\sim 250 \mu\text{K}$. By contrast, in the science cell the lifetime in an optical dipole trap (*ODT*) was measured to be more than 100 s. The latter lifetime is more than sufficient for an efficient forced evaporative cooling in an ODT.

²In our case a differential pumping stage consists of a tube, which reduces the opening-aperture from one vacuum region to the next one.

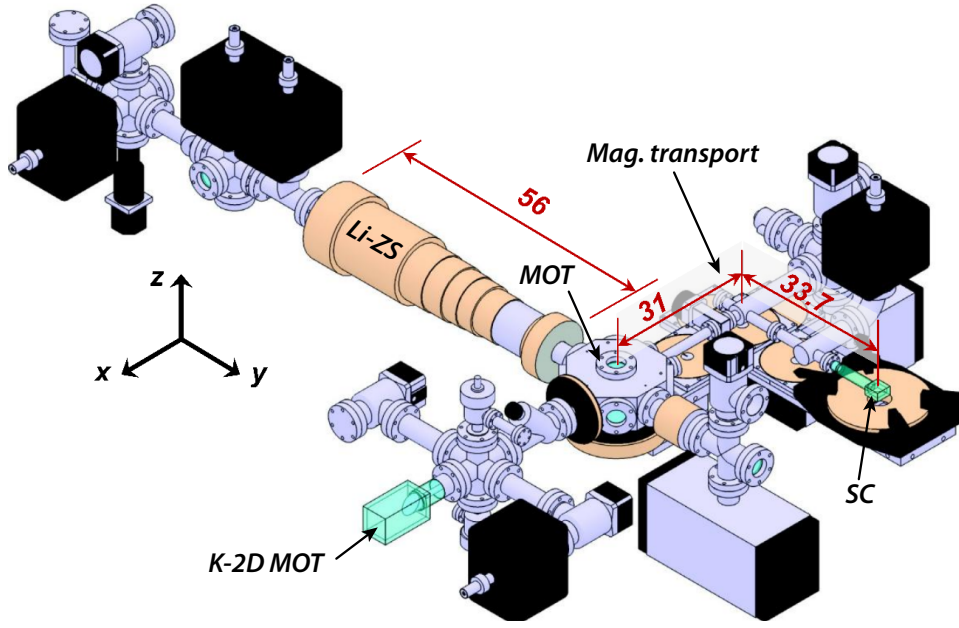


Figure 2.2: CAD-design of the FerMix vacuum assembly (adapted from [111]). The upper transport plate holding the transport coils is removed for better visibility. The length of the Zeeman slower and the magnetic transport are given in cm.

2.2.1 Lithium oven and Zeeman slower

Similar to most ultra-cold lithium experiments today, a Zeeman slower is implemented in the FerMix experiment for the purpose of pre-cooling ${}^6\text{Li}$ atoms [71]. The biggest advantage of the Zeeman slower is the high flux of pre-cooled atoms.

Originally, the atomic source is a highly enriched ${}^6\text{Li}$ -sample³ which is heated up in a metallic tube. This oven assembly is heated up to 470°C during the experimental operation and switched down to 270°C during the night. The oven is never switched off entirely to avoid clogging, especially around the 6 mm-wide aperture through which the atomic jet is released. Likewise, longer overheating (of few hours) to more than 600°C should be avoided, since the sample can be depleted and coat the colder vacuum parts around the Zeeman slower, which in turn would need to be re-heated to port the lithium back to the oven region [120, 121]. An *Omega* temperature controller regulates the temperature of the oven tube, operating the heating current-source by switching a MOSFET.

Once the hot jet of ${}^6\text{Li}$ leaves the oven, it is opposed by a red-detuned (450 MHz from the D_2 -transition line) circularly polarized laser beam (ZB in fig. 2.1), which enters the MOT-chamber through the window W_3 . The slowing process relies on the recoil of the atom, opposite to its travel direction, once it absorbs a photon from the counter-propagating beam. To adjust the Doppler-shift along the path, the magnetic field has to be varied: Slowed down atoms require a smaller Doppler-shift towards the MOT region in order to continue the cooling process. Fig. 2.3 shows the evolution of the magnetic field along the Zeeman slower.

The implemented Zeeman slower is of the "spin-flip" type: This avoids primarily the use of resonant light in the MOT region and therefore has no disturbing influence on the already trapped atoms. However, this design-consideration requires an additional repumping beam.

³The natural abundance of lithium is 5 % of ${}^6\text{Li}$ and 95 % of ${}^7\text{Li}$.

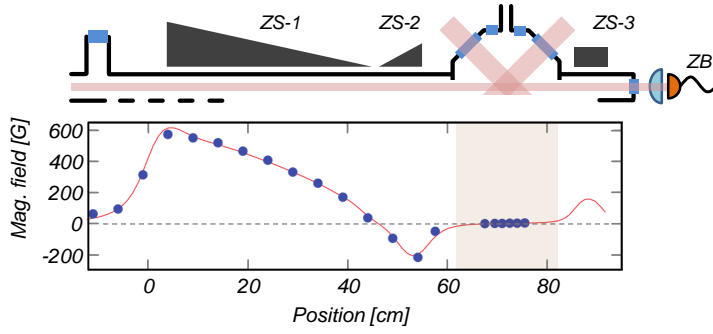


Figure 2.3

Magnetic field of the Zeeman slower, adapted from [108]. In the MOT region the field is compensated by ZS-3 to zero.

At a particular point, the axial magnetic field crosses zero and changes the sign. In this region the atoms might not follow adiabatically the magnetic field transition, losing their polarization and changing their spin state over an absorption cycle. That necessitates the generation of an additional repumping frequency, in contrast to the application of a "classical" Zeeman slower with constant magnetic sign. Another advantage of the spin-flip design is the lower current used to generate a lower field at the entrance of the slower for similar capture velocities, thereby reducing the overall heat dissipation of the coil assembly.

Apart from this, a compensation-coil ZS-3 is placed on the opposite side of the MOT chamber in order to cancel the residual magnetic field created by the Zeeman slower at the location of the MOT. The two additionally mounted windows W_2 permit the installation of a (short-distance) transverse-molasses cooling stage, in order to collimate the atomic beam from the oven and to further increase the loading flux. The only remaining disadvantage of the Zeeman-slowing technique is the presence of a hot ^6Li -beam whose velocity range exceeds either the capture velocity of the Zeeman slower or later of the MOT. However, in our case this effect is negligible as it can be observed on the combined (dual-species) MOT-phase: While the loading rate for ^{40}K indeed decreases in presence of the hot ^6Li -jet in the MOT chamber, the finally captured atom number of ^{40}K remains unchanged in the MOT.

2.2.2 Potassium 2D-MOT

The main reason for the implementation of a 2D-MOT for ^{40}K rather than a Zeeman slower is its very small natural abundance⁴ [122] and the high pricing for an enriched sample⁵. Very recently, it also became difficult to find a company producing enriched ^{40}K samples.

Our enriched 100 mg sample of potassium contains 4 % of ^{40}K (89.5 % of ^{39}K and 6.5 % of ^{41}K). The original source was a CF16-tube near the 2D-MOT glass cell (acting as a "oven"), which was heated moderately to create a sufficient vapor pressure. A malfunctioning of the surrounding heating caused a migration of the source from the oven. Since that incident, a cold point was installed as a controllable source (see fig. 2.4): While the 2D-MOT-glass cell and the surrounding vacuum parts are heated, water-cooled tubes are wound near the entrance of the 2D-MOT. For a sufficiently large temperature gradient, the potassium vapor condenses in the form of a crystalline deposit around the cold region. Contrariwise, decreasing the temperature difference between the hot surrounding and the cold point leads to an evaporation of potassium

⁴The natural abundance of potassium is 93.258 % of ^{39}K , 0.012 % of ^{40}K and 6.730 % of ^{41}K .

⁵In 2007 / 2008, the price for the originally placed 4 % - ^{40}K enriched sample was 4000 € per 100 mg. The price and availability discrepancy between ^{40}K and ^6Li is due to the significance of lithium in the nuclear industry. By contrary, pure ^{40}K has no specific industrial application.

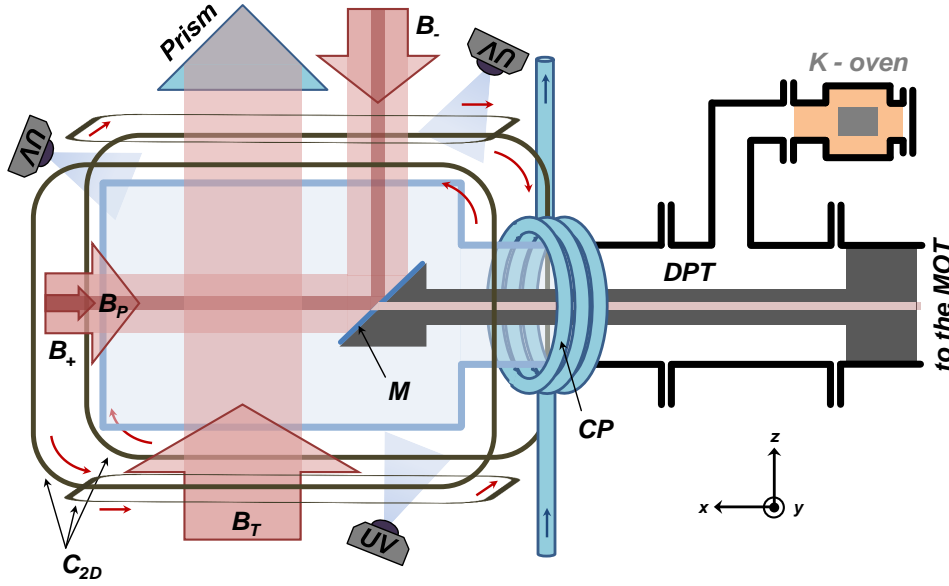


Figure 2.4: Schematic setup of the ^{40}K 2D-MOT. The square glass cell is denoted in blue, other vacuum parts in black. The abbreviations are: **DPT** – differential pumping tube; **M** – mirror surface of the DPT; **UV** – UV-LEDs for LIAD; B_-/B_+ – axial molasses beams; B_P – push beam; B_T – transversal cooling beam, the reflection by the prism inverts the helicity of the circular polarization (the second beam in y -dir. is not depicted); **CP** – cold point; C_{2D} – race-track coils (the red arrows denote the current-flow direction).

into the 2D-MOT cell, thereby increasing the vapor-pressure. A chiller (*T255P* of *ThermoTek, Inc.*) stabilizes the temperature of the distilled water or a cooling liquid (inhibited Glycol) circulating in the tubes around the cold point. During the night, the chiller is set to -2°C , while during operation of the experiment the temperature of the coolant is kept at 45°C .

The 2D-MOT as a pre-cooling stage for ^{40}K is widely used⁶ [71] and therefore we will omit a detailed description at this point. The only peculiarities of our setup are first, the axial molasses, created by the axial beams B_- and B_+ , and second, the smaller push-beam B_P which increases the atomic flux through the differential pumping tube (**DPT**) into the MOT chamber.

Additionally, UV-LEDs (*Roithner LaserTechnik LED395-66-60-110*) shining incoherent light at 395 nm on the 2D-MOT cell are installed to increase the vapor pressure. The underlying principle is known as light-induced atomic desorption (*LIAD*): Similar to the photo-electric effect, potassium atoms get released from the illuminated surface by absorbing a photon [123–125]. In our case, the main deposition of potassium was found on the differential pumping stage and of course in the region of the cold point. Three of the previously mentioned LEDs, with a total output-power of $\sim 1.4\text{ W}$, are directed towards these regions. Nevertheless, we found that continuous operation of the LEDs can disturb the MOT loading. Therefore, the light is being pulsed periodically at 12.5 Hz during the MOT loading phase (see appendix E for technical details).

Figure 2.5 shows an example of the MOT fluorescence signal emitted by the cloud and recorded during loading by a photo diode, with and without the UV-LEDs pulsing throughout the entire loading process. Keeping in mind, that at this stage the fluorescence signal represents only a

⁶ Another common technique is the implementation of ^{40}K dispensers with a direct loading of the MOT. However, this leads to lower loading rates and smaller total atom numbers (e.g. compare [123]).

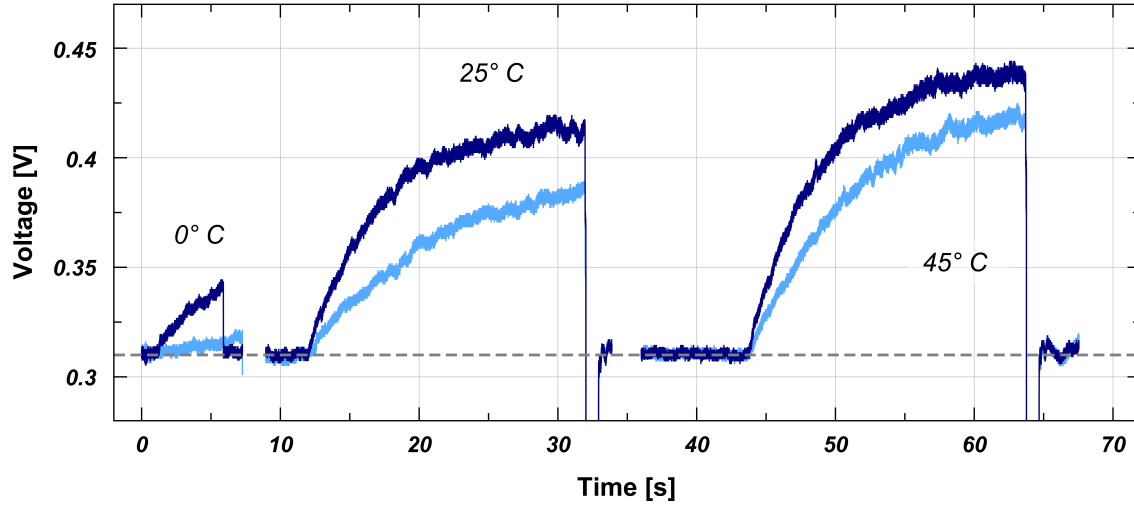


Figure 2.5: Fluorescence signal during MOT loading: Influence of LIAD through the UV-LEDs. The figure shows the loading curves for three different cold point temperatures (0°C , 25°C , 45°C), without the UV-LEDs (light blue) and with UV-LEDs (dark blue). The signal is recorded with the photo diode (PD) indicated in fig. 2.1. In presence of the pulsed blue light, the loading curves are steeper and a higher fluorescence level, and hence atom number is reached. For a quantitative analysis, atom-number images were taken to obtain the data points in fig. 2.6b.

qualitative detection method, we still see an increase of up to 20 % in the total fluorescence signal in presence of the UV-light.

For a further quantitative analysis, we record the atom numbers directly by taking absorption images. The result is summarized in fig. 2.6a, where the variable potassium vapor pressure in the 2D-MOT cell is depicted as a function of the cold point temperature, both with and without the application of the UV-light. The partial pressure of ^{40}K is smaller by the abundance factor 25. The complementary fig. 2.6b shows the loading rate of ^{40}K in the 3D-MOT. At the operation temperature of 40°C of the cold point, the UV-LEDs increase the peak pressure by 50 %. A similar increase is visible in the loading rate. However, the total atom number after 18 s of MOT loading is about 30 % higher with the application of UV-light than without.

2.3 Optical System

To operate the Zeeman slower, 2D-MOT and the common 3D-MOT, light of the appropriate wavelengths and detunings from the respective atomic transitions needs to be generated. For the cooling techniques mentioned so far, we use the D₂-line transitions of ^6Li and ^{40}K . In FerMix, the laser setup follows the *MOPA*-principle (**M**aster **O**scillator – **P**ower **A**mplifier): Light from a laser diode (*DL*), which is frequency locked to an atomic transition, is amplified by a tapered amplifier (*TA*). The light is further divided into multiple paths, and the frequencies of the beams are shifted by acousto-optical modulators (*AOM*). To reach large detunings from the lock-frequency, some AOMs are operated in double-path mode: once the beam got shifted, it is retro-reflected and diffracted a second time in the AOM on the way back, resulting in a doubled shift of the light frequency. AOMs are driven by radio-frequency signals projected on an internal crystal. The driving frequency (60 MHz to 300 MHz) can be varied by voltage

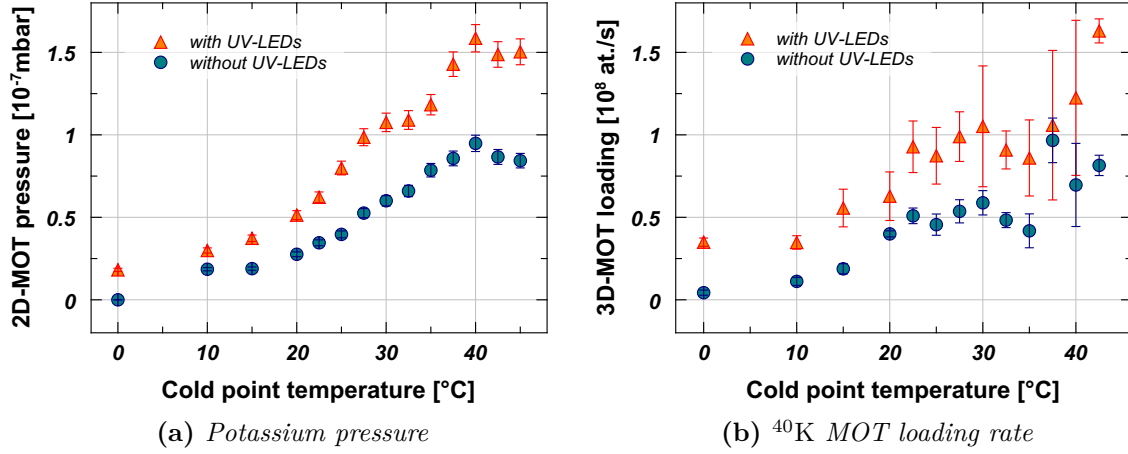


Figure 2.6: Characterization of the cold point performance with and without the LIAD-effect: **(a)** Potassium vapor pressure as a function of the cold point temperature. The vapor pressure was measured by light absorption in the 2D-MOT cell according to the technique described in appendix A in [108]. The error bars arise from the uncertainty of the temperature of the 2D-MOT glass cell walls. From the local heating and cooling, the temperature of the cell is estimated in between 30°C and 60°C . **(b)** ^{40}K loading rate into the 3D-MOT as a function of the cold point temperature.

controlled oscillators (*VCO*) as well as the RF-power (from 0 W to 2 W), which is controlled by current- or voltage-driven attenuators.

Since a single amplification stage results in insufficient power after splitting, the light is again amplified by a second TA. At this point, repumper and principal frequencies are mixed and both injected into the TA⁷ [126].

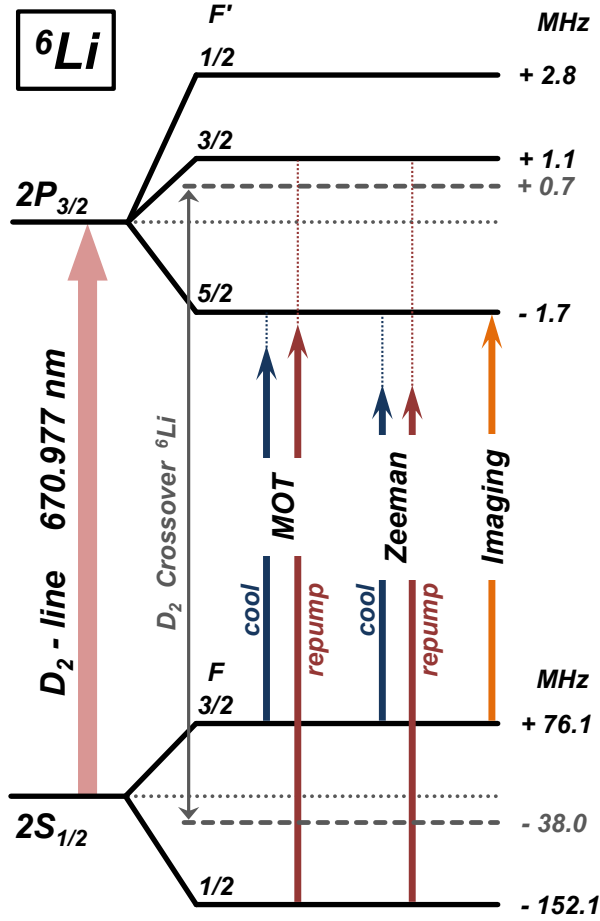
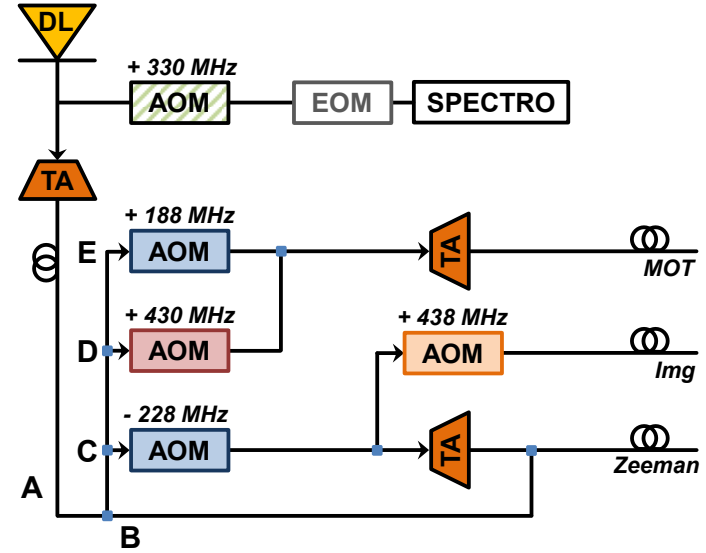
To avoid stray light during magnetic trapping, transport or further evaporation steps, the beams can be interrupted either in few μs by AOMs (see in the case of ^{40}K in fig. 2.8b) or by pre-triggered shutters (few ms-switching time) before being injected into the optical fibers⁸.

Since the amplification of a TA seeded with two different frequencies is non-linear, the final frequency composition of the cooling beams is monitored independently on a Fabry-Perot interferometer.

The optimized values for the frequency composition for the operation of the 2D-MOT, Zeeman slower and MOT can be found in previous works, like [108] or [111]. The actual total powers and frequencies of the different AOMs can be deduced from fig 2.8 and fig. 2.7. An example scheme of a MOPA-setup can be found in the appendix A, where the lattice laser setup is described. Some technical notes about AOM-VCOs are attached in appendix B. Moreover, a new design study for a TA-setup is described in appendix C.

⁷The only exception is the Zeeman slower repumper. Injecting the repumper frequency together with the principle frequency creates a side-band (+228 MHz) which would be resonant with the MOT-cooling transition and heat the ^6Li -MOT during loading.

⁸The resulting, not compensatable frequency shift by available AOM-models, makes it inconvenient to use AOMs as switches in the ^6Li setup in fig. 2.7b

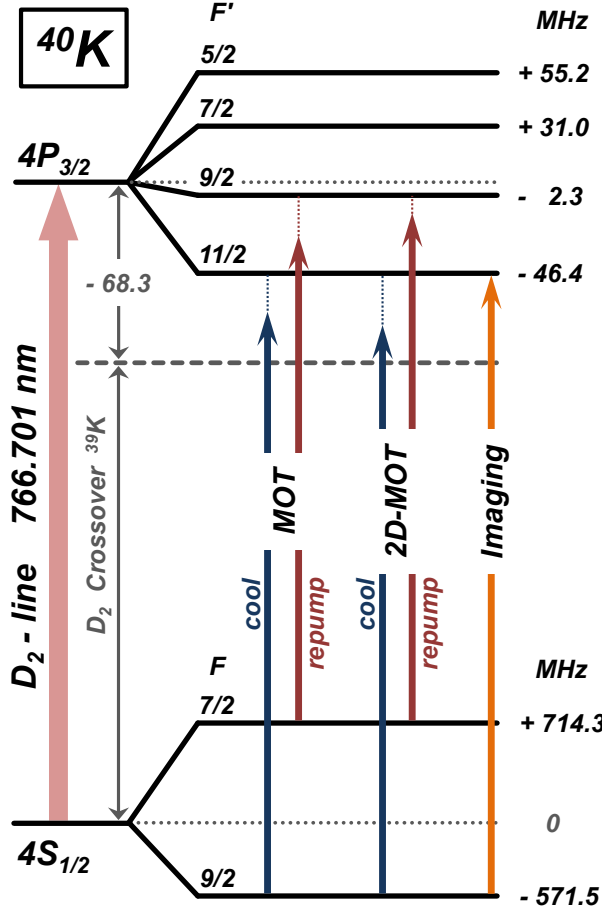
(a) D_2 -line and used cooling transition

(b) Schematic setup of the optical table

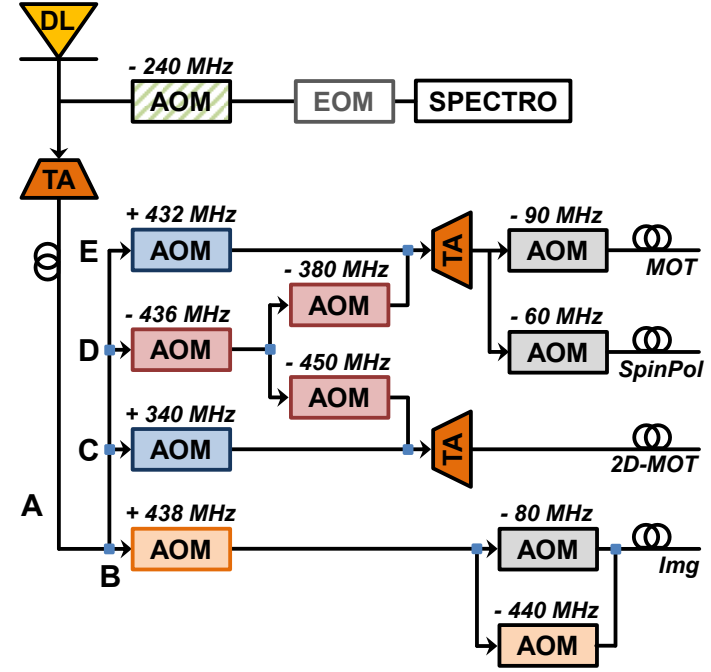
Power splitting (mW)					Fiber-output (mW)		
A	B	C	D	E	Zeeman	MOT	Img
150	30	33	31	40	39	135	5

(c) Power-splitting after the first TA and total fiber-output powers.

Figure 2.7: Optical setup for ${}^6\text{Li}$ D_2 -transitions. (a) Hyperfine structure of the D_2 -line and used cooling / imaging transitions. The master laser DL is locked on the crossover of ${}^6\text{Li}$. (b) Schematic setup of the optical table and the AOM-frequencies to generate the cooling light transitions. Red (blue) AOMs symbolize the repumper (principal)-light generation. **IMPORTANT:** The AOM at the entrance of the spectroscopy path shifts all frequencies by -330 MHz. (c) Power-splitting after the first TA for generating the different beams and total fiber-output.



(a) D_2 -line and used cooling transition



(b) Schematic setup of the optical table

Power splitting (mW)					Fiber-output (mW)			
A	B	C	D	E	2D-MOT	MOT	SpinPol	Img
270	7	40	155	35	400	240	32 (110)	3

(c) Power splitting after the first TA and total fiber-output powers.

Figure 2.8: Optical setup for ^{40}K D_2 -transitions. (a) Hyperfine-structure of the D_2 -line and used cooling / imaging transitions. The master laser DL is locked on the crossover of ^{39}K . (b) Schematic setup of the optical table and the AOM-frequencies to generate the cooling light transitions. Red (blue) AOMs symbolize the repumper (principal)-light generation. In case of the repumper light two (double-path) AOMs are needed to generate the large frequency shift of ~ 800 MHz. The second AOM (-440 MHz) in the imaging path is used for imaging at high bias-fields. **IMPORTANT:** The AOM at the entrance of the spectroscopy path shifts all frequencies by $+240$ MHz. (c) Power-splitting after the first TA for generating the different beams and total fiber output.

2.4 Common MOT

The magneto-optical trap is the first trapping and cooling step of any modern cold atom experiment nowadays. Three pairs of counter-propagating, circularly polarized, red-detuned beams and a magnetic quadrupole field, created by a pair of coils (C_{MOT} in fig. 2.1), cool and trap the atoms around the magnetic field's zero.

The MOT optics, especially the $\lambda/4$ plates for the preparation of circularly polarized light, are optimized for the wavelength of ^{40}K (766.7 nm)[127]. As it is very common, the horizontal beams are retro-reflected, while the vertical pair of beams are aligned independently (not depicted in fig. 2.1). The cooling light for ^6Li (671 nm)[128] is first overlapped with the ^{40}K -beam by dichroic mirrors, before it is splitted in totally four MOT-beams. Two windows, W_4 and W_5 , allow for a "live" observation during the loading process. A camera (Cam) directly records the two fluorescing clouds. Additionally, two photo-diodes (PD) record the fluorescence of each MOT separately (for an example of the recorded signal see above fig. 2.5). The fluorescence signals are easily distinguished by laser line filters for either 671 nm or 767 nm. Finally, an absorption picture of the cloud in the MOT chamber can be taken by a charge-coupled device ($CCD\ 1$). We capture about $2 \cdot 10^9$ atoms of ^6Li and $3.2 \cdot 10^9$ atoms of ^{40}K simultaneously. The single-species operation shows, on average, a slight increase of 10 % in atom numbers.

The MOT cooling scheme possesses a lower limit of the achievable temperatures, the so-called Doppler-limit,

$$k_B T_{\text{Doppler}} = \hbar \Gamma / 2 ,$$

which is $\approx 144\ \mu\text{K}$ for both, ^6Li and ^{40}K , approximating the linewidth by $\Gamma/2\pi \approx 6\ \text{MHz}$. However, due to technical constraints in the dual-species operation, the reachable temperatures after the MOT-phase are higher than these limits ($\sim 800\ \mu\text{K}$ for ^6Li and $\sim 300\ \mu\text{K}$ for ^{40}K). As a result, the clouds are too hot after the common MOT phase to either undergo a magnetic transport without high losses or to have an ensuing efficient forced evaporation inside a magnetic trap.

Therefore, the gray molasses, which is the subject of the next section, was implemented. However, for a better capture efficiency of the molasses, we increase the atomic density (atoms/cm³) of the cloud in a 4 ms long compressed MOT step ($CMOT$). During this step, the MOT-coil gradient increases linearly from 9 G/cm (the usual MOT gradient) to 40 G/cm, which results in a ~ 10 -times higher atomic density.

2.5 Gray Molasses Cooling

The gray molasses method on the D_1 transition line was first implemented in the FerMix machine [114], and is now used in many experiments to reach sub-Doppler temperatures. During this PhD, some investigations on the simultaneous operation of the cooling scheme on ^{40}K and ^6Li [129] and their possible mutual influence have been performed. We will keep the description short and only mention the significant parameters. A detailed discussion can be found in [111] and [110].

2.5.1 Motivation and main idea

A common technique to reach sub-Doppler temperatures is the Sisyphus cooling mechanism implemented in the form of a bright molasses [74]: Two counter-propagating, red-detuned (single-frequency) beams create a standing wave with a spatially periodic modulation of the polarization⁹. This in turn creates a spatially dependent Zeeman shift, resulting in a sinusoidal potential-form seen by the atoms. Together with the resulting light-shift of the addressed closed transition between the two involved states, a moving atom occupying a given stretched Zeeman state is more likely to be pumped into the other involved Zeeman state at the potential maximum than in the potential minimum. Therefore, a travelling atom "climbs" potential hills before being optically pumped back into the energetically lower lying state and repeating the trajectory in the periodic potential. On average, the atom climbs more potential "hills" than rolling down into "valleys", thereby transferring kinetic energy to potential energy. In a $\sigma^- - \sigma^+$ configuration of the counter-propagating beams the theoretical temperature limit is given by [71]:

$$k_B T_{\text{Molasse}} = 0.097 \cdot \frac{\hbar \Gamma^2}{4\Delta} \frac{I}{I_{\text{sat}}} \quad (\Delta \gg \Gamma) ,$$

where Δ is the detuning of the two beams from the resonance, Γ the width of the transition and I_{sat} the corresponding saturation intensity¹⁰. For vanishing intensities, the temperature limit is given by the photon-recoil limit,

$$k_B T_{\text{Recoil}} = 2\pi^2 \frac{\hbar^2}{m\lambda^2} ,$$

which in our case is 3.5 μK for ^6Li and 0.4 μK for ^{40}K .

The narrow structure of the excited state of the D_2 transition (at least for ^6Li , see fig. 2.7) compared to the linewidth of ~ 6 MHz rules out the implementation of a classical single frequency molasses: A closed transition is not present and the transition into other Zeeman sublevels leads to heating¹¹.

A solution is to use the D_1 -transition, which has the advantage of a larger hyperfine splitting of the excited state. Unfortunately, the D_1 -line does not provide a closed transition and therefore a single frequency molasses is not possible.

To overcome this problem, we can use a two-frequency beam which includes an additional repumping part (see fig. 2.11). Different from the bright molasses, where the repumper is used to pump atoms back on the closed transition, the resulting system in our case is known as a Λ -transition cycle [132, 133] (see embedded diagramm in fig. 2.9). Turning to the dressed state picture, it can be shown, that the chosen Λ -scheme with the main "cooling" transition on either $F \rightarrow F' = F$ (^6Li) or $F \rightarrow F' = F - 1$ (^{40}K) involves multiple¹² dark-states [135,

⁹Therefore the initially counter-propagating beams are either of orthogonal linear polarization or opposite circular polarization [71].

¹⁰Compared with the formula given in [71], we assumed a closed transition, setting the Clebsch-Gordan coefficient to $C_{ge} = 1$.

¹¹In case of ^{40}K , a molasses cooling-scheme involving two frequencies (principal and repumper) was implemented on the D_2 -line for a small atomic ensemble containing only $5 \cdot 10^7$ atoms, reaching temperatures as low as 15 μK [130, 131]. As will be mentioned later, we reach a similar temperature range with two magnitudes higher atom number.

¹²The mentioned transitions contain already at least one dark state even in presence of only one driving transition [134]. The implementation of the Λ -transition enhances the coherence of the bare states for a special choice of

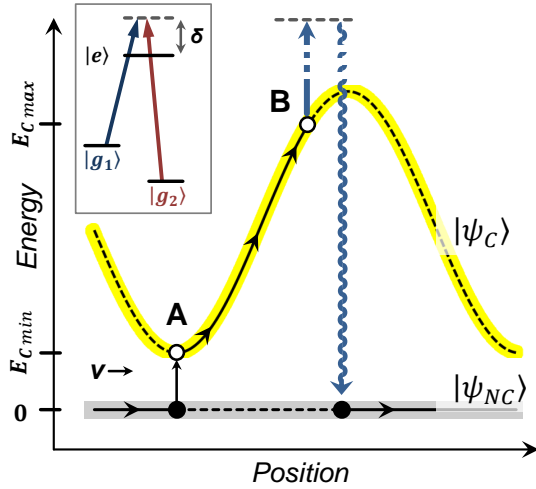


Figure 2.9

Illustration of the gray-molasses cooling scheme, adapted from [137]. The embedded figure in the left upper corner depicts a Λ transition in Raman-condition ($\Delta = 0$). In a simplified manner, the dressed state picture includes a dark $|\psi_{NC}\rangle$ state, which is not coupled to the light field and a bright state $|\psi_C\rangle$, whose eigenenergy is spatially modulated. Due to motional coupling, the atom gets transferred into the bright state valley (A). After losing kinetic energy by climbing the hill, the atom gets optically pumped back into the dark state (B). Being far detuned from the excited state, it is effectively never populated. Repetition of this cycle leads effectively to cooling, similar to the Sisyphus-effect in the bright molasses.

136]: eigenstates of the atom-light-interaction Hamiltonian that are linear combinations of the involved Zeeman sublevels of the ground-state with eigenenergy zero. Dark states do not interact with the light field. The remaining bright states (also linear combinations of the Zeeman levels in the ground-state manifold) contains a similar potential-modulation as in the case of the bright molasses scheme. Here the blue-detuning with respect to the excited state in the Λ -scheme is of special importance. In the blue-detuned case the bright state is light-shifted to positive energies, thus lying energetically higher than the dark state.

The resulting cooling mechanism, known as gray molasses [137], is a combination of the classical molasses (i.e. polarization-gradient cooling) and velocity-selective coherent population trapping (VSCPT) [138]. The mechanism is explained in a simplified manner in fig. 2.9: A hot atom, initially in the dark state, is primarily transferred into the bright state by motional coupling in a region of a bright state minimum. Since the energy difference between the bright state "valley" and the dark state is minimal at this point, the transfer probability is the highest. Once in the bright state the atom travels along its initial direction "uphill" in the potential energy evolution before it is pumped back to the dark state with highest probability at the maximum of the bright state potential¹³. As previously encountered in the bright molasses scheme, the atom loses kinetic energy by gaining potential energy over multiple cycles (Sisyphus effect).

2.5.2 Experimental realization

The resulting gray molasses picture in the dressed states shows that the attribution by cooling and repumping to the involved transitions is misleading. Nevertheless, we will keep these attributions to indicate the cooling beam as the one with higher intensity and the repumping beam as the one with lower intensity. The implemented transitions are depicted in fig. 2.11a and fig. 2.11b. For ^6Li (^{40}K) the power ratio of principal to repumper is found to be optimal (for cooling and atom capture efficiency) at a value of 20 : 1 (8 : 1). Regarding the total intensity I ,

the detuning δ and therefore increases the number of dark states [114].

¹³The excited state is effectively never populated, due to high detuning from the common excited-state in the Λ -scheme.

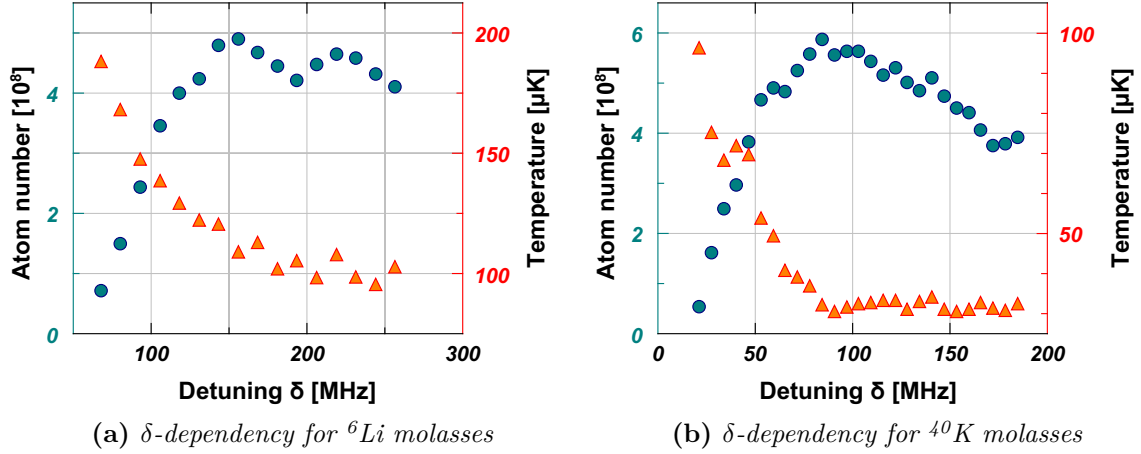


Figure 2.10: Performance of the gray molasses (atom number and temperature) of ${}^6\text{Li}$ and ${}^{40}\text{K}$ for different detunings δ (from [111]). For the current measurement, the atom number of the CMOT was reduced to $8 \cdot 10^8$ for ${}^6\text{Li}$ and $6 \cdot 10^8$ for ${}^{40}\text{K}$. Additionally, the cooling time is extended in case of ${}^{40}\text{K}$ to 9 ms. The final optimization of the cooling-intensity ramp and the residual bias compensation leads to slightly lower temperatures than indicated in this figure.

it can be shown that the capture velocity v_c of the gray molasses as well as the final equilibrium temperature T_{mol} are proportional to the intensity [111],

$$v_c \sim I/\delta^2 \quad \text{and} \quad k_B T_{\text{mol}} \sim I/\delta ,$$

with δ being the detuning from the common excited state (see fig. 2.9). Consequently, at the beginning of the molasses stage, a higher intensity is required to capture the hot atomic cloud, while afterwards, the intensity has to be lowered in order to achieve lower temperatures. The final optimized intensity ramp can be found in the summary in fig. 2.21.

Two important quantities to tune are the relative detuning of the repumper and principal beam Δ as well as the common detuning δ , since both set the coherence between the addressed bare ground states, and therefore define the emergence of dark states. The lowest temperatures are achieved in the Raman condition, where the detuning Δ is zero,

$$\Delta = |\omega_{\text{cool}} - \omega_{\text{repump}}| - (E_{|g_1\rangle} - E_{|g_2\rangle})/\hbar \equiv 0 .$$

An extensive study of the detuning δ [114, 129] yields the optimum values of $\delta = 4\Gamma \sim 151$ MHz for ${}^6\text{Li}$ and $\delta = 2.3\Gamma \sim 87$ MHz for ${}^{40}\text{K}$ (see fig. 2.10). At these values the atom number is maximized, while the temperatures are near their minimal asymptotic values. The frequency shift δ is accounted for within the locking part of the corresponding D_1 diode laser and the switching AOMs (which are also used to ramp down the intensity). The repumping frequency of the ${}^6\text{Li}$ -molasses beam and the cooling frequency in the case of ${}^{40}\text{K}$ are created as frequency side-bands of an electro-optical modulator (EOM) of either 228 MHz or 1286 MHz, respectively. Figure 2.11c shows the implementation in case of ${}^6\text{Li}$ with the corresponding frequencies. In the particular situation of ${}^6\text{Li}$, we take advantage of the small frequency difference of ~ 10 GHz between the D_1 and D_2 transition lines, to offset-lock the D_1 -system electronically on the

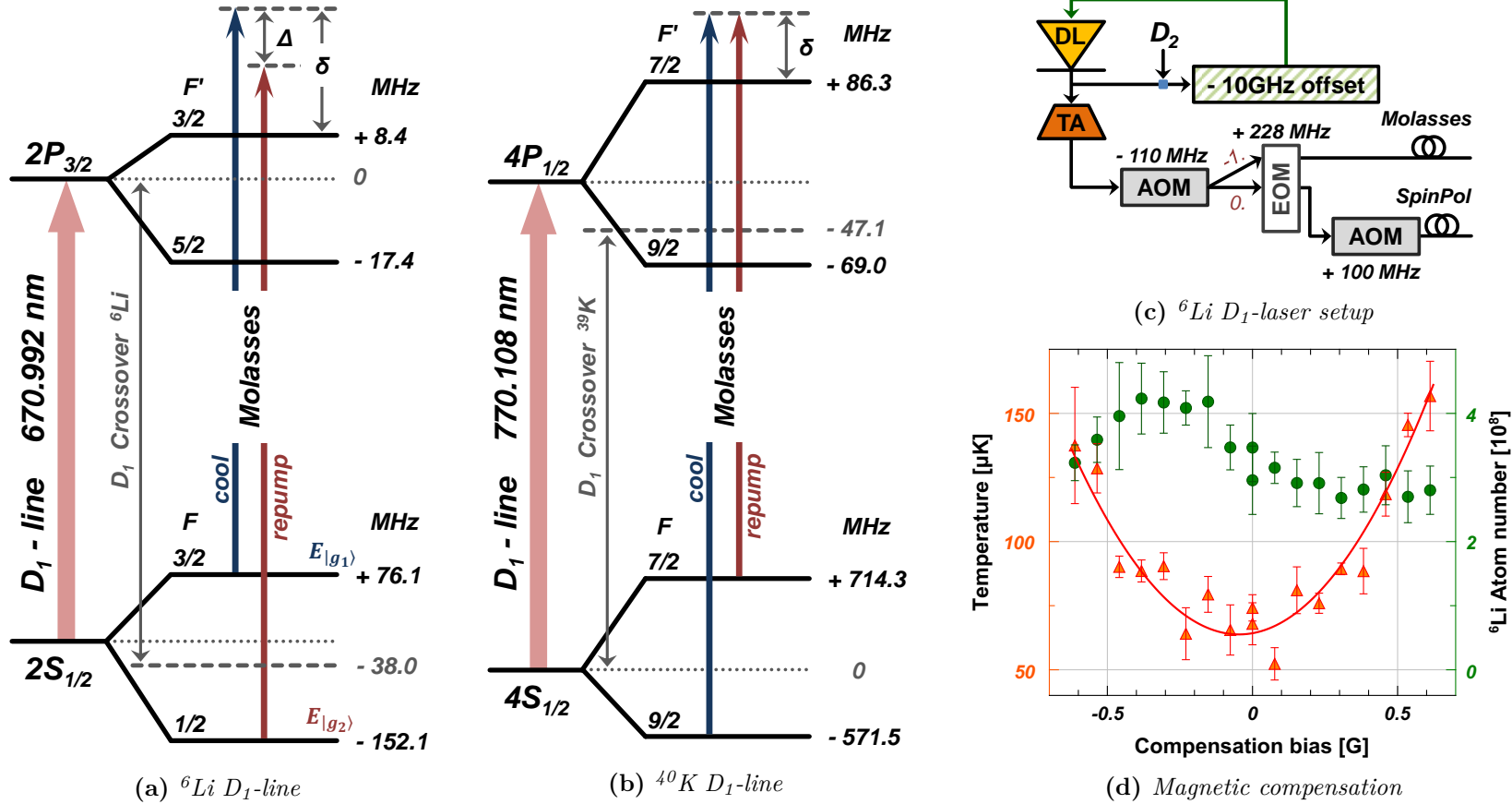


Figure 2.11: Gray molasses setup. (a) and (b) are depicting the transitions used for the gray molasses. In the ${}^6\text{Li}$ -scheme, the non-zero Raman-detuning Δ and the two hyperfine ground-states are labeled according to the Λ -scheme in fig. 2.9. (c) shows the 10 GHz offset-locking scheme for ${}^6\text{Li}$. The EOM creates the "repumping" frequency side-band. The zeroth order of the first D_1 switching AOM also passes through the EOM and is used later on for optical pumping (see sec. 2.6.2). (d) characterizes the temperature dependence of the molasses on parasitic magnetic fields which influence the light-induced Zeeman-shifts on which the molasses scheme is based. The atom number (measured after a subsequent optical pumping step) does not vary within error bars.

absorption spectroscopy of the D_2 -transition [110]¹⁴.

The spatial Zeeman splitting created in the molasses should be light induced only, thus any parasitic magnetic field has to be canceled. Therefore, we use three compensation coils around the optical table. The scan of the bias in one compensation coil in case of the ^6Li molasses is shown in fig. 2.11d. While the atom number is constant within error bars, the temperature increases by a factor three from 50 μK to 150 μK by having only a small bias of 0.6 G present.

After the 5 ms long gray molasses step we obtain $4 \cdot 10^8$ atoms of ^6Li and $1.4 \cdot 10^9$ atoms of ^{40}K at a usual temperature of $\sim 60 \mu\text{K}$ and $\sim 20 \mu\text{K}$ respectively. It remains unclear, why the reached temperatures are so far from the recoil-limit.

An alternative to the D_1 gray molasses, at least for ^6Li , is the implementation of an UV-MOT, which takes advantage of a smaller line-width and therefore a reduced Doppler-temperature limit [139, 140]¹⁵. However, the UV-technique requires a more complicated expensive laser setup, while in average not reaching better performances than the D_1 -cooling scheme. Numerous experiments around the world are now using the gray molasses technique for cooling down other species than the two presented above [142–146]. In [147] the gray molasses was continued to further cool the atomic ensemble after it had been loaded into an optical dipole trap.

2.6 Magnetic Trapping

The techniques of magnetic trapping and optical pumping described in this section prepare the basis for the chapter 3, where we will analyse the quasithermalization of non-interacting particles in a quadrupole-trap.

Magnetic trapping by a pair of coils in anti-Helmholtz configuration was one of the first trapping techniques for neutral atoms [148]: The magnetic field is created by having the same current flowing in opposite directions in the coaxial-arranged coil pair. It is one of the simplest magnetic trap implementations and it was the first trap in which quantum degeneracy was realized [149]. The pure setup of a coil-pair in anti-Helmholtz configuration is also referred to as a *quadrupole trap*.

The field near the origin O created by a pair of axially aligned coils [150] can be expressed by

$$\mathbf{B} \cong b \cdot \begin{pmatrix} x \\ y \\ -2z \end{pmatrix}. \quad (2.1)$$

The geometrical properties of the coil assembly can be summarized in the constant b , describing the gradient of the magnetic field (in units of G/cm). Atoms with a magnetic moment $\boldsymbol{\mu}$ obtain a potential energy of

$$E = -\boldsymbol{\mu} \cdot \mathbf{B} = -\mu_B g_F m_F |B|. \quad (2.2)$$

Thereby $\mu_B = e\hbar/2m_e$ is the Bohr magneton, g_F the Landé factor of the hyperfine state and m_F

¹⁴It should be emphasized, that the AOM in the locking-path of the D_2 systems shifts the locked frequency by +330 MHz (see fig. 2.7b) compared to the crossover-transition. Thus the first D_1 -switching AOM in fig. 2.11c (−110 MHz) together with the fine tuning of the 10 GHz-oscillator (~ 60 MHz) corrects the offset in order to achieve the cooling marked "cooling" transition in fig. 2.11a.

¹⁵The only approach of a narrow line cooling for ^{40}K published so far, can be found in [141]. While the 405 nm transition has a line-width of 1.2 MHz in this case, the blue transition at 323 nm for ^6Li has a line-width of 160 kHz only.

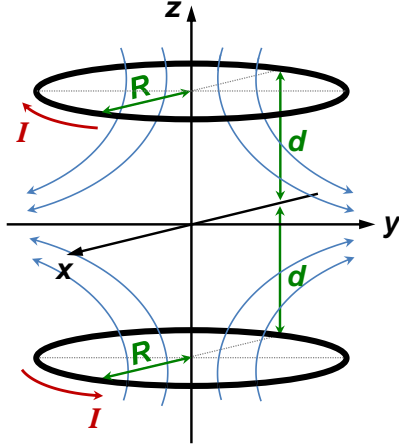


Figure 2.12

Illustration of a coil-pair of radius R and mutual distance $2d$ in anti-Helmholtz configuration. Blue lines denote magnetic field lines. Adapting the geometrical constraint from the Helmholtz-configuration, where $d = R$, the gradient-factor b of eq. (2.1) is in this particular approximation

$$b = \frac{48}{25\sqrt{5}} \frac{\mu_0 I}{R^2},$$

taking into account a single winding of radius R .

the number of the Zeeman sub-level, where the atomic state is quantized along the magnetic field. For the stretched states with the highest m_F number the magnetic moment is maximized, being $\mu \equiv \mu_B$. The potential energy of an atom with magnetic moment μ , which follows adiabatically the magnetic field near the trap center is given by:

$$U(\mathbf{r}) = \mu b \sqrt{x^2 + y^2 + 4z^2}. \quad (2.3)$$

The adiabatic following is important, since the scalar product in eq. (2.2) was simplified in eq. (2.3) to the simple product of the absolute values of the magnetic field \mathbf{B} and the magnetic moment of the atom $\boldsymbol{\mu}$: the magnetic moment of the atom is all the time aligned with the magnetic field. In the next section we will discuss, which states m_F can be trapped in the magnetic quadrupole potential.

2.6.1 Trappable ground states of ^6Li and ^{40}K

Depending on the sign of the magnetic moment and its evolution as a function of the magnetic field B , some atomic states can be trapped in magnetic minima (*low-field seeking states*). Other states (*high-field seeking states*) follow the magnetic fields towards its maxima. Local magnetic field maxima in static fields are forbidden by Maxwells equations, hence high-field seeking states are not trappable by static magnetic fields. Figure 2.13 shows the energy evolution of the ground states of ^6Li and ^{40}K . States with continuously increasing energy as a function of the magnetic field strength are low-field seeking states.

For ^6Li (fig. 2.13a) the ground state $2^2\text{S}_{1/2}$ contains four low-field seeking states in the low bias region. The Zeeman-state $|F = 1/2, m_F = -1/2\rangle$, is in a trappable low-field seeking-regime up to ~ 30 G. With further increasing bias it becomes a not-trappable high-field seeking state. Up to the turning point, the trap depth¹⁶ for this state is only 0.3 mK, which is lower than the achieved steady state temperatures in the experiment. On the contrary $|F = 3/2, m_F = -1/2\rangle$

¹⁶The trap-depth is calculated by the energy difference between the state at zero-field and the given magnetic field:

$$T = \frac{h}{k_B} \cdot \Delta E = \frac{h}{k_B} \cdot [E(B = 30 \text{ G}) - E(B = 0 \text{ G})],$$

where $h = 2\pi\hbar$ is the Planck constant and the B -field dependency of $E(F, m_F, B)$ can be obtained by the Breit-Rabi formula or from fig 2.13a.

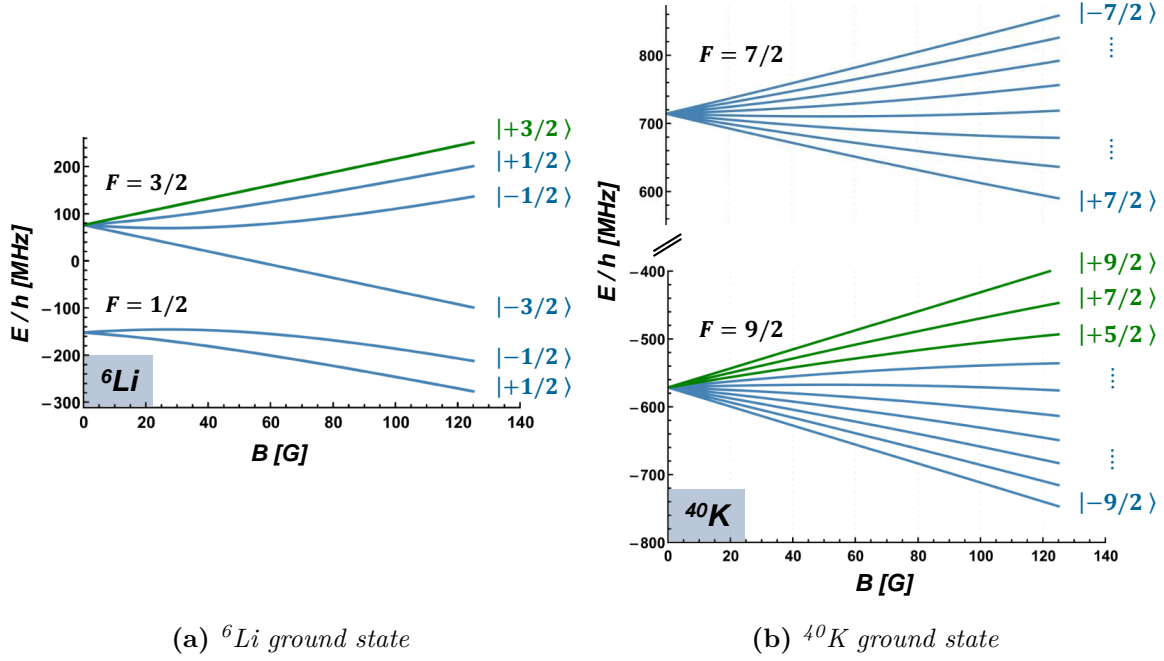


Figure 2.13: Zeeman-splitting of the hyperfine-ground states of ${}^6\text{Li}$ (a) and ${}^{40}\text{K}$ (b). The energy evolution of each Zeeman-state as a function of the bias field is calculated by applying the Breit-Rabi formula [151].

is a high-field-seeking state (having a negative-slope in fig. 2.13a) until ~ 25 G. From the remaining two states, $|F = 3/2, m_F = +1/2\rangle$ is not stable against spin-exchange collisions:

$$|F = 3/2, m_F = +1/2\rangle + |F = 3/2, m_F = +1/2\rangle \rightarrow |F = +3/2, m_F = +3/2\rangle + |F = 1/2, m_F = -1/2\rangle + E_{kin} . \quad (2.4)$$

The released kinetic energy is of the order of the hyperfine splitting (228.2 MHz), which corresponds to ~ 11 mK. This is sufficient to expel the colliding atoms from the trap. Finally, the only stable magnetically trappable Zeeman ground-state of ${}^6\text{Li}$ is the stretched state $|F = 3/2, m_F = +3/2\rangle$. It is energetically the highest Zeeman state of the $2^2\text{S}_{1/2}$ ground state.

For ${}^{40}\text{K}$ (fig. 2.13b) the picture is different, due to the inverted hyperfine structure: The hyperfine state with the larger magnetic moment is the energetically lower-lying $|F = 9/2\rangle$ manifold. This manifold contains the low-field seeking states $|F = 9/2, m_F = +9/2\rangle$ and $|9/2, +7/2\rangle$ which are important for the further evaporative cooling process. A sample consisting only of this two Zeeman-states is stable against spin-exchange collisions. However, in case of the presence of $|F = 9/2, m_F = +5/2\rangle$ states, spin-exchange collisions of the form

$$|9/2, +7/2\rangle + |9/2, +5/2\rangle \rightarrow |9/2, +9/2\rangle + |9/2, +3/2\rangle$$

are possible [152]. The heating and loss-rate for this process was studied in [149].

Clearly, in the previously discussed magnetic trapping potential described by eq. (2.1), the low-field seeking states will experience a resetting force towards the trap center. At the center, where the magnetic field vanishes, the atomic spin might not follow adiabatically the magnetic

field and thus the spin might flip to another state. This state in turn might be a high field seeking state and therefore the atom gets expelled from the trap. This mechanism is called *Majorana losses* and will be discussed in sec. 5.2.

2.6.2 Optical pumping

In the presence of the molasses-light, the atoms occupy a dressed state consisting of the two hyperfine ground states of $2^2S_{1/2}$ for ^6Li and $4^2S_{1/2}$ in the case of ^{40}K . Additionally, no magnetic field is present during the molasses phase. Once the molasses light is switched off, the atoms are distributed within the two hyperfine-state occupying a random Zeeman-state.

During 470 μs , we switch on a magnetic field of few Gauss (generated by the coils C_{SP} in fig. 2.1). Once the field is established (after $\sim 400 \mu\text{s}$), we apply optical pumping with a σ^+ -polarized beam to pump the atoms into the stretched, trappable Zeeman states $|F = 3/2, m_F = +3/2\rangle$ for ^6Li and $|F = 9/2, m_F = +9/2\rangle$ for ^{40}K .

- For ^6Li we use the D_1 -transition, since the hyperfine-structure of the D_2 -line is too narrow compared to the linewidth (5.9 MHz). The main pumping transition is $F = 3/2 \rightarrow F' = 3/2$. It is not a closed transition and atoms decaying in the $F = 1/2$ state are repumped to $F' = 3/2$ by the second frequency generated in the D_1 molasses beam (see scheme in fig. 2.11a). Recycling the molasses setup, the optical pumping beams are blue-detuned in this case. The spin polarization pulse is chosen to 50 μs for ^6Li .
- For ^{40}K , we use the MOT-light to drive optical pumping on the D_2 -line. The detuned principal beam (see fig. 2.8a) drives the closed transition $F = 9/2 \rightarrow F' = 11/2$ and $F = 9/2 \rightarrow F' = 9/2$. While the first transition is closed, and therefore no repumping is needed, it will lead to heating once the atom is in $m_F = +9/2$. In the second proposed transition the absorption cycle stops once the atom reaches $m_F = +9/2$, since no further state can be addressed by σ^+ -light in $F' = 9/2$. Meanwhile, atoms initially in the $F = 7/2$ hyperfine state or atoms which decayed within the $\Delta F = 0$ process, are addressed by the repumping beam and eventually decay into the $F = 9/2$ state. The principal-beam power is reduced to avoid excessive heating during the pumping process (for the optimized values see fig. 2.21). Also, the light pulse is applied during the last 70 μs of the spin-polarization step to reduce the heating.

The slightly different detunings from the usual MOT/ D_1 -transitions can be deduced from fig. 2.11a, fig. 2.8a and fig. 2.21. The duration of the spin-polarization step should be short, since the atoms are not trapped during this stage. Experimentally, the shortness is limited by the switch-on time of the previously mentioned magnetic field. Nevertheless, the power of the pumping beam can be varied: Figure 2.14 shows the total atom number captured subsequently in a magnetic trap of a gradient of 150 G/cm as a function of the optical pumping intensity. We fix the total pumping powers in terms of the saturation intensity¹⁷ at $2I_{\text{sat}}$ for ^6Li and $7I_{\text{sat}}$ for ^{40}K . In fig. 2.14b we observe a continuous increase in temperature by increasing the intensity of the pumping beam.

2.6.3 Spin-composition test

The trapped spin composition of the ^{40}K cloud can be tested to some extent by decreasing the magnetic trap gradient b . Indeed, atoms with different spin states have different potential

¹⁷For the D_1 -line of ^6Li the saturation intensity is $I_{\text{sat}} = 7.59 \text{ mW/cm}^2$ [128]. For the D_2 -line of ^{40}K the value is $I_{\text{sat}} = 1.75 \text{ mW/cm}^2$ [127].

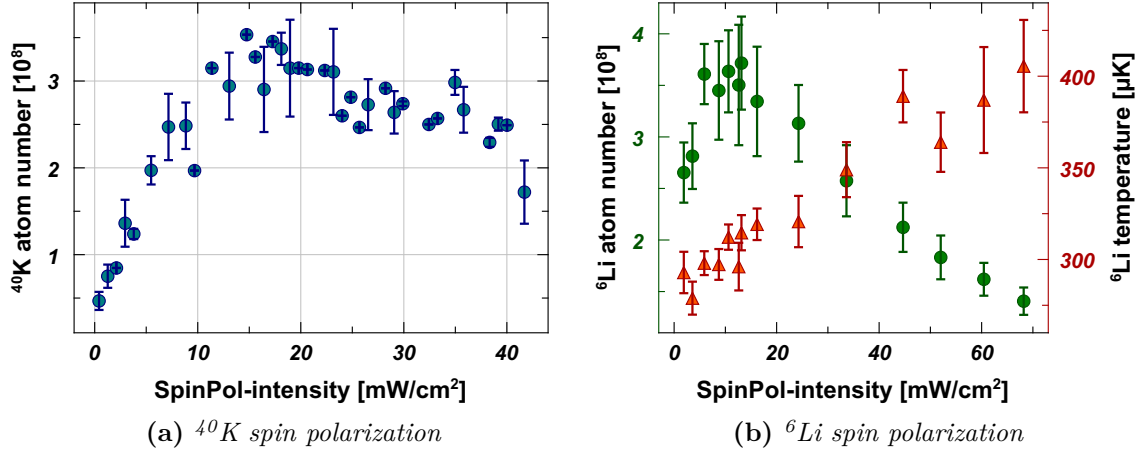


Figure 2.14: Number of magnetically trapped atoms (blue / green dots) as a function of optical pumping intensity. In (b) the temperature of the ^6Li cloud along the pumping direction is measured (red triangles) additionally. Both pumping beams have a waist of $\omega_0 \sim 5.1\text{ mm}$. The intensity is calculated as peak-intensity, $2P/\pi\omega_0^2$, where P is the total power of the beam.

energies in the magnetic trap. Combining eq. (2.2) and eq. (2.3) regarding the z -direction only:

$$E_{\text{trap-}z} = \mu b' |z| = \mu_B g_F m_F b' |z|, \quad \begin{cases} F_{\text{trap-}z} = -\mu_B g_F m_F b' \mathbf{e}_z & z > 0, \\ F_{\text{trap-}z} = +\mu_B g_F m_F b' \mathbf{e}_z & z < 0, \end{cases}$$

we will use $b' = 2b$ to denote the gradient along the strong-confining axis z . The second expression shows the restoring force of the trap along the z -direction (\mathbf{e}_z is the unity-vector in z -dir.). Now, including the gravitational force, we can formulate the following trapping condition for $z < 0$:

$$\mu_B g_F m_F b' \geq m_K g, \quad (2.5)$$

where $g = 9.81\text{ m/s}^2$ and m_K is the atomic mass of ^{40}K . Reducing the gradient b' of the trap will lead to spilling of the spin states with smaller Zeeman-number m_F first. Ideally, spin states with $m_F = 5/2$ are lost at $b' = 12.8\text{ G/cm}$, states with $m_F = 7/2$ at $b' = 9.1\text{ G/cm}$ and finally at $b' = 7.1\text{ G/cm}$, the stretched state $m_F = 9/2$ is not trapped anymore against gravity.

In fig. 2.15a the atom number as a function of the magnetic trap gradient b' is plotted. In the experimental sequence, the atoms are first trapped in a confining trap of high gradient of $b' = 150\text{ G/cm}$. Afterwards, the gradient is reduced in 100 ms to the different gradient- b' values and held at this value for another 500 ms before a picture is taken. Different from the previously described ideal picture, the atomic cloud has a non-zero temperature, and therefore obeys the Boltzman velocity distribution. At a given temperature, the finite size of the created trap gradient or even the boundaries of the experimental chamber compared to the cloud size lead to spilling of atoms from the trap before the values discussed above are reached. Additionally, ongoing evaporation, due to the lowered magnetic gradient (a process, which is performed not sufficient adiabatically in this case) leads to the washing out of discrete steps in fig. 2.15a. The complication of the idealized picture allows only a rough ratio estimation of the spin population. We estimate the proportion of a given spin state by averaging the atom number value in the vicinity of the corresponding calculated magnetic field gradient. However, it is so far the only

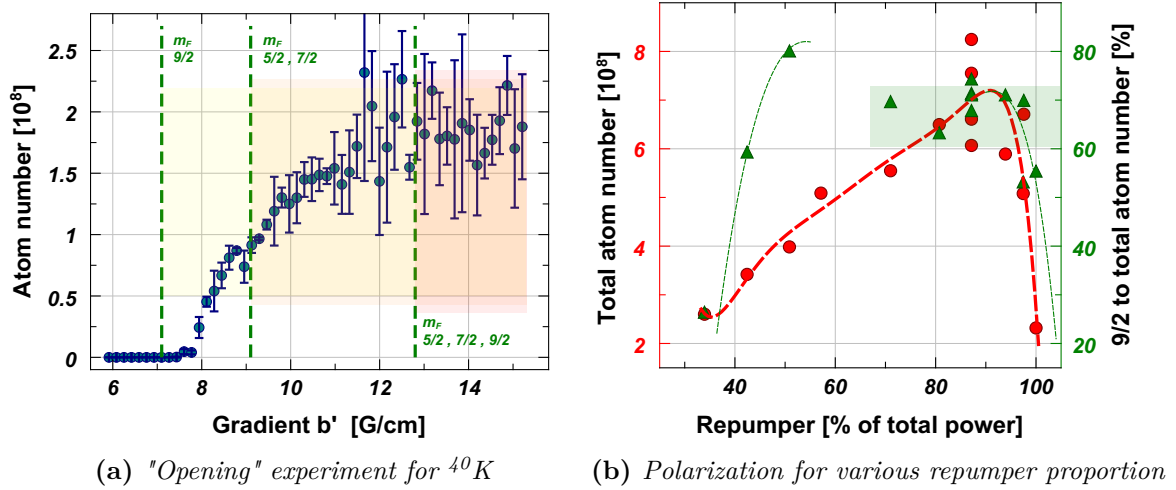


Figure 2.15: Spin composition analysis for ^{40}K : (a) Example of an "opening" experiment for ^{40}K . Lowering the gradient b' let the different spin states fall out of the trap against gravity. Green dotted lines mark the gradients (lower bound) at which the indicated spin-states are not held against gravity in the ideal case of zero temperature. (b) Polarization / total atom number for various repumper / principal proportion (the x-axis denotes the proportion of repumper to the total beam power in %). The red line is a polynomial fit to the total atom number trapped in a confining trap of 150 G/cm. Green triangles denote the proportion of $m_F = 9/2$ to the total atom number (in %). The optimum lies at $\sim 90\%$ repumper with $\sim 70\%$ of atoms in the stretched state.

spin detection method of the relatively hot cloud ($\sim 250\ \mu\text{K}$) in a magnetic trap.

The used spin-polarizing beam is bichromatic (see sec. 2.6.2) and the relative composition of principal and repumping beam is not obvious. In figure 2.15b this ratio was varied, while the total power was constant within 30 %. Apparently, most atoms are captured having the majority of 80 % to 90 % of repumper power in the pumping beam. The spin proportion of 9/2 in the total atom number fluctuates about $\pm 15\%$ not at least because of the above described difficulties to extract the spin composition. Nevertheless, at the above region of maximally loaded atom number, about 70 % of the atoms are in the stretched $m_F = 9/2$ state.

The optimal spin polarization at this stage is important, since it affects the later RF-evaporation in the science cell (see sec. 5.3.2). Afterwards, the only precise spin manipulation can be done once the atoms are loaded in an ODT.

2.6.4 Transport

In cold gases experiments, there are in principle different approaches to transport a cold cloud from the MOT-region to an UHV-section with better vacuum quality and greater optical access. The transport can be done optically by moving the focal point of a high-power laser beam [153, 154], by moving magnetically the trap center of a quadrupole trap [155] or even by a simple ballistic flight [156]. While the setup of an optical transport is comparably smaller and easier to implement, an advantage of a magnetic transport is its robustness: Once installed, no maintenance, like realignment of optics, is needed. Also going along angled trajectories is easily feasible with magnetic transports.

One realization of magnetic transport consist of a pair of coils mounted on a mechanical

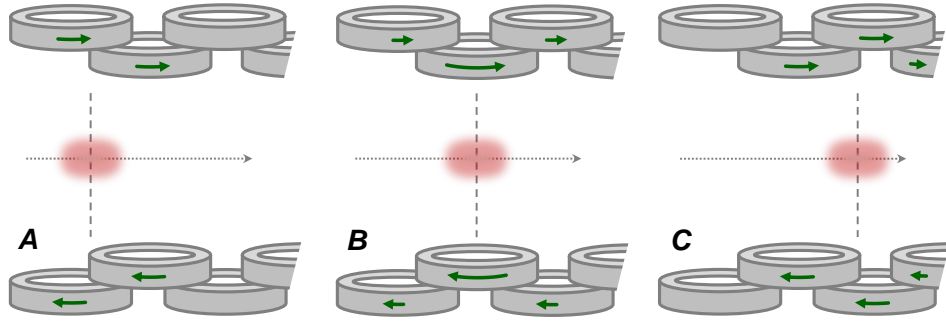


Figure 2.16: Principle of magnetic transport. The cloud is transported from A to C, while always three coil pairs are operated. This is necessary to keep the aspect-ratio of the trap constant as well as to allow for smooth switching of the currents. The length of the green arrows indicate the current direction and strength in each coil. The cloud is attracted towards the center of a quadrupole trap, which is a superposition of the three traps at each time. For more details see [111].

translation stage [157–159]. This design demands high mechanical stability and controlled acceleration behavior of the stage. In the FerMix experiment, the magnetic transport uses a different technique to avoid mechanical limitations: Twelve fixed pairs of partially overlapping coils are switched smoothly to move the magnetic trap center towards the science cell. Three coil pairs are always active at the same time to ensure a continuous movement without changing the trap aspect-ratio in order to avoid heating of the cloud. Figure 2.16 shows the principle of the magnetic transport. For a detailed discription of the transport implementation, the reader is referred to [111].

The transport plate holding the coil assembly is water cooled by a chiller (*Termotek P1020*). However, running consecutive transport sequences heats up the plate. By construction constraints the cooling plate is a solid brass-alloy block with a limited number of holes. This creates unavoidable Eddy-currents and therefore persistent magnetic fields (up to 12 ms around the science cell) depending on the strength of the switched gradient- or bias-fields.

The complete transport sequence takes 5.3 s during which the atoms are guided over a total distance of 64.7 cm including a 90° turning. Approximately 70 % of all ^{40}K and ^6Li arrive from the MOT chamber in the science cell. The clouds are heated¹⁸ by $\sim 200 \mu\text{K}$.

2.7 Absorption Imaging

In the FerMix experiment, we use absorption imaging to detect the atomic cloud. Therefore, the atoms are illuminated by a near resonant beam, whose profile is then recorded on a CCD camera. At the location of the atomic cloud the light is absorbed, which casts a shadow in the profile of the imaging beam. According to Beer-Lambert’s law, the transmission of a sample $T(x, y)$ is related to its optical depth $OD(x, y)$ by:

$$T(x, y) = e^{-OD(x, y)} . \quad (2.6)$$

¹⁸The arriving temperature is difficult to measure by the TOF-method, since the cloud dimensions exceed the capture region of the imaging system. For longer TOF-times the arriving cloud hits the walls of the science cell.

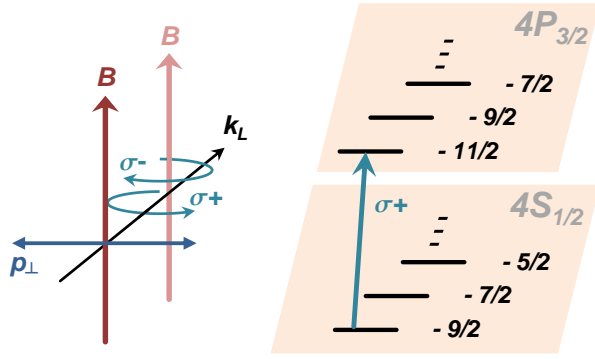

Figure 2.17

Illustration of $\sigma_+ + \sigma_-$ imaging at high magnetic fields in case of ^{40}K . The imaging beam \mathbf{k}_L propagates perpendicularly to the magnetic field \mathbf{B} . The orthogonal polarization \mathbf{p}_\perp can be represented locally as a superposition of σ^+ and σ^- . On the right, the utilized closed transition for ^{40}K is depicted. For sufficiently large bias field the σ^- transition is off-resonance.

If the probe beam-intensity is below the saturation intensity I_{sat} of the given atomic transition line, the optical density of the cloud can be approximated as:

$$OD_{\text{cloud}}(x, y) = \sigma n(x, y), \quad (2.7)$$

where $n(x, y)$ is the integrated column density along the beam direction z ,

$$n(x, y) = \int n(x, y, z) dz, \quad (2.8)$$

and σ the absorption cross section:

$$\sigma = \sigma_0 \frac{1}{1 + (2\Delta_{\text{Im}}/\Gamma)^2 + (I/I_{\text{sat}})} \quad (2.9)$$

of the atoms. In eq. (2.9), Γ denotes the linewidth of the imaging transition, $\Delta_{\text{Im}} = \omega - \omega_0$ the detuning of the imaging beam frequency ω from resonance $\omega_0 = 2\pi c/\lambda$, I the imaging beam intensity and σ_0 the resonance cross section of the used transition. The latter can be expressed as:

$$\sigma_0 = C^2 \cdot \frac{3\lambda^2}{2\pi}. \quad (2.10)$$

The last expression holds for circular polarized light-transitions, where C is the Clebsch-Gordon coefficient. For an unpolarized cloud, we average over all possible transitions revealing $C^2 = 0.4$ for ^{40}K and $C^2 = 0.5$ for ^6Li [108]. Furthermore, we drop the last term in the denominator of eq. (2.9) in the approximation of $I \ll I_{\text{sat}}$.

In the science cell, the cloud is imaged spin-selectively at high magnetic fields. Due to technical constraints, the imaging light is propagating orthogonal to the magnetic field and is superimposed with other beams on a polarization beam splitter. As a result, the imaging light is linearly polarized with the polarization orthogonal to the magnetic field \mathbf{B} . Locally, the polarization \mathbf{p}_\perp can be decomposed into an equal superposition of σ^+ and σ^- light. Figure 2.17 depicts the case of imaging for example a cloud of ^{40}K in the ground state $m_F = -9/2$. Provided that the splitting of the Zeeman states is larger than the linewidth of the imaging laser (typically 6 MHz), only the σ^+ part will be absorbed, forming a closed imaging transition cycle with the excited state $m_F = -11/2$. The scattering cross section is effectively reduced and hence the squared Clebsch-Gordon coefficient for ^{40}K in this case is $C^2 = 0.5$.

2.7.1 Technical realization

The aim of the technical realization of the absorption imaging is to deduce the pure transmission $T(x, y)$ of the atomic sample. Thus, eq. (2.6) and eq. (2.7) would allow to calculate the integrated column density $n(x, y)$.

Commonly, three images are necessary for reconstruction of $T_{\text{cloud}}(x, y)$ by absorption-imaging: In the first image the atoms absorb the imaging beam, hence casting a shadow on the image at their position. The absorbed light transfers sufficient kinetic energy to the atoms to leave the imaged area (therefore the absorption imaging is destructive). The second image records the light reference of the probe beam in absence of the atoms. The third image traces the dark noise on the camera, also including ambient light not originating from the imaging probe.

In our experiment we use a camera with double-shutter mode option (*Pixelfly QE 270XD*): During the electronic readout of the first taken image, the CCD-camera is ready for the exposure of a second image. This allows for consecutive imaging of either two species or two different spin states at high magnetic field within one experimental sequence only. Figure 2.18a shows the image taking sequence: The camera provides three TTL-outputs, "*BUSY*", "*CCD-Exposure*" and "*CCD-Readout*", signaling different operation states of the camera [160]. The CCD-Exposure TTL marks the exposure of the first image $t_{\text{exp1}} = t_2 - t_1$, which can be set by software (in our case $\sim 100 \mu\text{s}$). The first exposure is followed by a "dead time", $t_{\text{dead}} = t_3 - t_2 \sim 5 \mu\text{s}$, during which no exposure should be done. The ensuing TTL-signal of CCD-Readout can be divided into two parts, each 88 ms long. During the first part $t_{\text{read1}} = t_4 - t_3$ the first image, exposed during t_{exp1} , is read out. At the same time the CCD is ready for the exposure of the second image, $t_{\text{exp2}} = t_{\text{read1}}$. The final timing part, $t_{\text{read2}} = t_5 - t_4$ is used to read out the previously taken picture in t_{exp2} .

It takes only two triggers of the CCD to collect four images and to reconstruct the cloud transmission profile $T_{\text{cloud}}(x, y)$: At *trigger 1* the image *A* is recorded. The for the first 80 μs present laser pulse is absorbed by the atoms. The following dead time of the CCD is practically increased to 11 μs . During the first readout a second laser-pulse of 80 μs is shone on the camera to create the reference image *B*. Since in the double-shutter mode the camera is ready for the second exposure during the whole readout time of 88 ms, we can delay the second pulse which is much shorter. The delay is important and depends on the cloud temperature: Having absorbed the first probe-beam pulse, the cloud needs some time to leave the line of sight and therefore not to appear again on the second laser pulse at a shifted position. The delay is usually set to 60 ms.

At *trigger 2*, the noise / ambient-light images *C* and *D* are taken. Taking into account, that each time the second exposure time is much longer than the first one ($\sim 100 \mu\text{s}$ compared to 88 ms), the collected ambient-light differs. As clearly apparent from the images of fig. 2.18a the longer exposure by ambient light is sufficient to resolve even the layout of the picture edges.

The final transmission (image *E*) is calculated by normalizing the absorption by the reference without the noise included:

$$T_{\text{cloud}}(x, y) = \frac{I_A - I_C}{I_B - I_D} \equiv I_E, \quad (2.11)$$

where I_{A-D} are the intensities recorded by the CCD.

The sequence of imaging ^{40}K and ^6Li quasi-simultaneously within one sequence is shown in fig. 2.18b. The procedure is similar to the one described above, with the only difference, that the first exposure is used to record all images (absorption, reference and noise) for ^{40}K , while each

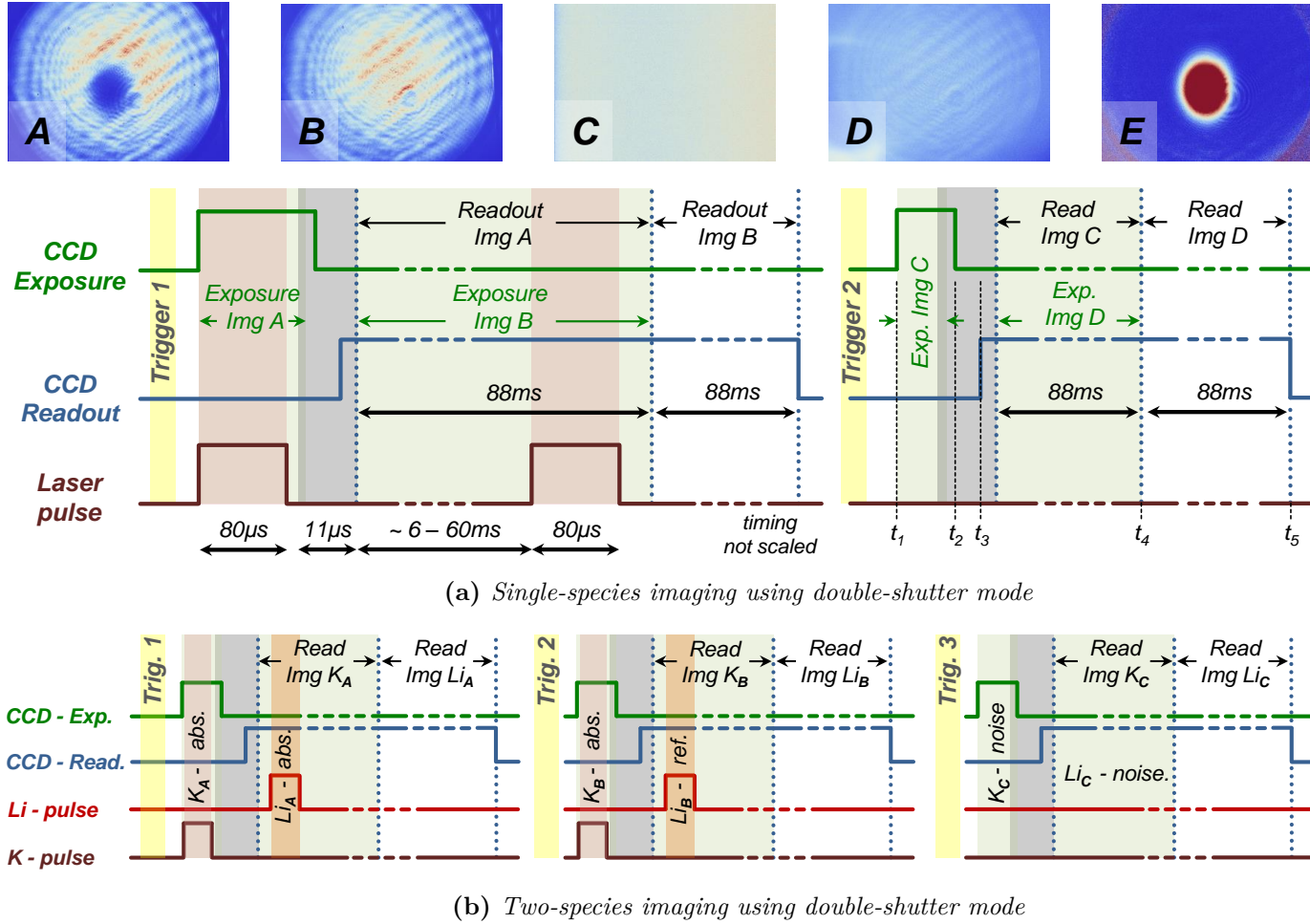
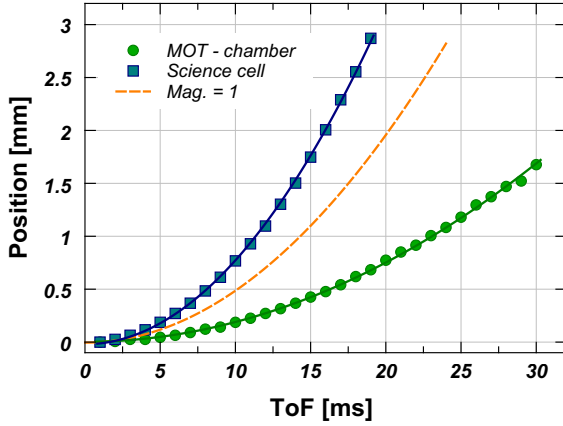


Figure 2.18: Imaging with PCO pixelfly CCD in double shutter mode. (a) Sequence of image-taking steps for absorption imaging of a ^{40}K cloud. The horizontal time axis is not scaled. Pictures A-D are the bare images collected by the camera, while E is the transmission image of the cloud, calculated by eq. 2.11. (b) Sequence for double-imaging: ^{40}K and ^6Li are imaged consecutively within one sequence.

**Figure 2.19**

Examples of calibrations of imaging magnifications by free fall. The dashed orange line denotes the free fall with $gt^2/2$, where $g = 9.81 \mu\text{m}/\text{ms}^2$. The green dots show experimental data of free fall in the main chamber after the gray molasses. The fitted line gives an effective $g' = 3.7 \mu\text{m}/\text{ms}^2$. Thus the imaging demagnifies by $1 : 2.65$. In contrast blue dots are free fall data measured in the science cell, where the atoms were released from the ODT after some evaporation. The fitted line reveals $g' = 15.8 \mu\text{m}/\text{ms}^2$, hence the imaging magnifies by $1.61 : 1$.

second exposure is dedicated to collect the images of ^6Li . In contrast to the single-species/-state imaging, now only three images per cloud are required to reconstruct the transmission-image (since there is only one noise / background image to collect). Also the delay between the first light-pulse (of ^{40}K) and the subsequent one (for ^6Li) has now to be as short as possible to not increase the relative TOF between the two clouds.

2.7.2 Calibration of the magnification

The atomic cloud is imaged through a lens system on the CCD. This allows for different magnification in different experimental regions. In the MOT chamber, where the hot cloud can extend during TOF over a 1 cm, it is even necessary to demagnify the captured region to image it entirely on the CCD chip¹⁹. One possibility to measure the magnification is by focusing a target of known size on the CCD and to compare its image to the actual target size. However, the problem remains that the target needs to be placed near the imaging plane, thus as close as possible to the imaged cloud. Regarding the dimensions of the vacuum chamber this might be challenging.

Even if the target measurement delivers a quite accurate first estimate of the magnification, there is a second possibility to check the magnification by free fall. A cold atomic sample has to fall in absence of any magnetic fields and its trajectory has to be recorded through time. Such a cold sample can be obtained after the gray molasses (sec. 2.5) or after some evaporative cooling in a ODT (sec. 5.3.4). In both cases the presence of magnetic fields, which could trap the cloud must be suppressed. Switching off magnetic fields would create eddy-currents and therefore unwanted gradients and acceleration forces.

Figure 2.19 shows the result of a free fall measurement for two different CCDs in our system. The dashed line shows the free fall with $gt^2/2$ at magnification $1 : 1$. Parabolas below this line correspond to demagnifying imaging lens-systems, while free-fall parabolas above the indicated dashed line are obtained by magnifying imaging systems.

¹⁹The chip of the used *Pixelfly QE 270XD* has a pixel-matrix size of $1392 \text{ px} \times 1024 \text{ px}$ with a squared pixel size of $6.45 \mu\text{m}$. Thus the overall chip-size is $\sim 9 \text{ mm} \times 6.6 \text{ mm}$.

2.7.3 Image analysis and temperature measurement

From the captured 2D cloud profiles, one can deduce the total atom number and temperature of the ensemble. The first quantity can be obtained by simply numerically integrating the profile. For non-degenerate clouds, we can fit a Gaussian function to the profile and integrate the fit to obtain the atom number and, depending on the confining potential, additionally the temperature. To decrease computational effort, the 2D-profile can be further numerically integrated to a 1D-profile:

$$n(x) = \int n(x, y) dy \equiv \sum_{\text{pixel-rows}} \frac{OD_{\text{cloud}}(x, y)}{\sigma} \times \text{pixel-size} \times \text{magnification} . \quad (2.12)$$

Supposing an harmonically trapped cloud, the profile can be fitted by a gaussian profile,

$$n(x) = A e^{(x-x_0)^2/2\sigma_0^2}$$

with amplitude A , shifted by x_0 and the width σ_0 . In absence of interactions, the width of the cloud, $\langle \Delta x^2 \rangle = \sigma^2$, will expand with time t according to

$$\sigma^2(t) = \sigma_0^2 + \frac{k_B T}{m} t^2 , \quad (2.13)$$

where T is the temperature of the cloud (see appendix sec. H.1.1 for a detailed derivation). Therefore it is possible to determine the temperature by fitting a Gaussian distribution function to cloud images taken at different TOF times t and by applying the above relation to the series of fitted widths $\sigma(t)$.

In case of a non-harmonically trapped cloud (and in absence of interactions), it is necessary to increase sufficiently the TOF-time, $t^2 \gg m\sigma_0^2/k_B T$, such that the initial shape and width can be neglected [108]. In this limit a Gaussian-fit can still be used to approximate the cloud shape, and the temperature can be estimated according to eq. (2.13). For long TOFs t the temperature can be estimated by

$$T_{\text{Li}} \approx 7 \cdot 10^{-4} \text{ ms}^2/\text{mm}^2 \times \frac{\sigma^2}{t^2} , \quad T_{40\text{K}} \approx 5 \cdot 10^{-3} \text{ ms}^2/\text{mm}^2 \times \frac{\sigma^2}{t^2} .$$

2.8 Computer System

The whole experimental machine is controlled by two *National Instruments PXI* systems which are connected to a PC. The system is widely expandable, but in our case we use only digital-card extensions (*NI PXI-6533*²⁰ and *NI PXIe-6536*) and analog-output cards (*NI PXI-6713*). The latter has a 12bit resolution on a voltage range from -10 V to 10 V . For an easier connectivity, we use a BNC adapter-card (*BNC-2110*) for the analog channels and a shielded connector-extension (*SCB-68A*) which includes screwable wire-to-board connectors. The current drain should not exceed 10 mA per analog or digital channel to ensure reliable control of the complete card-system.

²⁰The digital I/O card NI PXI-6533 is an old model and not available anymore. It has a voltage TTL-level output of 5 V . The follow-up model NI PXIe-6536 uses the modern TTL-level convention of 3.3 V .

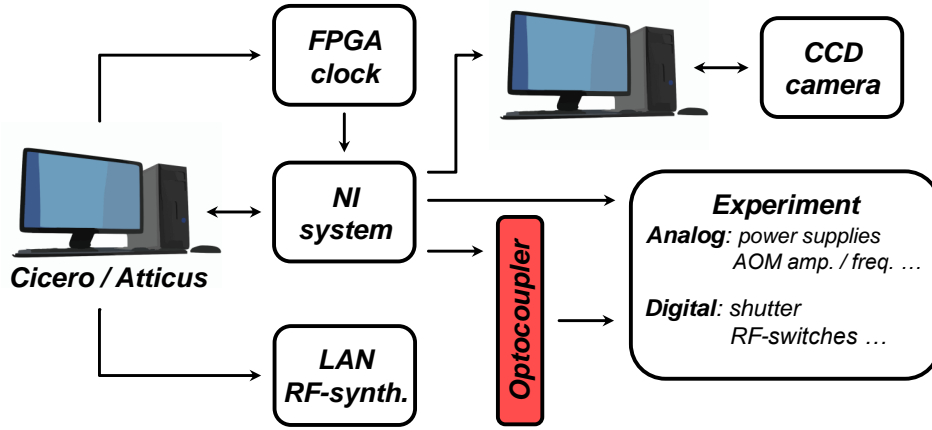


Figure 2.20: Schematic description of the computer control of the experiment. The CCD-camera is decoupled from the main operating computer and the NI-system. A second computer handles the CCD-software and hardware once receiving a trigger signal from the NI-system.

We use the programs *Cicero Word Generator* and *Atticus Server* developed by Aviv Keshet at MIT to operate the NI-system [161]. The server / client architecture facilitates programming of experimental sequences and provides a clear user-interface. Once the sequence is set, it is uploaded in form of buffers onto the NI-system which outputs the set values inside each buffer in time order at each clock cycle. Even if the NI-system, being a fully-operational FPGA, provides its own clock-source, we use an external FPGA (*Opal Kelly XEM 3001*) with variable clock speed. The variable clock speed allows for different resolution of experimental steps and therefore also for longer experimental sequences.

To protect the controlling unit from high voltages, for level shifting, to provide higher switching currents or even to simply avoid unwanted ground-loops, it is necessary to use optocoupling devices in between the NI-cards and the controlled devices. Each time only moderate switch-speed is required ($0.5\text{ }\mu\text{s}$ for TTL or $20\text{ }\mu\text{s}$ for analog signals) an optocoupler should be used. In appendix D few well known industrial test circuits with some modifications are presented for this reason. Finally fig. 2.20 summarizes the the actual computer setup of the FerMix experiment.

In the scope of this work, an additional device was build, which measures the 50 Hz oscillation of the mains voltage and emmits a trig once a the maximum of the waveform is reached. This synchronization becomes important for precise measurements, where the magnetic field need to be controlled up to $\Delta B = 100\text{ mG}$ (e.g for measurements using the inter-species Feshbach resonances of ^6Li and ^{40}K , which are only few G large [99]). At this level of magnetic field precision any electrical source running from the mains supply nearby the experiment creates a perturbation. The only solution to obtain reproducible conditions, is to start the experimental sequence synchronized to a fixed point of the oscillation waveform of the mains-supply in the laboratory. A description of the device can be found in appendix G.

2.9 Summary of the Sequence

At the end of this chapter, the reader can find the main starting experimental sequence, graphically summarized from the MOT-loading step until the final magnetic trap from which the atoms are magnetically transported to the science cell (fig. 2.21). It should be emphasized,

that in difference to the previous presentations in fig. 2.8 and fig. 2.7, where some indicated AOM-frequencies already included the double passage, the AOM frequencies in fig. 2.21 are the controlling frequencies, and hence always indicating the frequency shift during a *single* passage.

Table 2.1 summarizes characteristic temperatures and atom numbers after the discussed experimental stages. The temperatures are measured by successive TOF images. Hence the expansion velocity, fitted in the integrated 1D-profiles, can reveal two different temperatures. In the case of the spin-pol step, the asymmetry is clear, since the pumping beam is vertically aligned and heats the cloud only in one direction. The TOF-images are taken directly after the optical pumping, thus no time is left for thermalization. The particular case of the striking difference between the vertically and horizontally measured temperatures of ^6Li trapped alone in the magnetic quadrupole trap will be investigated in the following chapter 3.

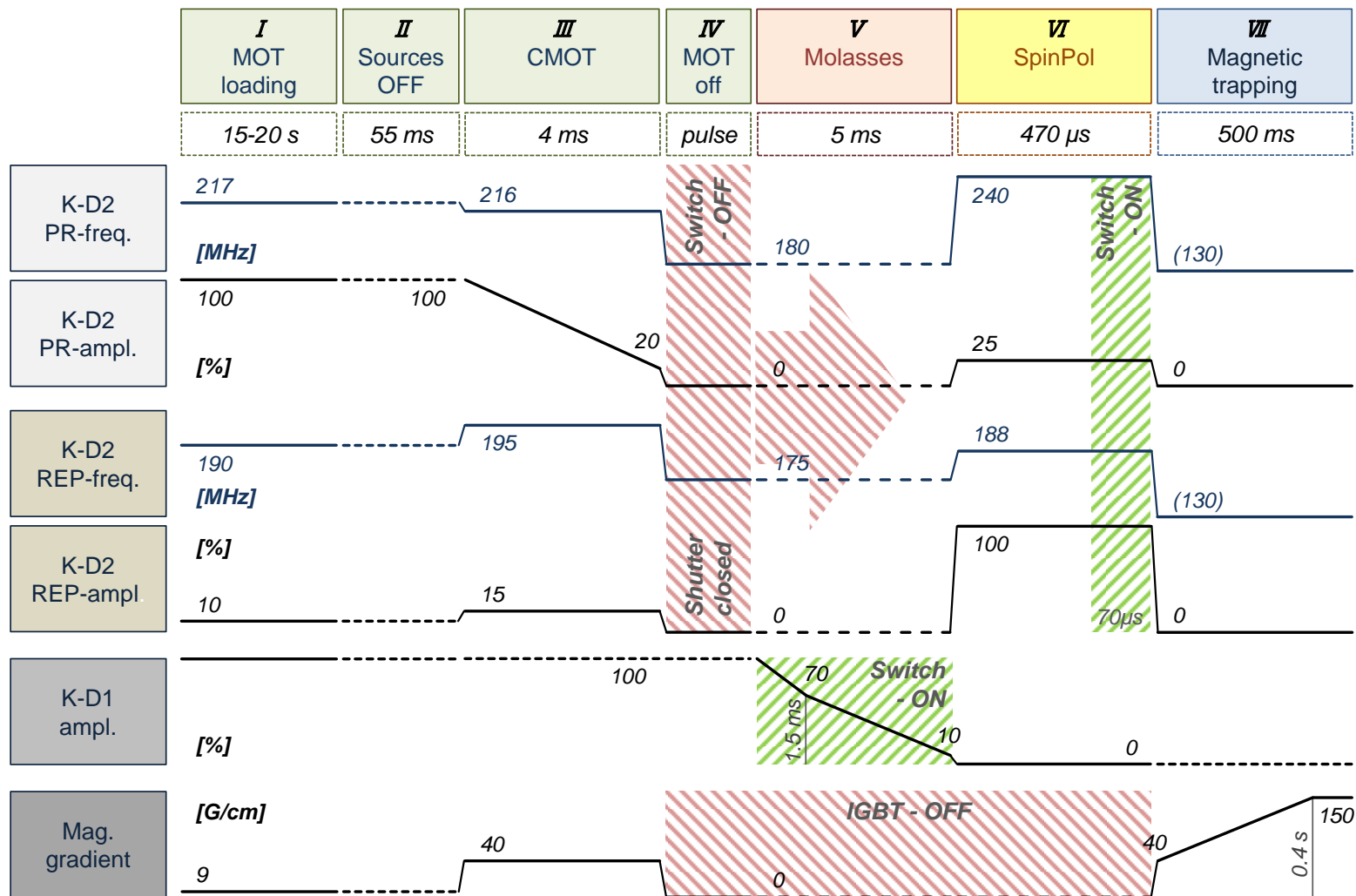


Figure 2.21: (a) Controlling parameters for the experimental sequence from MOT loading to the magnetic trapping in the MOT chamber - part one: AOM-controlling values for ^{40}K and the magnetic field gradient. For particular remarks see caption of part (b).

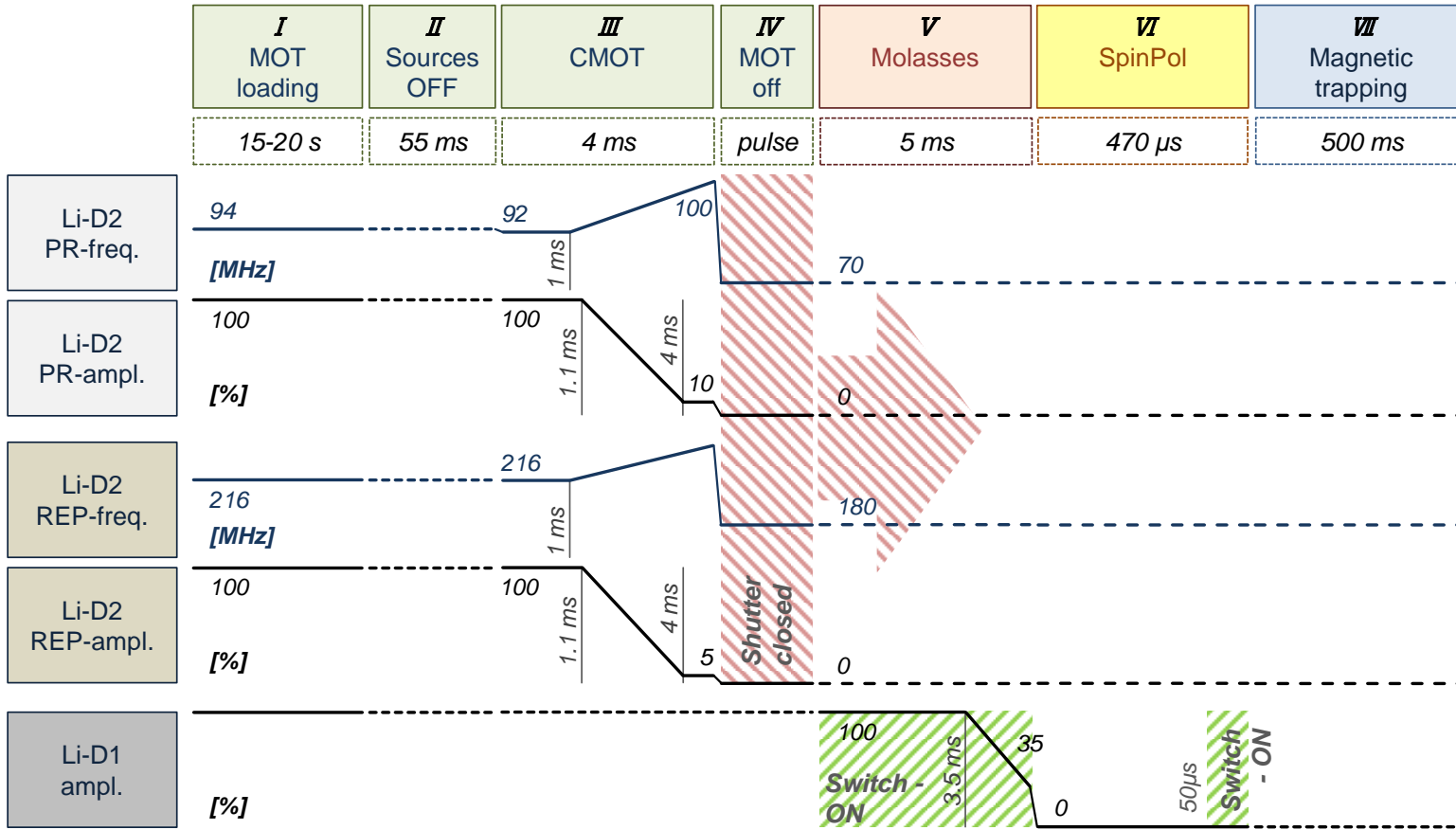


Figure 2.21: (b) Controlling parameters of the experimental sequence from MOT loading to the magnetic trapping in the MOT chamber - part one: AOM-controlling values for ${}^6\text{Li}$. Additionally to closing shutters and blocking the light by the corresponding AOM switches, we detune the cooling light from resonance and turn down the RF-power of the double-path AOMs. This in order leaves the TA-chips for some time without injection, but avoids resonant stray light, and hence heating of the magnetically trapped cloud. Not depicted are the control of the 2D-MOT repumper frequency, the Zeeman slower current (both used to optimize the atomic flux from the sources) and the molasses bias-compensation switches.

Table 2.1: Average temperatures and atom numbers in single and dual-species operation in the MOT chamber at different experimental stages. The atom number after the molasses is omitted, since during the cooling the atoms are occupying a dressed state, which is a linear combination of the two hyperfine ground states. By switching off the molasses beams, the state is projected in one of the hyperfine states. For the detection of the total atom number, the cloud needs to be pumped into the $F = 3/2$ -state of the $2S_{1/2}$ ground state in case of ^6Li or the $F = 9/2$ -state of the $4S_{1/2}$ ground hyperfine state for ^{40}K (see fig. 2.7 and fig. 2.8) during the subsequent spin-pol step. The temperature in the magnetic trap is recorded after a 100 ms hold-time in a trap gradient of $b' = 150 \text{ G/cm}$, which is the gradient at the beginning of the transport sequence. The temperatures are measured as expansion velocities of integrated 1D-profiles in each direction of the image through TOF and can thus differ. The particular difference of $90 \mu\text{K}$ in case of ^6Li trapped without ^{40}K in the quadrupole trap will be investigated in the next chapter 3.

	^6Li		^{40}K	
	<i>without ^{40}K</i>	<i>with ^{40}K</i>	<i>with ^6Li</i>	<i>without ^6Li</i>
Molasses	$68 \pm 3 \mu\text{K}$	$60 \pm 3 \mu\text{K}$	$32 \pm 4 \mu\text{K}$	$22 \pm 4 \mu\text{K}$
Spin-pol.	$143 \mu\text{K} / 283 \pm 10 \mu\text{K}$ $(4.6 \pm 0.6) \cdot 10^8$	$135 \mu\text{K} / 278 \pm 6 \mu\text{K}$ $(4.5 \pm 0.7) \cdot 10^8$	$38 \mu\text{K} / 75 \pm 4 \mu\text{K}$ $(1.3 \pm 0.2) \cdot 10^9$	$28 \mu\text{K} / 74 \pm 3 \mu\text{K}$ $(1.4 \pm 0.1) \cdot 10^9$
Mag.-trap	$230 \mu\text{K} / 316 \pm 8 \mu\text{K}$ $(4.6 \pm 0.4) \cdot 10^8$	$270 \mu\text{K} / 260 \pm 8 \mu\text{K}$ $(3.7 \pm 0.6) \cdot 10^8$	$287 \mu\text{K} / 270 \pm 4 \mu\text{K}$ $(1.3 \pm 0.2) \cdot 10^9$	$291 \mu\text{K} / 264 \pm 7 \mu\text{K}$ $(1.4 \pm 0.1) \cdot 10^9$

Quasithermalization of Non-Interacting Particles in a Quadrupole Trap

Thermalization is a well known process in nature: Two local thermal reservoirs, which are brought to contact thermalize towards a common temperature through collisions or radiative transfer. After some time, the ensemble reaches equilibrium and retrieves a classical Boltzmann distribution, well described by one single parameter - the temperature T .

However, sufficient interactions between the particles to exchange kinetic energy seem unavoidable to reach the new equilibrium. But what happens if the gas is collisionless? Does such a gas relax towards a steady state after an external excitation, even in absence of collisions? If it does, how will that steady state be described? In an isotropic harmonic trap and in absence of collisions, an excited breathing mode of the cloud would perform an undamped oscillation without directional change. However, for a harmonic trapping potential, it was shown by Kohn in [162] that even in presence of interactions, the center of mass of a particle cloud would oscillate endlessly and therefore the imparted energy would not be redistributed within the entire ensemble.

Owing to the large control over their physical properties, cold gases experiments are the predestined systems for the observation of principles of statistical physics and thermodynamics in particular [163].

In our experiment, the fermionic nature of the gas allows us to mimic the situation of a collisionless system: According to the Pauli exclusion principle, there are no s -wave collisions in a spin-polarized fermionic gas. In this chapter we will study the equilibrium properties of this collisionless ensemble inside a linear trapping potential as implemented by a magnetic quadrupole trap. The following results will show that a partial thermalization and energy redistribution takes place, even though the particles in the cloud do *not* interact. The underlying physics is given by the complexity of the single particle trajectories inside the trapping potential.

After a short motivation and the presentation of few preliminary observations (**sec. 3.1**), we will first develop a theoretical model describing the energy redistribution within the quadrupole trap in absence of interactions after an ideal excitation (**sec. 3.2**). We further discuss the corresponding experimental results and compare them with a more adjusted model (**sec. 3.4**). Even though the quadrupole trap is a well-established experimental tool in cold gases experiments [164], the following presented detailed study - as well theoretically as experimentally, extends to our knowledge the findings of cloud dynamics in the quadrupole potential that have so far been

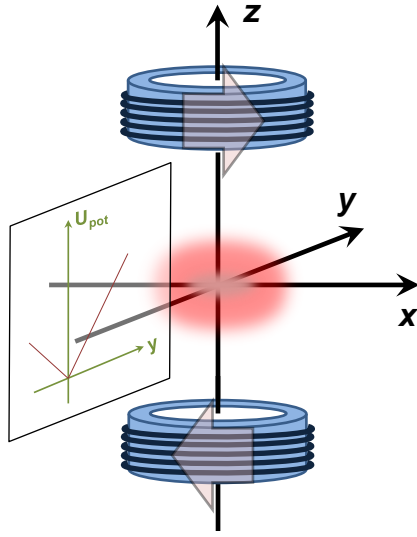


Figure 3.1

Creating a magnetic gradient field with a pair of coils in anti-Helmholtz configuration: The same current is running in opposite direction in the coils. The inlay shows a slice made in the function of the potential energy. In this projection, the potential is linear as a function of chosen coordinate. The cloud is depicted more compressed in z -direction, emphasizing the twice larger gradient factor in this direction. For a more detailed discription of the magnetic field see sec. 2.6 of the previous chapter 2.

published.

3.1 First Experimental Observations

The first insight of an absence of energy redistribution in a cloud of ${}^6\text{Li}$ below a given temperature in our experiment was presented in [111] (page 104): The experimental observation of two different expansion velocities for a thermal cloud of ${}^6\text{Li}$ appears as a contradiction to the coupled equation of motion in the quadrupole potential at first sight. To create a clear picture of the first experimental observation (also regarding the upcoming experiments), we will review briefly some experimental steps, which were described in chapter 2.

After the gray-molasses cooling stage (sec. 2.5), the atomic cloud obeys the Boltzmann distribution law, showing a symmetric expansion during TOF (table 2.1). Therefore, we attribute to the whole ensemble a given temperature ($\sim 60\text{ }\mu\text{K}$ for ${}^6\text{Li}$). In order to trap the cloud, we pump the atoms in the stretched Zeeman state by shining an optical pumping-beam along a given z -axis, which corresponds to the symmetry axis of the quadrupole trap used later on. Obviously, the cloud gets kicked and heated up, due to the recoil-energy of the absorbed photons during the $50\text{ }\mu\text{s}$ long pumping process – mostly along the direction of the pumping beam (up to $280\text{ }\mu\text{K}$, see table 2.1). Subsequently, a gradient field of 40 G/cm is switched on and adiabatically increased during 500 ms to a value of 150 G/cm . This field is created by a pair of coils operated in anti-Helmholtz configuration: same currents flowing in opposite directions (fig. 3.1).

The potential energy of an atom, which follows adiabatically the magnetic field created by the coil assembly is given by the quadrupole potential in eq. (2.3),

$$U_{\text{pot}}(\mathbf{r}) = \mu b \sqrt{x^2 + y^2 + 4z^2}.$$

From this expression, the symmetry properties of the trap are clearly visible: The confinement in z -axis direction is twice as large as in x - or y -direction.

In the first experiment, a cloud of ${}^6\text{Li}$ was loaded alone in the magnetic trap and trapped

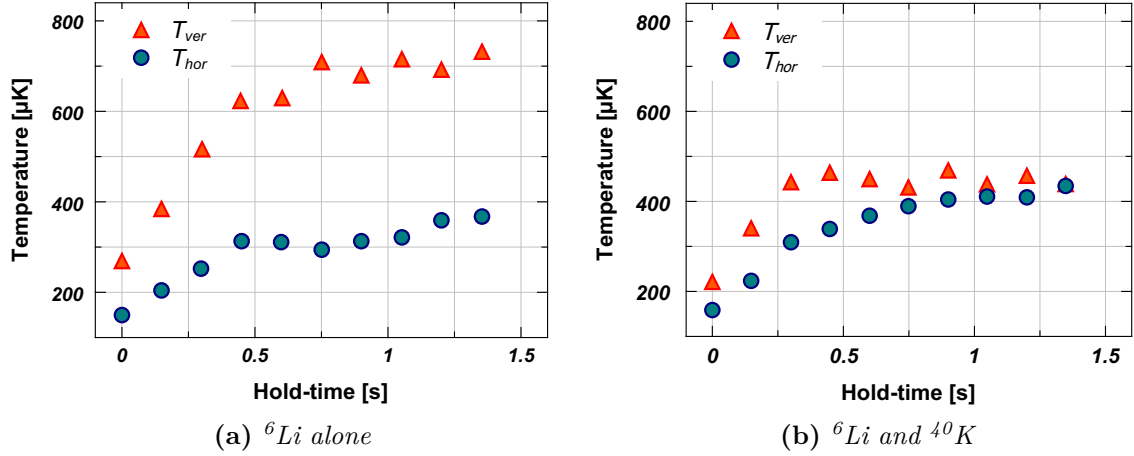


Figure 3.2: (a) ${}^6\text{Li}$ alone is captured in the magnetic trap for different hold times. The expansion velocity in vertical (z -dir. / red triangles) and in horizontal (x -dir. / blue circles) direction is measured by TOF experiments for each wait time in the trap. The expansion is expressed in effective temperatures T_{ver} and T_{hor} . (b) The same experiment is repeated with ${}^{40}\text{K}$ in addition being present in the trap. The inter-species collisions equilibrate the vertical and horizontal temperatures after $t \approx 1.5$ s. In both situations the magnetic gradient is compressed linearly from 40 G/cm to 135 G/cm in the first 450 ms. This adiabatic compression increases the temperature linearly during the first 0.5 s.

there for different hold times (fig. 3.2a). For each hold time the expansion is measured by taking a series of TOF-images. For each expansion direction, vertical (z -axis along the quadrupole coils) and horizontal (x -axis), we attribute a distinct *effective 1D-temperature* by

$$\frac{1}{2}k_B T_i = \frac{\langle p_i^2 \rangle}{2m}. \quad (3.1)$$

It is important to emphasize, that the (effective) temperatures T_i defined above and treated later on, do not fulfill the well defined notion of a isotropic temperature T : Given a Boltzmann distribution, the temperature is defined to be a isotropic quantity over the whole ensemble (heat bath). Conversely, distributions with different effective temperatures T_i are non-Boltzmann.

In fig. 3.2a, ${}^6\text{Li}$ alone does not thermalize towards a complete Boltzmann distribution: The temperatures between the two axis differ by $\Delta T_i \approx 400 \mu\text{K}$. On the other hand, the same experiment performed with ${}^{40}\text{K}$ being present in the magnetic trap additionally, shows a different behavior (fig. 3.2b): After 1.5 s of hold time the temperature of ${}^6\text{Li}$ measured in the two orthogonal directions equilibrates towards a common value of $T \approx 450 \mu\text{K}$. In this case, we have indeed a thermal Boltzmann distribution.

The shown behavior can be qualitatively explained by taking into account some trapping and collision properties of ${}^6\text{Li}$. First, following the discussion of sec. 2.6.1, the ground state $2^2\text{S}_{1/2}$ of ${}^6\text{Li}$ contains only one stable trappable low field seeking state – the stretched state $|F = 3/2, m_F = +3/2\rangle$. Since we are working with Fermions, Pauli exclusion forbids s -wave interactions. Furthermore, p -wave collisions are suppressed below $T \sim 6 \text{ mK}$ for ${}^6\text{Li}$, which applies to our temperature range. Considering this, we can assume that there are no collisions in the case of fig. 3.2a, where only ${}^6\text{Li}$ is trapped. Regarding the case of fig 3.2b, where ${}^{40}\text{K}$ is added, the collisions allowing thermalization are provided by the newly introduced species.

The collision process results in a complete thermalization of the ${}^6\text{Li}$ cloud towards one common temperature after 1.5 s.

On a single-particle level, the result of fig. 3.2a seems surprising, since the equations of motion in x - and z -directions are coupled. The total energy, i.e. the *single-particle Hamiltonian*, is described by:

$$H(\mathbf{r}, \mathbf{p}) = \frac{p^2}{2m} + U(\mathbf{r}) = \frac{p^2}{2m} + \mu b \sqrt{x^2 + y^2 + 4z^2}, \quad (3.2)$$

where the first term is the kinetic and the second the potential energy of the particle. It is important to emphasize, that due to the spin-polarized sample of ${}^6\text{Li}$ and the suppression of p -wave collisions in the relevant temperature range of $\sim 300 \mu\text{K} - 500 \mu\text{K}$ the system is *collisionless*: It poses a perfect mechanical system. Consequently, the equations of motion can be derived to

$$\begin{aligned} m \frac{d^2 x}{dt^2} &= - \frac{\mu b x}{\sqrt{x^2 + y^2 + 4z^2}}, \\ m \frac{d^2 z}{dt^2} &= - \frac{4\mu b z}{\sqrt{x^2 + y^2 + 4z^2}}, \end{aligned} \quad (3.3)$$

where the equation for the y -coordinate was dropped, due to its similarity to the one in x -direction. Compared to the case of a pure harmonic trapping, where the equation of motion decouple and the trap is clearly showing a non-ergodic (separable) behaviour¹, the different directions are coupled in our case of the quadrupole potential. Due to the non-separable Hamiltonian in eq. (3.2), the observed absence of complete thermalization and energy exchange between the axial direction and the horizontal plane is not obvious.

The absence of interactions allows to solve eq. 3.3 for a large particle number and average over the statistical ensemble using a manageable amount of computing power. This was done in [118] to explain results similar to fig. 3.2a and the following experimental findings. After proposing a more systematic experiment in the next section, we will explain theoretically the thermal decoupling of the directions z and the xy -plane by studying the phase space distribution function $f(\mathbf{r}, \mathbf{p}, t)$.

3.2 Experimental Concept

To study the evolution of an imparted momentum in the cloud, we propose a rather simple experiment (fig. 3.3): The cloud is in thermal equilibrium initially and therefore described by the Boltzmann distribution,

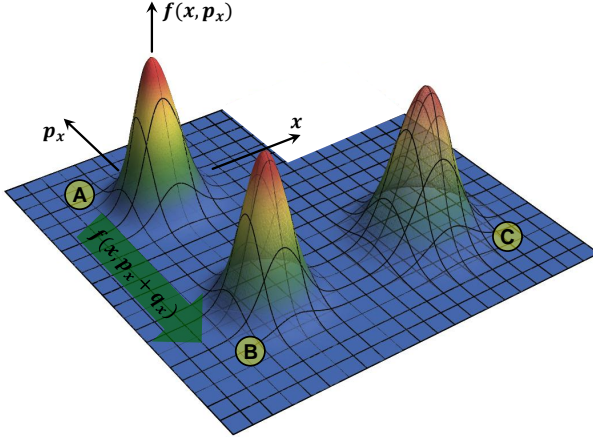
$$f_0(\mathbf{r}, \mathbf{p}) = \frac{1}{Z} e^{-\beta H(\mathbf{r}, \mathbf{p})}, \quad (3.4)$$

with the fugacity $Z = \exp(\beta \mu_c)$, where μ_c is the chemical potential, $\beta = 1/(k_B T)$ the usual temperature coefficient and $H(\mathbf{r}, \mathbf{p})$ the single particle Hamiltonian from eq. (3.2). The fugacity

¹In a harmonic potential $U = \sum_i m \omega_i^2 x_i^2 / 2$, the equation of motions (in absence of interactions) are simply

$$m \frac{d^2 x_i}{dt^2} = -m \omega_i^2 x_i.$$

The equation for x_i does not couple to other directions x_j ($i \neq j$). The particle stays on a given trajectory without discovering the whole phase space (we call the underlying Hamiltonian in the harmonic case *separable*). Thus the harmonic trap is considered as non-ergodic.

**Figure 3.3**

Concept of the "kick"-experiment – simplified illustration with only one momentum p_x and one space coordinate x . The initial thermal Boltzmann distribution **A** gets ideally shifted to **B** by the momentum q_x . The question: How will this shifted distribution evolve in time? The experimentally feasible kick will also effect a spatial displacement of the cloud, and eventual heating, which will lead to an overall spread and a spacial shift of the distribution in position space (case **C**).

Z can be used to normalize the distribution function $f_0(\mathbf{r}, \mathbf{p})$ either to 1, as a probability distribution, or to the total atom number².

At the time $t = 0$, we excite the cloud by giving the same momentum \mathbf{q} to each atom. As a result, the distribution function is shifted in phase space:

$$f(\mathbf{r}, \mathbf{p}, t = 0) = f_0(\mathbf{r}, \mathbf{p} - \mathbf{q}) . \quad (3.5)$$

The question to investigate will be: How does the shifted distribution evolve in the quadrupole potential? In this way, we should understand the origin behind the previously mentioned decoupling of the thermalization directions. Therefore, the final ($t \rightarrow \infty$) momentum redistribution of the imparted momentum \mathbf{q} is of particular interest.

The sudden momentum transfer is an idealized procedure. In the experimental procedure discussed later on, the momentum transfer will take some time τ during which the cloud will be also displaced in position space by δ , which is equivalent to an increase in potential energy. We will first discuss the momentum redistribution in case of the ideal kick situation and present the experimental results, before we will come back to the issue of the realistic kick situation in sec. 3.4.4.

²In the following we will normalize the distribution function f_0 to the total atom number N throughout this manuscript, hence

$$Z = \sqrt{\frac{2}{\pi}} \left(\frac{m}{\hbar^2} \right)^{3/2} \beta^{-9/2} (\mu b)^{-3} \frac{1}{N} ,$$

which is, as expected, a dimensionless quantity. For consistency, we will use the normalization factor of $(2\pi\hbar)^{-3}$ while integrating over the momentum space. However, in upcoming calculations, where dimensions play no role, we will omit this factor to shorten the notation.

3.3 Analytical Calculation of the Time Evolution of the Momentum

For a small imparted momentum $|q|$, we can expand the initial kicked distribution from eq. (3.5) in a Taylor series³ up to second order in \mathbf{q} :

$$\begin{aligned} f(\mathbf{r}, \mathbf{p}, t=0) &\approx f_0(\mathbf{r}, \mathbf{p}) \left\{ 1 - \frac{\beta}{2m} q^2 + \frac{\beta}{m} (\mathbf{p} \cdot \mathbf{q}) + \frac{\beta^2}{2m^2} (\mathbf{p} \cdot \mathbf{q})^2 + \dots \right\} \\ &= f_0(\mathbf{r}, \mathbf{p}) \alpha_0(\mathbf{r}, \mathbf{p}) . \end{aligned} \quad (3.6)$$

The solution of the collisionless Boltzmann equation describes the evolution of the density distribution in time:

$$\begin{aligned} \frac{\partial f(\mathbf{r}, \mathbf{p}, t)}{\partial t} &= - \left\{ \frac{\mathbf{p}}{m} \cdot \partial_{\mathbf{r}} - \nabla U(\mathbf{r}) \cdot \partial_{\mathbf{p}} \right\} f(\mathbf{r}, \mathbf{p}, t) \\ &= - \hat{\mathbf{L}} f(\mathbf{r}, \mathbf{p}, t) , \end{aligned} \quad (3.7)$$

with the initial condition at $t=0$ satisfying eq. (3.6). Some of the properties of the Liouville operator $\hat{\mathbf{L}}$ are discussed in section I.2. We assume the time evolving distribution $f(\mathbf{r}, \mathbf{p}, t)$ being of a similar product form as the initial condition:

$$f(\mathbf{r}, \mathbf{p}, t) = f_0(\mathbf{r}, \mathbf{p}) \alpha(\mathbf{r}, \mathbf{p}, t) . \quad (3.8)$$

Since the initial Boltzmann distribution $f_0(\mathbf{r}, \mathbf{p})$ is a stationary solution, $\hat{\mathbf{L}} f_0 = 0$, equation (3.7) breaks down to

$$\partial_t \alpha(\mathbf{r}, \mathbf{p}, t) = - \hat{\mathbf{L}} \alpha(\mathbf{r}, \mathbf{p}, t) , \quad (3.9)$$

with the the initial condition $\alpha(\mathbf{r}, \mathbf{p}, t=0) = \alpha_0(\mathbf{r}, \mathbf{p})$. A formal solution of the last equation can be given in form of

$$\alpha(\mathbf{r}, \mathbf{p}, t) = \exp(-t \hat{\mathbf{L}}) \alpha_0(\mathbf{r}, \mathbf{p}) . \quad (3.10)$$

In the experiment, there is no direct access to measure the density distribution function, but rather averaged quantities such as position $\langle x_i^2 \rangle$ or momentum $\langle p_i^2 \rangle$ can be deduced from cloud images. Knowing the underlying phase space distribution, the expectation value of a physical quantity $G(\mathbf{r}, \mathbf{p})$ is calculated by

$$\begin{aligned} \langle G \rangle &= \int d^3 \mathbf{r} d^3 \mathbf{p} f(\mathbf{r}, \mathbf{p}) G(\mathbf{r}, \mathbf{p}) \\ &= \int d^3 \mathbf{r} d^3 \mathbf{p} f_0(\mathbf{r}, \mathbf{p}) \alpha(\mathbf{r}, \mathbf{p}) G(\mathbf{r}, \mathbf{p}) \\ &= \langle G | \alpha(\mathbf{r}, \mathbf{p}) \rangle . \end{aligned} \quad (3.11)$$

³We have to use the multi-dimensional Taylor expansion up the second-order term, which is given by:

$$f(\mathbf{q}) \approx f(0) + \frac{\partial f}{\partial \mathbf{q}} \Big|_0 \cdot \mathbf{q} + \frac{1}{2} \sum_{ij} q_i \frac{\partial_{ij}^2 f}{\partial q_i \partial q_j} \Big|_0 q_j .$$

Hence the second order term is given by:

$$\frac{\partial_{ij}^2 f}{\partial q_i \partial q_j} \Big|_0 = \left(\frac{\beta^2}{m^2} p_i p_j - \frac{\beta}{m} \delta_{ij} \right) .$$

In the last line, by means of the solution-ansatz (3.8), the expectation value is re-interpreted as a scalar product (see appendix I.1), which will simplify the further calculation. With eq. (3.6) and the time evolution from eq. (3.10), the momentum expectation value results in

$$\begin{aligned} \langle p_i^2 \rangle_t &= \left\langle p_i^2 \left| e^{-t\hat{\mathbf{L}}} \alpha_0 \right. \right\rangle \\ &= \left\langle p_i^2 \left| 1 \right. \right\rangle \left(1 - \frac{\beta}{2m} q^2 \right) + \frac{\beta}{m} \left\langle p_i^2 \left| e^{-t\hat{\mathbf{L}}} (\mathbf{p} \cdot \mathbf{q}) \right. \right\rangle + \frac{\beta^2}{2m^2} \left\langle p_i^2 \left| e^{-t\hat{\mathbf{L}}} (\mathbf{p} \cdot \mathbf{q})^2 \right. \right\rangle. \end{aligned} \quad (3.12)$$

The second term is odd in the momentum coordinates p_j . Taking into account the symmetry properties of $\hat{\mathbf{L}}$ and the operator expression $\exp(-t\hat{\mathbf{L}})$, the integral in eq. (3.11) and therefore the second summand vanishes (appendix I.3). For the last term in eq. (3.12), we can expand the scalar product to distinguish odd and even terms in momentum:

$$\frac{\beta^2}{2m^2} \left\langle p_i^2 \left| e^{-t\hat{\mathbf{L}}} (\mathbf{p} \cdot \mathbf{q})^2 \right. \right\rangle = \frac{\beta^2}{2m^2} \sum_{j,k} q_j q_k \left\langle p_i^2 \left| e^{-t\hat{\mathbf{L}}} (p_j p_k) \right. \right\rangle.$$

With similar argumentation, terms with $j \neq k$ are odd in momentum coordinates and the corresponding integrals will vanish. With the remaining terms, $j = k$, we rewrite the last term of eq. (3.12) as

$$\frac{\beta^2}{2m^2} \left\langle p_i^2 \left| e^{-t\hat{\mathbf{L}}} (\mathbf{p} \cdot \mathbf{q})^2 \right. \right\rangle = \frac{1}{2} \sum_j q_j^2 \left\langle \frac{\beta p_i^2}{m} \left| e^{-t\hat{\mathbf{L}}} \left(\frac{\beta p_j^2}{m} \right) \right. \right\rangle,$$

and the momentum width simplifies to

$$\langle p_i^2 \rangle_t = \langle p_i^2 \left| 1 \right. \rangle + \frac{1}{2} \sum_j q_j^2 \left\langle \frac{\beta p_i^2}{m} \left| e^{-t\hat{\mathbf{L}}} \left(\frac{\beta p_j^2}{m} \right) - 1 \right. \right\rangle. \quad (3.13)$$

Initially at $t = 0^-$, before the kick, the cloud is not excited and the expectation value of the momentum is given by $\langle p_i^2 \rangle_{0-} = \langle p_i^2 \left| 1 \right. \rangle$. Following the previous description of the ideal kick, at $t = 0$ each atom receives a momentum \mathbf{q} , thus $\langle p_i^2 \rangle_0 = \langle p_i^2 \rangle_{0-} + q_i^2$. Hence, setting $t = 0$ imposes:

$$q_i^2 \stackrel{!}{=} \frac{1}{2} \sum_j q_j^2 \left\langle \frac{\beta p_i^2}{m} \left| \frac{\beta p_j^2}{m} - 1 \right. \right\rangle, \quad \Leftrightarrow \quad \left\langle \frac{\beta p_i^2}{m} \left| \frac{\beta p_j^2}{m} - 1 \right. \right\rangle \stackrel{!}{=} 2\delta_{ij}. \quad (3.14)$$

The last identity allows to recast eq. (3.13) to

$$\langle p_i^2 \rangle_t = \langle p_i^2 \rangle_{0-} + \frac{1}{2} \sum_j q_j^2 \theta_{ij}(t), \quad (3.15)$$

where the matrix $\theta_{ij}(t)$,

$$\theta_{ij}(t) = \left\langle \frac{\beta p_i^2}{m} \left| \left[e^{-t\hat{\mathbf{L}}} - 1 \right] \left(\frac{\beta p_j^2}{m} \right) \right. \right\rangle + 2\delta_{ij}, \quad (3.16)$$

describes the distribution of the imparted momentum \mathbf{q} on the average momentum $\langle p_i^2 \rangle$ in all three directions. In sec. I.4, we show that θ_{ij} is an even function of time t and more importantly,

that the distribution matrix is symmetric:

$$\theta_{ij}(t) = \theta_{ji}(t) . \quad (3.17)$$

This already reduces the number of matrix elements, which have to be determined, to six.

3.3.1 Analytical prediction of the steady state

To predict the final steady state in the limit of $t \rightarrow \infty$, where we expect the excited cloud to be in equilibrium, we take advantage of the Virial theorem. Applied to our case of a quadrupole potential ($n = 1$, see sec. I.5) it states:

$$2\langle E_{\text{kin}} \rangle = \langle U_{\text{pot}} \rangle , \quad (3.18)$$

i.e. the expectation value of the kinetic energy E_{kin} is twice as large as for the potential energy U_{pot} . Thus the expectation value of the total energy right after the kick (i.e., the momentum transfer \mathbf{q}) can be expressed as:

$$\langle E_{\text{tot}} \rangle_0 = \langle E_{\text{tot}} \rangle_{0^-} + q^2/2m = 3\langle E_{\text{kin}} \rangle_{0^-} + q^2/2m , \quad (3.19)$$

where, $t = 0^-$ denotes the moment in time directly before the kick, similar to the discussion preceding eq. (3.15). On the other hand, the Virial theorem also holds for the total energy of the steady state at $t \rightarrow \infty$, so that eq. (3.15) can be expressed in multiples of the kinetic energy:

$$\langle E_{\text{tot}} \rangle_{+\infty} = 3\langle E_{\text{kin}} \rangle_{+\infty} = 3\langle E_{\text{kin}} \rangle_{0^-} + \frac{3}{2} \sum_{ij} \theta_{ij}(\infty) \frac{q_j^2}{2m} . \quad (3.20)$$

Considering energy conservation, we can compare the energy after the kick, eq. (3.19), to the total energy of the steady state to deduce the condition

$$\sum_i \theta_{ij}(\infty) = \frac{2}{3} . \quad (3.21)$$

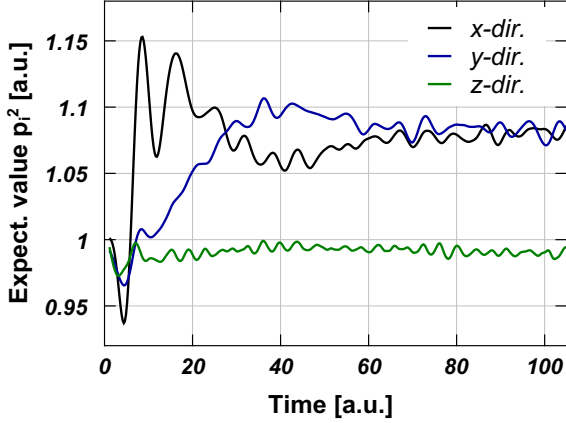
Additionally to eq. (3.17), this condition reduces the number of unknown matrix elements of θ_{ij} to three. Taking into account the rotational symmetry of the quadrupole potential around the coil-axis z , it is justified to assume, that there should be no difference between an imparted momentum in x - or y -direction. Hence, we will set for the steady state

$$\theta_{xx}(\infty) = \theta_{yy}(\infty) . \quad (3.22)$$

Together with eq. (3.17), only two parameters, ν_1 and ν_2 , remain undetermined in the momentum distribution matrix:

$$\theta_{ij}(\infty) = \begin{pmatrix} \nu_1 & 1/3 - \nu_1 + \nu_2/2 & 1/3 - \nu_2/2 \\ 1/3 - \nu_1 + \nu_2/2 & \nu_1 & 1/3 - \nu_2/2 \\ 1/3 - \nu_2/2 & 1/3 - \nu_2/2 & \nu_2 \end{pmatrix} \quad (3.23)$$

It turns out to be difficult to solve the problem strictly analytically. We take advantage of the collisionless nature of the system and its simplicity in order to perform computational phase


Figure 3.4

Time evolution of the expectation value of $\langle p_i^2 \rangle_t$ for each direction ($i = x, y, z$) after a momentum kick $\mathbf{q} = (1, 0, 0)$ in x -direction. The curves are results of computational simulations of the phase space trajectories of 10^4 particles. Clearly, the x -dir. (black line) gets heated up, but a part of the energy gets redistributed into the y -dir. (blue line), in that way equilibrating the expectation values $\langle p_x^2 \rangle_\infty = \langle p_y^2 \rangle_\infty$ after sufficient time. The kinetic energy contribution in z -dir. (green line) is not affected by the kick.

space trajectory calculations for 10^4 particles, by applying the equations of motion from eq. (3.3) to each of them⁴. For an initial kick in x -direction, $\mathbf{q} = (1, 0, 0)$, we record the expectation value of the momentum squared $\langle p_i^2 \rangle_t$ after each time step, i.e. simulating the unknown evolution of eq. (3.15). The result of one such computational run is presented in fig. 3.4. Clearly, a steady state is reached after some time, and while $\langle p_z^2 \rangle$ remains unchanged, the imparted kinetic energy gets distributed equally among the x - and y -directions. The first condition of unchanged z -momentum squared directly yields $\nu_2 = 2/3$ and the second observation of $\langle p_x^2 \rangle_\infty = \langle p_y^2 \rangle_\infty$ for the unity x -kick reveals $\nu_1 = 1/3$. To obtain all the missing information, a simulation of a kick along the x -direction is sufficient and an additional simulation for an excitation along the symmetry-axis z is not necessary.

Finally the *predicted ideal kick transfer coefficients* are:

$$\begin{aligned} \langle p_x^2 \rangle_\infty &= \langle p_x^2 \rangle_{0-} + \frac{1}{6} q_X^2 \quad \text{and} \quad \langle p_z^2 \rangle_\infty = \langle p_z^2 \rangle_{0-} \quad \text{for a } x\text{-kick } \mathbf{q}_X = (q_X, 0, 0) \\ \langle p_z^2 \rangle_\infty &= \langle p_z^2 \rangle_{0-} + \frac{1}{3} q_Z^2 \quad \text{and} \quad \langle p_x^2 \rangle_\infty = \langle p_x^2 \rangle_{0-} \quad \text{for a } z\text{-kick } \mathbf{q}_Z = (0, 0, q_Z) \end{aligned} \quad (3.24)$$

We only mentioned the relations between the x - and z -directions explicitly, since these will be the observation-axis in the experimental realization later on.

3.4 Experimental Study of the Momentum Transfer

To verify the momentum redistribution behaviour and the decoupling of the momentum transfer between the xy -plane and the z -symmetry axis, we need to transfer instantaneously a momentum \mathbf{q} to the atomic cloud, which is previously in thermal equilibrium.

There are two ways to excite a magnetically trapped cloud in the experiment: Either by shining in resonant light or by magnetically distorting the trap itself. The first variant led to uncontrollable losses from the magnetic trap: The applied near-resonant beam depumped the ^6Li -atoms from the trappable stretched state to untrapped Zeeman states and led to excessive heating for stronger momentum-excitations. Also, the current experimental setup around the MOT-chamber, where the kick experiments are performed, does not allow for an independent excitation beam within the xy -plane.

⁴For a detailed description of the applied numerical tools and further performed simulations see [118]

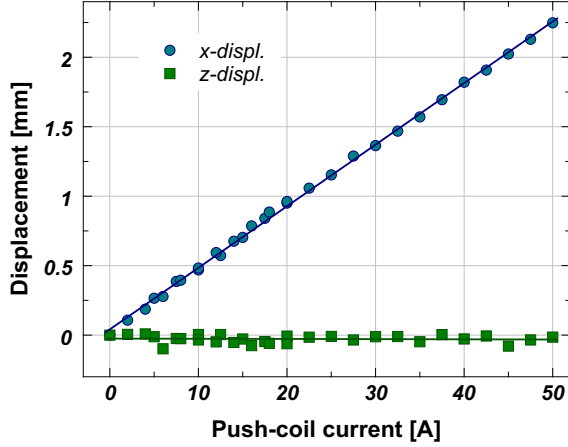


Figure 3.5

Trap displacement by the push coil of the quadrupole trap formed by the MOT coils C_{MOT} (see fig. 2.1). The position of the trap center is recorded by imaging in situ a cloud of ${}^6\text{Li}$, which is **adiabatically** displaced by continuously ($\sim 300\text{ ms}$) turning on variable current values in the push coil. In contrast to the kick measurements performed later on, the cloud has sufficient time to follow the displaced trap center. The measurement proves that the trap center can be displaced by multiples of the cloud size r_0 from eq. (3.26).

We therefore use the second possibility of a magnetic "kick"-realization, which will be described in the following sections.

3.4.1 Magnetic kick

For a magnetic kick of the trapped cloud, we use two different coils in the MOT chamber: The cloud is initially trapped in a quadrupole trap with strong gradient b' (gradient value along z , $b' = 2b$) created by the MOT coils (see fig. 2.1). We use the single *Push* coil of the transport to kick the atoms in x direction and the pair of spin-pol coils C_{SP} in Helmholtz configuration to perform a kick in z -direction. In this way, the magnetic trap center is displaced by an offset bias \mathbf{B}_0 (see eq. (2.1)) leading to

$$\mathbf{B}_{\text{shifted-grad.}} = b \cdot \begin{pmatrix} x \\ y \\ -2z \end{pmatrix} + \mathbf{B}_0. \quad (3.25)$$

As shown in figure 3.5, the trapped cloud and therefore the center of the quadrupole potential can be displaced by up to 2.4 mm in x -direction without changing the z -position of the cloud by using the push coil. Similar displacement is possible with the Helmholtz-configuration of the spin-pol coils. We compare these displacements with the extension of the cloud in the quadrupole trap, which can be approximated by

$$r_0 = k_B T / \mu_B b. \quad (3.26)$$

For a ${}^6\text{Li}$ cloud with a temperature of $T = 300\text{ }\mu\text{K}$, confined in a trap with a gradient factor of $b' = 2b = 120\text{ G/cm}$, the extension of the cloud is $r_0 \approx 0.74\text{ mm}$. Hence following the result from fig. 3.5, the cloud can be displaced by more than three times the estimated cloud size.

Other useful orders of magnitude for scaling the kick process are the average atomic velocity,

$$v_0 = \sqrt{k_B T / m_{\text{Li}}} \approx 0.64\text{ m/s}, \quad (3.27)$$

and the time it takes an atom to travel through the extension r_0 of the whole trapped cloud,

$$t_0 = r_0 / v_0 \approx 1.16\text{ ms}. \quad (3.28)$$

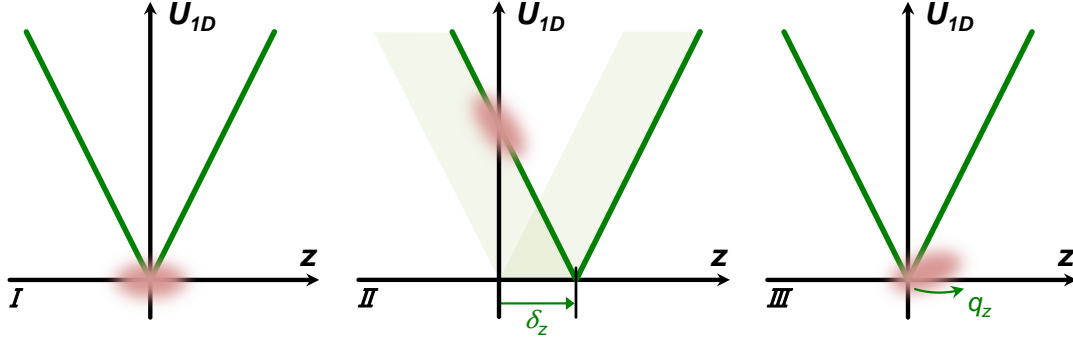


Figure 3.6: Illustration of the magnetic kick procedure. For simplification, the situation is depicted in 1D. (I) Initially, the cloud is trapped in the minimum of the linear potential $U_{1D}(z)$. (II) During a short duration τ , the center of the trap is shifted by δ_z using the spin-pol coil pair (C_{SP} in fig. 2.1) in case of a z -displacement. Sitting on the gradient slope, the cloud acquires a momentum q_z . (III) The offset-bias is switched off after the kick time τ and the cloud evolves with momentum q_z in the initial trap geometry.

Figure 3.6 illustrates the kick procedure: During a short time τ the initial trapping potential U created by the magnetic field \mathbf{B} is displaced by a constant magnetic offset-field \mathbf{B}_0 . According to eq. (3.25), this results in a shift of the trapping minimum by an amount of

$$\delta = -(B_{0x}, B_{0y}, B_{0z}/2)/b \quad (3.29)$$

in position space. In order to avoid unwanted oscillations through the trap center during the displacement and therefore in turn a non uniform force acting on the atoms, we need to ensure the condition $\delta > r_0$. Without crossing the new displaced zero, the cloud experiences a force given by $-\Delta U(\mathbf{r} - \delta)$, which is either

$$\mathbf{F}_{\delta_x} = -\mu_B b \hat{\mathbf{e}}_x, \quad \text{or} \quad \mathbf{F}_{\delta_z} = -2\mu_B b \hat{\mathbf{e}}_z$$

for a pure displacement in x -direction or z -direction respectively.

The displacement duration τ ranges from 100 μs to 1.2 ms depending on the applied kick direction or rather displacement coil(s) in use. Ideally, the kick time τ is short enough, so that the displacement of the cloud d (not to be confused with the *trap* displacement $\delta > r_0$) in the shifted potential can be neglected in comparison to the cloud extension:

$$d_x \approx \frac{\mu_B b}{m} \frac{\tau^2}{2} \leq r_0, \quad \text{or} \quad d_z \approx \frac{2\mu_B b}{m} \frac{\tau^2}{2} \leq r_0. \quad (3.30)$$

Using the estimated cloud size from eq. (3.26), the upper bound for the kick time is given by $\tau_x < 1.6 \text{ ms}$ and $\tau_z < 1.2 \text{ ms}$. This condition is similarly expressed by comparing the displacement time to the characteristic time-scale from eq. (3.28), $\tau \leq t_0$.

After the time τ , the shifting offset bias-field \mathbf{B}_0 is switched off. The acquired momentum during the kick phase is thus roughly estimated by $q_x \sim \mu_B b \tau$ and $q_z \sim 2\mu_B b \tau$. In section 3.4.4, we will discuss a more accurate estimation of the acquired energy during the described kick procedure.

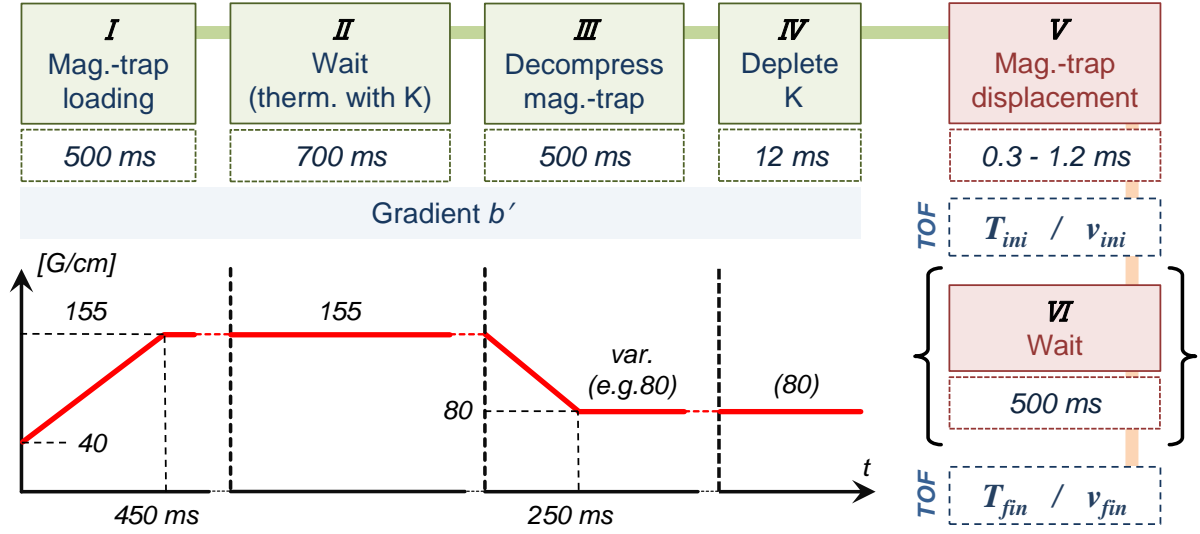


Figure 3.7: Experimental sequence for the "kick"-measurements. The sequence follows the steps described in fig. 2.21. We first prepare a well thermalized sample of ${}^6\text{Li}$ through collisions with the simultaneously trapped ${}^{40}\text{K}$ -cloud (**I-III**). After depleting ${}^{40}\text{K}$ from the trap (**IV**) by shining in resonant light, we perform the actual kick measurement (**V-VI**). For the experimental evaluation, we perform TOF-measurements directly after the kick and after a wait time of 500 ms. This allows the determination of the imparted velocity by the kick and of the temperature increase in the newly reached steady state.

3.4.2 Experimental sequence

The experimental sequence to test the predicted energy redistribution and direction decoupling from eq. (3.24) is illustrated in fig. 3.7. The depicted experimental steps follow the usual experimental procedure summarized in sec. 2.9.

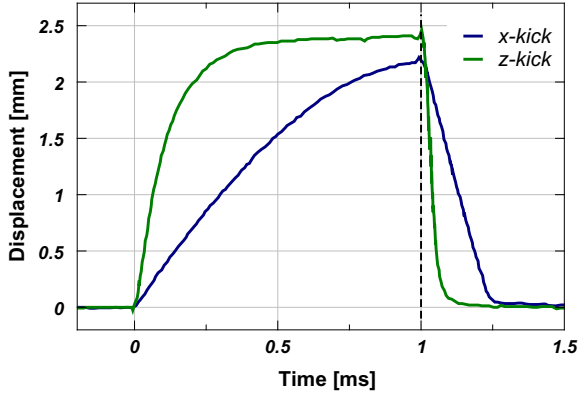
We start with ${}^6\text{Li}$ and ${}^{40}\text{K}$ loaded in the magnetic quadrupole trap which is created by the MOT-coils (**I**). To obtain a well thermalized cloud of ${}^6\text{Li}$ through inter-species collisions (see discussion in sec. 3.1 and temperatures in table 2.1), we hold both clouds for 700 ms in the compressed trap (**II**). Afterwards, we lower the trapping gradient within 250 ms to a value at which the final kick experiment will be performed (e.g. $b' = 80$ G/cm in **III**). At this gradient, we hold both species for additional 250 ms, before ${}^{40}\text{K}$ gets removed from the trap by shining in a resonant light pulse (**IV**). After this procedure, we usually obtain a cloud of ${}^6\text{Li}$ with $\sim 1 \cdot 10^8$ atoms, well thermalized at a temperature slightly below 300 K⁵. In step **V**, the actual kick is performed: Asking the maximal current value from the power supplies we close either the MOSFET or the IGBT, which are used as switches for the current in the push- or spinpol-coil respectively, for a short duration of $\tau = 0.3$ ms – 1.2 ms.

The current increase in the coils as well as the decrease after a 1 ms kick are depicted in fig. 3.8. It should be emphasized at this point, that the depicted current curves are measured

⁵The atom number and temperature for ${}^6\text{Li}$ are measured after step IV in a quadrupole trap gradient of $b' = 150$ G/cm. In case of adiabatic compression / decompression from a gradient b'_i to a value of b'_f , the temperature changes from T_i to T_f according to

$$T_f/T_i = (b_f/b_i)^{2/3} ,$$

due to phase space density conservation within an adiabatic process.

**Figure 3.8**

Switching dynamics of the coils performing the kick. For the magnetic kick, we continuously ask the maximum current from the power supplies and just switch a MOSFET (spin-pol coils) or an IGBT (push coil) during the kick time τ . For the diagram, we switch on at 0 ms and off after 1 ms and record the current in the coils by using a current transducer. Knowing the maximal current, we rescale the diagram with the maximal recorded displacement (see fig 3.5). The push coil, which is used for x-kicks, shows a slower overall switching performance, by taking up to $230\mu\text{s}$ to switch off.

by a current transducer attached around the power supply cables leading to the coils. As will be described later on, it does not represent the real magnetic field. So far, we can only claim that kicks along the x -direction performed by the push coil need to have a duration of at least $300\mu\text{s}$, to allow for a displacement larger than r_0 (eq. (3.26)) – a limitation imposed by the slow rise of the current in the particular coil.

We record the initial temperature T_{ini} and velocity v_{ini} by measuring the expansion and the center position of the cloud directly after the kick through TOF-images. By adding a 500 ms wait step (VI), we permit the cloud to reach a steady state⁶ and record the final temperature T_f and velocity v_f again by taking successive TOF images. According to sec. 2.7.3, we integrate the 2D-absorption images either along the x -axis to analyze the 1D- z -profile or along the z -axis to obtain the 1D- x -profile and its evolution. Thus, we deduce two 1D-quasi temperatures and the velocities along each direction.

A major experimental problem are eddy currents supported by the steel chamber itself and by the large metal surface of the optical table underneath the experimental chamber. The duration of the remaining magnetic fields depends of the amplitude of the switched gradient or constant magnetic fields and is estimated to be up to 5 ms. This time scale is comparable to the executed TOF times for ^6Li and thus, images show a deformed cloud shape due to inhomogeneous temporary Zeeman shifts, which in turn complicates the evaluation (i.e. fitting a Gaussian profile). Higher TOF-times at the given temperature ($\sim 300\mu\text{K}$) show a diluted cloud and hence a low detectivity, due to the low mass and therefore higher expansion velocity of the ^6Li -gas (compared to a cloud of ^{40}K at the same temperature). Since we are not interested in the atom number as an observable, we use a highly saturated imaging probe-beam with a saturation parameter of $s = 24$ to image the cloud⁷. This results in a power-broadening of the absorption resonance from the natural linewidth of the used D_2 -line (of $\Gamma \approx 6\text{ MHz}$) to $\Gamma' = \Gamma\sqrt{1+s} = 30\text{ MHz}$. The broadening is found to be sufficient to smear-out the temporary spatially-varying Zeeman shifts, created by the eddy currents over the extension of the cloud.

However, considering the kick procedure during which the quadrupole trap gets displaced by an additional offset bias, we have to take into account the unavoidable effect of eddy currents as

⁶See the next section, where fig. 3.10 justifies the choice of the wait duration.

⁷The increased saturation parameter corresponds to an increase of the imaging beam power from usually $100\mu\text{W}$ to 1.2 mW .

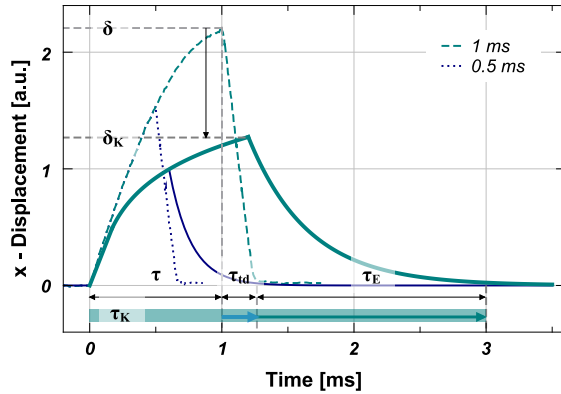


Figure 3.9

Estimation of the influence of eddy currents on the kick displacement for the push coil (x -kick). The solid lines are blind estimates of the displacement evolution, related to the build up of parasitic magnetic fields around the MOT chamber for a kick of 1 ms and 0.5 ms. The estimation is built on the recorded current evolution in the push coil from fig. 3.8 (here as dashed / dotted lines). Surely, the induced fields will first work against the current increase (thus $\delta_K < \delta$) and afterwards sustain the rapidly descending field ($\tau_K = \tau + \tau_{td} + \tau_E > \tau$).

well. This might be crucial especially for x -displacements, since according to fig. 3.8 the current rises slowly towards the maximum value in the particular case of the push coil. Figure 3.9 shows an estimated picture of the eddy currents affecting the x -kick displacement through time: First the surrounding conducting surfaces try to compensate the increase of the magnetic field, hence the reached maximal displacement δ_K will be smaller than assumed. Similarly, the switching-off time will be extended over the intrinsic turn down time τ_{td} of the coil towards τ_E . In total, we will have underestimated the kick time $\tau_K > \tau$ and overestimated the achieved displacement $\delta_K < \delta$. Unfortunately, it is not possible to measure the influence and the form of the eddy-current induced magnetic field distortion at the place of the atoms directly, notably at this time scale. However in sec. 3.4.4, we will calculate the transferred energy as a function of the kick displacement δ_K and therefore infer the magnitude of the realistically performed displacement in presence of the parasitic magnetic fields.

At the end, we mention the peculiarity of the line of sight of the imaging system in fig. 2.1 in the MOT chamber: While the kick directions are well aligned with the x and z -axis, the imaging plane is turned by 45° around the z -axis. Consequently, for x -kicks we observe along a rotated direction the redistribution of the energy in the xy -plane. It should be noted, that under these circumstances, the dimensions need to be rescaled by a factor of $\sqrt{2}$ to determine the kick velocity.

3.4.3 Experimental results

Figure 3.10 shows the evolution of the center-of-mass position as well as the transformation of the cloud width σ through time after a kick in x -direction performed by the push coil. As already indicated by the preliminary results from sec. 3.1 and suggested by the numerical simulation in fig. 3.4, the oscillations of the center of mass are damped and the cloud reaches a steady state after ~ 60 ms. The fitted decay time by $\exp(-t/\tau_{\text{decay}})$ varies for different kick durations between 10 ms to 30 ms. Hence the expected wait time of 500 ms before recording the steady state 1D-temperatures (mentioned in fig. 3.7) is largely sufficient.

In the x -kick situation presented in fig. 3.10, the z -position of the cloud center is not affected, as justified by symmetry arguments. We observe a similar behavior in case of a z -kick, where the oscillations are restricted to the z -center-of-mass position only. Regarding the cloud width after TOF in the depicted x -kick-case, we see a clear spread of the x -width σ_x after few oscillations, resulting in a higher momentum-spread. Therefore, we expect a temperature increase in the

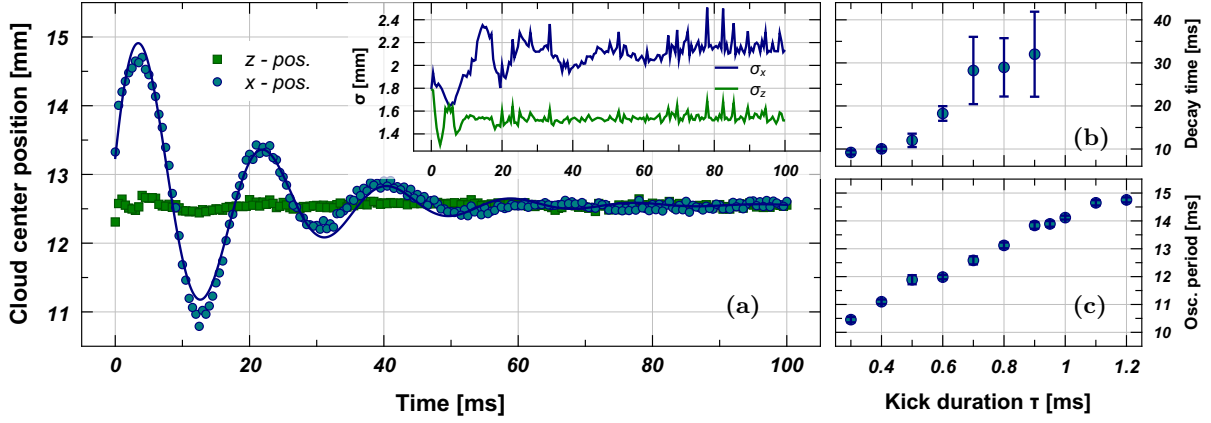


Figure 3.10: Cloud oscillation after performing a kick in x -direction with the push coil. The main figure (a) shows the damped oscillation in x -position of the center of mass of the cloud through time, performed in a trap of a gradient $b' = 80$ G/cm. By contrast, there is barely any movement on the z -axis. The embedded figure presents the corresponding evolution of the cloud width σ . Center-of-mass position and width are recorded after a TOF of 1 ms. On the left side, the decay time (b) and the oscillation period (c) as a function of the performed kick time τ_K are depicted. The last two figures are deduced from measurements in a gradient of $b' = 150$ G/cm.

x -direction. In contrast, the width σ_z along the orthogonal direction is only affected right after the kick, but stabilizes at a slightly smaller width (1.8 mm at the kick start to 1.6 mm at the end). This partial cooling effect will be discussed in greater detail further on in the text.

Fig. 3.10 verifies experimentally, that the cloud relaxes towards a new steady state, despite the absence of collisions. The only acting force is due to the confining linear potential and there is no further correlation between the single particles. But yet the rethermalization effect is purely statistical and is based on the dephasing of the single-particle trajectories as they oscillate in the potential.

We further studied the steady state temperature as a function of the acquired kick momentum. According to the theoretical prediction from eq. (3.24), the relation to test is summarized by

$$\langle p_i^2 \rangle_\infty = \langle p_i^2 \rangle_{0-} + \alpha_{X/Zi} \cdot q_{X/Z}^2 \quad \Leftrightarrow \quad \frac{1}{2} k_B \Delta T_i = \alpha_{X/Zi} \cdot \frac{q_{X/Z}^2}{2m}, \quad (3.31)$$

where we used eq. (3.1) to convert kinetic energy into an effective temperature for one degree of freedom. The capital letters X or Z in the index indicate the kick direction, e.g. $\mathbf{q}_X = (q_X, 0, 0)$, while the following lower case $i = x, z$ marks the detection direction of the redistributed imparted momentum $q_{X/Z}$. To work in dimensionless units and to have a better overview over the magnitude of the imparted momentum and temperature increase, we divide eq. (3.31) by the initial temperature of the cloud:

$$\frac{\Delta T_i}{T_{0i}} = \alpha_{X/Zi} \cdot \left(\frac{q_{X/Z}}{\sqrt{m k_B T_{0i}}} \right)^2 = \alpha_{X/Zi} \cdot \eta_{X/Zi}^2. \quad (3.32)$$

In this way the kick momentum $q_{X/Z}$ is expressed in units of the average atomic velocity v_0 from eq. (3.27), $\eta = q_{X/Z}/(mv_0)$.

The relation in eq. (3.32) translates to the recorded experimental quantities from fig. 3.7 for

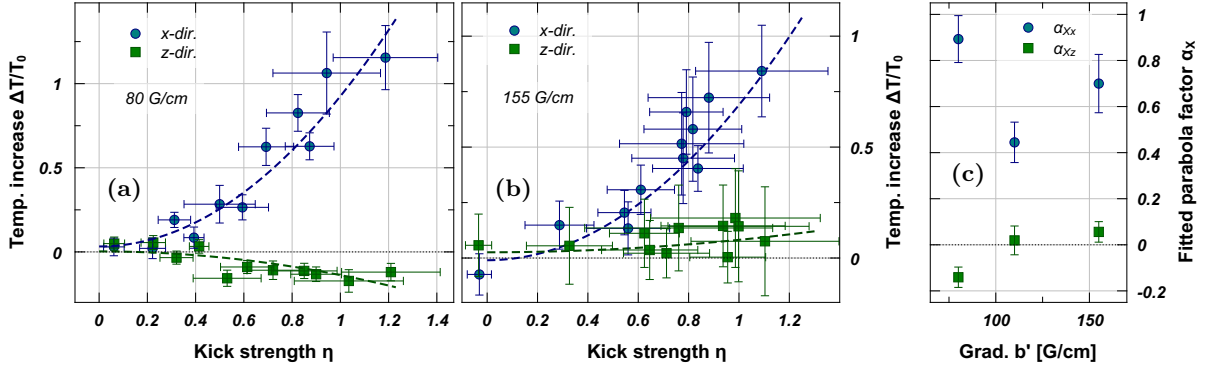


Figure 3.11: Momentum transfer measurements for x -kicks. Figure (a) and (b) depict each a measurement for the temperature increase / decrease in x and z -dir. as a function of the kick strength η . Thea kicks are performed in x -dir. in a particular trap gradient of $b' = 80$ G/cm and $b' = 155$ G/cm correspondingly. The dashed lines are fits according to eq. (3.34). The rightmost plot (c) summarizes the fitted parameters α_{Xi} for measurements performed in different gradients. As before, blue color tones correspond to the x -dir., while the z -dir. is represented in green colors.

example in the case of a kick in x -direction by

$$\frac{\Delta T_i}{T_{0i}} = \frac{T_{\text{fin}i}}{T_{\text{ini}i}} - 1 \quad \text{and} \quad \eta_{Xi} = \sqrt{\frac{m}{k_B T_{\text{ini}i}}} (v_{\text{ini}x} - v_{\text{fin}x}) , \quad (3.33)$$

where T_{ini} and v_{ini} are the temperature and velocity recorded directly after the kick is performed, while T_{fin} and v_{fin} are recorded after a 500 ms wait time, when the cloud reached the new steady state. Even though we supposed to start from a thermalized cloud of ^6Li , there might be a small discrepancy between $T_{\text{ini}x}$ and $T_{\text{ini}z}$, which leads to slightly different η_{Xx} and η_{Xz} coordinate for the same kick strength.

Figure 3.11 shows the result for a x -kick performed in different trap gradients b' : The figures (a) and (b) depict two examples of kick measurements in a gradient of $b' = 80$ G/cm and $b' = 155$ G/cm. Each temperature, T_{fin} and T_{ini} , is deduced from 10 different TOF-times (for TOFs in between 1.5 ms and 3.2 ms), whereby each TOF is repeated 8 times. The linear fit, either for the center position as a function of time or for $\sigma^2(t^2)$ as described by eq. (2.13), yields the velocity and temperature respectively and the corresponding error. We fit the parabolic function from eq. (3.32) with an additional offset a ,

$$\frac{\Delta T_i}{T_{0i}} = a + \alpha_{Xi} \cdot \eta_{Xi}^2 , \quad (3.34)$$

which accounts for residual heating sources during the 500 ms wait time, which are not kick related (e.g. parasitic light sources or current fluctuations in the coils). The value of a is not relevant for the later evaluation (as it is found to be of a magnitude smaller than α).

The same measurement is performed in different magnetic trap gradients. Each time we observe clear decoupling between the kick-direction x and the z -axis. Only for the lowest trap gradient of $b' = 80$ G/cm, we witness a minor cooling effect in z -dir. with increasing kick strength η_X (fig. 3.11 (a)). The last diagram (c) in fig. 3.11 summarizes the fitted kick transfer factors α_X for all the utilized gradients. Following the discussion of sec. 3.3, the theoretical

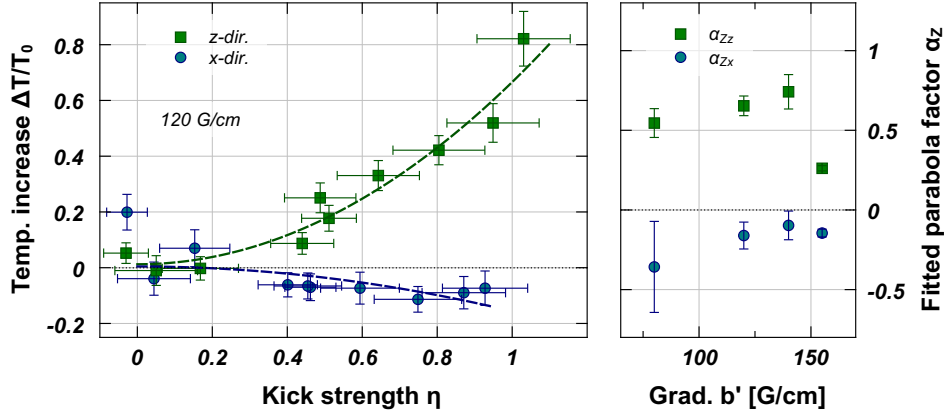


Figure 3.12: Momentum transfer measurements for z -kicks. Similar to fig. 3.11, the left figure shows a measurement for a z -kick performed in a trap of gradient $b' = 120$ G/cm, while the right one summarizes the corresponding fit-parameters α_{zi} along x and z , for kicks along z performed in different trap gradients.

energy redistribution (3.24) does not depend on the trap gradient b' . Interpreting the observed gradient dependency as the influence of eddy currents during TOF, we can average over the recorded factors to derive the energy transfer coefficients for the x -kick:

$$x\text{-kick: } \frac{\Delta T_x}{T_{0x}} = (0.68 \pm 0.13) \cdot \eta^2, \quad \frac{\Delta T_z}{T_{0z}} = (-0.02 \pm 0.06) \cdot \eta^2. \quad (3.35)$$

It is important to emphasize once again, that the deduced 1D-temperatures are not classical temperatures of a Boltzmann distribution: The final, steady state cloud shows two different expansion velocities in x and z -direction after the kick and hence an isotropic temperature in the sense of a Boltzmann distribution can *not* be attributed. However, in terms of kinetic energy we can attribute two different *quasi*-temperatures to the cloud.

The corresponding results for the z -kick are presented in fig. 3.12. We observe again a clear decoupling between the kick direction and the orthogonal axis x . In difference to the previously discussed x -kick situation, we always observe pronounced cooling for increasing kick strength on the orthogonal direction – for all gradients b' , the fitted coefficients $\alpha_{zx} < 0$. The corresponding averaged transfer coefficients are:

$$z\text{-kick: } \frac{\Delta T_x}{T_{0x}} = (-0.19 \pm 0.06) \cdot \eta^2, \quad \frac{\Delta T_z}{T_{0z}} = (0.55 \pm 0.1) \cdot \eta^2. \quad (3.36)$$

We attribute the pronounced cooling to the imperfection of the magnetic-kick performed by the spin-pol coil pair. Regarding the error bars, the cooling effect becomes negligible at gradients above $b' = 100$ G/cm.

Apart from a more pronounced cooling effect in the z -kick situation, we observe quantitatively very well an anisotropy in the energy redistribution in both kick cases. This behavior suggests a well approximated decoupling of the symmetry axis z and the xy -plane of the trapping potential, even though the trapping potential itself is non separable (see eq. (3.3)). Numerical simulations show a slight cooling effect as well, but only on the order of $\alpha_{xz} \approx \alpha_{zx} \approx -0.006$ [118]. We attribute the more pronounced cooling in the z -kick-case to cloud distortions during switching-off

of the magnetic field gradient before TOF, since the axial gradient b' is twice as large as along the x - or y -axis.

Clearly, the experimentally observed coefficients are not in agreement with the (ideal) theoretical predictions of eq. (3.24), where the z -transfer coefficient is $\alpha_{Zz} = 1/3$ and the x -coefficient $\alpha_{Xx} = 1/6$. In order to investigate this contradiction, we have to find the right estimation of the transferred energy during our particular kick procedure, which will be the subject of the next section.

3.4.4 Realistic kick estimation

As stated in sec. 3.2 and has become apparent in the description of the kick procedure in fig. 3.6, we do not transfer the same momentum \mathbf{q} to each single atom. Rather an average energy, kinetic and potential, is transferred to the cloud during the described kick process. Still holding on to the ideal prediction developed in sec. 3.3, we can reformulate eq. (3.24) as a dependence on the imparted energy rather than as a function of the transferred momentum. In order to achieve this, we will have to determine the relation between the average acquired total energy $\langle \Delta E_{\text{kick}} \rangle$ during the kick and the kick momentum $\langle \mathbf{q} \rangle$, which being an easily accessible quantity is measured directly in the experiments performed in sec. 3.4.3. Once this relation is established for our kick process, the rewritten redistribution relations (eq. (3.31)) in terms of imparted total energy,

$$\frac{1}{2} k_B \Delta T_i = \alpha_{X/Zi} \cdot \frac{q_{X/Z}^2}{2m} \quad \Rightarrow \quad \frac{1}{2} k_B \Delta T_i = \alpha_{X/Zi} \cdot \langle \Delta E_{\text{kick}}(q_{X/Z}) \rangle = \alpha'_{X/Zi} \cdot \frac{q_{X/Z}^2}{2m},$$

will account as well for the imparted potential energy and allow an estimation of the performed cloud displacement during the kick.

Acquired average momentum

In the displaced trap (during the time τ) the acquired average momentum \mathbf{q} is calculated accordingly to eq. (3.11) by:

$$\langle \mathbf{q} \rangle = \int d^3 \mathbf{r} d^3 \mathbf{p} f(\mathbf{r}, \mathbf{p}, \tau) \mathbf{p} = \int d^3 \mathbf{r}_0 d^3 \mathbf{p}_0 f_0(\mathbf{r}_0, \mathbf{p}_0) \mathbf{p}(\tau, \mathbf{p}_0, \mathbf{r}_0);. \quad (3.37)$$

Instead of determining the phase space distribution $f(\mathbf{r}, \mathbf{p}, \tau)$ in the displaced trap, we will assume only short excitation times τ and perturbatively develop the momentum coordinate through time in the displaced potential:

$$\begin{aligned} \mathbf{p}(\tau, \mathbf{p}_0, \mathbf{r}_0) &\approx \mathbf{p}_0 + \tau \partial_t \mathbf{p} + \frac{\tau^2}{2} \partial_t^2 \mathbf{p} \\ &= \mathbf{p}_0 + \tau \mathbf{F}_\delta + \frac{\tau^2}{2} \frac{1}{m} (\mathbf{p}_0 \cdot \nabla_r) \mathbf{F}_\delta. \end{aligned} \quad (3.38)$$

Thereby the acting force is given by the displaced trapping potential,

$$\mathbf{F}_\delta = -\nabla_r U(\mathbf{r} - \delta). \quad (3.39)$$

Due to symmetry reasons, the integral over $\mathbf{p}_0 f_0(\mathbf{r}_0, \mathbf{p}_0)$ vanishes. Thus, the average transferred momentum is linear in τ :

$$\langle \mathbf{q} \rangle = \tau \int d^3\mathbf{r}_0 d^3\mathbf{p}_0 f_0(\mathbf{r}_0, \mathbf{p}_0) \mathbf{F}_\delta . \quad (3.40)$$

The linear dependence on the excitation time τ is not surprising, since even in the rough estimation of the imparted momentum at the end of sec. 3.4.1 by $\langle \mathbf{q} \rangle \sim \mu b \tau$, the transferred momentum scaled linear with the kick time.

Acquired kinetic energy

Proceeding similarly to the estimation of the imparted average momentum in the average trap, we can calculate the average kinetic energy:

$$\begin{aligned} \langle E_{\text{kin}} \rangle &= \int d^3\mathbf{r}_0 d^3\mathbf{p}_0 f_0(\mathbf{r}_0, \mathbf{p}_0) \frac{\mathbf{p}(\tau)^2}{2m} \\ &= \int d^3\mathbf{r}_0 d^3\mathbf{p}_0 f_0 \left\{ \mathbf{p}_0^2 + 2\tau \mathbf{p}_0 \mathbf{F}_\delta + \tau^2 \left(\mathbf{F}_\delta^2 + \frac{\mathbf{p}_0}{m} (\mathbf{p}_0 \cdot \nabla_r) \mathbf{F}_\delta \right) \right\} . \end{aligned} \quad (3.41)$$

In the last step we inserted the developed momentum expression from eq. (3.38) and kept only terms up to second order in τ . The first term represents the expectation value of the kinetic energy in the unshifted trap. In the second term, we will introduce the Liouville operator, eq. (3.7), to replace the spacial derivative

$$\hat{L} - \mathbf{F}_0 \partial_{p_0} = \frac{\mathbf{p}_0}{m} \cdot \nabla_r , \quad \mathbf{F}_0 = -\nabla_r U(\mathbf{r}) . \quad (3.42)$$

Since $f_0(\mathbf{r}_0, \mathbf{p}_0)$ is a stationary solution of the Liouville operator, we can use the identity shown in eq. (I.6) to rewrite

$$\begin{aligned} \int d^3\mathbf{r}_0 d^3\mathbf{p}_0 f_0 \frac{\mathbf{p}_0}{m} (\mathbf{p}_0 \cdot \nabla_r) \mathbf{F}_\delta &= \int d^3\mathbf{r}_0 d^3\mathbf{p}_0 f_0 \left(\frac{\mathbf{p}_0}{m} \cdot \nabla_r \right) (\mathbf{p}_0 \mathbf{F}_\delta) \\ &= - \int d^3\mathbf{r}_0 d^3\mathbf{p}_0 f_0 (\mathbf{F}_0 \partial_{p_0}) (\mathbf{p}_0 \mathbf{F}_\delta) \\ &= - \int d^3\mathbf{r}_0 d^3\mathbf{p}_0 f_0 \mathbf{F}_0 \mathbf{F}_\delta . \end{aligned}$$

Putting it all together, the expectation value of the kinetic energy is given by:

$$\langle E_{\text{kin}} \rangle = \langle E_{\text{kin}0} \rangle + \frac{\tau^2}{2m} \int d^3\mathbf{r}_0 d^3\mathbf{p}_0 f_0(\mathbf{r}_0, \mathbf{p}_0) \mathbf{F}_\delta (\mathbf{F}_\delta - \mathbf{F}_0) . \quad (3.43)$$

In case of zero displacement, $\delta = 0$, the kinetic energy remains unchanged and there is obviously no heating.

Acquired potential energy

For the expectation value of the potential energy, we will develop the displacement \mathbf{r} , similar as it was done for the kinetic energy and the momentum \mathbf{p} in eq. (3.38):

$$\begin{aligned} \mathbf{r}(\tau, \mathbf{p}_0, \mathbf{r}_0) &\approx \mathbf{r}_0 + \tau \partial_t \mathbf{r} + \frac{\tau^2}{2} \partial_t^2 \mathbf{r} \\ &= \mathbf{r}_0 + \tau \frac{\mathbf{p}_0}{m} + \frac{\tau^2}{2} \frac{\mathbf{F}_\delta}{m} . \end{aligned} \quad (3.44)$$

Inserting this evolution in the potential energy $U(\mathbf{r}(\tau))$, we can further develop the potential around the unperturbed energy $U(\mathbf{r}_0)$. Keeping only terms up to second order in τ , we obtain the approximation (see appendix-sec. I.6 for more details):

$$U(\mathbf{r}(\tau)) \approx U(\mathbf{r}_0) + \tau \frac{\mathbf{p}_0}{m} \partial_r U(\mathbf{r}_0) + \frac{\tau^2}{2} \left\{ \frac{\mathbf{F}_\delta}{m} \partial_r U(\mathbf{r}_0) + \left(\frac{\mathbf{p}_0}{m} \nabla_r \right)^2 U(\mathbf{r}_0) \right\} . \quad (3.45)$$

The average acquired potential energy is calculated through

$$\langle E_{\text{pot}} \rangle = \int d^3 \mathbf{r}_0 d^3 \mathbf{p}_0 f_0(\mathbf{r}_0, \mathbf{p}_0) U(\mathbf{r}(\tau, \mathbf{p}_0, \mathbf{r}_0)) . \quad (3.46)$$

Inserting the previously discussed evolution of $U(\mathbf{r}(\tau))$ from eq. (3.45), the first term, $U(\mathbf{r}_0)$, will represent the average potential energy in the unshifted trap, while the second term, which is linear in \mathbf{p}_0 , will vanish throughout the integration over momentum. Therefore, the transferred potential energy shows only a second order dependency on the kick time τ , similar to the case of the kinetic energy in eq. (3.43).

Once again, introducing the Liouville operator through the substitution of eq. (3.42), we obtain

$$\begin{aligned} \int d^3 \mathbf{r}_0 d^3 \mathbf{p}_0 f_0 \left(\frac{\mathbf{p}_0}{m} \nabla_r \right)^2 &= \\ \int d^3 \mathbf{r}_0 d^3 \mathbf{p}_0 f_0 \left\{ \hat{\mathbf{L}} \left(\frac{\mathbf{p}_0}{m} \nabla_r U(\mathbf{r}_0) \right) + \frac{1}{m} \left(\nabla_r U(\mathbf{r}_0) \right)^2 \right\} . \end{aligned}$$

Applying $\hat{\mathbf{L}}$ on the stationary solution $f_0(\mathbf{r}_0, \mathbf{p}_0)$ through the scalar product property shown in eq. (I.6), the first summand vanishes. Thus, the potential energy in eq. (3.46) results in

$$\langle E_{\text{pot}} \rangle = \langle E_{\text{pot}0} \rangle + \frac{\tau^2}{2m} \int d^3 \mathbf{r}_0 d^3 \mathbf{p}_0 f_0(\mathbf{r}_0, \mathbf{p}_0) \mathbf{F}_0 (\mathbf{F}_0 - \mathbf{F}_\delta) . \quad (3.47)$$

Acquired total energy and relation to average momentum

Combining the results of the estimated acquired kinetic and potential energies from eq. (3.43) and eq. (3.47), the increase in energy $\langle \Delta E_{\text{kick}} \rangle$ through the kick procedure yields

$$\langle \Delta E_{\text{kick}} \rangle = \frac{\tau^2}{2m} \int d^3 \mathbf{r}_0 d^3 \mathbf{p}_0 f_0(\mathbf{r}_0, \mathbf{p}_0) (\mathbf{F}_0 - \mathbf{F}_\delta)^2 . \quad (3.48)$$

The idealized kick picture deals with the average momentum $\langle \mathbf{q} \rangle$ (eq. (3.40)), which can be interpreted as kinetic energy

$$\frac{\langle \mathbf{q} \rangle^2}{2m} = \frac{\tau^2}{2m} \left\{ \int d^3 \mathbf{r}_0 d^3 \mathbf{p}_0 f_0(\mathbf{r}_0, \mathbf{p}_0) \mathbf{F}_\delta \right\}^2, \quad (3.49)$$

obtained by each single atom. Following the motivation at the beginning of this section, we are interested in the relation of the ideally estimated kick momentum (3.49) and the imparted energy (3.48). Indeed, since in the experiment we measure the initial cloud velocity right after the kick and consequently set this velocity into relation to the acquired heating, we need to find the transfer factor between the imparted momentum and the imparted total energy.

In both integrals above, we can evaluate the momentum integration. Together with the normalization of $f_0(\mathbf{r}_0, \mathbf{p}_0)$ through the fugacity Z , we obtain:

$$\epsilon_\delta = \langle \Delta E_{\text{kick}} \rangle / \left(\frac{\langle \mathbf{q} \rangle^2}{2m} \right) = \frac{4\pi}{(\beta\mu b)^3} \int d^3 \mathbf{r}_0 e^{-\beta U(\mathbf{r}_0)} (\mathbf{F}_0 - \mathbf{F}_\delta)^2 / \left\{ \int d^3 \mathbf{r}_0 e^{-\beta U(\mathbf{r}_0)} \mathbf{F}_\delta \right\}^2 \quad (3.50)$$

In the present approximation, the adjustment factor ϵ_δ depends solely on the displacement δ and not on the kick duration τ . The integrals are evaluated numerically for different x and z -kicks, by displacing either in x -dir. by $\boldsymbol{\delta}_X = (\delta, 0, 0)$ or in z -dir. by $\boldsymbol{\delta}_Z = (0, 0, \delta)$. The results are multiplied by 1/6 or 1/3, for a x -kick or for a z -kick correspondingly, according to the ideal kick relations from (3.24), resulting in the corrected transfer factors:

$$\alpha'_{Xx} = \frac{1}{6} \epsilon_{\delta_X}, \quad \text{and} \quad \alpha'_{Zz} = \frac{1}{3} \epsilon_{\delta_Z}. \quad (3.51)$$

The new transfer factors $\alpha'_{Xx/Zz}$ incorporate the relation between the (also measured) momentum of the cloud transferred through the kick and the entirely transferred energy, which includes also the previously neglected potential part.

Figure 3.13 shows the transfer factors α' as a function of the displacement δ in mm for the different trap gradients b' applied in the corresponding experiments. For the z -kick, the experimental value of $\alpha'_{Zz} = (0.55 \pm 0.1)$ from eq. (3.36) is, within error bars, in very good agreement with the transfer factors for all displacements larger than $\delta \geq 0.5$ mm.

In case of the x -kick, fig. 3.13b suggests that the large transfer factor found in eq. (3.35), $\alpha'_{Xx} = (0.68 \pm 0.13)$, can be justified only for displacements smaller than $\delta \leq 0.5$ mm. Indeed, recalling the discussion at the end of sec. 3.4.2, where the influence of parasitic magnetic fields on the kick displacement was estimated (see fig. 3.9), we assumed already smaller displacements than indicated by the push coil current value. Now we can tell, that the displacement δ realized experimentally is below the estimated cloud extension of $r_0 \approx 0.74$ mm (see sec. 3.4.1 and fig. 3.6). During the kick we transferred both, potential and kinetic energy to the cloud rather than momentum solely. Remarkably, in the realized displacement range the two transfer factors get adjusted around a value of ~ 0.5 : While the pure decoupling model distributes the energy in the entire plane in case of a x - or y -kick, therefore leading to a transfer factor $\alpha_{Xx} = \alpha_{Zz}/2$ (see eq. (3.24)), the weaker confinement of the quadrupole potential along the x - and y -axis ($b = b'/2$) favors a larger potential energy transfer compared to the z -kick in the performed experiment.

The gradient dependence of the $\alpha'_{X/Z}$ -coefficients in fig. 3.13 is much less pronounced than in

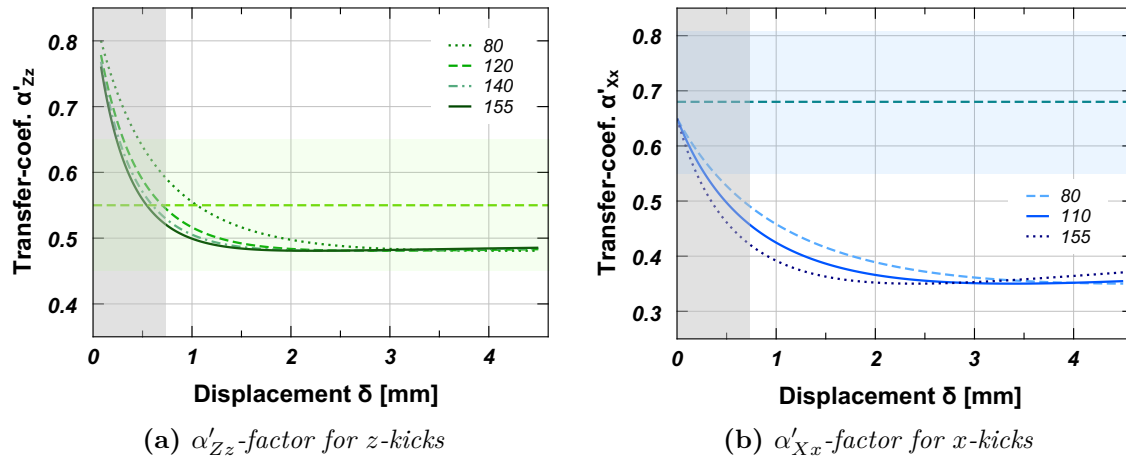


Figure 3.13: Corrected kick transfer factors α'_{zz} (a) and α'_{xx} (b) according to eq. (3.51) as a function of the trap displacement δ in mm for the different corresponding experimental gradients b' . The dashed straight lines and the green / blue colored regions indicate the experimentally measured transfer factors and the corresponding error bar regions from eq. (3.36) and eq. (3.35). The gray regions mark the approximate extension of the cloud, $r_0 \approx 0.74$ mm.

the experiment. Thus the recorded deviation of the transfer factors for different trap gradients b' in fig. 3.11 and fig. 3.12 (c) is rather attributed to the eddy current imperfections during the final switching of the quadrupole trap before TOF than to differently acquired potential energy contributions for different gradients.

In conclusion we should point out, that even though the momentum transfer factors of the ideally kicked system needed to be adjusted to explain the experimental results, due to the imparted potential energy, the physics of the energetically decoupled symmetry axis z from the transverse xy -trapping plane in the quadrupole potential remains unchanged and was well reproduced by the experimental findings.

3.5 Conclusion

In summary, this chapter treated the thermalization of a cloud in a magnetic quadrupole trap in absence of interactions. Indeed, in the quadrupole potential a excited cloud of non-interacting spin-polarized ^6Li fermions relaxes towards a steady state. Unlike a Boltzmann distribution, this equilibrium state is not described by an isotropic temperature anymore, but rather by two distinct effective temperatures along the symmetry axis z and the orthogonal xy -plane of the trapping potential. We experimentally observe the decoupling between these directions after a magnetic kick of the cloud. Either the imparted energy is redistributed within the xy -plane, in case the kick direction was within the plane or we observe a spread of the momentum distribution along the (trapping) symmetry-axis only, provided that the kick was performed along this axis. We call this observation a quasi-thermalization effect, since a classical thermodynamic equilibrium is only achieved within the xy -plane.

The observations are well described by a theoretical model, taking into account realistic excitations in the experimental setup. However, a completely analytical derivation of the

momentum transfer in eq. (3.24) can be the subject of further theoretical work⁸. A possible approach could be to explore the role of the entropy in this system. Indeed, since the cloud is collisionless the entropy is a conserved quantity. Besides, ensembles of non-interacting particles provide an example of generalized Gibbs ensembles as studied in [165].

The results of this section in conjunction with the interpretation of the system as harmonically trapped Weyl-fermions, which will be the subject of the next chapter (see sec. 4.1), are published in [166].

⁸We remind, that at the end of sec. 3.3, we used the result of a numerical simulation to deduce the coefficients of the momentum transfer matrix θ_{ij} from the final analytical result in eq. (3.23).

Quantum Simulation in the Quadrupole Potential - Spin-Orbit-Coupling in a Non-Interacting Gas

We mentioned in the introduction (ch. 1), that nowadays ultra-cold gases experiments serve as tunable simulation tools for a wide range of otherwise not accessible systems. In this chapter, we will show how a experimental setup can serve for this purpose in two particular cases.

In the first example, we will revisit the properties of magnetically trapped non-interacting spin polarized ${}^6\text{Li}$ atoms in a quadrupole potential. With a particular canonical mapping this system can be interpreted as a harmonically confined ensemble of non-interacting massless particles (sec. 4.1). A second more elaborate example will allow us to study a non-Abelian potential in form of a spin-orbit coupled (*SOC*) system.

4.1 Simulation of Massless Harmonically Trapped Non-Interacting Particles

The peculiarity of the experimentally realized single particle Hamiltonian from eq. (3.2),

$$H_{\text{Li}}(\mathbf{r}, \mathbf{p}) = \frac{p^2}{2m} + \mu b \left\{ \sum_{i=1}^3 \gamma_i^2 x_i^2 \right\}^{1/2} \quad \text{with} \quad \gamma_1 = \gamma_2 = 1 \quad \text{and} \quad \gamma_3 = -2, \quad (4.1)$$

to exclude any form of interaction term, allows for a canonical mapping to an analogous system. Following the slightly changed notation convention above, we are defining new position and momentum coordinates $\{X_i, P_i\}$, exchanging the previously attributed roles of the phase space coordinates:

$$X_i = c \frac{p_i}{\mu b \gamma_i} \quad \text{and} \quad P_i = -\frac{1}{c} \mu b \gamma_i x_i. \quad (4.2)$$

The newly introduced constant c represents an arbitrary velocity scale and adjusts the dimensionality of the new coordinates. We recall that the above transformation is canonical, because the new coordinates inherit the same Poisson-bracket relation as the original coordinates x_i and p_i ,

$$[X_k, P_l] = [x_k, p_l] = i\hbar \delta_{kl}.$$

Inserting the canonical mapping into eq. (4.1) reveals the transformed Hamiltonian,

$$H_{m=0}(\mathbf{R}, \mathbf{P}) = c \cdot |\mathbf{P}| + \frac{k_0}{2} \sum_i \gamma_i^2 X_i^2, \quad k_0 = \frac{(\mu b)^2}{mc^2}. \quad (4.3)$$

The first term describes the kinetic energy of a massless particle traveling at a constant velocity¹ c , while the second term corresponds to an anisotropic harmonic trapping potential with frequencies $\omega_i = \gamma_i \sqrt{k_0/m}$ along the directions X_i . A peculiarity of the massless particle in a harmonic trap, compared to a massive particle in the same trapping situation, is manifested in the first term of eq. (4.3): While a massless particle moves at constant velocity c its massive harmonically trapped counterpart would rather oscillate at a constant frequency.

Due to this canonical mapping the studied system of an ensemble of massive particles in a quadrupole potential is equivalent to the case of massless particles confined in an harmonic trapping potential². We can now translate our findings directly on the second case, by inverting the role of momentum and position.

The performed (ideal) momentum kick of the ${}^6\text{Li}$ -cloud corresponds to a spatial displacement of the massless particle ensemble. The different equilibrium temperatures of the cloud, $T_i = \langle p_i^2 \rangle_\infty / mk_B$, will translate into final widths of the spatial distributions, $k_0 \gamma_i \langle X_i^2 \rangle_\infty$.

Transferring the observed dynamics of ${}^6\text{Li}$ in the quadrupole potential, we can conclude that the displaced massless ensemble will *not* oscillate forever, but rather converge to a steady state. This behavior conflicts with the physics of a massive particle, which once excited in a harmonic potential will oscillate forever on a given trajectory in the harmonic trapping potential.

The steady state of the massless particle ensemble, described by the position spread $\langle X_i^2 \rangle_\infty$ along the three spatial directions, will show a decoupling of the symmetry axis Z from the XY -plane: If the initial displacement excitation is performed in X or Y -dir. the ensemble will relax towards an distribution with increased spread within the XY -plane,

$$\langle X^2 \rangle_\infty = \langle Y^2 \rangle_\infty > \langle X^2 \rangle_{t=0},$$

without influencing the Z -direction.

The analogy can be pushed further, by considering the atomic spin, which does not necessarily follow the magnetic field adiabatically. The general Hamiltonian describing an atom with magnetic moment $\boldsymbol{\mu} = \mu \hat{\boldsymbol{\sigma}}$ in this setup is given by (see eq. (2.2))

$$H_{\text{Mag. general}}(\mathbf{r}, \mathbf{p}) = \frac{p^2}{2m} - \mu \hat{\boldsymbol{\sigma}} \cdot \mathbf{B}(\mathbf{r}), \quad (4.4)$$

where $\hat{\boldsymbol{\sigma}}$ is a vector consisting of Pauli-matrices and $B_i = b\gamma_i x_i$. Contrary to the previously presented case of eq. (4.1) (or following the discussion preceding eq. (2.2)), the second term

¹We recall the relativistic energy-momentum relation,

$$E = \sqrt{(pc)^2 + (mc^2)^2},$$

for a particle with momentum p and mass m . In this formulation, c represents the speed of light. For a massless particle, only the first summand remains.

²A first trapping of quasi-particles by an external potential was purposed in [167] as an application on quantum dots.

above does not a priori assume adiabatic following of the magnetic field by the atomic spin. We can still use the canonical mapping from eq. (4.2) obtaining the spin-including version of eq. (4.3),

$$H_{\text{Weyl}}(\mathbf{R}, \mathbf{P}) = c \hat{\boldsymbol{\sigma}} \cdot \mathbf{P} + \frac{k_0}{2} \sum_i \gamma_i^2 X_i^2, \quad k_0 = \frac{(\mu b)^2}{mc^2}. \quad (4.5)$$

The particular form of the first term corresponds to the kinetic energy of a massless Weyl particle (see for example [168]). Weyl particles were introduced as massless solutions to the Dirac equation [169]³ and provide a description for spin 1/2 matter fields. However, in the particular form as written down above, Weyl fermions are described as low energy excitations of electrons in crystalline structures (Dirac semimetals) obeying a linear dispersion relation around so-called Weyl point [170]. The observation of this excitation spectra is currently a hot-topic in solid state physics and material sciences [171–173].

Using the Heisenberg picture, we derive the following two equivalent equations for the time evolution of the spin-observable in addition to the previously discussed behavior of momentum and position coordinates:

$$\dot{\boldsymbol{\sigma}}_{\text{Mag-general}} = \frac{2\mu}{\hbar} (\hat{\boldsymbol{\sigma}} \times \mathbf{B}) \quad \Leftrightarrow \quad \dot{\boldsymbol{\sigma}}_{\text{Weyl}} = \frac{2c}{\hbar} (\mathbf{P} \times \hat{\boldsymbol{\sigma}}). \quad (4.6)$$

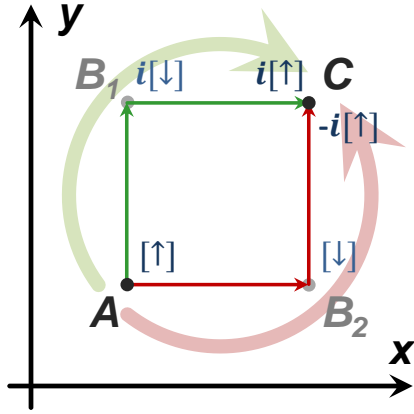
The first equation describes the coupling of the spin to the magnetic field \mathbf{B} in the classical system, while the canonical mapping of the same equation describes the coupling of the momentum \mathbf{P} to the spin of the Weyl particle. We remind ourselves of the previously mentioned effect of Majorana losses: If the classical spin of an atom does not follow adiabatically the magnetic field (for example at the trap center of the quadrupole trap, where the magnetic field vanishes and the potential slope changes the sign), the spin might flip to a not trappable state and the atom is lost from the trap. Now in analogy, we can state that if the rate of change of the Weyl-particle's momentum \mathbf{P} is too fast, the spin will not follow adiabatically the momentum and the helicity of the Weyl-particle will not be conserved. A changed helicity suppresses back scattering of the particle from potential wells and leads to 100 % transmission of the trapping potential. This effect is known as the Klein paradox [174]: Originally describing electron-tunneling through an infinitely large potential barrier, it applies in a similar way to massless particles, which tunnel through a barrier by flipping to negative energy states (thus changing the helicity). So far, the only existing experimental realization of the Klein-paradoxon was achieved in trapped $^{40}\text{Ca}^+$ ions [175]. Ref. [176] proposes to observe the Klein-paradoxon in a setup of graphene-layers.

The relation between Majorana losses and the breakdown of adiabatic following between momentum and the spin of a Weyl-fermion opens up new possibilities to study an otherwise not accessible system.

4.2 Spin-Orbit Coupling

In recent years, the topic of spin-orbit coupling (*SOC*) particularly attracted the attention of the cold-gas community, proposing the design and observation of so far not directly accessible and tunable systems. The initial ("historical") motivation was to mimic various quantum phenomena

³The Weyl particle was introduced through Hermann Weyl in 1929 on the attempt to find an unified theory for gravity and electromagnetic fields.


Figure 4.1

Aharonov-Bohm experiment in a non-Abelian vector field from eq. (4.9) [183]. We imagine a particle with the state $\uparrow = (1, 0)$ traveling from A to C along two different paths – green, through B_1 and red, passing B_2 . On the green path, the spin is manipulated first by $\hat{\sigma}_y$ and subsequently by $\hat{\sigma}_x$, while on the red path the action is inverted. This yields a phase shift of π at the end between two particles travelling on the two distinct trajectories. Practically, this could result in interference effects in this kind of non-Abelian vector fields.

which involve charged particles in an external magnetic field, like the fractional quantum Hall effect [177, 178]. Since today's typical cold gas experiments are performed with neutral atoms, the first approach was to design an implementation, which could be interpreted effectively as an action on a charged particle. Following this path, the action of the Coriolis force on a stirred BEC can be interpreted similarly to the action of a magnetic field forcing a charged particle to travel along a circular trajectory by means of the Lorentz force. However, the maximal reachable rotation frequency in such a system is limited by the trapping confinement [179]. To overcome this limitation, a light-induced coupling scheme, including a Raman transition was proposed in [180], which showed the same appearance of vortices as the previously actively stirred cloud [181]. The realized Hamiltonian included a coupling of the atomic spin to its external motion, giving rise to a band-structure-like dependence of the eigenenergy on the particle's momentum [182]. This effect is called spin-orbit coupling. In difference to the coupling of the electron's spin to its angular momentum (leading to the fine structure of the atomic spectrum), in the present case the spin of the atom (as an "internal" degree of freedom) couples to its "external" motion.

A more general form of SOC is known as the Rashba-Dresselhaus effect (based on the work of G. Dresselhaus [184] and E. I. Rashba, see [185] and earlier publications), which arises in two-dimensional semiconductors and explains phenomena related to topological insulators [186, 187]. Currently, this research area is of great interest, since it serves for technical realizations in the domain of spintronics [188], a promising approach to increase computational power in the future. The Hamiltonian describing these systems contains the Rashba-Dresselhaus SOC-term, which recasts to the common form [189]

$$U_{\text{non-Abelian}} = \kappa (p_x \hat{\sigma}_x + p_y \hat{\sigma}_y) , \quad (4.7)$$

with the Pauli-matrices

$$\hat{\sigma}_x = \begin{pmatrix} 0 & 1 \\ 1 & 0 \end{pmatrix} \quad \text{and} \quad \hat{\sigma}_y = \begin{pmatrix} 0 & -i \\ i & 0 \end{pmatrix} \quad (4.8)$$

and the coupling-strength parameter κ . The entire Hamiltonian (including the kinetic energy) can be brought to the form [190]

$$H \sim \frac{1}{2m} (\mathbf{p} - \mathbf{A})^2 \quad \text{with} \quad \mathbf{A} = -\hbar\kappa (\mathbf{e}_x \hat{\sigma}_x + \mathbf{e}_y \hat{\sigma}_y) , \quad (4.9)$$

where $\mathbf{e}_{x,y}$ are unit-vectors in x - or y -direction. The last Hamiltonian is similarly used to

describe a charged particle in a magnetic field represented by a vector-potential \mathbf{A} . Notably, in our case the two components of the vectorfield do not commute,

$$[\hat{\sigma}_x, \hat{\sigma}_y] = 2i\hat{\sigma}_z = 2i \begin{pmatrix} 1 & 0 \\ 0 & -1 \end{pmatrix}, \quad (4.10)$$

thus \mathbf{A} is referred to as a non-Abelian vectorfield. The phase acquired by a particle traveling in such a vector field is trajectory dependent and can be exploit in an Aharonov-Bohm-like experiment [183] (see fig. 4.1). Non-Abelian vector fields are also used for the discription of magnetic monopoles [191, 192]. For the sake of completeness, we mention that the associated artificial magnetic field of a non-Abelian potential \mathbf{A} is obtained by

$$\mathbf{B} = \nabla \times \mathbf{A} + \frac{1}{i\hbar} \mathbf{A} \times \mathbf{A}.$$

As mentioned in the beginning, there are multiple proposals of implementing non-Abelian SOC in ultra-cold gases [193]: Most of them suggest a realization either by driving Raman transitions in geometrically arranged beam configurations [194–196] or by tailored lattice implementation [197]. In interacting 2D-Bose-Einstein condensates, the non-Abelian SOC promises a rich ground state structure [198] and even the emergence of various lattice-structures [199].

In the following, we will propose an implementation of non-Abelian SOC in a gas of non-interacting fermions.

4.3 Realization of Non-Abelian Spin-Orbit-Coupling

Our particular realization of the SOC-Hamiltonian consists of the combination of an optical dipole trap potential (*ODT*) and a magnetic field configuration created by four Ioffe bars. We will first discuss the two potentials separately and then present the mapping of the combined potential onto a SOC-system.

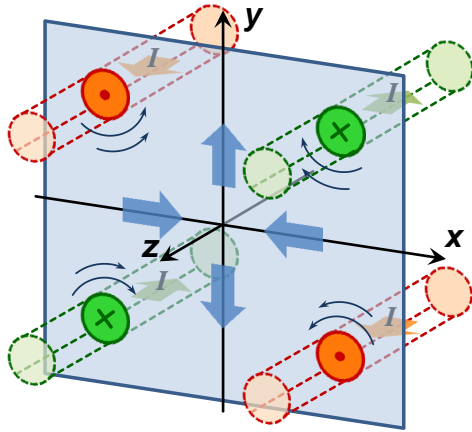
4.3.1 ODT potential

The dipolar potential exerted by a linear polarized laser beam on an atom is described by [200]

$$U_{\text{dip}}(\mathbf{r}) = \frac{\pi c^2 \Gamma}{2\omega_0^3} \left\{ \frac{2}{\Delta_{D_2}} + \frac{1}{\Delta_{D_1}} \right\} I(\mathbf{r}). \quad (4.11)$$

In the expression, $\omega_0 = 2\pi c/\lambda_{D_1}$ denotes the resonance frequency of the atomic D_1 -transition, Γ the corresponding line-width, $\Delta_{D_i} = \omega_L - \omega_{D_i}$ the detuning of the laser-frequency ω_L with respect to the corresponding D_i -transition line and $I(\mathbf{r})$ the intensity profile of the beam. Given a Gaussian beam with total power P propagating in z -direction, the intensity profile is expressed as

$$I(r, z) = \frac{2P}{\pi w^2(z)} \exp\left(-\frac{2r^2}{w^2(z)}\right) \quad \text{with} \quad w(z) = w_0 \sqrt{1 + \left(\frac{z}{z_R}\right)^2}, \quad (4.12)$$


Figure 4.2

Magnetic field derivation for a setup of four Ioffe bars. Through symmetry considerations and Maxwell's equations we derive the magnetic field in the xy -plane close to the origin, supposing infinitely long bars. The four bars (indicated by the cylindric cross sections) are symmetrically aligned, parallel to the z -axis. Opposite bars support the same current (I) but in different directions (green bars in $-z$ and red bars in z -direction). Small arrows within the xy -plane indicate the magnetic field-lines near the bars, while the broad blue arrows illustrate the asymptotic field directions near the x - and y -axis.

where w_0 is the beam waist and $z_R = \pi w_0^2 / \lambda_L$ the Rayleigh length. At the vicinity of the origin, we can approximate the potential of eq. (4.11) by an harmonic potential,

$$U_{\text{dip-harm.}}(r, z) = U_0 \cdot \left\{ 1 - \frac{2r^2}{w_0^2} - \frac{z^2}{z_R^2} \right\} \quad \text{with} \quad U_0 = U_{\text{dip}}(0). \quad (4.13)$$

For red-detuned laser beams ($\omega_L < \omega_0$), $U_0 < 0$ and the potential is attractive (trapping-case), while for blue detuned frequencies ($\omega_L > \omega_0$), $U_0 > 0$ and the potential is repulsive. The corresponding frequencies in the trapping case ($U_0 < 0$) are

$$\omega_r^2 = -4U_0/mw_0^2 \quad \text{and} \quad \omega_z^2 = -2U_0/mz_R^2 \quad (4.14)$$

in radial and in axial direction respectively.

In the following SOC-scheme, we will consider a far red-detuned ODT ($\lambda_L = 1064$ nm compared to the D_1 - ^6Li wavelength of $\lambda_{\text{D}_1} = 671$ nm). Hence the amplitude U_0 of the dipole potential will be negative, according to the previously decided sign-conventions.

4.3.2 Potential created by four Ioffe bars

The potential created by four Ioffe bars, as they are depicted in fig. 4.2, can be easily approximated in the vicinity of z -axis of the setup, by applying simple symmetry arguments to the solution of Maxwell's equations.

Supposing, that the same current I circulates in the four bars in the directions indicated in fig. 4.2, we can approximate the field far away from the bars by a linear ansatz,

$$\mathbf{B}(\mathbf{r}) = \mathbf{b}_{ji} \mathbf{r}, \quad (4.15)$$

with a 3×3 matrix of constant elements \mathbf{b}_{ji} (j marks the row- and i the column number). Furthermore, we will assume the bars to be much longer than the expansion of the cloud. In that way, no magnetic field component is found in z -direction and the field does not depend on the z -coordinate,

$$b_{zk} = 0, \quad k \in \{x, y, z\} \quad \text{and} \quad b_{xz} = b_{yz} = 0.$$

The problem is now fully reduced to the xy -plane. Moreover, following the asymptotic behavior

of the magnetic field lines near the symmetry x -axis (y -axis), the field should have a vanishing y -component (x -component) for $y = 0$ ($x = 0$), hence

$$b_{yx} = 0 \quad \text{and} \quad b_{xy} = 0 .$$

Finally, from the Maxwell equation $\text{div } \mathbf{B} = 0$, we obtain $b = b_{xx} = -b_{yy}$. In summary, the magnetic field evolution from the ansatz in eq. (4.15) for four symmetrically arranged Ioffe bars reduces to

$$\mathbf{B} = b(x \mathbf{e}_x - y \mathbf{e}_y) , \quad (4.16)$$

with unit vectors \mathbf{e}_x and \mathbf{e}_y along the x - and y - axis. According to eq. (2.2), the potential energy of a spin-1/2-atom with arbitrary spin orientation $\boldsymbol{\mu} = \mu \hat{\boldsymbol{\sigma}}$ in the field described by eq. (4.16) results in

$$U_{\text{Ioffe}}(x, y) = -\mu b(x \hat{\sigma}_x - y \hat{\sigma}_y) . \quad (4.17)$$

As usually, $\hat{\sigma}_{x,y}$ denote the first two 2×2 Pauli matrices mentioned earlier in eq. (4.8). Regarding the linear form of the trapping potential in eq. (4.17), it resembles the potential of the previously treated quadrupole trap for $z = 0$ ⁴.

In order to realize the spin-1/2-system, we will apply the potential on ⁶Li in its lowest hyperfine state $F = 1/2$. The magnetic moment⁵ for each of the two possible Zeeman states yields $|\mu| \approx \mu_B/3$.

4.3.3 SOC-Hamiltonian through canonical mapping

Superimposing the potential created by the four Ioffe bars with a red-detuned single beam ODT, aligned along the z -axis, we obtain the single particle Hamiltonian of the form

$$H_{\text{SOC}}(\mathbf{r}, \mathbf{p}) = \frac{p^2}{2m} + \underbrace{\frac{m\omega_r^2}{2}(x^2 + y^2) + \frac{m\omega_z^2}{2}z^2}_{\text{single-beam ODT}} - \underbrace{\mu b(x \hat{\sigma}_x - y \hat{\sigma}_y)}_{\text{Ioffe-bars}} . \quad (4.18)$$

We perform an equivalent canonical mapping to the one realized in eq. (4.2), which exchanges the role of momentum \mathbf{p} and position \mathbf{r} by defining the new momentum coordinates \mathbf{P} ,

$$P_x = m\omega_r x , \quad P_y = -m\omega_r y , \quad P_z = p_z , \quad (4.19)$$

⁴In the case where the spin of the atom follows the magnetic field adiabatically, thus if the spin state is the eigenstate of eq. (4.17), the potential energy seen by the atom is the eigenenergy of the potential,

$$U_{\text{Ioffe Eigenstate}}(x, y) = \mu b \sqrt{x^2 + y^2} .$$

⁵The magnetic moment is calculated by $\mu_B g_F m_F$ with

$$g_F \approx 2 \frac{F(F+1) - I(I+1) + J(J+1)}{2F(F+1)} ,$$

where we ignored the contribution from the nuclear spin ($g_I \ll g_J$) and approximated $g_J \approx 2$. For ⁶Li the nuclear spin is $I = 1$ and $J = 1/2$ (for $F = 1/2$).

and position coordinates \mathbf{X} ,

$$X = -p_x/m\omega_r, \quad Y = p_y/m\omega_r, \quad Z = z. \quad (4.20)$$

This time, the mapping translates to the appropriate units and we omit the introduction of an arbitrary scaling constant. It is easily verified that the new coordinates \mathbf{P}, \mathbf{X} satisfy the same commutation relations as the old ones, $[X_i, P_j] = [x_i, p_j] = i\hbar\delta_{ij}$. In the new coordinates, the Hamiltonian is rewritten as

$$H_{\text{SOC-mapped}}(\mathbf{R}, \mathbf{P}) = \frac{P^2}{2m} + \frac{m\omega_r^2}{2}(X^2 + Y^2) + \frac{m\omega_z^2}{2}Z^2 - \frac{\mu b}{m\omega_r}(P_x\hat{\sigma}_x + P_y\hat{\sigma}_y), \quad (4.21)$$

where we identify the Rashba-Dresselhaus spin-orbit coupling expression from eq. (4.7) in the last term. The mapped system in eq. (4.21) describes spin-orbit coupled harmonically trapped spin-1/2 particles in absence of interactions. The advantage of the "real" system in eq. (4.18) lies in the opportunity to observe the effect of SOC directly in position space, without reducing the momentum picture from the imaged cloud distribution (i.e. through a series of TOF-images). Therefore the particular donut-shaped ground state distribution of the momentum, which will be discussed in the next section, can be observed directly in position space.

4.4 Ground State of a SOC System

The eigenenergies of eq. (4.18) can be calculated readily by diagonalisation of the involved Pauli matrices, which yields

$$E_{\pm} = \frac{p^2}{2m} + U_{\text{dip}}(\mathbf{r}) \pm \mu b \sqrt{x^2 + y^2}. \quad (4.22)$$

The corresponding normalized eigenstates are

$$\mathbf{e}_{\pm} = \frac{1}{\sqrt{2}} \begin{pmatrix} (x + iy) / \sqrt{x^2 + y^2} \\ \mp 1 \end{pmatrix}, \quad (4.23)$$

which is a combination of the spin-up and down states⁶.

The lower energy branch E_- is depicted in fig. 4.3a as a function of the position coordinates $\{x, y\}$ for a fixed momentum p . It shows a minimum on a ring of radius r

$$r_{\min} e^{-2r_{\min}^2/w^2(z)} = -\frac{1}{4} \mu b \frac{w^4(z)}{w_0^2 U_0}, \quad (4.24)$$

Whereby we used the exact expression of the dipolar potential from eq. (4.12) and used as previously defined $U_0 = U_{\text{dip}}(0) < 0$, due to the red-detuned (attractive) ODT. The exact solution of eq. (4.24) is described by a Lambert- \mathcal{W} function, which will be treated later on in a different context in sec. 5.4.3. For the current discussion, we can simply calculate the maximum value of the left-hand side of eq. (4.24) and therefore formulate the condition

$$\mu b < 2 e^{-1/2} |U_0|/w_0, \quad (4.25)$$

⁶The spin-up $(1, 0)$ and spin-down $(0, 1)$ states are the eigenstates of $\hat{\sigma}_z$ and are used as the basis of the representation of the Hamiltonian in eq. (4.18).

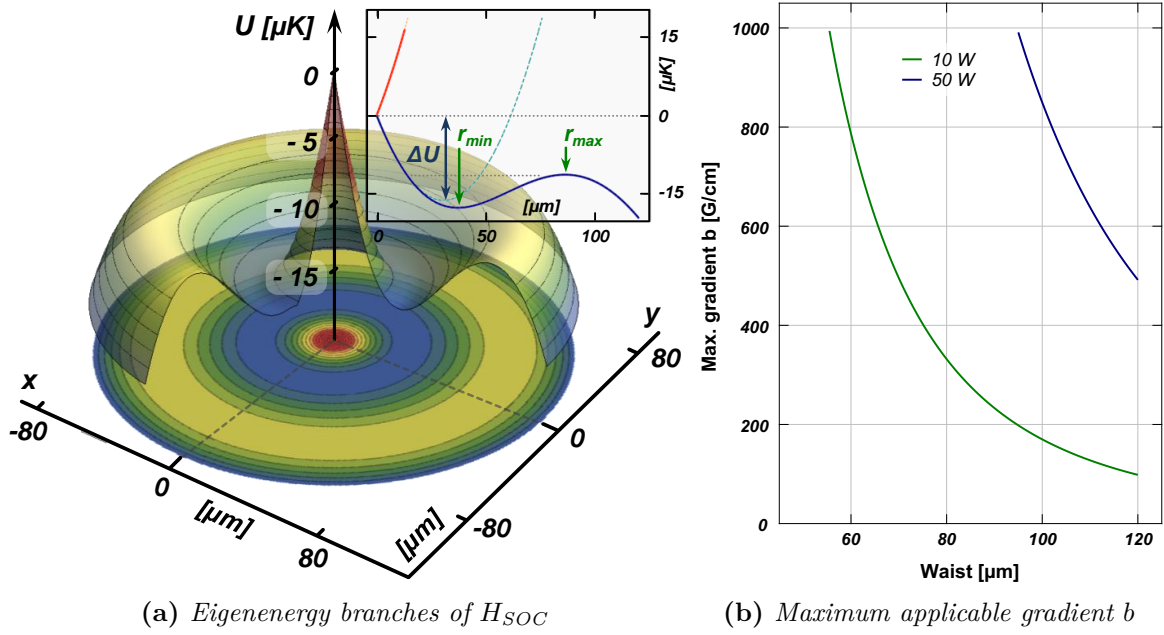


Figure 4.3: Eigenenergy branches of the SOC-system. (a) Sombrero-hat potential of the lower energy branch $E_-(x, y)$ at the waist position ($z = 0$) for an ODT power of 50 W focused to $w_0 = 120 \mu\text{m}$ with a gradient $b = 400 \text{ G/cm}$. The embedded figure depicts a 1D-cut (blue line) through the axial symmetric potential, which possesses a ring-shaped minimum of radius r_{\min} and a maximal potential barrier at r_{\max} . For large gradients, the trapping barrier is smaller than the energy-gap ΔU calculated by the harmonic approximation (dashed line) in eq. (4.27). The red line shows the E_+ -branch. (b) Maximal applicable gradients (in the range of $b < 0.1 \text{ T/cm}$) to observe a ring structure within the lower branch E_- as a function of the waist w_0 for two ODT-powers, 10 W and 50 W.

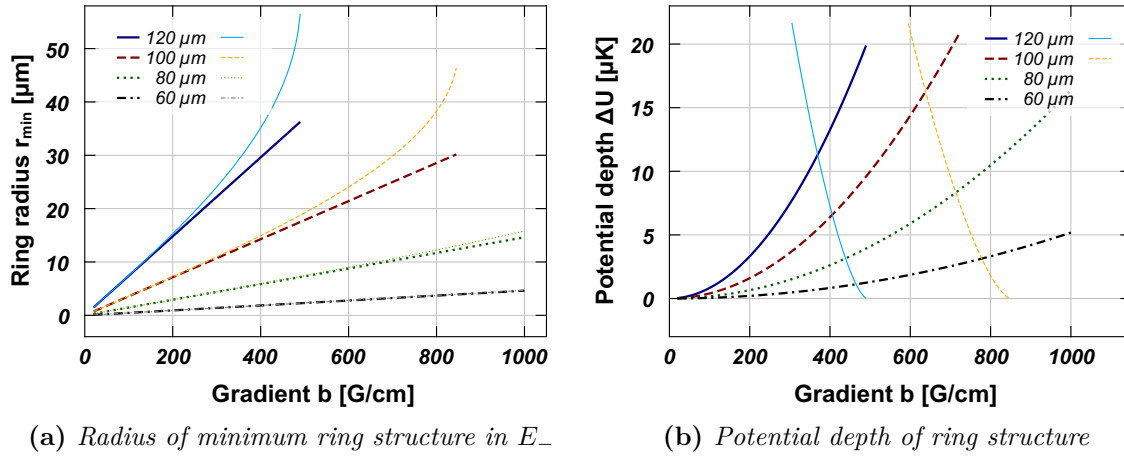


Figure 4.4: Characterization of the ring structure of the lower SOC energy branch. (a) depicts the radius r_{\min} of the ring for an ODT of 50 W and four different waist sizes as a function of the gradient b . The radii are calculated according to eq. (4.26), while for three waist sizes the thinner lines depict the non-approximated radii supposing the realistic Gaussian ODT-potential form. In (b), the trap depth $E_+(0) - E_-(r_{\min})$ for the same waist sizes is shown as a function of the gradient. For the largest two waist sizes, we included the trap depth $E_-(r_{\max}) - E_-(r_{\min})$, where r_{\max} denotes the potential height of the lower branch (see fig. 4.3a).

for which a solution for r_{\min} in eq. (4.24) exists. Eq. (4.25) imposes an upper bound on the gradient b . We will analyze a possible experimental realization in spin-polarized non-interacting ^6Li in one of the two Zeeman states of the $F = 1/2$ hyperfine state. For the absolute ground state $|F = 1/2, m_F = +1/2\rangle$, we find $\mu = -\mu_b/3 < 0$, which leads to a sign exchange in eq. (4.22) and the inversion of the two energy bands, but otherwise does not affect the physics of the lower energy branch. Concerning the optical confinement, we suppose a red-detuned, high power ODT of 1064 nm. Figure 4.3b shows the maximal possible gradient b in the technically feasible range (up to 0.1 T cm) as a function of different waist sizes w_0 for two power values of the ODT.

Applying the harmonic approximation of the ODT potential, the radius of the ring of minima for the lower energy branch yields

$$r_{\min} = \mu b / m\omega_r^2. \quad (4.26)$$

Hence the energy gap between the upper branch $E_+(0)$ and the lower one at the minimum $E_-(r_{\min})$ is

$$\Delta U = \frac{1}{2} \frac{(\mu b)^2}{m\omega_r^2}. \quad (4.27)$$

Fig. 4.4 depicts the radius r_{\min} (a) and the lower-branch-depth according to the last equation (b) as a function of the applied gradient b for different waists of a 50 W-ODT. Additionally, we included the exact solution for the ring radius in fig. 4.4a, supposing the exact Gaussian shape of the ODT potential. Similarly, in fig. 4.4b we plotted the potential depth in the lower energy branch for the two waists of 120 μm and 100 μm . Indeed, for increasing gradients, the larger ring distance reduces the potential barrier of the ODT, which leads to a lower temperature limit. Therefore for large gradients b the temperature limit is governed not by the energy gap between E_+ and E_- (in order to avoid the population of the upper branch), but rather by the reduced ODT height (in order to maintain a sufficient confinement of the cloud – see fig. 4.3a).

Clearly, the whole lower-energy-band structure becomes smaller with decreasing waist size – therefore we will consider a quite powerful ODT of 50 W and a larger waist of 120 μm as the optimal realization scenario. In a gradient of about 380 G/cm, we expect to observe a ring structure on the order of $r_{\min} = 25 \mu\text{m}$, provided the confined gas is sufficiently cold ($T < 10 \mu\text{K}$).

As a last remark, it should be mentioned that we omitted the effect of gravity in the y -direction, which breaks the cylindrical symmetry. Indeed, it should be negligible compared to the magnetic gradient term for large b -values. Otherwise, the z -axis (axial ODT-direction) can be oriented along gravity and in case of a weak axial confinement supported by an additional crossed ODT beam with larger waist.

4.4.1 Density distribution

In the harmonic approximation, it is possible to determine analytically the spatial density distribution, assuming a thermal Boltzmann distribution. Integrating the distribution in eq. (3.4) over the momentum coordinates \mathbf{p} reveals

$$n(\mathbf{r}) = \int \frac{d^3\mathbf{p}}{(2\pi\hbar)^3} \frac{1}{Z} e^{-\beta H_{\text{SOC}}(\mathbf{r}, \mathbf{p})} = \left(\frac{m}{2\pi\hbar^2\beta} \right)^{3/2} \frac{1}{Z} e^{-\beta U(\mathbf{r})}, \quad (4.28)$$

where $U(\mathbf{r})$ contains both trapping potentials from eq. (4.18) and Z normalizes the density to the atom number. We will observe the atom distribution by taking images along the ODT z -axis. Further integration along the z direction, expanding the exponential in a Taylor-series and using the property $\hat{\sigma}_i^2 = 1$ the 2D-density yields

$$n(r) = \frac{m}{2\pi\hbar^3\beta^2\omega_z} \frac{1}{Z} e^{-\beta \frac{m}{2}\omega_r^2 r^2} \left\{ \cosh(\beta\mu br) + \frac{1}{r} \sinh(\beta\mu br) (\hat{\sigma}_x x - \hat{\sigma}_y y) \right\}. \quad (4.29)$$

Strictly speaking, the last expression is rather a density operator than a pure observable. Only after projecting on the eigenstates, we obtain the spatial 2D-density distribution

$$n_{\pm}(r) \equiv \mathbf{e}_{\pm}^{\dagger} n(r) \mathbf{e}_{\pm} = \frac{m}{2\pi\hbar^3\beta^2\omega_z} \frac{1}{Z} e^{-\beta \frac{m}{2}\omega_r^2 r^2} \{ \cosh(\beta\mu br) \mp \sinh(\beta\mu br) \}. \quad (4.30)$$

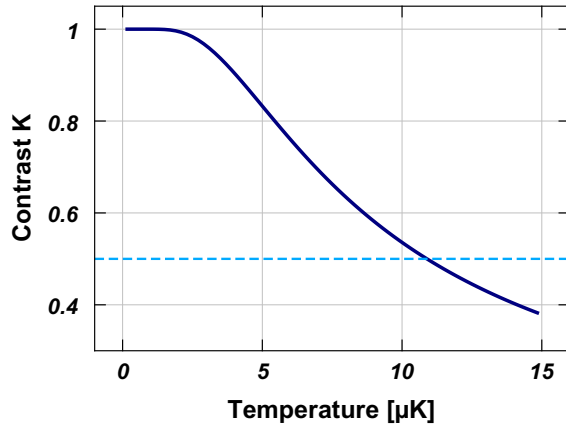
The total atom number in the upper and lower energy branches is obtained through

$$\begin{aligned} N_{\pm} &= 2\pi \int_0^{\infty} n_{\pm}(r) r \, dr \\ &= \frac{1}{\hbar^3\beta^3\omega_r^2\omega_z} \frac{1}{Z} \left[1 + \sqrt{\pi}\eta e^{\eta^2} \{ \text{Erf}(\eta) \mp 1 \} \right] \quad \text{with} \quad \text{Erf}(x) = \frac{2}{\sqrt{\pi}} \int_0^x e^{-t^2} dt, \end{aligned} \quad (4.31)$$

where we introduced the error-function $\text{Erf}(x)$ and the dimensionless quantity

$$\eta = b\mu \sqrt{\frac{\beta}{2m\omega_r^2}}, \quad (4.32)$$

to shorten the notation. Under the previously considered experimental circumstances ($b = 600 \text{ G/cm}$, $P = 50 \text{ W}$, $w_0 = 80 \mu\text{m}$ and a cloud temperature of $T < 40 \mu\text{K}$), the parameter η takes values $\eta < 2$. Finally, the fugacity Z can be eliminated in eq. (4.30) and the density


Figure 4.5

Density contrast between the maximum density at r_{\min} and the minimal density at the origin of the lower energy branch E_- , supposing the suggested experimental conditions of $P = 50$ W, $w_0 = 120 \mu\text{m}$ and $b = 380$ G/cm. In the supposed temperature range (fig. 4.4b), the contrast is $K > 0.5$ (dashed line) for temperatures $T < 11 \mu\text{K}$.

distributions of the upper and lower energy branches can be expressed by

$$n_{\pm}(r) = \frac{N_{\pm}}{2\pi} \zeta e^{-\frac{\zeta}{2}r^2} \frac{\cosh(\kappa r) \mp \sinh(\kappa r)}{1 + \sqrt{\pi}\eta e^{\eta^2} \{\text{Erf}(\eta) \mp 1\}} \quad \text{with} \quad \kappa = \beta\mu b, \quad \zeta = m\beta\omega_r^2 = \frac{1}{2} \frac{\kappa^2}{\eta^2}. \quad (4.33)$$

For the lower energy branch density distribution $n_-(r_{\min})$, we find a density maximum at the previously calculated position $r_{\min} = \kappa/\zeta$ from eq. (4.26). The density expression in the last equation allows to calculate (within the harmonic approximation) the contrast between the potential maximum at the origin and the ring structure at r_{\min} by

$$K = \frac{n_-(\kappa/\zeta) - n_-(0)}{n_-(\kappa/\zeta) + n_-(0)} = \frac{e^{-\kappa^2/2\zeta} \left\{ \cosh\left(\frac{\kappa^2}{\zeta}\right) + \sinh\left(\frac{\kappa^2}{\zeta}\right) \right\} - 1}{e^{-\kappa^2/2\zeta} \left\{ \cosh\left(\frac{\kappa^2}{\zeta}\right) + \sinh\left(\frac{\kappa^2}{\zeta}\right) \right\} + 1}. \quad (4.34)$$

The contrast is plotted in fig. 4.5 for the previously suggested experimental situation as a function of temperature. An acceptable contrast ($K > 0.5$) is achieved for temperatures below $11 \mu\text{K}$. To be able to judge if such a temperature is achievable, it has to be compared to the Fermi temperature T_{F-} , which gives the threshold for the onset of quantum behavior in the gas. The Fermi temperature will be discussed in greater detail in the following chapter 5. In appendix J, we show that for the proposed experimental parameters $T_{F-} < 1 \mu\text{K}$. The discussed range is therefore still in the classical regime, and should be experimentally achievable with a reasonably large ensemble of $\sim 10^5$ atoms.

In case the temperature of the spin-polarized ^6Li ensemble is below the mentioned thresholds, it should be possible – the necessary imaging resolution provided – to observe a donut-shaped density distribution by imaging along the z -axis. Particular caution should be taken to the spin orientation within the distribution regarding the probe-beam polarization during imaging: Since the atoms are in the eigenstate e_- , their spin follows basically the magnetic field lines. In order to avoid spatial variation of the Clebsch-Gordon coefficient during imaging, it might be necessary to switch adiabatically from the magnetic gradient b to a constant magnetic field (e.g. created by a coil pair in Helmholtz-configuration), thus orienting the spins along the same axis.

4.5 Conclusion

In this chapter, we presented two examples for quantum simulations using a spin-polarized non-interacting ${}^6\text{Li}$ in two different potentials. The first implementation of the non-interacting gas in a quadrupole potential can be canonically mapped to a harmonically trapped system of massless particles. It allows the direct translation of the experimentally observed behavior of ${}^6\text{Li}$ from chapter 3 to the properties of the trapped mass-less particles, like the observed isotropic distribution of the imparted energy within the xy -plane in case of an excitation within the plane. In the massless counterpart system, the imparted energy would similarly be redistributed within a plane of equal harmonic trapping frequencies – an effect which is contrary to the physics of harmonically trapped massive particles.

In the second implementation, we proposed the simulation of a non-Abelian spin-orbit coupling potential, also based on the mapping of the Hamiltonian of non-interacting ${}^6\text{Li}$ atoms in a tailored potential, which combines a 2D-linear quadrupole trap and a single-beam ODT. This Hamiltonian possesses a non-trivial momentum ground state, which in our proposal can be directly deduced from the real-space image of the atoms. We estimated the effect for realistic experimentally reproducible parameters and therefore prepared the path for future experimental observations.

Pathway to Quantum Degenerate ^{40}K

The first chapters of the manuscript were devoted to classical phenomena arising at low phase space density (PSD). When temperature is further reduced, we enter the quantum regime, where interactions and quantum statistics become dominant. In this chapter we will discuss the cooling proceedings performed in the science cell of the experiment. Since the limitations of the active laser cooling techniques presented in chapter 2 do not allow to reach the desired region of phase space density, we continue the cooling process of the atoms by evaporation. The better vacuum in the science cell allows for long evaporation times, and the full optical access of the glass cell permits for a versatile optical setup for high power lasers and imaging from all directions. Implementing different stages of evaporation as well as spin manipulation techniques, we will show how ^{40}K is cooled down to the quantum degenerate regime in its absolute ground state.

The current chapter is dedicated to the evaporation process implemented for ^{40}K only. As far as it concerns ^6Li , the arrival conditions in the science cell will be mentioned as well as the application of the plug beam on the cloud.

After the presentation of the actual technical setup around the science cell in sec. 5.1, the chapter is split into four major parts:

- **Section 5.2** continues the discussion of the magnetic quadrupole trap, this time by focusing in more detail on the previously mentioned Majorana losses at the trap center. We present measurements quantifying the losses, as well as a solution in form of a repulsive potential barrier, which plugs the zero magnetic field.
- **Section 5.3** discusses the evaporation as a method of cooling. In the course of the section we develop a simplified model, which is further on used to quantify the evaporation sequences performed on the ^{40}K cloud. We perform RF-evaporation in the magnetic trap, as well as optical evaporation in a single and crossed ODT. In this section we also briefly address the spin manipulation performed on ^{40}K .
- **Section 5.4** presents the effects of the magnetic field on the evaporated cloud. Here, we will characterize the magnetic curvature created by the bias coils and perform a qualitative detection of Feshbach resonances in two different spin mixtures.
- **Section 5.5** presents the experimental characterization of the quantum degenerate Fermi gas of ^{40}K , obtained at the end of the evaporation sequence. Particularly, we discuss

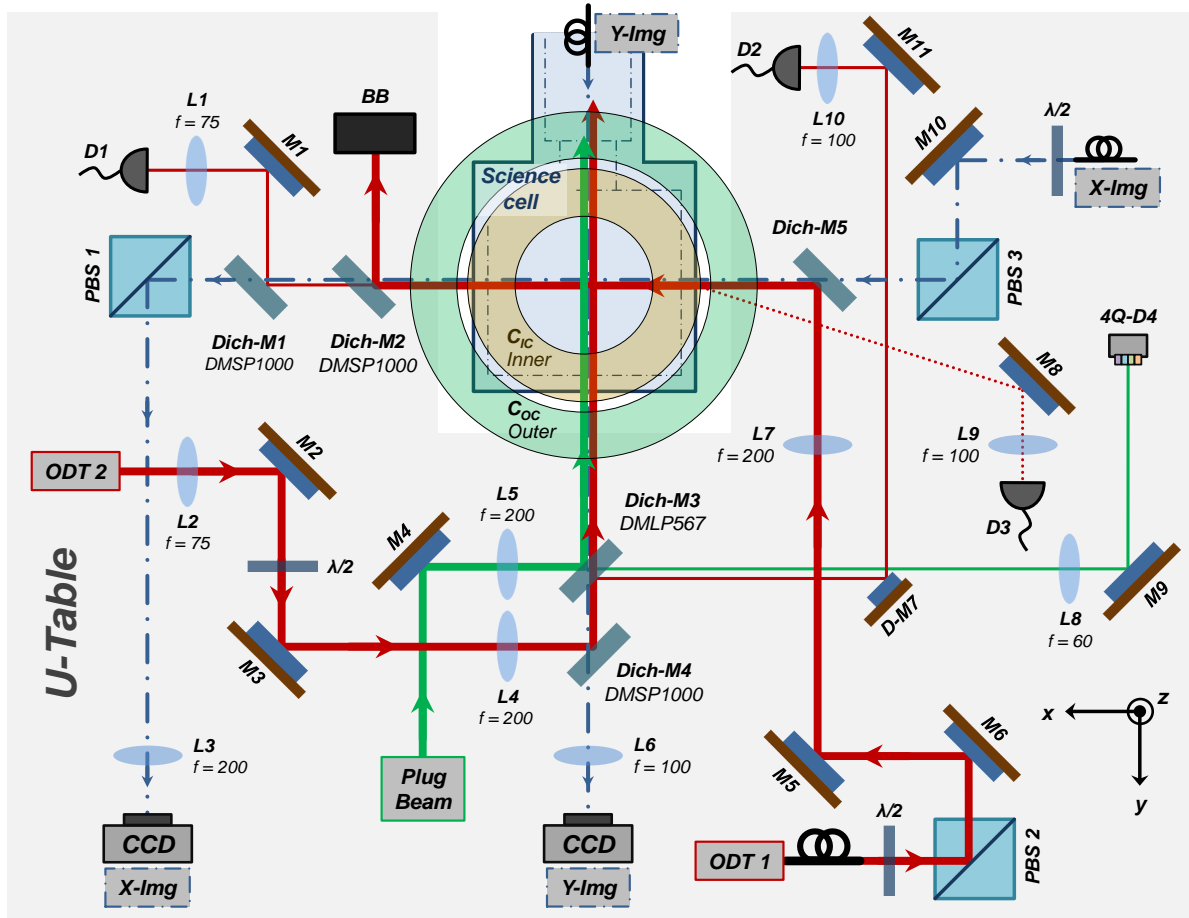


Figure 5.1: Details of the optic and magnetic setup around the science chamber. The RF-antennas and three compensation coils which are placed around the U-table for compensating/creating an offset bias in each direction are not depicted. The mirrors M3 and M4 are held in piezoelectric mounts and can be readjusted during the experimental sequence. The photodiode D3 captures a back reflection of the science cell. For further details see description in the text.

the distinction of a thermal Gaussian distribution and its quantum degenerate Fermi counterpart at low temperatures.

5.1 Setup Around the Science Cell

The setup of all the implemented devices, either optical or magnetic, which will be presented throughout this chapter, are depicted in fig. 5.1. On the high-power laser side it includes a crossed dipole trap (*Innolight Mephisto MOPA 25 W*) and a plug-laser for the magnetic quadrupole trap (*Coherent Verdi V12*).

The beams for the crossed dipole trap are split from the same laser by a high power AOM: The first order of the crossed dipole trap is fibered (*ODT1*), while the zero order is once again switched by an AOM and serves after free propagation as a second arm (*ODT2*). The later beam is aligned with respect to ODT1 by a piezoelectric mirror (*M3*). The approximated waists of the high power lasers are summarized in table 5.1. The power of both trapping lasers, ODT1 and

ODT2, are monitored by photo diodes $D3$ and $D2$ through logarithmic amplifiers, and stabilised by PID-circuits acting on the corresponding AOMs in a feedback-loop over the complete power range (from ~ 10 W down to ~ 10 mW) [110]. For the ODT1-beam, an additional linear-response photo diode $D1$ is installed for monitoring. Since the plug-beam is used at a constant power throughout the evaporation sequence, we only monitor its position on a four-quadrant photo diode $4Q-D4$. Therefore, the plug position can be marked and re-adjusted by a piezoelectric mirror $M4$.

Table 5.1: Technical characteristics of the high power lasers and the magnetic field coils, mentioned in the setup of fig. 5.1. For the magnetic fields the indicated values correspond to a current of 1 A in the coils.

<i>Lasers</i>	<i>ODT 1</i>	<i>ODT 2</i>	<i>Plug beam</i>
Wavelength λ_L	1064 nm	1064 nm	532 nm
Waist w_0	$\sim 40 \mu\text{m}$	$\sim 300 \mu\text{m}$	$\sim 20 \mu\text{m}$
<i>Magnetic</i>	<i>Gradient</i> $b' = 2b$	<i>Bias</i> B_0	<i>Curvature</i> B_0'' (axial)
Inner coil C_{IC}	2.5 G/cm	8 G	+0.31 G/cm ²
Outer coil C_{OC}	0.24 G/cm	2.05 G	−0.026 G/cm ²

On the magnetic field side, two pairs of coils (inner- C_{IC} and outer-coils C_{OC}) can be used either in anti-Helmholtz (for magnetic trapping) or in Helmholtz-configuration (for generating a constant bias field). The related curvature in the latter configuration is of opposite sign and therefore can be compensated (see sec. 5.4.2). The corresponding technical parameters for the gradient and bias configuration can be extracted from table 5.1.

The three different RF-antennas installed around the science chamber are not depicted in fig. 5.1. These antennas are used to drive magnetic dipole transitions, either for RF-evaporation in the magnetic quadrupole trap (1 GHz to 1.3 GHz in case of ^{40}K), for adiabatic Landau-Zeener transfer from positive to negative Zeeman sublevels (1 MHz to 15 MHz) or for creating balanced mixtures of neighboring Zeeman levels (20 MHz to 50 MHz). Each antenna and the corresponding RF-source covers one of the mentioned frequency scopes.

The current setup contains two imaging axes: One along the x - and another along the y -axis of the system. Both possess different magnifications, which are calibrated according to the free-fall experiment presented in sec. 2.7.2. An additional access along the z -axis is possible, but is reserved for the future installation of a high resolution imaging system with an objective near the glass cell. The same fibers (for both installed imaging axes) provide resonant light for imaging at zero bias, as well as light at higher shifted frequency for the purpose of spin selective imaging in presence of a high bias field (220 G to 280 G, see corresponding AOM in fig. 2.8b). The imaging beams, just like the different high power laser beams of the plug and the ODT, are overlapped by means of dichroic mirrors.

5.2 Majorana Losses and Plugged Quadrupole Trap

At the end of the transport to the science cell, the atomic cloud is transferred into the final quadrupole trap, which is created by the inner coils C_{IC} (see fig. 5.1). In this trap, the radio frequency driven (RF) evaporation is performed, in order to reach sufficient low temperatures for a subsequent loading of the atomic cloud into an optical dipole trap.

As indicated at previous points, apart from background collisions, Majorana losses are the main loss mechanism in the quadrupole trap: When the oscillation frequency is small compared to the Larmor frequency, the trapped spin states follow adiabatically the local magnetic field. However, for rapid spatial field variations, given at the trap center where the magnetic field vanishes, the spin of the atom might flip to a not trappable high field seeking spin state.

For the estimation of the limit for the adiabatic following, the magnetic field-changes, seen by the atom, are compared to the Larmor frequency [201]

$$\omega_L = \frac{\mu B}{\hbar}.$$

This conditions links the kinetic energy of the atom (and thus the temperature T of the trapped cloud) to the loss rate Γ_{Maj} by [202]:

$$\Gamma_{\text{Maj}} = \chi \frac{\hbar}{m} \left(\frac{\mu b}{k_B T} \right)^2, \quad (5.1)$$

where $\chi \approx 0.16$ is a dimensionless geometrical factor, which might depend on the actual value of the spin (see following up experimental results). Since Majorana losses affect mostly the low energy atoms of the thermal distribution, which are occupying lower regions of the trap, and therefore most likely cross the zero of the magnetic field, an effective heating is associated with the loss mechanism [203]:

$$\frac{\dot{T}}{T} = \frac{4}{9} \Gamma_{\text{Maj}}. \quad (5.2)$$

Regarding the RF-forced evaporative cooling in a quadrupole trap, the Majorana losses can be crucial, as they increase quadratically with decreasing temperature and most likely limit the achievable lowest temperature in the trap. Applying eq. (5.2) and eq. (5.1) the temperature evolution of the trapped gas through time results in

$$T(t) = \sqrt{T_0^2 + \gamma t}, \quad \text{with} \quad \gamma = \frac{8}{9} \chi \frac{\hbar}{m} \left(\frac{\mu b}{k_B} \right)^2. \quad (5.3)$$

Figure 5.2 shows the atom number decay and heating evolution of ^{40}K cloud, trapped in a trap of strong gradient $b' = 2b = 250 \text{ G/cm}$. Two temperature-cases are distinguished: Once the experiment is performed after arrival in the science cell ($\sim 500 \mu\text{K}$, blue dots / curve) and another time after an RF-evaporation to $\sim 200 \mu\text{K}$. Similar to [203], we use the temperature evolution to fit the geometrical factor χ , using eq. (5.3) with T_0 and γ as free parameters. In the first case of the hot cloud, we fit a factor of $\chi|_{500 \mu\text{K}} = 0.110 \pm 0.002$, while in the second colder ensemble the factor yields $\chi|_{200 \mu\text{K}} = 0.043 \pm 0.001$. We explain the discrepancy from the observation of a constant factor χ in ^{87}Rb (see [203]) by the fact, that more than one spin state is trappable in the case of ^{40}K (see sec. 2.6.1). Hence, the spin-flip at the trap bottom does

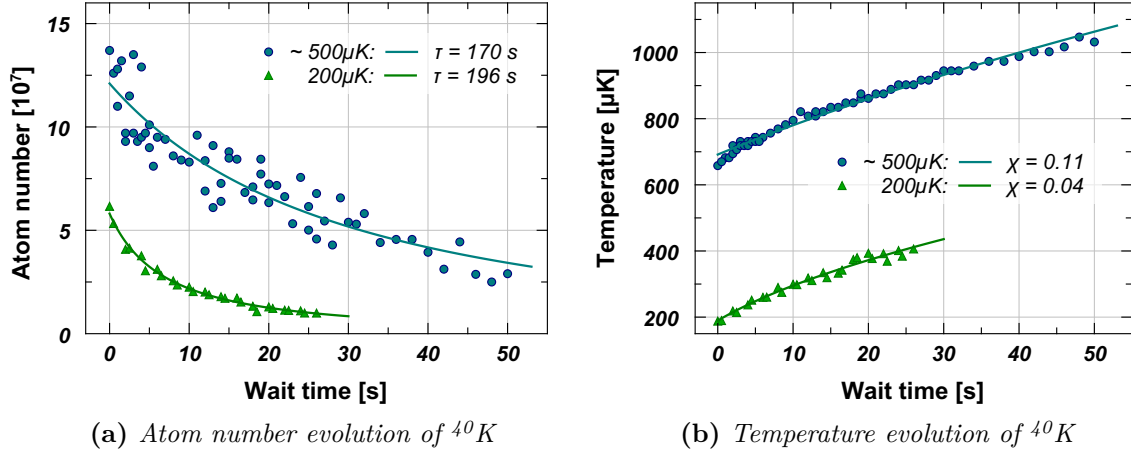


Figure 5.2: Lifetime and heating rate of ^{40}K in a (not plugged) quadrupole trap. The diagrams show the result of two measurements at different temperatures ($\sim 500\mu\text{K}$ blue circles and $200\mu\text{K}$ green triangles). The lower temperature is reached by a foregoing RF-evaporation. For fitting the heating rate in (b), eq. (5.3) was applied. With the obtained parameters, we determine the background collision rate $\Gamma_b = 1/\tau$, by fitting eq. (5.5) to the atom number evolution in (a).

not necessary lead to losses, since the new spin state might remain trapped. We assume the loss rate in eq. (5.1) to be smaller than in case of single spin state trappable cases. However, the possible temperature dependence of the χ -factor is not obvious and can be part of future investigations on ^6Li (which possesses only one trappable Zeeman state in the ground state).

The atom losses are governed by the collision rate Γ_b with the background gas (vacuum quality) and of course the Majorana losses Γ_{Maj} ,

$$\frac{\dot{N}}{N} = -\Gamma_b - \Gamma_{\text{Maj}}(T). \quad (5.4)$$

The collisions with the background lead to losses only, and do not heat up the cloud in this model. The solution of eq. (5.4) is obtained by

$$N(t) = C \left(T_0^2 + \gamma t \right)^{-9/8} \exp \left(-\frac{\Gamma_b}{\gamma} \left(T_0^2 + \gamma t \right) \right), \quad (5.5)$$

where C is a free parameter, related to the initial atom number. The initial temperature T_0 of the gas and the parameter γ were obtained through the fits in fig. 5.2b. We use C and $\Gamma_b = 1/\tau$ as the only free parameters in eq. (5.5) to obtain through fitting of the atom number evolution in fig. 5.2a the "vacuum"-lifetimes $\tau|_{500\mu\text{K}} \approx 170\text{ s}$ and $\tau|_{200\mu\text{K}} \approx 196\text{ s}$.

Finally, from eq. (5.1) it is obvious, that the loss rate increases for higher trap confinement (which might be important in order to increase the collision rate during evaporation), and is inversely proportional to the atomic mass m . At similar gradients the loss rate is about 7 times higher for ^6Li than for ^{40}K .

To avoid Majorana losses, we installed a green laser with a total output power of 12 W), plugging the center of the quadrupole trap. After passing a switching AOM and some beam shaping optics we focus the remaining $P = 7\text{ W}$ of green light at a wavelength of 532 nm to a waist of $w_0 \approx 20\mu\text{m}$ on the trap center. The laser is blue detuned with respect to the D1 and

D2 transitions of both ^6Li and ^{40}K , acting as a repulsive dipole force. The barrier height of the plug is calculated by eq. (4.11) and eq. (4.12) to

$$U_0 = \frac{\pi c^2 \Gamma}{2\omega_0^2} \left\{ \frac{2}{\Delta_{D2}} + \frac{1}{\Delta_{D1}} \right\} \cdot \frac{2P}{\pi w_0^2}. \quad (5.6)$$

Transforming the potential energy into temperature, it results in a barrier of $803 \mu\text{K}$ for ^{40}K and $776 \mu\text{K}$ for ^6Li .

The total trapping potential changes in presence of the plug beam. The setup geometry is depicted in fig. 2.1 and fig. 5.1: The green laser propagates in y -direction, while the quadrupole coils are aligned along the z -axis. Including gravity the total potential in the xz -plane is given by:

$$\begin{aligned} U(x, y, z) &= U_{\text{mag}} + U_{\text{plug}} + mgz = \\ &= \mu b \sqrt{x^2 + y^2 + 4z^2} + U_0 e^{-2(x^2 + z^2)/w_0^2} + mgz. \end{aligned} \quad (5.7)$$

In this expression we omitted the y -dependency of the optical potential U_{plug} compared to eq. (4.12), supposing that the Rayleigh length $y_R = \pi w_0^2/\lambda$ (in our case 2.4 mm) is much larger than the trapped atomic sample (about 0.2 mm). The potential profile is depicted in fig. 5.3a setting $y = 0$: Around the two symmetric minima the resulting trap can be approximated by a harmonic potential.

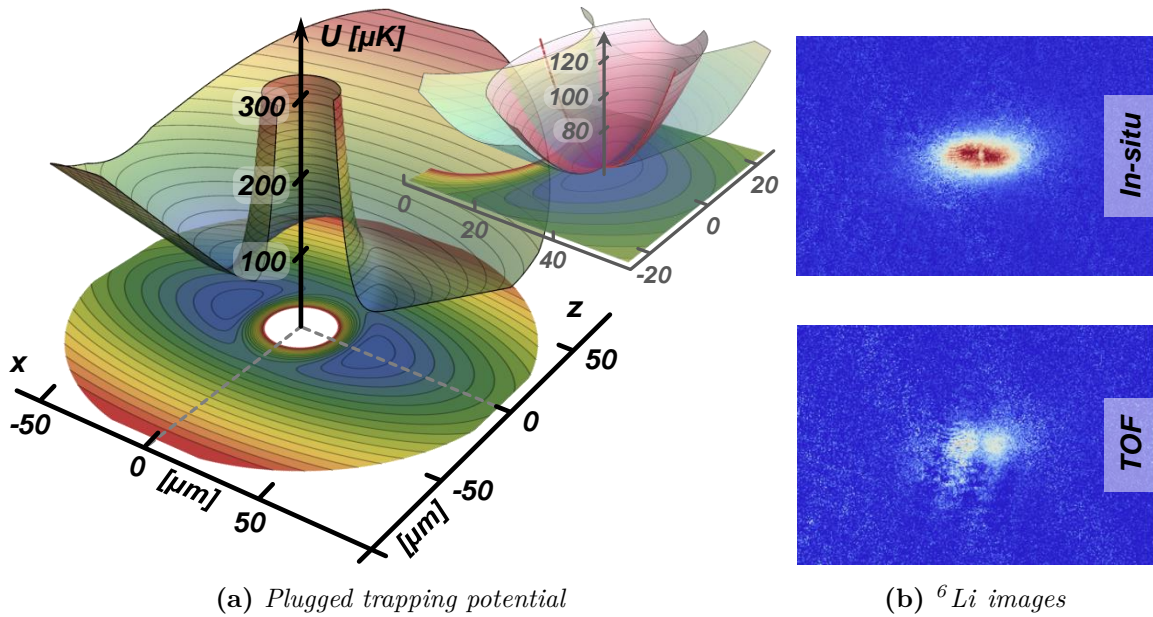


Figure 5.3: Potential of a plugged quadrupole trap. (a) Contour plot of the potential energy (U/k_B in μK) for ^6Li as a function of the position (in μm) around the magnetic trap center at the origin. The trap gradient is set to $b' = 250 \text{ G/cm}$. The plug-beam at 532 nm is assumed to be perfectly aligned on the zero of the magnetic trap with a waist of $20 \mu\text{m}$ and a total power of 7 W . In this configuration the trap height created by the green laser at the origin is about $780 \mu\text{K}$. The embedded figure shows a harmonic approximation of the resulting trapping potential at one of the two minima. (b) In situ (top) and 1 ms TOF image (bottom) of a ^6Li cloud in the plugged trap.

Finally, the right part of fig. 5.3b depicts a ^6Li cloud imaged in situ, with the plug well aligned

at the center of the trap (top) as well as the cloud after a short TOF (1 ms) expansion. In the TOF picture the separation of the cloud into two parts, which have previously occupied the two potential minima, is clearly visible.

Unfortunately, the setup shows a limited pointing stability: The heating of the transport plate (thus movement of the magnetic field zero) and optical instability obliges to realign the beam after approximately 40 min of experimental operation. The pointing stability can be "increased" by increasing the waist of the plug beam at the expense of the trap height. However, the used waist of $w_0 = 20 \mu\text{m}$ was found to be already the upper limit to significantly reduce the Majorana loss rate in our experiment. Nevertheless, it was possible to cool about $1 \cdot 10^6$ ^6Li atoms down to $\sim 100 \mu\text{K}$ by sympathetic cooling with ^{40}K . At that point most of the initially loaded $2 \cdot 10^9$ ^{40}K atoms were lost ($1 \cdot 10^5$ remained) throughout the RF-evaporation sequence¹.

In the upcoming sections we will consider working with ^{40}K solely, in order to achieve a large quantum degenerate sample. The stabilization of the plug and the improvement of the sympathetic cooling of ^6Li in the magnetic trap, as well as the efficient loading of both species in an ODT, will be the subject of future work in our group.

5.3 Evaporative Cooling of ^{40}K

The main objective to reach the quantum degenerate regime is equivalent to the effort to increase the phase space density PSD , which is generally defined as:

$$PSD = n_0 \lambda_{\text{dB}}^3, \quad (5.8)$$

where n_0 is the peak density and $\lambda_{\text{dB}} = (2\pi\hbar^2/mk_B T)^{1/2}$ the de-Broglie wavelength of an atom of mass m at temperature T . In the course of this section we will derive more convenient expressions for the PSD which will be trap related. As mentioned previously in chapter 1, we enter the quantum degenerate regime, once the $PSD \approx 1$. So far, the only known way to achieve the desired densities at low enough temperatures is evaporative cooling.

In the next section we will first present a (simplified) theory of evaporative cooling, before we discuss in detail the experimentally achieved evaporation performances in the magnetic and optical traps.

5.3.1 Principle of evaporative cooling

Evaporation is a well known process of the daily researchers life: A hot cup of coffee (or tea) gets colder, while parts of the hot exposed liquid phase convert to the gaseous state and leave the cup. The remaining part thermalizes through interactions towards a colder temperature. Nothing else than the described process happens during evaporative cooling of an atomic ensemble in a trap potential. Generally speaking, evaporation describes the process of energetic particles leaving a system with a finite binding energy [76]. The remaining ensemble relaxes through inter-particle collisions towards a thermal distribution of lower temperature. The rethermalization is based on elastic collisions. Dealing with Fermions at lower temperatures, where p -wave collisions vanish

¹We remind, that due to the p -wave scattering threshold at $\sim 6 \text{ mK}$ and the single trappable spin state for ^6Li , only sympathetic cooling is possible in the magnetic trap.

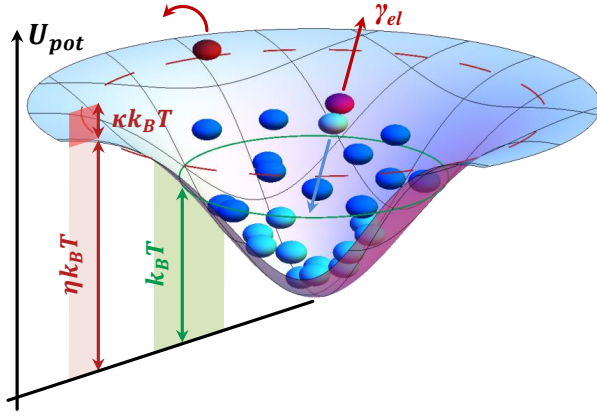

Figure 5.4

Illustration of the evaporation process of trapped atoms. The total trap height is given by $\eta k_B T$, where T is the temperature of the ensemble. Colder atoms are located at lower potential energies, thus lying lower in the trap. Atoms which are exceeding with their kinetic energy the potential height, are lost from the trap, owning an energy in the range of $(\eta + \kappa) k_B T$. During an evaporation process, elastic collisions at the rate of γ_{el} lead to cooling of the gas: In a collision process an atom leaves the trap carrying away part of the ensembles energy.

[204], it is important to ensure, that the spin mixture is well balanced, in order to provide sufficient collision partners and maintain the thermalization dynamics.

The strategy for evaporative cooling, is to cut the thermal distribution at a given energy bound $\eta k_B T$, which is higher than the average thermal energy $k_B T$ (see fig. 5.4). The cut is performed by either transferring the attributed share of the ensemble to not trapped states (in case of the radio-frequency driven (*RF*-) evaporation in a magnetic trap – see sec. 5.3.2) or by lowering the energy height of the trapping potential (in case of the evaporation in an optical dipole trap – see sec. 5.3.4). We will briefly recap the simplified description of the evaporation process presented in [205], providing in that way a theoretical framework for the performed measurements.

Supposing a trapping potential in 3D of the form $U(\mathbf{r}) \sim r^{3/\delta}$, we can express all important quantities as functions of the temperature T and atom number N . Table 5.2 summarizes this quantities of which the phase space density PSD, as well as the elastic collision rate γ_{el} , are of special interest for our discussion.

We will consider a simplified picture, taking into account only elastic collisions. We consider that only a small part of the particles dN , $dN \ll N$, leaves the trap, therefore having each one at least an energy of $(\eta + \kappa) k_B T$, slightly higher than the potential height ($\kappa \ll \eta$). In order to leave the trap, the dN atoms took away the necessary energy dE from the rest of the ensemble. Since each of the leaving atoms had the same average contribution to the internal energy of the cloud, which is according to the Virial theorem $\left(\frac{3}{2} + \delta\right) k_B T$, the energy taken away from the ensemble is given by:

$$dE = dN \left[(\eta + \kappa) - \left(\frac{3}{2} + \delta \right) \right] k_B T .$$

The remaining $(N - dN)$ particles, which had former the total energy

$$E = (N - dN) \left(\frac{3}{2} + \delta \right) k_B T ,$$

will thermalize from the temperature T to $T - dT$, provided that sufficient elastic collisions take place within the remaining ensemble. Hence, energy conservation imposes

$$(N - dN) \left(\frac{3}{2} + \delta \right) k_B T - dE = (N - dN) \left(\frac{3}{2} + \delta \right) k_B (T - dT) .$$

Internal energy E	$= N \left(\frac{3}{2} + \delta \right) k_B T$
Spatial volume V_ℓ	$\sim T^\delta$
Spatial density n	$\sim N \cdot T^{-\delta}$
Phase space density PSD	$\sim N \cdot T^{-(\delta + \frac{3}{2})}$
Average velocity v	$\sim T^{1/2}$
Elastic collision rate $n\sigma_{\text{el}}v$	$\sim N \cdot T^{\frac{1}{2}-\delta}$

Table 5.2

Scaling of different evaporation related quantities with atom number N and temperature T for a power law potential in 3D of the form $\sim r^{3/\delta}$. In case of a linear potential (magnetic quadrupole trap) $\delta = 3$, while for a harmonic potential we set $\delta = 3/2$. The expression for the internal energy follows directly from the virial theorem. For a detailed derivation and further discussion see [205].

Inserting dE from the previous equation and simplifying the expression, results in

$$\frac{dT}{T} = \alpha \frac{dN}{N}, \quad \text{with} \quad \alpha = \frac{\eta + \kappa}{\frac{3}{2} + \delta} - 1. \quad (5.9)$$

The relation between an initial temperature T_1 and a final temperature T_2 after evaporation is governed by a power-law relation to the corresponding change in atom number, $T_1/T_2 = (N_1/N_2)^\alpha$. For an evaporation process, which includes elastic collisions only, all the quantities in table 5.2 can be related directly to the atom number, by replacing $T \sim N^\alpha$. Accordingly, the phase space density will scale as

$$\frac{d(\text{PSD})}{\text{PSD}} = \alpha' \frac{dN}{N} = \left[1 - \left(\delta + \frac{3}{2} \right) \alpha \right] \frac{dN}{N}. \quad (5.10)$$

If the PSD has to increase with decreasing atom number, the prefactor has to be negative. According to the analysis in [206] and [207] we can set $\kappa \approx 1$ for very large η values. Therefore neglecting κ with respect to η , we thus formulate the necessary condition

$$\eta > \delta + \frac{5}{2}. \quad (5.11)$$

As stated before, the evolution of the elastic collision rate γ_{el} through time is also an important benchmark quantity of the evaporation. We will approximate the collision rate, by [208]

$$\gamma_{\text{el}} = n\sigma_{\text{el}}v \approx \frac{1}{2} \langle n \rangle \langle \sigma_{\text{el}} v_{\text{rel}} \rangle \approx \frac{1}{2} \frac{n_0}{2^\delta} \sigma_0 \sqrt{2} \langle v \rangle, \quad (5.12)$$

where the average density, $\langle n \rangle = n_0/2^\delta$, with the peak density n_0 , and the average relative velocity, $\langle v_{\text{rel}} \rangle = \sqrt{2} \langle v \rangle$ with $\langle v \rangle = (8k_B T / \pi m)^{1/2}$, are calculated by means of the corresponding phase space distributions². The average collision cross section σ_0 in eq. (5.12) is obtained

²The average quantities are deduced from the phase space distribution function of the form $f(\mathbf{r}, \mathbf{p}) = \exp\{-\beta H(\mathbf{r}, \mathbf{p})\} / Z$, where Z normalizes the function to the atom number N . The expectation value of a quantity A is calculated by

$$\langle A(\mathbf{r}, \mathbf{p}) \rangle = \frac{1}{(2\pi\hbar)^3} \int d^3\mathbf{r} d^3\mathbf{p} A(\mathbf{r}, \mathbf{p}) f(\mathbf{r}, \mathbf{p}) / N.$$

For the density, A is set to $n = n_0 \exp\{-\beta U(\mathbf{r})\}$, while for the velocity it is simply replaced by $|\mathbf{p}|/m$.

through the corresponding scattering length a for sufficiently small momenta by [85]

$$\sigma(k) = g_\alpha \frac{4\pi a^2}{1 + k^2 a^2} \quad \text{for } k = p/\hbar \ll 1/a, \quad \sigma_0 = 4\pi g_\alpha a^2, \quad (5.13)$$

with $g_\alpha = 1$, except for special cases, like the thermalization of a single-species Boltzmann gas of identical spin states, where $g_\alpha = 2$. Since we will always use a spin mixture in the trap, we will set $g_\alpha = 1$ for the further calculations. It should be mentioned, that in eq. (5.12) the first factor of $1/2$ avoids the double counting of the collision by integrating over all the possible collision partners. Hence, in the presented form, eq. (5.12) is only valid in case all particles can interact with each other. Dealing with two fermionic spin states with densities $\langle n_1 \rangle$ and $\langle n_2 \rangle$, which can only interact through s -wave collisions, the collision rate is approximated by

$$\gamma_{\text{el}} = \frac{1}{2} \frac{2\langle n_1 \rangle \langle n_2 \rangle}{\langle n_1 \rangle + \langle n_2 \rangle} \langle \sigma_{\text{el}} v_{\text{rel}} \rangle. \quad (5.14)$$

While the first $1/2$ -factor avoids again the double counting, the collision rate $\langle n_{j \neq i} \rangle \langle \sigma_{\text{el}} v_{\text{rel}} \rangle$ for each spin state i is weighted by $\langle n_i \rangle / \langle n_{\text{total}} \rangle$. Indeed, for a balanced mixture with $\langle n_1 \rangle = \langle n_2 \rangle = \langle n_{\text{total}} \rangle / 2$, the collision rate scales as $\langle n_{\text{total}} \rangle / 4$, in contrast to the case of eq. (5.12), where the rate would be twice as large, since all particles are possible collision partners. According to the preceding discussion, the elastic collision rate γ_{el} scales as

$$\frac{d\gamma_{\text{el}}}{\gamma_{\text{el}}} = \left[1 - \left(\delta - \frac{1}{2} \right) \alpha \right] \frac{dN}{N} \quad (5.15)$$

throughout the evaporation.

Demanding an increasing collision rate (with decreasing atom number) through the evaporation process, reaching thereby the *runaway* regime, requires according to this simple model a slightly higher cut-values than described by eq. (5.11)³. More precisely, the comparison of the elastic collision rate to inelastic collisions or trap losses, like Majorana spin-flips, are an indicator for the efficiency of the process. If the loss processes dominate, the temperature will not decrease accordingly to the described scaling. Since losses directly influence the lifetime of the gas in the trap, a basic thumb rule tells that the evaporation sequence should be shorter than the lifetime.

A more detailed model describing the evaporation, which also includes inelastic collisions, can be found in [206, 209] or in the publications [205] and [76]. Within the scope of the current thesis, we will use the presented simplified relations eq. (5.11) and eq. (5.10) for deducing the relevant quantities from the experimental measurements.

5.3.2 RF evaporation in a magnetic trap

After the transport from the magnetic trap in the MOT chamber to the science cell, the atoms are trapped and evaporated in a quadrupole trap of $b' \approx 250 \text{ G/cm}$. The arriving cloud of ^{40}K has a spin composition of 65 % of the atoms being in the stretched $m_F = +9/2$ Zeeman state, 30 % in the $m_F = +7/2$ -state and 5 % of a $m_F = 5/2$ minority in the common hyperfine ground state $F = 9/2$. These numbers are obtained by the method described in sec. 2.6.3 and might fluctuate by less than 10 % from shot to shot.

³The values in this case are $\eta > 6.3$ for the quadrupole trap ($\delta = 3$) and $\eta > 6$ for the harmonic trap ($\delta = 3/2$).

In this spin composition, s -wave collisions between the two different spin-state majorities, as well as p -wave collisions between two $m_F = 9/2$ -atoms, lead to the thermalization of the gas. Even though the p -wave scattering cross section is strongly temperature dependent, we will approximate the total scattering process by the s -wave scattering length $a = 169.7a_0$ [210], expressed in terms of the Bohr-radius $a_0 \approx 52.92$ pm and use for the collision rate estimation the equation (5.12)⁴.

The PSD of the gas is determined by eq. (5.8), with the peak density n_0 calculated by⁵

$$n_0 = \frac{1}{4\pi} \left(\frac{\mu_B b}{k_B T} \right)^3 \cdot N, \quad (5.16)$$

where we took into account only the magnetic moment of the stretched state.

During the evaporation sequence, we emit radio frequency (RF) in the range of 1150 MHz to 1286 MHz through an antenna near the science cell on the atoms. The RF drives transitions from the lower ground state manifold $F = 9/2$ to the energetically higher lying $F = 7/2$ (see the ground state scheme in fig. 2.13b). Hotter atoms are occupying higher regions of the magnetic trapping potential and therefore subjected to a higher bias field. Hence, only a given energy contingent of the cloud is resonant to the RF transition. These atoms are transferred to the $|F = 7/2, m_F = +7/2\rangle$ state (which is a high field seeking state) and are lost from the trap. Technically, both trapped spin states, $|F = 9/2, m_F = +9/2\rangle$ and $|F = 9/2, m_F = +7/2\rangle$, can be addressed by the RF. However, for a fixed RF-value the transition

$$|F = 9/2, m_F = +9/2\rangle \rightarrow |F = 7/2, m_F = +7/2\rangle$$

has the lowest energy and therefore addresses a lower temperature range in the trap, compared to the possible transitions from the $|F = 9/2, m_F = +7/2\rangle$ state. Using the Breit-Rabi formula, we can link the driving resonant transition frequency ν at a given bias value B_{cut} to a "cut" temperature T_{cut} through

$$2\pi\hbar\nu = E_0 - \hbar \left[\delta_{+9/2}(B_{\text{cut}}) - \delta_{+7/2}(B_{\text{cut}}) \right] \quad \text{with} \quad B_{\text{cut}} = k_B T_{\text{cut}} / \mu_B. \quad (5.17)$$

The relevant Zeeman shifts $\delta_{+7/2}(B) < 0$ and $\delta_{+9/2}(B) > 0$, as well as the energy splitting E_0 between the two hyperfine ground states at zero magnetic field are illustrated in fig. 5.5. The mapping of the cut-temperature does not depend on the particular gradient. The arriving ^{40}K cloud is fully depleted from the trap by driving a RF-ramp adiabatically from a low value 1100 MHz $\rightarrow T_{\text{cut}} \approx 5$ mK up to 1285.8 MHz $\rightarrow T_{\text{cut}} \approx 0$ K.

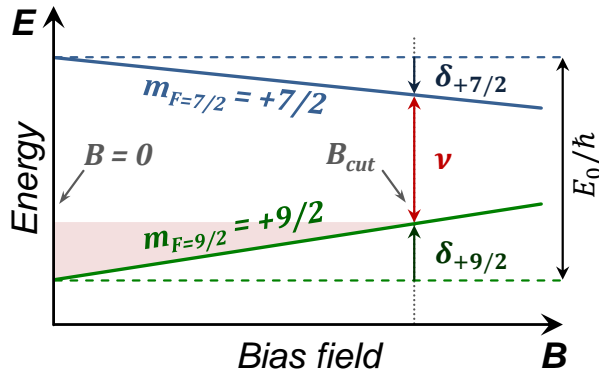
Two examples of the temperature and atom number evolution through two different evaporation sequences are depicted in fig. 5.6 (a) to (c). For both sequences we perform a linear RF-ramp from 1150 MHz ($T_{\text{cut}} \approx 3.7$ mK) to 1260 MHz ($T_{\text{cut}} \approx 0.7$ mK). The main difference is the

⁴By presuming the triplet scattering length and neglecting the singlet scattering length $a_s = 104.4a_0$, we follow the discussion in [204], where the collision process is found to be strongly triplet-dominated for our spin mixture of $m_F = +9/2$ and $m_F = +7/2$.

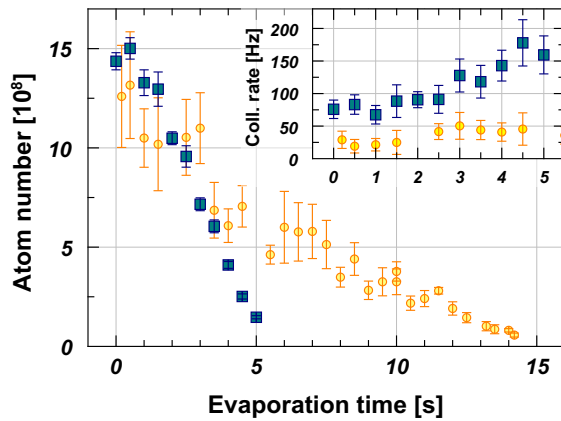
⁵The peak density n_0 is deduced from the integral over the phase space density $f(\mathbf{r}, \mathbf{p}) = \exp(-\beta H(\mathbf{r}, \mathbf{p})) / Z$, which is normalized to the atom number N ,

$$n(\mathbf{r}) = \frac{1}{(2\pi\hbar)^3} \int d^3\mathbf{p} f(\mathbf{r}, \mathbf{p}) = n_0 e^{-U(\mathbf{r})/k_B T}.$$

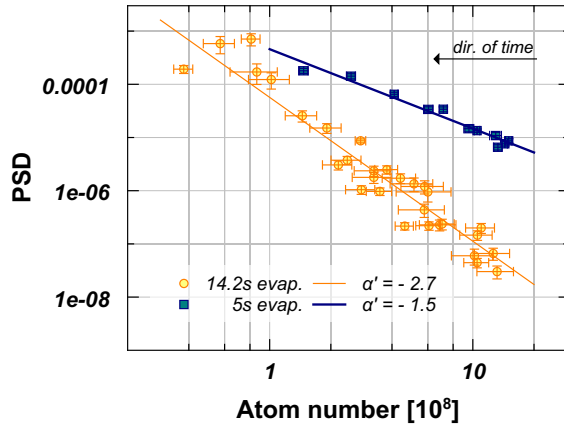
$U(\mathbf{r})$ denotes thereby the trapping potential.


Figure 5.5

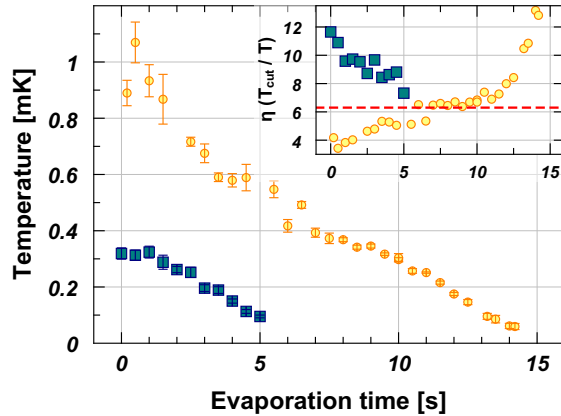
RF transition in magnetically trapped ^{40}K . Driving RF at the frequency ν , transfers the atoms at a bias B_{cut} , which are resonant to the depicted transition from the $+9/2$ state into the $+7/2$ of the higher lying manifold. The energy evolution of the two states with the bias field is calculated by the Breit-Rabi formula (fig. 2.13b). Eq. 5.17 links the resonant B_{cut} position to an effective cut temperature T_{cut} .



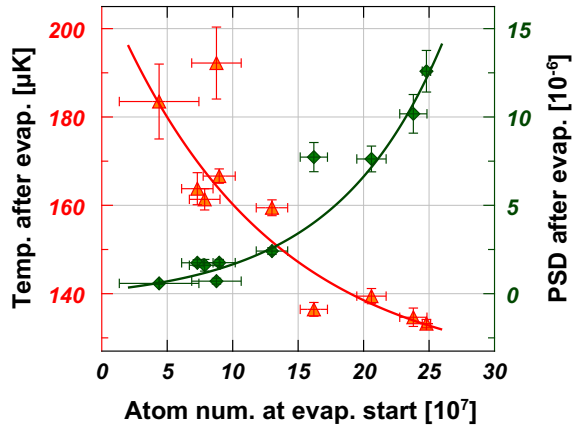
(a) Atom number evolution



(b) Performance evaluation



(c) Temperature evolution



(d) Initial atom number dependency

Figure 5.6: Characterization of the RF-evaporation in the magnetic trap. (a)–(b) depict the performance of two RF-sequences, both performing a linear RF-ramp from 1150 MHz to 1260 MHz but with different speed: One in 5 s (blue squares) and the other in 14.2 s. For the shorter sequence the temperature is determined by RF-thermometry, while the shorter sequence is characterized by TOF measurements. (d) presents the dependence of the RF-evaporation performance on variable initial atom numbers. For the last measurement the initial temperature and the linear RF-ramp are kept constant.

duration of the RF-ramp: Blue data points depict the characterization of a ramp of 5 s-total duration, while orange points are representing a ramp of 15 s. Another important distinction is the determination of the cloud temperature. While the orange data points are obtained by TOF measurements, the blue data is measured by RF-thermometry in the magnetic trap [110]. The latter method applies short RF-sweeps to different final frequencies, measuring subsequently the remaining atom number in the trap (compare fig. 5.5). This allows a direct probing of the thermal distribution of the cloud. Nevertheless, the RF-method is accompanied by a weak evaporation process, whereas the TOF method overestimates the temperature for hotter ensembles, due to fitting-issues of the large expanding cloud. At the beginning of the evaporation, the temperature lies in between the two measured data sets, leading to $\sim 0.5\text{ mK}$, which is by the way in good agreement with the arrival temperature in fig. 5.2a. For the following discussion, we will take the measurement related peculiarity aside, which is only relevant for the first second of the performed evaporation ramp.

Regarding the first 5 s of both evaporation sequences, the collision rate is lower in the case of the 14.2 s long sequence (see embedded figure in fig. 5.6a). Meanwhile, the blue data points of the short ramp show a continuous increase in the collision rate. Similarly, the η -parameter, indicating the truncation temperature in relation to the cloud temperature, exceeds the minimally indicated value of $\eta_{\min} \approx 6$ only after 6 s for the longer sequence. After the first 6 s, the longer ramp has a slightly better RF-performance, than the shorter sequence: This benchmark gets revealed by the fitted slope of $\alpha' = -2.7 \pm 0.2$, compared to $\alpha' = -1.5 \pm 0.1$ for the shorter sequence in the logarithmic plot of the PSD as a function of the atom number in fig. 5.6b (see eq. (5.10)). From the fit we calculate an effective cut parameter of $\eta \approx 7$ for the 5 s sequence and $\eta \approx 8$ for the longer sequence (in the limit of $\kappa \ll \eta$). However, this values are *averaged* values over the entire evaporation cycle.

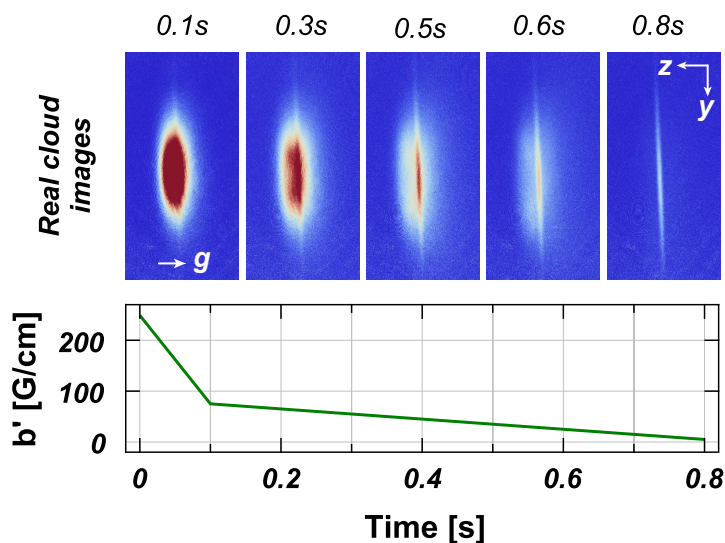
Regarding the cut range in MHz, the last 7 s of the longer sequence are equal to the last $\sim 3.5\text{ s}$ of the short sequence. Since the finally reached PSD is within error bars similar, we use the shorter 5 s-RF sequence to evaporate the atomic cloud to $100\text{ }\mu\text{K}$, leaving about $2 \cdot 10^8$ ^{40}K atoms. Concerning the gradient field, we found the value of $b' \approx 250\text{ G/cm}$ a good compromise between collision rate and lifetime at lower temperatures⁶. Using the repulsive green laser to plug the center of the magnetic trap, we achieve similar temperatures with 20 % higher atom numbers.

Finally, another important relation is the evaporation performance for different initial atom numbers. Fig. 5.6d shows the reached final temperatures and PSD values as a function of initially loaded atom number at the beginning of the evaporation ramp. The ramp itself and the temperature of the initial cloud were not varied. Clearly, for smaller atom numbers the collision rate gets reduced and therefore the evaporation becomes less efficient.

5.3.3 Loading a single beam ODT from a quadrupole trap

In order to reach lower temperatures and higher PSD values, we need to overcome the constraint of increasing Majorana losses and reduced lifetime. Therefore, we load the atoms into an ODT and continue there the evaporation. Generally, the advantage of an ODT in comparison to the magnetic quadrupole trap is its Zeeman-state-independence: especially the absolute ground state $|F = 9/2, m_F = -9/2\rangle$, which is a high-field seeking state, can now be trapped and studied.

⁶In the current setup a gradient of $b' = 370\text{ G/cm}$ can be created by the inner coils.


Figure 5.7

Loading a single-beam ODT from the magnetic trap. The gradient is continuously reduced from $b' = 250 \text{ G/cm}$ to $b' = 5 \text{ G/cm}$ within 800 ms. During the "opening" of the magnetic trap, atoms fall into the 10 W-single-beam ODT, which is aligned $2w_0 \approx 80 \mu\text{m}$ below the magnetic trap center. Since the ODT is present during the entire RF-evaporation, an overlap with the magnetic trap center would attract atoms and increase Majorana losses.

The application of an ODT becomes unavoidable in case a constant bias field has to be applied for using Feshbach resonances (see sec. 5.4.3).

To describe the ODT potential, we will utilize for simplicity the harmonic approximation of an ODT propagating in z direction, which is according to eq. (4.13),

$$U_{\text{dip-harm.}}(r, z) = \frac{m}{2} \left\{ \omega_r^2 r^2 + \omega_z^2 z^2 \right\} - U_0, \quad (5.18)$$

where, compared to eq. (4.14), we absorbed the negative sign of $U_{\text{dip}}(0) < 0$ for a red detuned ODT into the radial (ω_r) and axial (ω_z) frequencies, redefining $U_0 = |U_{\text{dip}}(0)|$. For the sake of completeness, we repeat the expressions for the frequencies,

$$\omega_{\text{rad}} \equiv \omega_r = \sqrt{4U_0/mw_0^2} \quad \text{and} \quad \omega_{\text{ax}} \equiv \omega_z = \sqrt{2U_0/mz_R^2}, \quad (5.19)$$

where the waist w_0 for the particular ODT configuration is given in table 5.1, while the trap depth U_0 is calculated by eq. (5.6), inserting the corresponding D₁- and D₂-line data of ^{40}K and the laser wavelength of $\lambda = 1064 \text{ nm}$.

To load the single-beam ODT from the magnetic trap, we do not switch off abruptly the magnetic field in order to load the ODT1. We rather adiabatically reduce the trapping gradient (see fig. 5.7) from its initial value of $b' = 250 \text{ G/cm}$ to $b' = 5 \text{ G/cm}$ in 0.8 s and let the atoms "fall" into the ODT1 potential. The ODT1 is displaced spatially by $d \approx 2w_0 \approx 80 \mu\text{m}$ below the magnetic trap center: A direct overlap with the center of the quadrupole trap would drastically increase the Majorana losses during the opening process of the trap. The relative position of the trap center and the ODT beam is fine tuned by three compensation coils surrounding the science cell.

The detailed analytic description of the dynamic transfer is more complicated and goes beyond the scope of this thesis. An theoretical approach, which analyzes the combined optical and magnetic potentials by adiabatic opening of the quadrupole trap can be found in [211] and [110]. Experimentally we manage to transfer $3 \cdot 10^7$ of the magnetically trapped atoms into the ODT1, which is about 15 %. Overall, we observe experimentally a not trivial dependence of the transfer efficiency on the temperature and PSD after the RF-evaporation for loading the ODT

from the magnetic trap.

At the end of the adiabatic opening we leave a small gradient of $b' = 5 \text{ G/cm}$ in combination with the ODT1, thereby increasing the otherwise weak axial confinement to $\omega_{\text{mag.-ax}} \approx 25 \text{ Hz}$. During the loading process a part of the cloud gets evaporated, so that in turn after a hold time of 100 ms in the final hybrid-trap, the cloud temperature decreases to $60 \text{ }\mu\text{K}$.

5.3.4 Evaporative cooling in an ODT

The forced evaporation process in an ODT is driven by lowering the trapping potential height U_0 through the laser power P (see eq. (5.6) and eq. (5.18)). Thus, at every evaporation step the trapping frequencies ω_i will change according to eq. (5.19). The peak density, necessary in order to calculate the PSD throughout the evaporation process is determined by

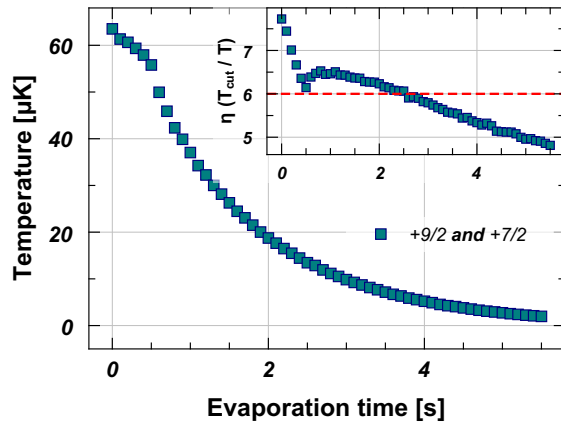
$$n_0 = \frac{1}{2\sqrt{2}} \left(\frac{m}{\pi k_B T} \right)^{3/2} \omega_x \omega_y \omega_z \cdot N. \quad (5.20)$$

A precise determination of the trap frequencies is possible by exciting an oscillation of the cloud inside the ODT, either magnetically or by a short compression / decompression of the trap itself (i.e. by increasing / decreasing the power P). Unfortunately, reliable results of this frequency measurements can be only obtained for an already sufficiently cold cloud (see fig. 5.17 in sec. 5.5.4) and scaled back for the high-power case. Still, in this section we will estimate the frequencies through the measured power and waist size.

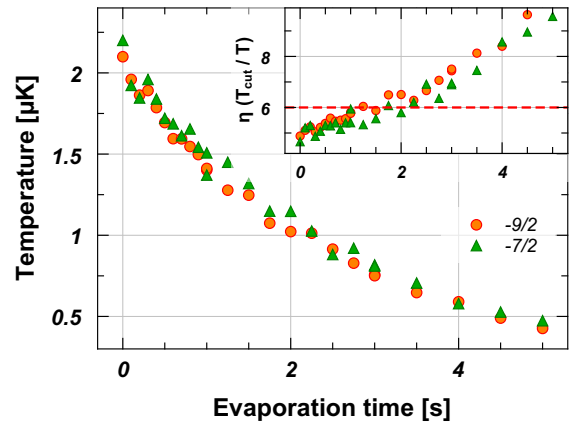
Evaporation in the single ODT

The first evaporation step follows directly the previously described loading step in the hybrid trap: the axial confinement of the ODT1 is reinforced by a low magnetic curvature. The evaporation sequence is performed by reducing the ODT1 power exponentially within 5.5 s from 10 W to 250 mW. The evolution of the temperature, total atom number and PSD are characterized on the left side of fig. 5.8: The loaded atom number of $\sim 2 \cdot 10^7$ reduces by a factor three to $\sim 7 \cdot 10^6$ (fig. 5.8b), while the temperature decreases by a factor 30 from initially $60 \text{ }\mu\text{K}$ to $2 \text{ }\mu\text{K}$ (fig. 5.8a). The logarithmic plot of the PSD as a function of the atom number reveals a slope of $\alpha' = -3.3 \pm 0.1$ (fig. 5.8c), which corresponds to $\eta + \kappa \approx 7$. This is a relatively high value, compared to the directly evaluated decreasing η -values from the embedded diagram in fig. 5.8a. Hence, with decreasing trap height the exceeding energy of the atoms leaving the trap ($\kappa k_B T$) increases.

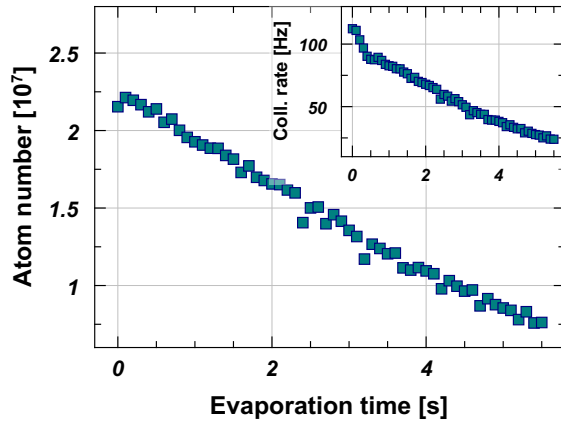
Since shortly after loading the ODT1 the temperature drops below $100 \text{ }\mu\text{K}$, we can neglect p -wave interactions [212] and use eq. (5.14) for estimating the purely s -wave collision rate. The composition of the gas is approximately 70 % in the $|F = 9/2, m_F = +9/2\rangle$ -Zeeman state and 30 % in $|F = 9/2, m_F = +7/2\rangle$. The small proportion ($< 5\%$) of $m_F = +5/2$ can be neglected. Contrary to the case of the magnetic evaporation, the collision rate decreases with the lowered confinement in case of the ODT evaporation [213] (see embedded figure in fig. 5.8b). Especially the low axial confinement and frequency (compared to the radial ones) makes it difficult to continue the evaporation efficiently. We stop the evaporation at this point and switch on a second ODT beam in y -direction, before continuing the evaporation in a crossed ODT.



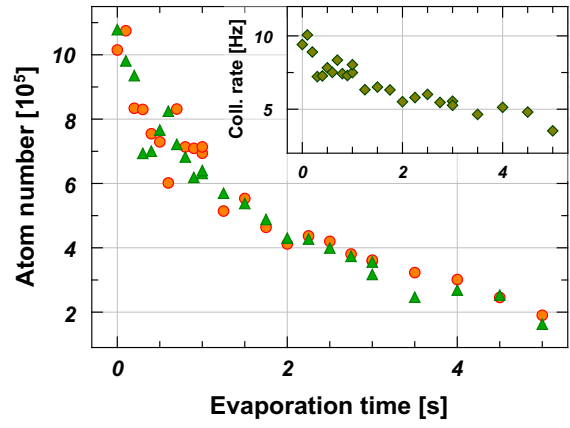
(a) Temperature evolution – single beam ODT



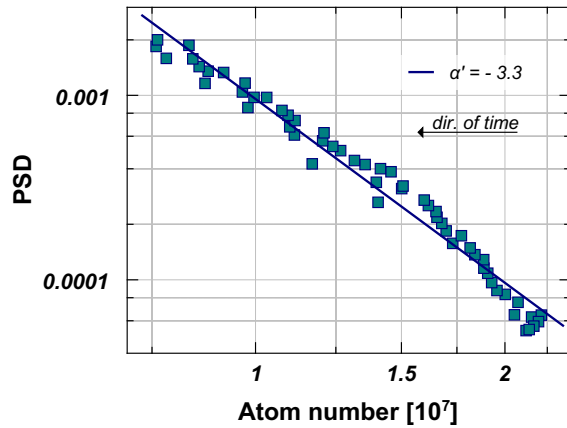
(d) Temperature evolution – crossed ODT



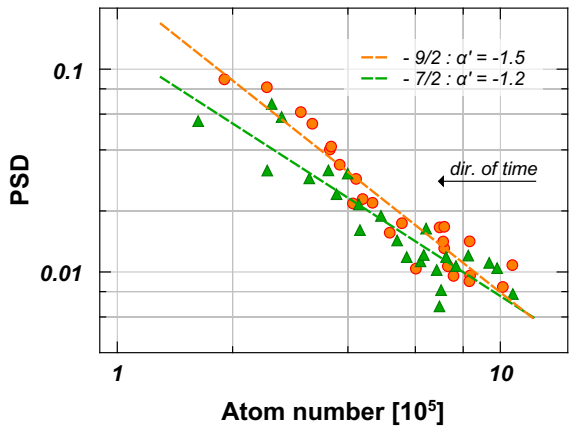
(b) Atom number evolution – single beam ODT



(e) Atom number evolution – crossed ODT



(c) PSD increase – single beam ODT



(f) PSD increase – crossed ODT

Figure 5.8: Characterization of the ODT evaporation, in a single-beam ODT (left part, (a)–(c)) and positive spin states, and in a crossed ODT after a spin-flip to negative spin states (right part, (d)–(f)). In the latter case we image spin selectively $m_F = -9/2$ (orange dots) and $m_F = -7/2$ (green triangles).

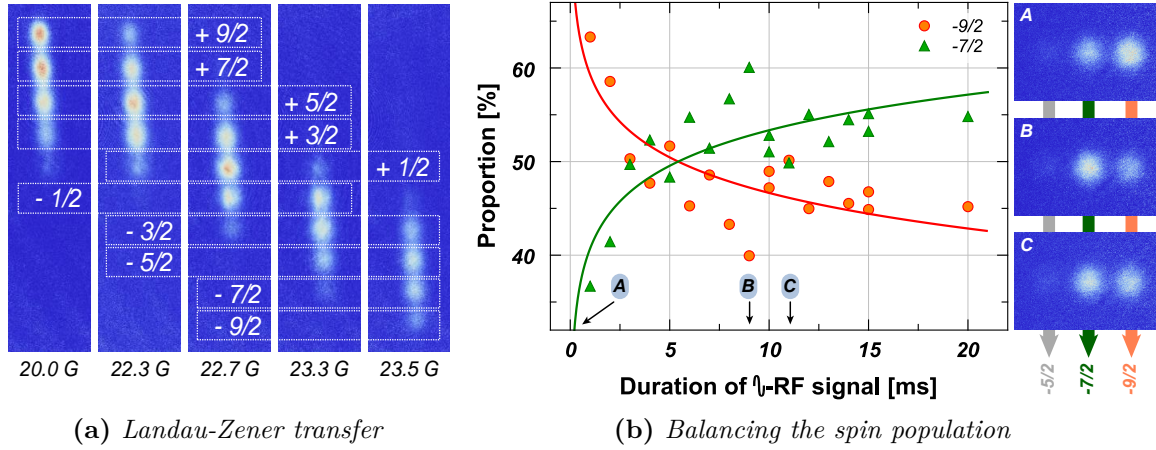


Figure 5.9: Spin manipulation of ^{40}K . (a) shows Stern-Gerlach expansions of the spin mixtures after a Landau Zeeman transfer performed with the same linear RF-ramp from 6.5 MHz to 5.5 MHz in 10 ms but at different bias values. The transfer starts with a mixture of $|m_F = +9/2\rangle$ and $|m_F = +7/2\rangle$ solely. At 25 G, we obtain an imbalanced mixture of $|m_F = -9/2\rangle$ and $|m_F = -7/2\rangle$ only (see image A in (b)). Afterwards, we balance the mixture by driving a triangle-wave-form RF-signal for different time duration (b). The optimal equilibrium is obtained after ~ 10 ms.

Spin-flip and mixture preparation

Prior to the loading of the crossed ODT and the continuation of the evaporation, we perform a spin manipulation step: First, after the remaining gradient is switched off, a bias is applied to maintain the quantization axis. Subsequently, we perform a Landau-Zener transfer of the spin state by driving a linear RF-ramp from 6.5 MHz to 5.5 MHz in 10 ms [214]. In that way we transfer the ensemble within the $F = 9/2$ -hyperfine manifold from $|m_F = +9/2\rangle$ and $|m_F = +7/2\rangle$ to the lower lying states $|m_F = -9/2\rangle$ and $|m_F = -7/2\rangle$ (fig. 5.9a). For the given frequency range, the optimal bias field to mirror the positive spin states into the negative ones is found to be at 25 G. Afterwards, at a higher bias field of 117 G, we balance the population of the new spin mixture in the two lowest negative states. This is accomplished by driving a triangle-wave-form of the RF-signal in-between 28.5 MHz and 30 MHz at a rate of 1 kHz for 20 ms. The high rate of the signal ensures that the atoms do not follow adiabatically the frequency in form of Rabi-oscillations, but rather incoherently populate both spin states.

The complete spin preparation process takes about 200 ms. During the procedure the cloud heats up from $\sim 2\ \mu\text{K}$ to $3\ \mu\text{K}$ to $4\ \mu\text{K}$, and less than 20% of the initial atoms get lost. Finally this leaves us with $\sim 5 \cdot 10^6$ atoms in the two lowest Zeeman states for the rest of the evaporation towards quantum degeneracy.

Evaporation in the crossed ODT

After the first evaporation sequence and the spin preparation in the single-beam ODT1, we load the atoms in a crossed ODT by switching on the second perpendicular ODT arm (ODT2 in fig. 5.1). In that way we increase the axial confinement at low power for the rest of the

evaporation. The new trapping frequencies are a composition of the two traps,

$$\begin{aligned}\omega_x &= \sqrt{\omega_{\text{ax-1}}^2 + \omega_{\text{rad-2}}^2} \approx \omega_{\text{rad-2}} , \\ \omega_y &= \sqrt{\omega_{\text{rad-1}}^2 + \omega_{\text{ax-2}}^2} \approx \omega_{\text{rad-1}} , \\ \omega_z &= \sqrt{\omega_{\text{rad-1}}^2 + \omega_{\text{rad-2}}^2} .\end{aligned}\tag{5.21}$$

To mark the frequencies, we used the notation corresponding to the directions indicated in fig. 5.1, while the index numbers indicate the corresponding ODT beam. Regarding the beam power at the start, the ODT2 is linearly turned up to 4.8 W, while the ODT1 remains at its final power of 250 mW, which is reached at the end of the first evaporation step. Following eq. (5.21), the axial frequency of ODT1 increases from ~ 1 Hz (or ~ 25 Hz in presence of the magnetic gradient in case of the hybrid-trap) to $\omega_x \approx 190$ Hz. Since the axial frequencies of each laser are negligible compared to the radial ones, the frequencies ω_x and ω_y can be approximated by the dominating corresponding radial confinement.

The second part of the optical evaporation is done in the two lowest negative Zeeman states, $|m_F = -9/2\rangle$ and $|m_F = -7/2\rangle$, by decreasing exponentially the power of ODT1 from 250 mW down to 40 mW solely. We increase the bias field to 240 G to apply spin selective imaging⁷, thereby detecting the atom number and temperature evolution (right side of fig. 5.8) for both populations separately.

After loading the crossed ODT, we lose about half of the atoms, but manage to reduce the temperature: The recorded evaporation process in fig. 5.8e starts with $2.2 \cdot 10^6$ atoms in total (compared to $5 \cdot 10^6$ after the spin preparation in the single ODT1), while the temperature at the beginning is $\sim 2.2 \mu\text{K}$ for each spin state (compared to the heated cloud at $3 \mu\text{K}$ to $4 \mu\text{K}$ after the spin preparation). We attribute this observation to a fast evaporation during the compression along the ODT1 axis, which is done by increasing the power of the second ODT2 arm.

During the depicted 5 s long evaporation, the two spin composition remains balanced (fig. 5.8e) and both spin states reach a temperature of $0.5 \mu\text{K}$ (fig. 5.8d) with $2 \cdot 10^5$ atoms per state. Judging on the PSD evolution, the evaporation is less efficient than in the previous case of the single ODT. We fit a slope of $\alpha'_{-9/2} = -1.5 \pm 0.1$ for the PSD evolution of $|m_F = -9/2\rangle$ and $\alpha'_{-7/2} = -1.2 \pm 0.1$ for the increase in the logarithmic plot of $|m_F = -7/2\rangle$ (fig. 5.8f).

Evaporation sequence overview

In the depicted characterization, we reach approximately $T/T_F \approx 1$, with T_F being the Fermi temperature (see eq. (5.50)). We achieve much higher PSD by increasing the evaporation time of the second step to 14 s. In fig. 5.10 we present a summary of the experimental sequence, which was performed for obtaining a degenerate sample of ^{40}K in the lowest two spin states, $m_F = -9/2$ and $m_F = -7/2$. The evaluation of the results will be discussed later in sec. 5.5. The chosen bias field splitting between the two coil pairs and its evolution in the sequence, will be the subject of the next section.

⁷The bias value of 240 G is lying on the BCS side of the ~ 7 G-wide Feshbach resonance, located at 202 G. Hence the scattering length corresponds to the background value of $a_{\text{bg}} = 167a_0$ [212].

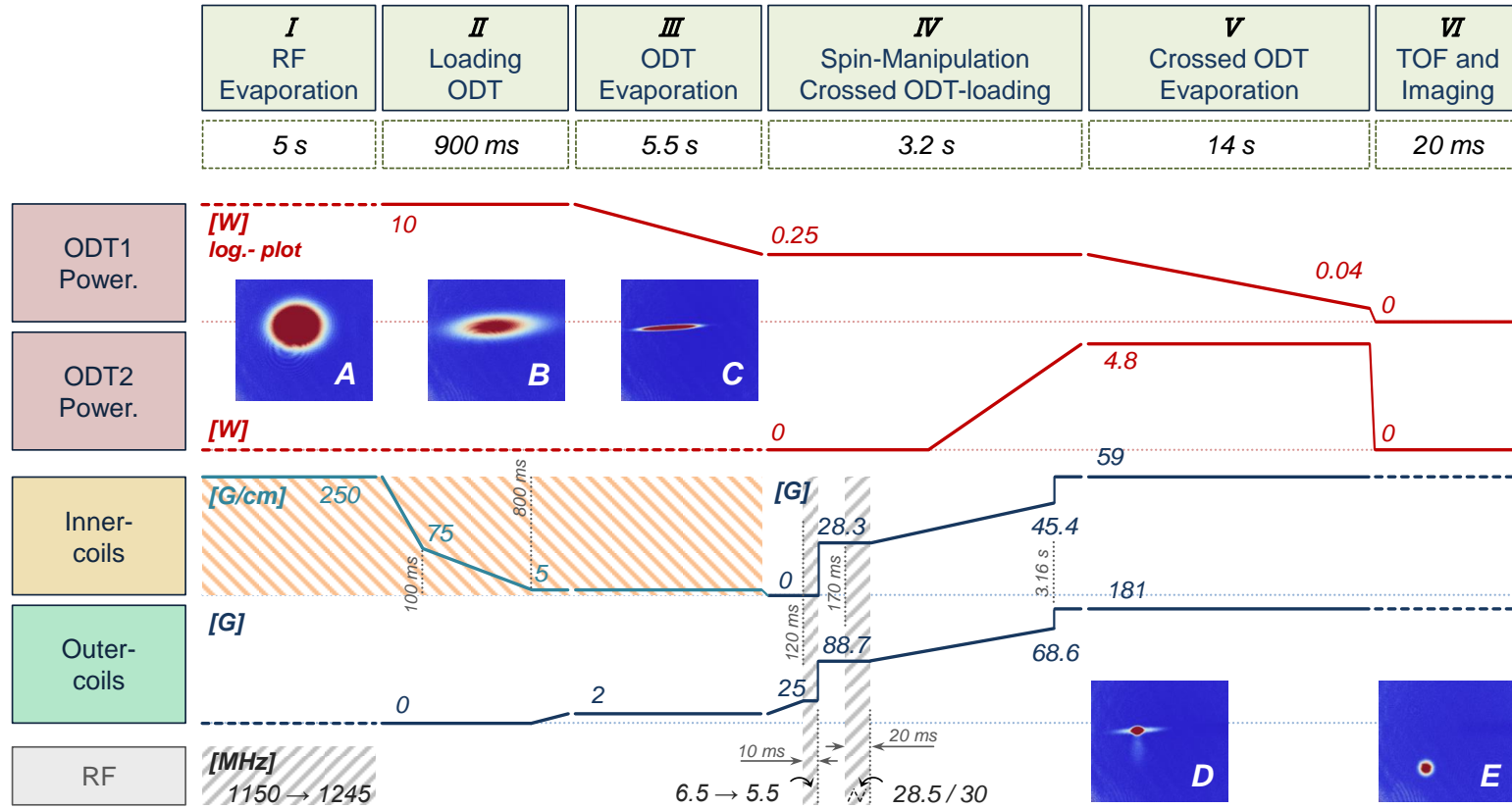
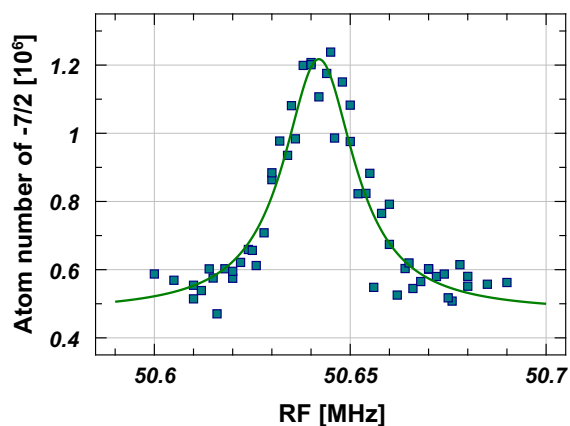


Figure 5.10: The final optimized evaporation sequence. The power evolution of the two dipole trap beams, ODT1 (in logarithmic scale) and ODT2, as well as the bias field distribution between the two coil pairs, inner coils C_{IC} and outer coils C_{OC} is depicted. The bias field is switched in such a way, that the curvature is compensated and appearing Feshbach resonances are avoided (for further details see next section). The insets show real cloud TOF images after RF-evaporation (A), after loading the single-beam ODT (B), after evaporation in the single-beam ODT (C), after loading the crossed ODT (D) and after the complete evaporation cycle (E). For the last image the cloud expands very slowly due to the low temperature and falls visibly during the 20 ms TOF through the imaged area.

**Figure 5.11**

RF-spectroscopy for precise bias measurement: At a fixed bias value we scan the RF-transition between the $-9/2$ and $-7/2$ Zeeman states. Afterwards, we image at the same bias spin selectively the $-7/2$ state. The measurement was performed for a mixed bias of inner and outer coils to compensate the magnetic curvature. The Lorentzian fit reveals a center frequency of 50.642 MHz which corresponds to 241.6 G according to the Breit-Rabi formula.

5.4 Magnetic Field Effects

In this section we will explore the influence of magnetic curvature and Feshbach resonances on the optically trapped atoms. Regarding the technical setup described in sec. 5.1, we have two pairs of coils (inner and outer coils) to adjust the magnetic field. We will first present a method to measure precisely the magnitude of the created bias field and then discuss a method to quantify the curvature of the same. In the last part, we present the measurement of the Feshbach resonances between the two mixtures $m_F = \{+9/2, +7/2\}$ and $m_F = \{-9/2, -7/2\}$.

5.4.1 Precise measurement of the bias field

The bias values given in tab. 5.1 are values measured by a Hall-sensor, done before the coils were installed in the experimental setup. They are in good agreement to the calculated values, based on the coil design [111]. Performing spin sensitive measurements on the atoms allows for a more precise determination of the bias field magnitude. One possibility is to use the spin selective imaging at a high bias field. In this case the resonance imaging frequency is Zeeman shifted according to the Breit-Rabi formula. This method is only limited by the linewidth of the probe-laser.

A more precise determination is possible by RF-spectroscopy, driving magnetic dipole transitions between two neighboring hyperfine states. The measurement starts with an unbalanced mixture of the two spin states $m_F = -9/2$ and $m_F = -7/2$ at an expected bias value of 240 G, with the minority of the atoms in the $-7/2$ -state (30 %). Similar to an optical imaging frequency scan, we shine for a duration of 300 ms constant RF in the range of 49 MHz to 52 MHz on the optically trapped cloud, suspecting the resonance at 50.42 MHz at a bias field of 240 G for the transition $-9/2 \rightarrow -7/2$, based on the Breit-Rabi formula. After a short TOF we image (at the same bias field) spin selectively the $-7/2$ population. Fig. 5.11 depicts the result of the RF-scan. A Lorentz-function fit reveals the resonance frequency of the transfer at $\omega_{\text{RF}} = 50.642$ MHz and a width of $\Gamma_{\text{RF}} \approx 44$ kHz. To avoid broadening of the transition-width, sufficiently weak RF-signal should be applied. Converting then again the resonance value according to the Breit-Rabi formula to a bias field, which corresponds to a particular Zeeman splitting between the states $m_F = -9/2$ and $m_F = -7/2$, yields the exact field value of 241.6 G.

The precise determination and knowledge of the bias field is important for the application of narrow Feshbach resonances and the high field imaging.

5.4.2 Role of magnetic curvature

By creating a high homogeneous magnetic field \mathbf{B} with a pair of coils in Helmholtz-configuration, we have to take into account the curvature of the magnetic field. Indeed, due to Maxwell's equation the value of the magnetic field close to the coil center is given by the general expression [215]

$$\mathbf{B} = B_0 \cdot \begin{pmatrix} 0 \\ 0 \\ 1 \end{pmatrix} + B_0'' \cdot \begin{pmatrix} -zx \\ -zy \\ z^2 - r^2/2 \end{pmatrix}, \quad (5.22)$$

with B_0 ([G]) and B_0'' ([G/cm²]) being geometry specific and current dependent coefficients and $r^2 = x^2 + y^2$ being the usual radial coordinate. The values per 1 A for the two coil pairs nearby the science cell are listed in table 5.1. As mentioned in sec. 2.6 the energy of an atom, which follows adiabatically the magnetic field is calculated by $E = -\mu_B g_F m_F |B|$. We can approximate the absolute value of the magnetic field $|B|$ near the origin by neglecting terms of second order in B_0''/B_0 ,

$$|B| \approx B_0 + B_0'' \left(z^2 - \frac{r^2}{2} \right). \quad (5.23)$$

In this approximation we deduce a harmonic potential form, by introducing the trapping frequency $\omega_{\text{curv}} = (\mu_B g_F m_F B_0''/m)^{1/2}$,

$$U_{\text{mag-curv}} = U_0 + \frac{m}{2} \left\{ \omega_{\text{curv}}^2 r^2 - \left(\sqrt{2} \omega_{\text{curv}} \right)^2 z^2 \right\}, \quad (5.24)$$

with $U_0 = -\mu_B g_F m_F B_0$. For negative Zeeman states ($m_F < 0$) and in case of negative curvature $B_0'' < 0$, the frequency ω_{curv} is a real number, while for $B_0'' > 0$ the two terms in curly brackets in eq. (5.24) exchange their sign: Either the potential is trapping in the xy -plane and repulsive in z -direction or the other way around, depending on the sign of the curvature B_0'' and the actual Zeeman state.

In our experiment we are constrained to the maximum currents of 30 A in the inner coils and about 150 A in the outer coils in Helmholtz-configuration, which corresponds to curvature frequencies of $\omega_{\text{curv}}/2\pi = 5.7$ Hz and $\omega_{\text{curv}}/2\pi = 3.6$ Hz. Following the discussion in the appendix-sec. H.2, where we derive the TOF expansion of the cloud in a curvature field (see eq. (H.18) and eq. (H.19)), we need to perform TOF's, which are longer than 25 ms, in order to distinguish the curvature effect from a free expansion. The TOF, in turn, is limited by the reachable temperatures and by the expansion of the cloud in the anti-trapping directions of the curvature. Therefore the direct measurement of the curvature through the TOF expansion is only possible to a limited extend.

However, the experiment presented below reveals clearly the influence of the curvature on the trapping as well as its effect on the evaporation process: After loading the crossed ODT we have a strong confinement along the y - and z - directions of $\omega_{y,z}/2\pi \approx 350$ Hz, while the confinement along the x -axis is comparably smaller, $\omega_x/2\pi \approx 30$ Hz. Under this conditions we increase each time the bias field to 240 G using both coils, the inner and outer ones, but in different proportions. According to table 5.1 the current in the inner (I_{IC}) and the outer coils (I_{OC}) has to be chosen by $I_{\text{IC}} = (240 - 2.05 I_{\text{OC}})/8$ to realize always a magnetic field value of 240 G. For each combination we hold the atoms for 3 s in the crossed trap. To ensure the same imaging conditions, we switch each time back to the outer coils only and record the atom

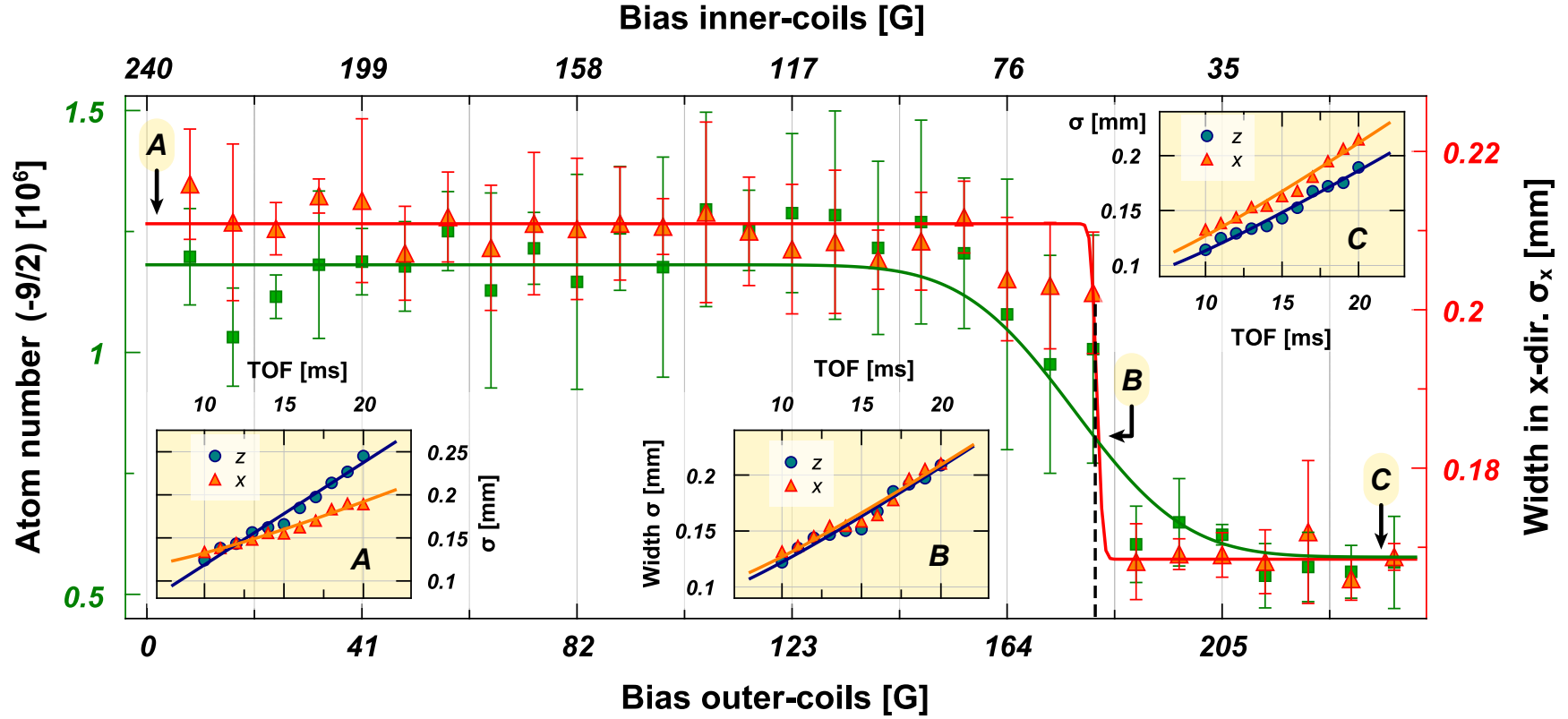


Figure 5.12: Curvature compensation experiment: The cloud is held in the crossed ODT for 3 s at 240 G, created by the inner and outer coils, both contributing to the field value in different proportions. For the TOF and imaging we switch to 240 G created by the outer coil pair only and record the atom number (green squares) and width (red triangles) along the weakest trapping axis ($\omega_x \approx 190$ Hz) of the $m_F = -9/2$ spin state. The influence of the curvature on the trapping frequency manifests as an evaporation process on the atom number and temperature. The insets A–C show TOFs performed at the marked mixed bias values: Due to the stronger curvature of the inner coils the difference in the cloud expansion along the two orthogonal axis x and z is more pronounced in A than in B.

number (of $m_F = -9/2$) and the width of the cloud along the x -axis.

The results are shown in fig. 5.12. For a bias field created by the inner coils, the curvature is confining in the x -direction for *negative* spin states, therefore increasing the trapping frequency along x . In the opposite case of outer coils usage only, the curvature is repulsive in the same direction and hence decreases the trapping frequency ω_x . We observe a higher atom number and greater cloud width σ_x in the predominant use of the inner coils to create the field of 240 G, due to the higher trap frequency, while the opposite effect – atom losses and evaporation to lower temperature and smaller cloud width σ_x – is observed for the dominating outer coils. The effect is still weak and the smooth increase of the frequency ω_x is beyond the error bars. Nevertheless, the fitted error functions allow for an estimation of the transition point, where the two curvatures compensate each other at $B_{OC} = 180 \pm 2$ G and similarly $B_{IC} = 60 \pm 2$ G. Using the theoretical curvature values of tab. 5.1, we can easily formulate the condition of zero curvature for an arbitrary field B , finding that for 240 G we require a partition of the bias field by $B_{OC} = 181$ G and $B_{IC} = 59$ G, in good agreement with the performed experiment. For an arbitrary field B the currents in the coils have to be chosen according to

$$I_{OC}(B) = B / \left(2.05 + 8 \cdot \frac{0.026}{0.31} \right) \quad \text{and} \quad I_{IC}(B) = I_{OC}(B) \cdot \frac{0.026}{0.31}, \quad (5.25)$$

following the values in tab. 5.1.

The additionally performed TOF measurements at 240 G in presence of the inner coils (A), outer coils (C) and at the compensated curvature (B) confirm the previous behavior (see embedded diagrams in fig. 5.12): In the cases A and C we observe different expansion velocities of the width along the two directions, whereby in case of A the effect is more pronounced since the curvature of the inner coils is stronger than the one of the outer coils. By contrary in the compensated case B we observe a uniform expansion along the x - and z -directions. Besides, the fitted models (orange and blue curves), are the ones for the free expansion according to eq. (2.13) and fit very well the data points as mentioned in the beginning to this section, underlining the difficulty of the curvature determination by pure TOF recording.

The compensation of the curvature is not only important during the evaporation process, in case when a strong bias field is applied (see fig. 5.10), but especially during TOF, when the precise determination of the cloud profile is necessary, as we will see later by evaluating the Thomas-Fermi profile of a degenerate ensemble.

5.4.3 Feshbach resonances

Feshbach resonances are a well known and established technique for tuning the interaction strength between the atoms in cold gas experiments [85]. By modifying the energy level of the common molecular bound state potential of the colliding partners, one effectively controls the scattering length in the gas. The tuning of the scattering length is most commonly achieved by applying a magnetic bias field B and therefore changing the Zeeman splitting and the energy level of the bound state of the collision partners. For s -wave scattering resonance, the evolution of the scattering length $a(B)$ can be described in the simple form [216]:

$$a(B) = a_{bg} \left(1 - \frac{\Delta B}{B - B_0} \right), \quad (5.26)$$

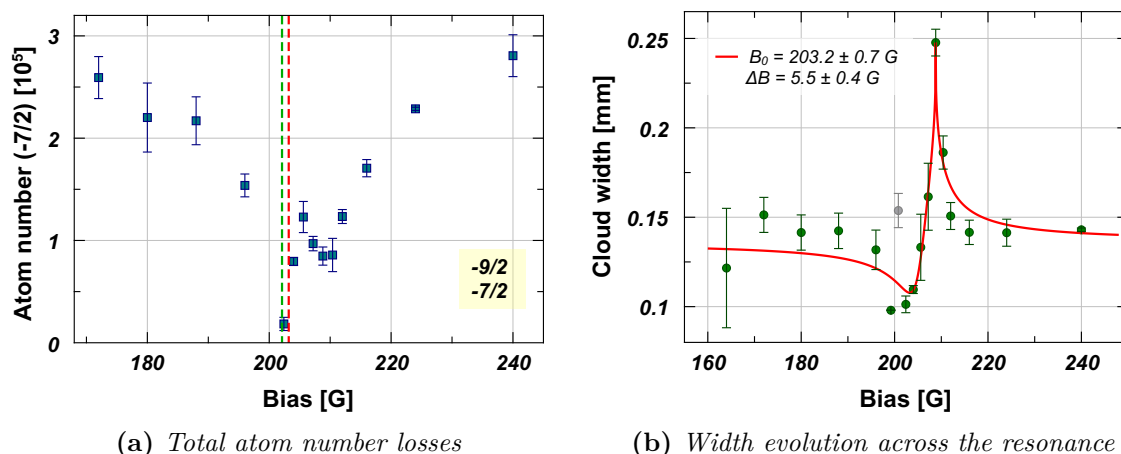


Figure 5.13: *s*-wave Feshbach resonance in the $m_F = \{-9/2, -7/2\}$ mixture. The bias scan during evaporation is performed on a balanced mixture of the two lowest negative Zeeman states. We image spin selectively the $-7/2$ -state by ramping in 15 ms the bias field above the resonance to 240 G. The center of the loss feature in (a) coincides within error bars with the fitted resonance characteristics from (b) according to eq. (5.35). The fit parameters are found to be $B_0 = 203.2 \text{ G}$, $\Delta B = 5.5 \text{ G}$, $P_1 = 0.58 \pm 0.2$, $P_2 = 0.71 \pm 0.24$ and $S_0 = 0.25 \pm 0.03 \text{ mm}$ for the cloud size at zero-crossing. The literature values are $B_0 = 203.2 \text{ G}$ and $\Delta B = 7.8 \text{ G}$ [217] (green dashed line). The omitted gray data point in (b) arises from heating due to three body losses through the neighboring *p*-wave resonance for $m_F = -7/2$ -states.

with the background scattering length a_{bg} and the two quantities B_0 (resonance position) and ΔB (resonance width), which characterize the Feshbach resonance entirely. In this section we will present two characterizations of Feshbach resonances, namely in case of scattering in the positive spin state mixture $m_F = \{+9/2, +7/2\}$ and the negative counter-part, $m_F = \{-9/2, -7/2\}$. These are the two mixtures which appear in the previously discussed evaporation sequence.

We perform an evaporation step in the crossed ODT at different bias values B in order to determine the effect of variable scattering length and to measure experimentally the position B_0 and width ΔB of the resonance. In case of the positive spin state mixture we switch off the bias field to record the atom number (fig. 5.14), while for the negative spin mixture we always ramp in 15 ms to a field of 240 G and image the $-7/2$ spin state only (fig. 5.13). For the depicted measurements we balance the negative spin mixture (50 % in $m_F = -9/2$ and 50 % in $m_F = -7/2$) but do not balance the positive one ($\sim 2/3$ of the atoms are in $m_F = +9/2$ and the rest occupies the $m_F = +7/2$ state).

The center and width of the resonance can be identified either from the atom-loss feature or from the width evolution. The latter one allows a more precise determination, since the final cloud width S is related to the temperature T by $S \sim \sqrt{T}$ (see eq. (2.13)), which in turn depends on the collision properties during the evaporation sequence. We follow the discussion presented in [212] to derive a similar fit-model for the width evolution through a *s*-wave Feshbach resonance scan.

Through the evaporation cycle we lower the trap depth $U(t)$ through time according to

$$U(t) = U_0 e^{-t/\tau_{\text{evap}}},$$

with the evaporation time constant τ_{evap} . This time is chosen to be much longer than the timescale of

elastic collisions,

$$\tau_{\text{evap}} \gg \tau_{\text{el}} = 1/\gamma_{\text{el}} . \quad (5.27)$$

Additionally, the cut parameter $\eta = U(t)/k_B T$ is supposed to be large to neglect non-evaporation related spilling of the atoms from the trap and to be constant through the sequence. We assume a constant cut parameter η throughout the entire evaporation, therefore setting

$$\frac{\dot{T}}{T} \approx \frac{\dot{U}(t)}{U(t)} = -1/\tau_{\text{evap}} . \quad (5.28)$$

During the evaporation the temperature scales with the atom number according to eq. (5.9) ($\delta = 3/2$ for a harmonic trap and $\kappa \approx 1$ for large η [206, 207]) as

$$\frac{\dot{T}}{T} \approx \frac{1}{3}(\eta - 2) \frac{\dot{N}}{N} + \frac{\dot{U}}{2U} . \quad (5.29)$$

The last term accounts for the adiabatic decompression of the cloud, which scales the temperature T in the case of an harmonic trap as $T \sim \sqrt{U}$.

For $\eta \gg 1$ the evolution of the atom number through the evaporation can be approximated by the elastic collision γ_{el} rate from eq. (5.12) by [75, 205]

$$\frac{\dot{N}}{N} \approx -\gamma_{\text{el}} e^{-\eta} (\eta - 4) = -n\sigma_{\text{el}} v e^{-\eta} (\eta - 4) . \quad (5.30)$$

The last three equations determine the dependency of η on the cross section σ in case of adiabatic decompression of the trap during evaporation:

$$e^\eta = \frac{2}{3}\tau_{\text{evap}} n\sigma_{\text{el}} v (\eta - 2) (\eta - 4) \approx \frac{2}{3}\tau_{\text{evap}} n\sigma_{\text{el}} v \eta^2 , \quad (5.31)$$

whereby we approximated in the last step the expression for large η -values. This is a very rough approximation and ideally valid for very large η only. The solution of the last equation is defined as Lambert- \mathcal{W} function [218] or product logarithm function. The $\mathcal{W}(x)$ -functions are defined as a solution of the equation

$$x = \mathcal{W}(x) \cdot e^{\mathcal{W}(x)} . \quad (5.32)$$

In terms of the Lambert- \mathcal{W} function the solution of eq. (5.31) restricted to positive η -values yields

$$\eta(\sigma_{\text{el}}) = -2\mathcal{W}\left(-\frac{s_0}{2} \frac{1}{\sqrt{\sigma_{\text{el}}}}\right) \quad \text{with} \quad \frac{1}{s_0^2} = \frac{2}{3}\tau_{\text{evap}} n v . \quad (5.33)$$

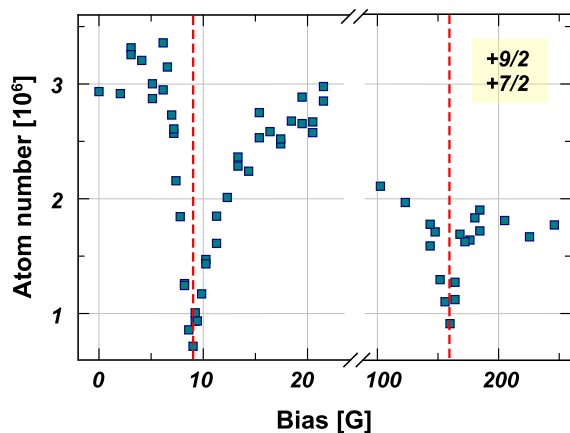
Finally, through the exact expression of $\sigma_{\text{el}}(k, a)$ in eq. (5.13) we establish the relation between the cut parameter η and the field dependent scattering length $a(B)$. The missing link between η and the recorded final cloud width S can be deduced from the definition of η at the previously mentioned condition of constant η throughout the evaporation,

$$S \sim 1/\sqrt{\eta} .$$

At zero-crossing of the resonance the scattering length vanishes and $\sigma_{\text{el}} = 0$. Thus the adiabatic compression would lead to the maximum recorded size S_0 . In all the other cases, the variable scattering cross section reveals a cooling effect. We expect therefore a simple model of the form

$$S(B) = S_0 \left(1 - \frac{1}{\sqrt{\eta(B)}}\right) , \quad (5.34)$$

to describe the width evolution as a function of the magnetic field B . Inserting eq. (5.33), the general cross section from eq. (5.13) and the expression of eq. (5.26) for the scattering length across a Feshbach


Figure 5.14

d-wave Feshbach resonances in the $m_F = \{+9/2, +7/2\}$ mixture. The diagram depicts the final atom number recorded after a 5 s long evaporation step in the crossed ODT performed at different bias values. The measurement is done in an imbalanced mixture, containing $\sim 70\%$ of a $+9/2$ -spin state majority. Two atom-loss features at 9 G and 160 G mark the positions of two Feshbach resonances (red lines). In the current experiment we do not image spin selectively.

resonance, results in a model of the form

$$S(B) = S_0 \left\{ 1 - \left(-2\mathcal{W} \left[-\frac{1}{2P_2} \sqrt{1 + P_1^2 \left(1 - \frac{\Delta B}{B - B_0} \right)} \right] \right)^{-1/2} \right\} \quad (5.35)$$

The parameters P_1 , P_2 incorporate the background scattering length a_{bg} , the evaporation time τ_{evap} , the density n , the relative velocity v and the momentum dependency of the scattering. The first parameter S_0 denotes the hypothetical cloud width at zero-crossing of the resonance, since thermal equilibrium cannot be maintained in absence of interactions. It should be emphasized at this point, that the model is only valid in case of *s*-wave Feshbach resonances, since we applied the corresponding expression from eq. (5.26).

In fig. 5.13b we fit the derived model to the width evolution across the resonance for the negative spin mixture $m_F = \{-9/2, -7/2\}$. We find the resonance position at $B_0 = 203.2 \pm 0.7$ G and a width of $\Delta B = 5.5 \pm 0.4$ G, which is not far from the previously determined values in [219, 220] ($B_0 = 202.10 \pm 0.07$ G and $\Delta B = 7.8 \pm 0.6$ G [217]). One particular data point (gray in fig. 5.13b) is omitted from the analysis: A nearby *p*-wave resonance of $m_F = -7/2$ -states ($B_0 \sim 198.8$ G) leads to heating through two-body losses [221]. For the negative spin mixture, the central position of the atom loss feature in fig. 5.13a coincides within error bars with the width-determined resonance position.

During the preparation of this manuscript we discovered that the two observed resonances in the positive state mixture $m_F = \{+9/2, +7/2\}$, which are depicted in fig. 5.14, were not reported so far⁸. After a private communication with Dr. Eite Tiesinga, who provided us thankfully some theory scattering data, we identified the two loss features around 9 G and 160 G as *d*-wave Feshbach resonances. Since in this cases the scattering is strongly temperature dependent, we can not apply the model above. For an extensive study it is necessary to record the lifetime of the ensemble around the loss features at variable temperatures, in order to obtain the loss-parameters of the resonance [223].

In the evaporation sequence (see fig. 5.10) we avoid long hold-times nearby the Feshbach resonances due to the observed atom losses: The spin-flip from positive to negative Zeeman states is performed at 25 G, well above the Feshbach resonance from fig. 5.14 and the entire

⁸We refer to [222] for a summary of so far experimentally observed Feshbach resonances.

evaporation in the crossed ODT in the negative spin states is completed at high bias field of 240 G, above the resonance of fig. 5.13. For the mentioned evaporation step, the increase of the scattering cross section nearby the resonance was not favorable compared to the observed atom losses⁹.

5.5 Degenerate Fermi Gas in a Harmonic Trapping Potential

Once we have reached the ultra low temperature regime, it becomes necessary to describe the fermionic ensemble by the Fermi-Dirac statistics, rather than by a Boltzmann distribution. An important measure, describing by how far the gas is determined by the quantum statistics, is its temperature T in relation to the Fermi temperature T_F . This quantity will depend on the atom number and the trapping frequencies.

In the course of this section, we will derive the appropriate density profile and perform a benchmark for the deviation of the Gaussian profile from the corresponding quantum-model as a function of the cloud temperature. Later on, we will apply the derived profile functions to real cloud images and evaluate the T/T_F -value of the ensemble.

5.5.1 Fermi-Dirac distribution

The Fermi-Dirac distribution is described by the phase space density

$$f_{\text{FD}}(\mathbf{r}, \mathbf{p}) = \frac{1}{Z e^{\beta H(\mathbf{r}, \mathbf{p})} + 1}, \quad (5.36)$$

with the usual notation of $\beta = 1/(k_B T)$. The fugacity $Z = \exp(\beta \mu_c)$, which depends on the chemical potential μ_c will be used to normalize the phase space density in eq. (5.36) to the total atom number N . In the following, we assume a harmonic trapping potential with distinct frequencies ω_i ,

$$H(\mathbf{r}, \mathbf{p}) = \frac{\mathbf{p}^2}{2m} + \frac{m}{2} \sum_i \omega_i^2 x_i^2. \quad (5.37)$$

Furthermore, we will consider sufficiently low temperatures from now on, and a spin polarized ensemble, in order to neglect any interaction terms.

To obtain the density profile, we integrate the phase space density over the momentum coordinates,

$$n(\mathbf{r}) = \frac{1}{(2\pi\hbar)^3} \int d^3\mathbf{p} f_{\text{FD}}(\mathbf{r}, \mathbf{p}) = -\frac{1}{\hbar^3} \left(\frac{m}{2\pi} k_B T \right)^{3/2} \mathbf{Li}_{3/2} \left[-Z \exp \left(-\beta \frac{m}{2} \sum_i \omega_i^2 x_i^2 \right) \right]. \quad (5.38)$$

In the last expression we used the polylogarithmic function \mathbf{Li}_n of order n , which is defined by the integral expression

$$\mathbf{Li}_{1+n}[-Z] = -\frac{1}{(k_B T)^{1+n} \Gamma(1+n)} \int_0^\infty d\epsilon \frac{\epsilon^n}{\frac{1}{Z} e^{\beta\epsilon} + 1}, \quad (5.39)$$

⁹This behavior is contrary to the experimental observation in ⁶Li [224, 225], where the large Feshbach resonances are used to increase the collision rate during evaporation in order to decrease the evaporation time [226, 227].

where $\Gamma(n)$ is the Gamma-function with the relevant value of $\Gamma(3/2) = \sqrt{\pi}/2$. For the further calculations, the series expansion of the polylogarithmic functions is particularly important,

$$\mathbf{Li}_n[Z] = \sum_{k=1}^{\infty} Z^k / k^n . \quad (5.40)$$

Applying the last identity we determine the 2D- and 1D-density profiles by further integrating eq. (5.38) to

$$n_{2D}(x, y) = \int n(\mathbf{r}) dz = -\frac{1}{\hbar^3} \frac{m}{2\pi\omega_z} (k_B T)^2 \mathbf{Li}_2 \left[-Z \exp \left(-\beta \frac{m}{2} \{ \omega_x^2 x^2 + \omega_y^2 y^2 \} \right) \right] , \quad (5.41)$$

and

$$n_{1D}(x) = \int n(x, y) dy = -\sqrt{\frac{m}{2\pi}} \frac{(k_B T)^{5/2}}{\hbar^3 \omega_y \omega_z} \mathbf{Li}_{5/2} \left[-Z \exp \left(-\beta \frac{m \omega_x^2 x^2}{2} \right) \right] . \quad (5.42)$$

The corresponding TOF evolutions in free space are given in the appendix sec. H.1.1.

Finally, integrating over the last coordinate, reveals the relation of the fugacity Z to the total atom number,

$$N = -\frac{1}{\hbar^3 \omega_x \omega_y \omega_z} (k_B T)^3 \mathbf{Li}_3[-Z] . \quad (5.43)$$

A direct replacement of the fugacity Z by the total atom number N is not trivial. After a brief discussion of the particular case of zero-temperature, we will link the fugacity Z directly to the temperature T in terms of the Fermi temperature T_F , which is the desired measure for the quantum nature of the gas.

5.5.2 At zero temperature - The Fermi energy

At $T = 0$, we can distinguish two cases for the density distribution in eq. (5.36),

$$\left. \begin{aligned} E > \mu_c &\Rightarrow \lim_{T \rightarrow 0} f_{\text{FD}}(E) = 0 \\ E < \mu_c &\Rightarrow \lim_{T \rightarrow 0} f_{\text{FD}}(E) = 1 \end{aligned} \right\} f_{T=0} = \Theta(\mu_c - E) , \quad (5.44)$$

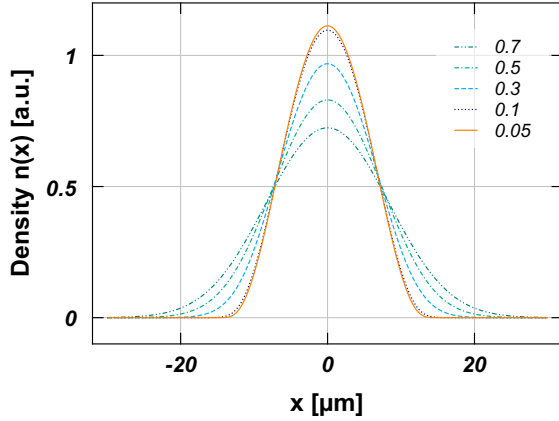
where we replaced the Hamiltonian $H(\mathbf{r}, \mathbf{p})$ in the phase space density f_{FD} by the total energy E , obeying the same expression in eq. (5.37). The phase space distribution is now given by a step-function, describing the occupation of all possible energy levels E below an energy bound, given by the chemical potential μ_c . This is valid for a spin-polarized gas: for two spin components each energy level can be occupied twice – by two different spin states each time.

As previously, we calculate the density distributions for the harmonic potential by simple integration. The integral over the momentum is performed over a sphere in momentum space, which sets the condition

$$\mu_c \geq \frac{m}{2} \sum \omega_i^2 x_i^2 .$$

We will only mention the 3D- and 1D-cases for the density distribution, which are

$$n_{T=0}(\mathbf{r}) = \frac{\sqrt{2} m^{3/2}}{3\pi^2 \hbar^3} \left\{ \mu_c - \frac{m}{2} \sum \omega_i^2 x_i^2 \right\}^{3/2} \Theta \left(\mu_c - \frac{m}{2} \sum \omega_i^2 x_i^2 \right) , \quad (5.45)$$


Figure 5.15

1D-Fermi profiles for different T/T_F values. For the plot, we chose later-on relevant experimental parameters of $N = 1.5 \cdot 10^5$ and the trap frequencies $\omega_x = 2\pi \cdot 154$ Hz, $\omega_y = 2\pi \cdot 160$ Hz and $\omega_z = 2\pi \cdot 25$ Hz.

and

$$n_{T=0}(x) = \frac{2^{5/2} \sqrt{m}}{15\pi \hbar^3 \omega_y \omega_z} \left\{ \mu_c - \frac{m}{2} \omega_x^2 x^2 \right\}^{5/2} \Theta \left(\mu_c - \frac{m}{2} \omega_x^2 x^2 \right). \quad (5.46)$$

The complete integration yields the atom number N , or equivalently

$$\mu_c = E_F = k_B T_F = \hbar \bar{\omega} (6N)^{1/3} \quad \text{with} \quad \bar{\omega} = (\omega_x \omega_y \omega_z)^{1/3}. \quad (5.47)$$

At zero temperature, the chemical potential μ_c is equal to the Fermi energy E_F , which describes the highest occupied energy level in the ground state ($T = 0$). Indeed, since all fermions occupying lower levels than E_F can not acquire the next, already occupied, energy level (due to the Pauli blocking), the potential to undergo a phase transition or reaction of any kind, is limited to the outer-energy-shell E_F -fermions. For the sake of completeness, we mention the expression of the Fermi temperature in a magnetic quadrupole trap of gradient b , derived in the same way to

$$T_{F-\text{Mag-trap}} = \frac{3^{2/3}}{2k_B} \left(\frac{35\pi}{2} N \right)^{2/9} \frac{(\hbar \mu b)^{2/3}}{m^{1/3}}. \quad (5.48)$$

Eliminating the atom number dependency in eq. (5.43) by means of the definition of the Fermi temperature T_F in eq. (5.47), we link the fugacity Z at any temperature T to the ratio T/T_F :

$$\text{Li}_3[-Z] = -\frac{1}{6 (T/T_F)^3}. \quad (5.49)$$

Therefore, fitting the fugacity Z as a free parameter to a real atom clouds, reveals directly the wanted T/T_F -parametrization of the imaged cloud distribution.

It is now possible to formulate more precisely the condition for entering the quantum regime, by relating the temperature to the Fermi temperature through $T/T_F \leq 1$. Furthermore, we can link the PSD from eq. (5.8) in case of a harmonic trapping to the T/T_F ratio in case of a non-degenerate sample (fitted by a Gaussian distribution), by replacing the atom number N

with eq. (5.47)¹⁰,

$$\text{PSD} = \frac{1}{6} \frac{1}{(T/T_F)^3} = -\text{Li}_3[-Z] , \quad (5.50)$$

thereby including the frequency and atom number dependency in the Fermi temperature T_F . In conclusion, the statement of $T/T_F \leq 1$ for entering the quantum degenerate regime is equivalent to $\text{PSD} \geq 1/6$ in case of harmonic trapping. Figure 5.15 shows 1D-Fermi profiles for different temperatures T , but fixed trapping frequencies ω_i and atom number N (therefore at same Fermi temperature T_F).

5.5.3 Comparison of Fermi and Gaussian profiles

In order to demonstrate the deviation of the Fermi profile from a Gaussian-fit, we generate the 1D-profiles according to eq. (5.42) for different T/T_F factors. Therefore, we fix the atom number to $1.5 \cdot 10^5$ and the trap frequencies to $\omega_x = 2\pi \cdot 154 \text{ Hz}$, $\omega_y = 2\pi \cdot 160 \text{ Hz}$, $\omega_z = 2\pi \cdot 25 \text{ Hz}$ and vary only the temperature T as a free parameter. The chosen frequencies and atom number correspond to experimentally realized conditions later-on. For different T , we sample each time the 1D-Fermi density distribution in steps of $2 \mu\text{m}$, cutting the distribution below a fixed density. Afterwards, the resulting data is fitted by a normalized Gaussian distribution,

$$n_{\text{Gauss}}(x) = \sqrt{\frac{m}{2\pi}} \frac{\omega_x N}{(k_B T)^{1/2}} \exp\left(-\beta \frac{m\omega_x^2 x^2}{2}\right) . \quad (5.51)$$

We fix the frequency ω_x and fit the atom number N and temperature T as the only free parameters in the Gaussian model above. While the resulting atom number is within few percent in good agreement with the fixed one in the Fermi model ($1.5 \cdot 10^5$), the temperature T_{Gauss} shows an important deviation with decreasing T/T_F . Figure 5.16 shows the fit results of the temperature T_{Gauss} (expressed in units of the Fermi temperature T_F) in relation to the true T/T_F values. Around $T/T_F \sim 0.3$ the Gaussian temperature starts to deviate from the true result approaching a limit of $T_{\text{Gauss}}/T_F \approx 0.3$ for further decreasing temperature. The deviation of the Gaussian profile from the quantum degenerate Fermi profile at low T/T_F manifests on the wings of the density distribution: The Gaussian function shows a greater width and lower steepness.

5.5.4 Evaluation of the experimental results

At the end of the current section, we will present the evaluation of the experimentally obtained density distributions after the evaporation sequence presented in sec. 5.3. We let the cloud evolve during a long TOF of 20 ms, in order to avoid over saturation on the imaging (appearing due to the high cloud-density). The cloud expands freely in a curvature-compensated bias field of 240 G. The bias allows to perform spin selective imaging of the two component gas. We will neglect for the current analysis the s -wave interactions between the $m_F = -9/2$ and $m_F = -7/2$

¹⁰Similarly we find the relation for the magnetic quadrupole trap to be

$$(T/T_F)_{\text{Mag.-trap}} = \frac{2}{3^{2/3}} \left(\sqrt{\frac{2}{\pi}} \frac{1}{35 \text{ PSD}} \right)^{2/9} .$$

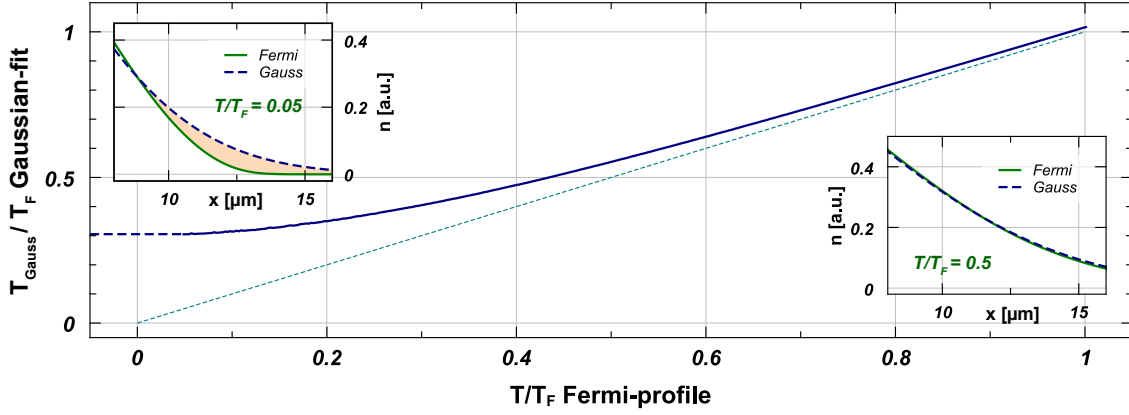


Figure 5.16: Gaussian-fits to Fermi profiles – deviation at the low temperature limit. For the diagram we generated Fermi profiles according to eq. (5.42) for different T/T_F temperatures (x -axis of the diagram above) and used the sampled data to fit a Gaussian distribution, according to eq. (5.51). We suppose the same trapping frequency ω_x , but leave the atom number N and the temperature T_{Gauss} as a free parameter. The fitted "Gaussian" temperature, in units of the Fermi temperature, is depicted on the y -axis. Around $T/T_F \approx 0.3$ the fitted Gaussian temperature deviates from the real temperature T (the dashed line marks $T = T_{\text{Gauss}}$). The fit-deviation gets visually pronounced on the wings of the distribution function (see embedded figures).

states, by fitting the profile derived in eq. (5.42). Strictly speaking, we would have to turn the bias field to the zero-crossing of the Feshbach resonance before imaging, in order to have indeed no interactions present during TOF. However, far away from the Feshbach resonance, the interaction energy V_0 can be neglected in comparison to the total energy of the gas:

$$k_B T \gg V_0, \quad V_0 = \frac{4\pi a \hbar^2}{m}. \quad (5.52)$$

For the estimation, we used the background scattering length $a \approx 167a_0$ and an approximate temperature of $T/T_F = 0.2$.

Different from a temperature measurement by a TOF series, we can normally determine the temperature in the quantum degenerate regime directly from one fit to an image of the density profile of the distribution. To allow for a representative fit result, we average over 3 to 4 images with same experimental conditions. For this purpose, each image gets fitted by a Gaussian, in order to find the center of the distribution and to overlay the images accordingly.

The so obtained 2D-profile is further integrated into two 1D-profiles, in order to reduce the noise and to facilitate the computational effort of the fit procedure (see sec. 5.5.1). The TOF evolution of the density profile from eq. (5.42) is derived in the appendix sec. H.1.1, leading to eq. (H.11):

$$n_{\text{fit}}(x, t) = -A(t) \cdot \text{Li}_{5/2} \left[-Z \exp \left(-(x - x_0)^2 / 2 \sigma^2(t) \right) \right] + \kappa \cdot x + \epsilon. \quad (5.53)$$

On one side, there are the pure image related fit parameters, like the position offset x_0 of the distribution in the chosen coordinate system, the background offset ϵ and finally the tilt κ , originating from the decline of light power on the image by an off-centered probe beam. At the

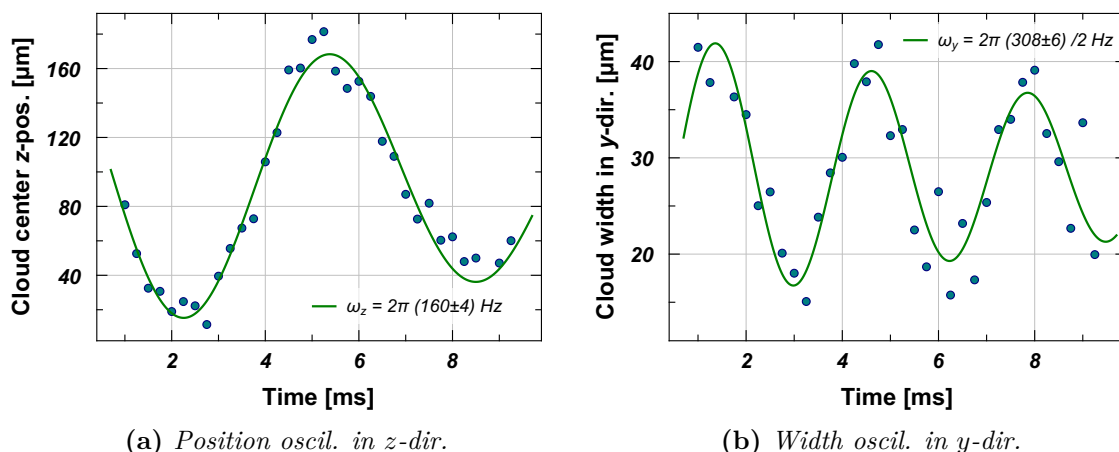


Figure 5.17: Measurement of trap frequencies in the crossed ODT. By switching off the ODT beams for 0.8 ms and on again we induce either center-of-mass oscillations (a) or a breathing-mode (b). In the first case we obtain through fitting directly the trap frequency, while in the second case the fit is twice as large as the trap frequency (width oscillations).

same time, the remaining three parameters, $A(t)$, Z and $\sigma(t)$ are distribution related quantities,

$$A(t) = \sqrt{\frac{m}{2\pi}} \frac{(k_B T)^{5/2}}{\hbar^3 \omega_y \omega_z} \frac{1}{\sqrt{1 + \omega_x^2 t^2}}, \quad \text{and} \quad \sigma^2(t) = \frac{1 + \omega_x^2 t^2}{m \omega_x^2} k_B T. \quad (5.54)$$

In return, the atom number N is included (in combination with the trap frequencies – see eq. (5.47) and eq. (5.49)) within the fit parameter (fugacity) Z . Unlike for a Gaussian fit function, we have two variables which directly modify the fit amplitude, namely Z and A , while the latter one is restricted after all by the width σ through its common relation to the temperature T . Hence, we fix $A(t)$ by the fit value of the width σ ,

$$A(t) = \frac{m^3}{\sqrt{2\pi} \hbar^3} \frac{\omega_x^5}{\omega_y \omega_z} \frac{\sigma^5(t)}{(1 + \omega_x^2 t^2)^3}. \quad (5.55)$$

To further reduce the number of fitting parameters and in particular to ensure that the amplitude $A(t)$ is determined by σ , we measure experimentally the final trap frequencies and insert them as fixed parameters into the model.

The trapping frequencies of the crossed ODT are measured by exciting an oscillation of the cloud within the trap. Therefore, the ODT is switched off abruptly for ~ 0.8 ms and then switched on again to its initial power. The evolution of the cloud is recorded after various hold times, showing two kinds of oscillatory behaviors: Either the entire cloud moves, therefore the fit to the trajectory of the center-of-mass of the cloud reveals the frequency, or a breathing-mode is excited, where the width of the cloud oscillates. In the latter case, the fitted oscillation of the width through time yields twice the trapping frequency. In this way, we determine the three frequencies $\omega_x/2\pi \approx 25$ Hz, $\omega_y/2\pi \approx 154$ Hz and $\omega_z/2\pi \approx 160$ Hz.

We use as fitting program *Mathematica* (by *Wolfram Research*), since it includes the polylogarithmic functions of half-integer order out of the box, as well as highly developed fitting routines. To accelerate the fitting routine, we first fit to the integrated 1D-profiles a Gaussian

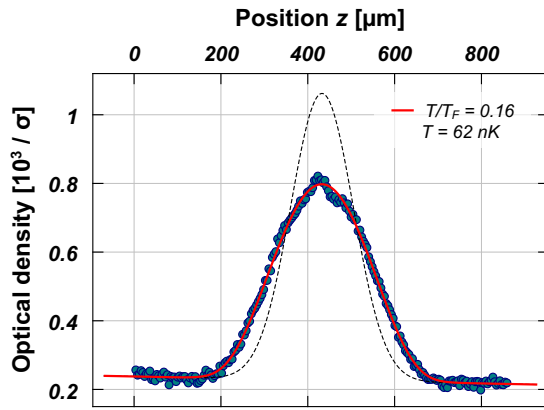
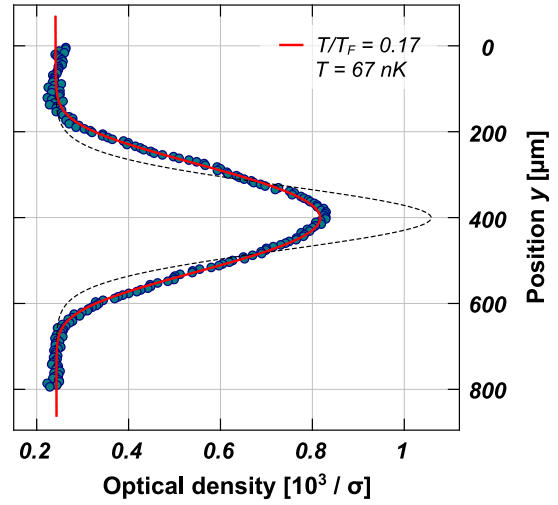
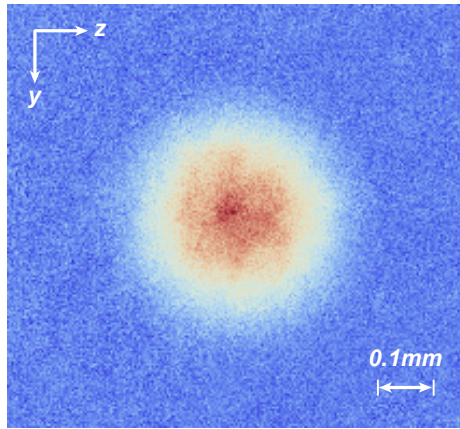


Figure 5.18: Image and analysis of 1D-integrated density profiles of a degenerate cloud of ^{40}K in the $m_F = -9/2$ state after 20 ms TOF. The optical density is expressed in terms of the absorption cross section σ (see eq. (2.7) in sec. 2.7) and is averaged over four images. The red curve is a Fermi fit according to eq. (5.53). The dashed black curve represents a Gaussian distribution for the corresponding temperature and atom number obtained by the Fermi fit.



function and extract x_0 , κ , ϵ and σ which are subsequently passed as initial guesses to the fit routine, which fits in turn directly eq. (5.53).

The result of the Fermi fit to a degenerate ensemble in the $m_F = -9/2$ ground state is shown in fig. 5.18. The depicted 2D-image is an average of four experimental runs with same conditions. The image shows an expansion to a total size of 0.4 mm after 20 ms of TOF. The two integrated 1D-profiles show similar fit results of $T/T_F \approx 0.16 \pm 0.01$ for an ensemble of $1.5 \cdot 10^5$ atoms at a temperature of 62 ± 5 nK as a lower bound. Slightly higher temperatures are obtained for the $m_F = -7/2$ -state, due to a small imbalance in atom number, and therefore lower Fermi temperature. In fig. 5.18 we plotted in dashed lines the equivalent Gaussian distributions in the underlying harmonic trapping potential, which would correspond to the same temperature and atom number obtained by the Fermi fit. Neglecting the fermionic nature and hence the blocking of already occupied states, the Gauss distribution shows a narrower profile than the Fermi one.

The absence of curvature facilitates the fit function and reduces the required parameters: In presence of curvature we would have to know precisely the curvature frequencies in a more complex fit function (see appendix sec. H.2.2).

5.6 Conclusion

In this chapter we analyzed theoretically and experimentally the evaporative cooling of ^{40}K to quantum degeneracy. Therefore, we implemented a RF-forced evaporation step in the magnetic quadrupole trap, as well as evaporative cooling stages in two different ODT geometries. A careful choice of the bias field during the sequence is required, since on the one hand, it effects the trapping and expansion of the cloud (through not compensated curvature effects), and on the other hand reduces atom losses (through Feshbach resonances). By designing a suitable experimental sequence, we achieve a degenerate sample of $m_F = \{-9/2, -7/2\}$ ground state mixture, where a precise analysis of the $-9/2$ density profile reveals a temperature of 62 nK, which corresponds to $T/T_F \approx 0.16$ in terms of the Fermi temperature.

In a next experimental step, we can ramp adiabatically the bias field from 240 G to the Feshbach resonance characterized in fig. 5.13b in order to observe directly a superfluid of fermions at the unitarity regime[228, 229], since the achieved temperature is below the condensation temperature T_C of the fermionic pairs[230].

Summary and Outlook

In this manuscript we discussed two experiments, carried out with two different ultra-cold fermionic species discovering the effects of two distinct statistical regimes.

First, we studied the energy redistribution within an ensemble of non-interacting particles, realized by spin-polarized ^6Li , in a non-separable potential in the classical regime (described initially by a Boltzmann-distribution). We have shown that, even in the absence of interactions, such a system relaxes towards a steady-state after an excitation and that the energy is not equally redistributed within the cloud. We observe a spatial separation of the thermalization into the xy -plane and the symmetry z -axis. Consequently, we describe the resulting distribution with two distinct quasi-temperatures in the plane and along the symmetry axis (thus we refer to the effect of the energy-redistribution after excitation as quasi-thermalization).

The problem of quasi-thermalization can be further extended by analyzing the dependence on the trap-anisotropy and dimensionality of the system, which is partially discussed in [118]. Indeed, the quadrupole-trap can be generalized to the potential

$$U_{\text{pot}} = \sqrt{x^2 + y^2 + \gamma z^2} \quad \text{with} \quad \gamma \geq 1 .$$

The behavior in the limit of $\gamma \rightarrow 1$ becomes particularly interesting, due to the symmetry-breaking of the potential. First numerical results show a sudden change in the energy-distribution coefficients at $\gamma = 1$, being similar to the coefficients $1/6$ and $1/3$ derived in sec. 3.3.1 (see eq. (3.24) of the final "kick"-evaluation). Nevertheless, in the case of a spherically symmetric potential ($\gamma = 1$), the energy imparted through a momentum-kick along a distinct direction is not redistributed equally over the entire trap sphere. In this case, only a minor part of the energy is redistributed in the plane perpendicular to the kick-direction, therefore remaining a non-isotropic problem.

The absence of interactions and the particular form of the quadrupole potential allows to map the single-particle Hamiltonian to an analogous system of a harmonically trapped massless particles. The interpretation of the previous results permits a unique insight into an otherwise not accessible system, like the Weyl-particles. Furthermore, based on a similar idea, we propose the realization of a non-Abelian potential. As stated in the introduction, these two examples are perfect illustrations of a cold gas experiment serving as a simulation tool. It should be emphasized, that here it operates as a *classical* simulation tool, since we use the quantum nature

of ^6Li as a Fermion to avoid interactions only.

In the second part we reached the quantum-degenerate regime with ^{40}K . At this point, interactions become important in order to perform efficient evaporative cooling. We characterized the evaporation in three different trap configurations: the quadrupole trap, the single beam optical dipole trap and the crossed dipole trap. In difference to Bosons, Fermions do not condense into a common ground-state, but rather occupy one by one the lowest lying energy states at zero-temperature. We demonstrated how the (classical) Gaussian distribution deviates from the (quantum) Fermi-Dirac-distribution by lowering the ensemble temperature. We finally obtained a spin-mixture in the two lowest Zeeman-states at $T/T_F \approx 0.16$.

This opens the way to study superfluidity in the BCS-BEC crossover [89] by sweeping the bias field to different values around the Feshbach resonance, characterized in sec. 5.4.3. Using the lattice-laser at 808 nm (which is described in appendix A) these observations can be extended to the quasi-two-dimensional case.

Another step is the sympathetic cooling of ^6Li to achieve double-degeneracy in the FerMix experiment. Based on the observations of the sympathetic cooling of ^6Li by ^{40}K during the RF-evaporation (see sec. 5.2), we decided to install a high-power optical dipole trap (300 W IPG multi-mode fiber-laser) to transfer both atomic species at a higher temperature from the quadrupole trap of the science cell into an optical dipole trap. Longer life-times and the use of the broad Feshbach resonance of ^6Li will facilitate further the sympathetic evaporation. Later on, the colder atomic sample can be transferred into the previously used crossed-dipole trap (see fig. 5.1) in order to work in a single-mode dipole-trap stabilized at low power.

Again implementing the 2D-lattice setup opens up the possibility to study a mixed dimensional system with a free ^6Li gas surrounding multilayers of confined 2D ^{40}K . By tuning the interaction-strength of the 3D ^6Li gas, theoretical models suggest the observation of long-range interactions between the 2D layers [117].

Finally, being one of few experimental machines world wide operating with two fermionic species simultaneously, FerMix owns the flexibility to explore and simulate a vast range of physical systems in the universe of ultra cold atomic gases.

Lattice Laser Setup

In this appendix section we will discuss some details of the constructed 808 nm laser system, which should be implemented as a lattice in our experiment. Apart from a short motivation of the intended application, the current chapter serves especially as an example of a typical *MOPA* system (**M**aster **O**scillator – **P**ower **A**mplifier setup).

A.1 A Lattice Laser for ^{40}K in Presence of ^6Li

The desired experimental realization requires to generate a standing wave, what would confine in its maxima ^{40}K atoms but ideally not ^6Li . The latter should represent a free 3D-gas around the confined multiple 2D- ^{40}K systems (see fig. A.1). Even in absence of ^6Li this allows to investigate for example the superfluid transition by tuning the interaction via a Feshbach resonance in a pure 2D- ^{40}K fermionic system [231].

Another suggested application, which includes a composite system of both species, is the observation of mediated interactions between neighboring 2D- ^{40}K sites through the free ^6Li gas, by tuning the interactions within ^6Li or ^6Li and ^{40}K by a possible Feshbach resonances [118], in order to simulate multilayer systems in analogy to condensed matter topics [117].

The trapping laser beam of wavelength λ_L will be retro-reflected, in order to create a standing wave. According to the discussion in sec. 4.3.1, the trapping potential of a standing wave optical

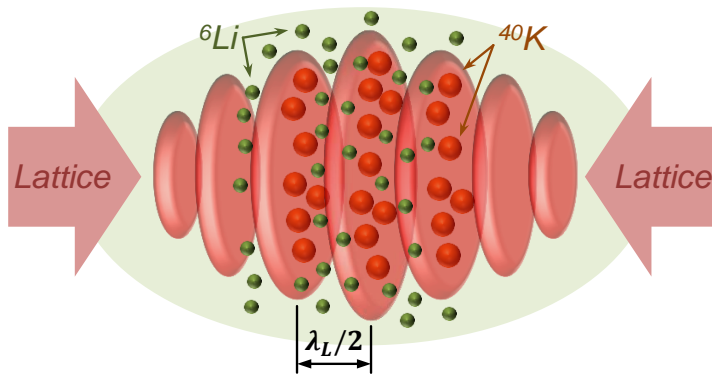


Figure A.1

2D-lattice illustration: ^{40}K is captured in the maxima of the standing wave, while ^6Li constitutes a free gas, which can be used to mediate long range interactions between the layers of ^{40}K .

dipole trap in z -direction can be approximated by [200]

$$U_{\text{sw-ODT}}(r, z) = U_{\text{sw}0} \cdot \cos^2(k_L z) \left\{ 1 - \frac{2r^2}{w_0^2} - \frac{z^2}{z_r^2} \right\} \quad \text{with} \quad k_L = 2\pi/\lambda_L \quad \text{and} \quad U_{\text{sw}0} = 4U_0, \quad (\text{A.1})$$

forming pancake-like traps at a periodic distance of $\lambda_L/2$. Compared with the expression for a single beam ODT in eq. (4.13) the trap depth $U_{\text{sw}0}$ is four times larger due to the interference effect of the incoming and retro-reflected beam (four times the intensity at the place of the antinodes of the standing wave). We find the radial frequency

$$\omega_r^2 = \frac{-4U_{\text{sw}0}}{mw_0^2} \cdot \cos^2(k_L z), \quad (\text{A.2})$$

which is similar to the expression in eq. (4.14) modulated by the standing wave term along the z -direction¹. For the axial direction the frequency at the center of the trap ($z = 0$) yields

$$\omega_z^2 = -\frac{2U_{\text{sw}0}}{m} \left\{ k_L^2 + \frac{1}{z_R^2} \right\} \approx -\frac{2U_{\text{sw}0}}{m} k_L^2 \quad (\text{A.3})$$

where, for reasonable waist sizes w_0 , the Rayleigh-length z_R -related term can be neglected, since $1/\lambda_L \gg 1/z_R$. The heating rate in the optical lattice is related to the average scattering rate Γ_{sc} , describing the rate of absorbing a lattice photon and hence heating of the ensemble by $3k_B T_R/2 = E_R$ [200],

$$\dot{T} = \frac{1}{3} T_R \Gamma_{\text{sc}} \quad \text{with} \quad \Gamma_{\text{sc}} = \frac{\Gamma_{\text{D}_1}}{\hbar |\Delta_{\text{D}_1}|} |U_{\text{sw}0}|. \quad (\text{A.4})$$

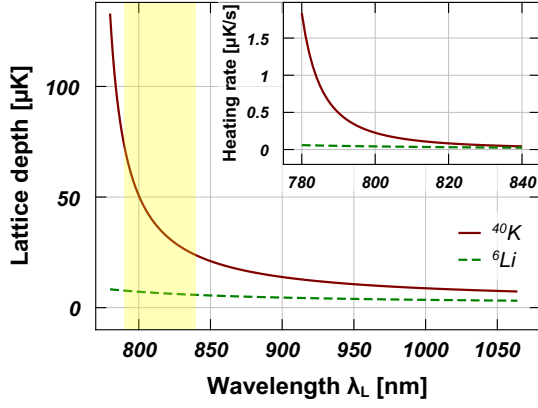
To obtain the scattering rate we use the linewidth and detuning from the element specific D_1 transition line. For different lattice wavelengths λ_L we plot in fig. A.2a the heating rate and the trap depth $U_{\text{sw}0}$ for a fixed waist of $w_0 = 100 \mu\text{m}$ and total power of $P = 250 \text{ mW}$. A sufficient difference in the trap depth for ^6Li and ^{40}K is found in the marked region of 790 nm to 840 nm, while the heating rate diminishes towards larger detunings from the atomic transitions. We decided to chose a wavelength of 808 nm, taking into account the availability of diodes and TAs in the mentioned wavelength range.

Apart from the trap depth and the heating rate, another important quantity for the lattice choice for the desired two species experiment is the tunneling time between neighboring sites and the heating rate of the lattice trap. The tunneling time τ ultimately limits the experimental sequence duration and is calculated through the parameter J , which describes the kinetic energy gain through the hopping between nearest neighbor sites [232]

$$\tau \approx \frac{\hbar}{4J} \approx \frac{\sqrt{\pi}}{16} \frac{\hbar}{E_R} \left(\frac{E_R}{U_{\text{sw}0}} \right)^{3/4} \exp \left[2\sqrt{\frac{U_{\text{sw}0}}{E_R}} \right] \quad \text{for} \quad U_{\text{sw}0} \gg E_R = \hbar^2 k_L^2 / 2m. \quad (\text{A.5})$$

The above approximation is only valid if the recoil energy E_R of an absorbed lattice photon is much smaller than the lattice potential height. In table A.2b we summarize the experimental quantities for a lattice of 808 nm with a power of $P = 250 \text{ mW}$ focused on a waist size of $w_0 = 100 \mu\text{m}$.

¹We follow here the conventions taken in sec. 4.3.1, where $U_0 < 0$ for attractive, red detuned dipole traps. Hence, the frequencies are well defined positive quantities.



(a) Trap depth and heating rate

	808 nm	⁶ Li	⁴⁰ K
Depth U_{sw0}		6.8 μ K	41 μ K
Heating rate \dot{T}		0.04 μ K/s	0.14 μ K/s
Radial ω_r		3.1 kHz	2.9 kHz
Axial ω_z		1670 kHz	1600 kHz
Tunneling time		5 μ s	100 s

(b) Lattice at 808 nm

Figure A.2: Choosing the lattice wavelength: (a) Lattice trap depth U_{sw0} (in μ K) and heating rate \dot{T} (in μ K/s) as a function of the lattice wavelength λ_L . In (b) we calculate the characteristic quantities for a lattice choice of $\lambda_L = 808$ nm and a total beam power of $P = 250$ mW, focused on a waist of $w_0 = 100$ μ m.

A.2 An Example of a MOPA System

The entire MOPA setup for the 2D-lattice laser is depicted in fig. A.3. The master oscillator is represented by a self-injected single-mode diode (*Thorlabs M9-808-0150*, total output power 150 mW at 808 nm) together with a grating (*Thorlabs GH13-18U*) in Littrow configuration, which builds up an external cavity. This narrows the linewidth and allows for a (not yet implemented) locking scheme through driving the grating with an piezoelectric actuator [233]. We implemented a compact wavelength meter (*Thorlabs CCS175/M*) and a scanning Fabry-Perot interferometer (*Thorlabs SA200-5B*) in the setup to monitor the wavelength position and stability. The signal of the two devices can be used further to stabilize the wavelength through the diode current or the grating. At the moment we are using a laser line filter (*Semrock LL01-808-12.5*) in front of the fiber output. A possible frequency drift in the MHz-range is less crucial, due to the far detuning of the laser compared to the D_1 and D_2 transition lines of ^{40}K and ^6Li .

The tapered amplifier (TA, model *EYP-TPA-080-0100-4006-CMT04-0000* fabricated by Eagleyard photonics) serves as the power amplifier of the system. The initial diode output power of max. 30 mW (in the self-injection-grating application) can be amplified up to 1 W. The temperature and power characteristics of the used TA chip model are depicted in fig. A.4. The output of the TA and the diode are protected by optical isolators (*Thorlabs IOT-5-780-VLP* and *Isowave I-80-SD-5M*) against high power back reflections, which would damage the chips and decrease their lifetime and stability. A $\lambda/2$ -wave plate in front of the TA allows to adjust the polarization of the seed beam, since the TA possesses a preferred polarization axis for amplification. We do not implement additional beam shaping through lenses for the seed beam and focus the collimated beam on the TA input-aperture through a 4.51 mm lens, the same focal length which is used for previously collimating the diode output. The output lens L_4 in conjunction with the cylindrical lens L_5 collimates the amplified output beam of the TA, which by design has two differently fast diverging axis. The additional telescope consisting of L_5 and

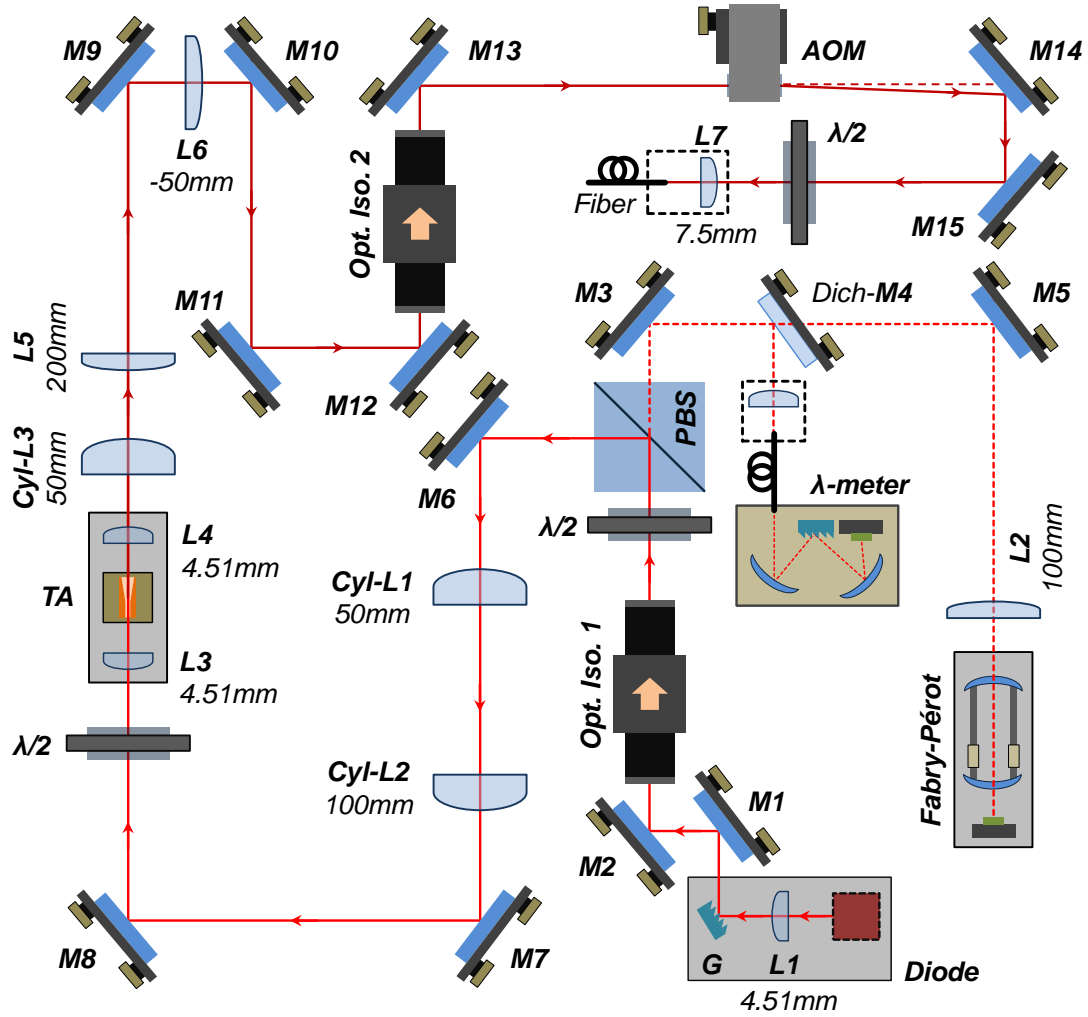


Figure A.3: Optical setup of the 808 nm MOPA laser system: The light of the diode is amplified by the TA chip. Later on, the light is sent through a single-mode polarization maintaining fiber to the science cell, where it is focused on the atomic cloud and retro-reflected to create the previously described 2D-lattice system. See text for further description of the MOPA setup.

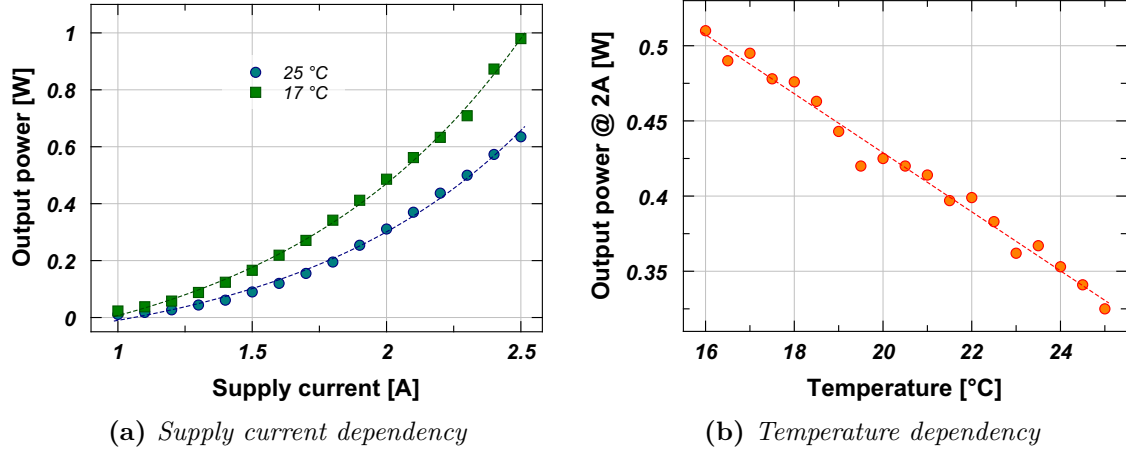


Figure A.4: TA performance for variable currents and chip temperature, recorded for the TA chip EYP-TPA-080-0100-4006-CMT04-0000 of Eagleyard photonics. (a) Output power of the TA for variable supply current at two different temperatures. (b) Output power for fixed supply current of 2 A as a function of chip temperature. The seed power was fixed for all measurements at 25 mW.

$L6$ decreases further the beam size for an optimal fiber coupling.

Finally, an AOM (*IntraAction ATM-1101A2* – 110 MHz) allows for switching of the light beam (and a possible intensity stabilization) before it is coupled into a fiber and send to the optical table around the science cell.

The optical setup near the science cell is planned for a self-interfering retro-reflected beam with a waist of 100 μm at the location of the atomic cloud.

Notes on AOM Drivers

In all cold atom experiments AOMs are used to either vary the light frequency and intensity or simply for fast switching of light beams. Apart from the fast switching, all mentioned operations are ruled out through the driver, which is basically the RF-source for the AOM-crystal. Figure B.1a shows a scheme of an AOM-driver. It consists of a voltage controlled oscillator *VCO* and a voltage variable attenuator *VVA*. Previously, we used in our experiment the bare components *POS-200* (100 MHz to 200 MHz VCO) and *PAS-2* (Attenuator/Switch) of *Mini-Circuits*. The PAS-attenuator is current-controlled and thus can not be directly operated by the analog voltage control-channels of our experiment. An additional circuit including an operational amplifier is advisable. Also the POS VCO-component needs sufficient screening: Two POS operated in the same enclosure pick up each others RF-output. The main difficulty is the pin-package, which needs to be soldered to a custom printed circuit board, which in turn need to be designed in a way to reduce power losses.

An easier implementation can be done by using the screened Mini-circuit models *ZX95-310A* for the VCO and *ZX73-2500* for the VVA. These models are slightly more expensive¹ but offer directly a SMA connection. Only the control and supply voltage leads need to be soldered to the components. The frequency-voltage dependence of the *ZX95-310A* VCO can be well approximated by one, or even more precisely by two linear functions. By contrast, the attenuator *ZX73-2500* shows a highly non linear behavior towards higher attenuation (see figure. B.1b). The full function can be programmed in the experimental controlling system, but since the complete off-switching is accomplished by an additional switch (*ZAS-1* of Mini-Circuits) placed before the amplifier, higher attenuation than -10 dBm is not required. Hence we can limit in our application the operation to the linear regime in fig. B.1b. Nevertheless, the additional switch can be omitted by introducing for instance a multiplexer before the control-channel of the VVA: At a high-TTL signal it would connect the voltage control of the VVA to zero, thus asking the maximal attenuation of ~ 47 dBm. Otherwise, (for a low-TTL signal,) the multiplexer would forward the usual analog-control voltage, which will operate as previously on the linear regime of the VVA. This solution requires some additional electronics, but avoids RF-power losses on the *ZAS-1* switch.

Finally, in order to optimize the light power distribution between the different orders of refraction in the AOM crystal, we mount the AOM on a tilt mount (*KM100PM/M* of Thorlabs)

¹The ZX95-310A and ZX73-2500 cost about 50€ each. It is more expensive than the POS-VCO (15€) but comparable to the attenuator PAS, which is about the same price.

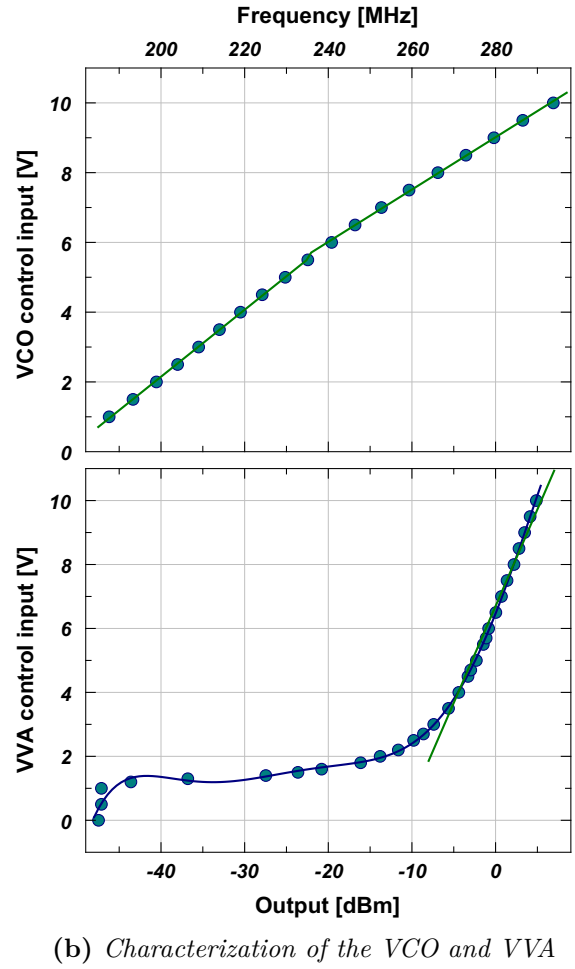
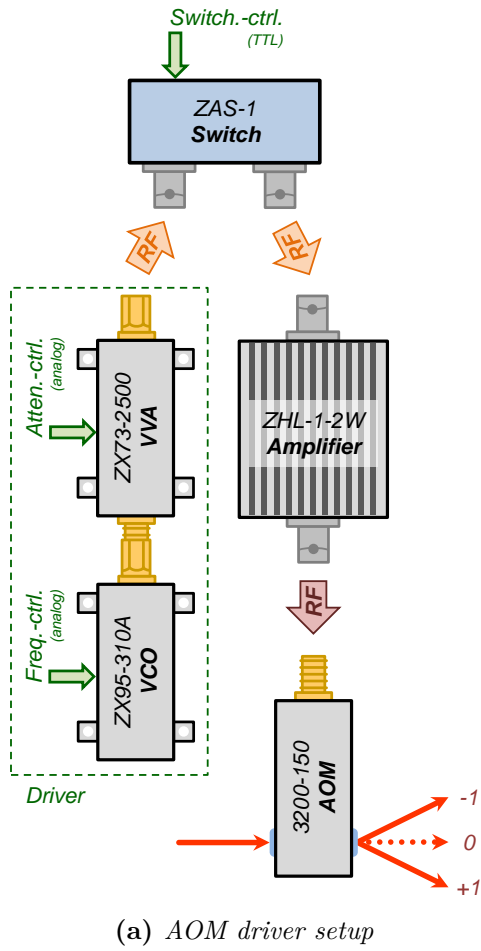


Figure B.1: AOM driver setup and VCO / VVA characterization. The graphs are inverted, since on the computer-control-side we are interested in the voltage which needs to be applied to receive the desired output power.

to adjust precisely the incident angle of the beam. To mount the standard AOMs of *Crystal Technology* on the Thorlabs tilt-mount, we use a self made adapter plates (see fig. B.2).

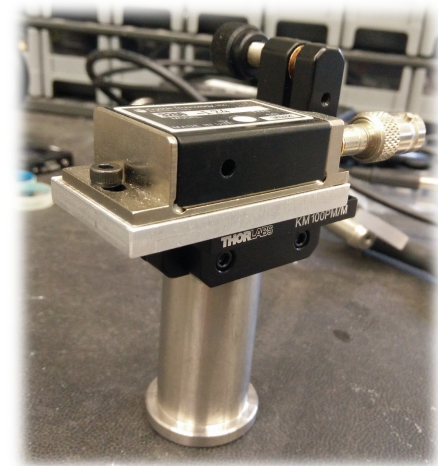
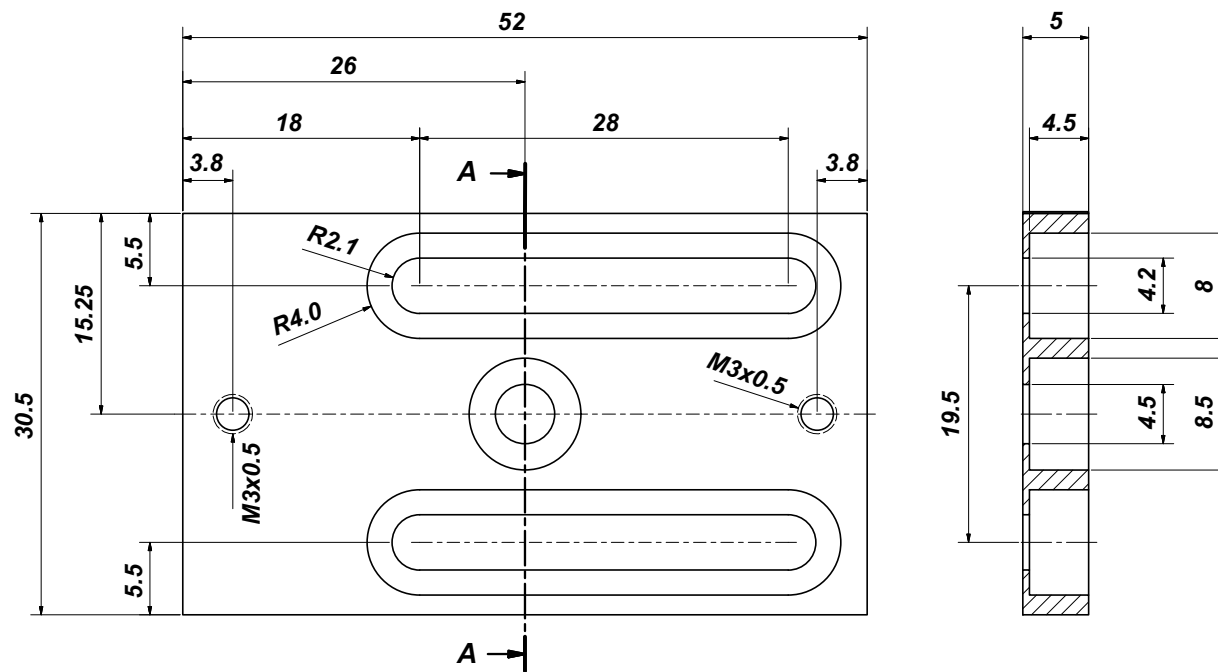


Figure B.2: Adapter for mounting Crystal Technology AOMs (like the depicted 200 MHz-model, AOMO 3200-124) to the kinematic prism mount KM100PM/M of Thorlabs.

New TA Support Design

In this appendix section a new design for a support of a *C-mount* type tapered amplifier (TA) is presented. TA's are widely used to increase the total light power in a given wavelength range. Therefore a low-power seed beam (15 mW–30 mW) is injected into the TA chip and amplified up to 0.5 W–3 W, depending on the TA model, the injected wavelength and the current applied to the chip.

The C-mount TA chip design, fabricated by *eagleyard photonics*, is depicted in fig. C.1. For amplifying the ^{40}K cooling light at 767 nm we use the particular model *EYP-TPA-0765-01500-3006-CMT03-0000*, which dimensions are depicted in the previously mentioned figure. Apart from the mechanical support of the chip itself, the mounting need to provide some space for the electrical wiring options including the necessary connectors and a temperature stabilization of the chip through a thermoelectric cooler (TEC or Peltier-element). The most challenging part of the design is the implementation of collimating lenses nearby the in- and output of the TA: We use lenses of the focal length $f = 4.51$ mm (*Thorlabs C230TMD-B*) to focus the seed beam on the input aperture (3 μm wide) of the chip and to collimate the fast diverging output beam. The precise positioning of the lenses is crucial for the optimal seeding of the chip on one side, in order to inject all the seed power as well as for the collimating of the output beam on the other side, in order to realize an optimal beam shaping for an injection into an optical single-mode fiber later on.

By the notion of a "new" design, we refer to the TA support realized earlier in our group (see

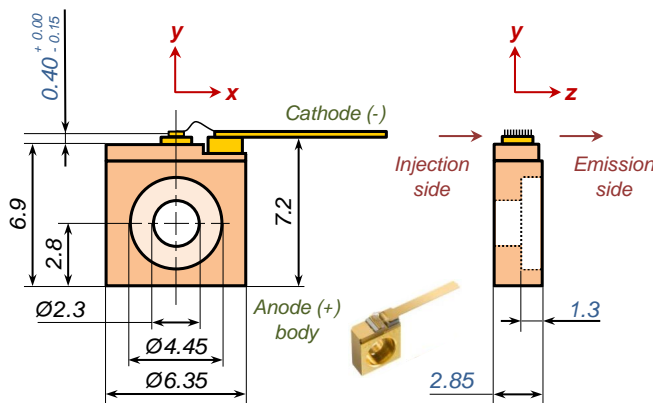


Figure C.1

Dimensions and design of C-mount TA chip as fabricated by eagleyard photonics. The dimensions are taken from the particular model EYP-TPA-0765-01500-3006-CMT03-0000. TA chips, which are designed for different output-power or wavelength may vary in the dimensions noted in blue. For more information see [234].

[108]) which, in a similar but slightly elaborated form, is presented in [235]. In both cases an optimal positioning of the lenses presents few difficulties: In our home-made design the lenses, which are mounted in a aluminum cylinder, are simply clamped in metallic parts and fixed by a screw. Hence, after collimation the lenses move significantly during the fixing process and therefore the optimal collimation position gets lost. In [235] a precise machining of the parts and a thread positioning system avoids this issues. However, apart from the requirement of precise machining of the parts, the system is also lacking in a full range xy -positioning of the lenses, in order to align the chip center and the lenses concentrically.

Presentation of the new design

The new design of the TA support, including all technical drawings, which are realized by the departments engineer Arnaud Leclercq (apart from the Thorlabs parts), are presented on the following pages. For the precise positioning of the lenses we use the following Thorlabs parts (fig. C.2):

- For the z -alignment we implement the translation stage **DT12/M**. The stage has a travel range of 12.7 mm.
- To fix the translation stage accordingly, we use few parts sold in combination with the base plate **DT12B/M**. The intended parts are the two mounting-cleats for a part fixing by M3 screws.
- For the xy -concentric alignment of the lenses and the TA chip we utilize the translation precision lens-mount **LM05XY/M**. It permits a fine adjustment of ± 1 mm.
- We use the adapter **S05TM09** in order to install the used lens (**C230TMD-B**) in the previously mentioned xy -translation mount.

All parts together with the lens cost about 300€ and need to be bought twice (for the input- and output side). The mounting-cleats, mentioned at the second bullet-point above, are included in the first version of the design, but seem not to be necessary for the fixing of the z -translation stage, due to the large travel range and the additional M4 thread at the bottom of the stage.

The mounted assembly of the two stages by an adapter plate is depicted in fig. C.3. It is mounted to the left and right side walls of the TA mount (see fig. C.9 or fig. C.11). It should be noted, that the mounting of the lens inside the xy -translation stage should be done in such a way, that the flat surface of the plan-convex lens can be brought as close as possible to the TA ship on both sides. If necessary we use additional 0.5"-lens tubes of Thorlabs (see fig. C.11 C and E).

The main part of the design is the base unit (fig. C.4–fig. C.6). The massive block acquires the heat from the TA chip through a Peltier-element. A water cycle with three connectors (**1/8" NPT 27** connectors) is provided in order to avoid the heating of the optical table around the mount. Thereby it is recommended to turn the two water connectors to the injection side of the complete installation. In that way the water connections are not hindering the installation of an additional collimation lens on the output side beyond the TA mount. This will be anyway necessary to further collimate the fast diverging output beam. The mount provides recesses for two BNC-connectors and two D-Sub-15 (*DA-15*), symmetrically arranged by the sides of the mount. The base unit was machined in our workshop using duralumin as material.

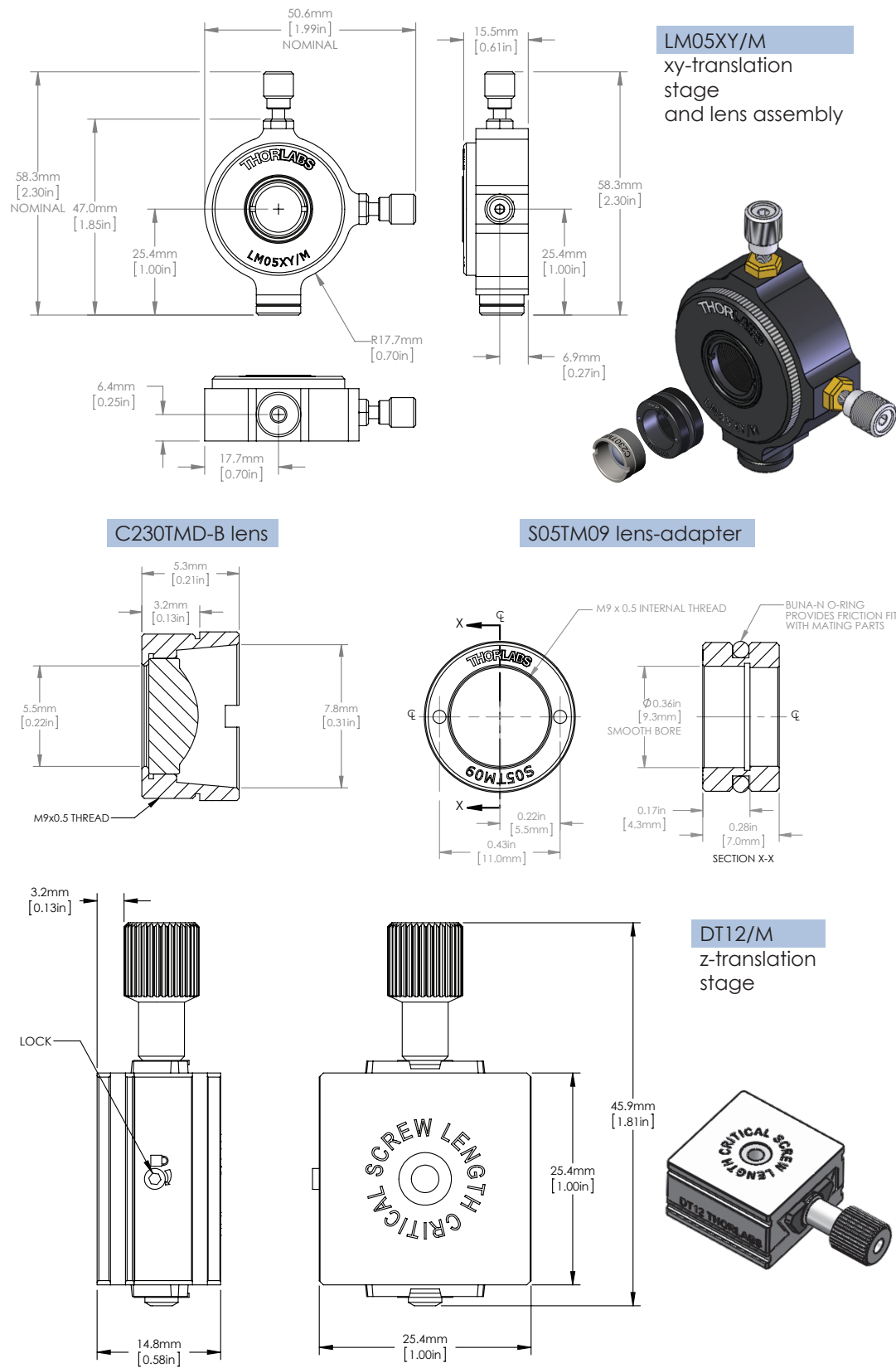


Figure C.2: Dimensions and technical drawings of the included Thorlabs parts used in the proposed TA setup. Images and drawings are taken from www.thorlabs.com.

The chip is mounted on a two-part holder, consisting of a small base (fig. C.7) and the actual TA chip holder (fig. C.8). Both pieces are aligned by means of two metal pins (embedded drawing in fig. C.7) and three M3 screws. Heat conducting compound (thermal paste) should be applied between the two parts to assure a sufficient thermal transfer. Both parts are machined using brass as material for optimal heat transfer from the TA chip.

The base plate is mounted on the previously mentioned base unit by six M4-screws, thereby clamping the Peltier-element between the two parts (the green marked surface recess in fig. C.4 allows for the placement of 40 mm \times 40 mm TEC elements). We use the TEC model *TEC1-12705T125* of Roithner Lasertechnik GmbH with total cooling power of 52 W at maximal 5 A. The complete TA holder serves as anode (positive pole) of the TA chip. Plastic screws should be used to fix the TA holder base-plate (fig. C.7) to the base unit (fig. C.4) in case an isolation to the base unit and the optical table is desired.

Concerning the electric wiring of the chip, the anode (+) is directly connected through the body to the chip holder. Therefore the anode is connected by attaching a cable through a lug / crimp terminal to one of the two side screws (M3) of the chip holder in fig. C.8. We solder directly a cable to the cathode (-). It is recommended to realize the connection from the chip to the external connector in "two steps" by two distinct cables (see fig. C.11 D) in order to avoid stress to the chip cathode during the mounting of the connector. Therefore an isolation piece (made from plastic – see embedded CAD in fig. C.5) is screwed (by a plastic M3-screw) in the base unit and presents an isolated area to connect two terminals. We use drivers from Newport (*500B* series) to provide a regulated current to the TA chip.

The temperature of the chip is measured either through a NTC thermistor (e.g. *B57861S* series of EPCOS) placed inside the 2.5 mm side hole in the chip holder in fig. C.8 or by clamping an isolated thermistor (e.g. *B57703M* series of EPCOS) under one of the M3 side screws of the same part (similar to the anode connection). The part in fig. C.8 has large 2 mm left and right cutouts on the sides to place M3-lugs. We use temperature controllers from Thorlabs (*TED350* or the smaller model *TED200C*) to stabilize the temperature through the TEC element.

At the moment of preparation of the present manuscript, the new TA support is tested for its long-time stability in our experiment.

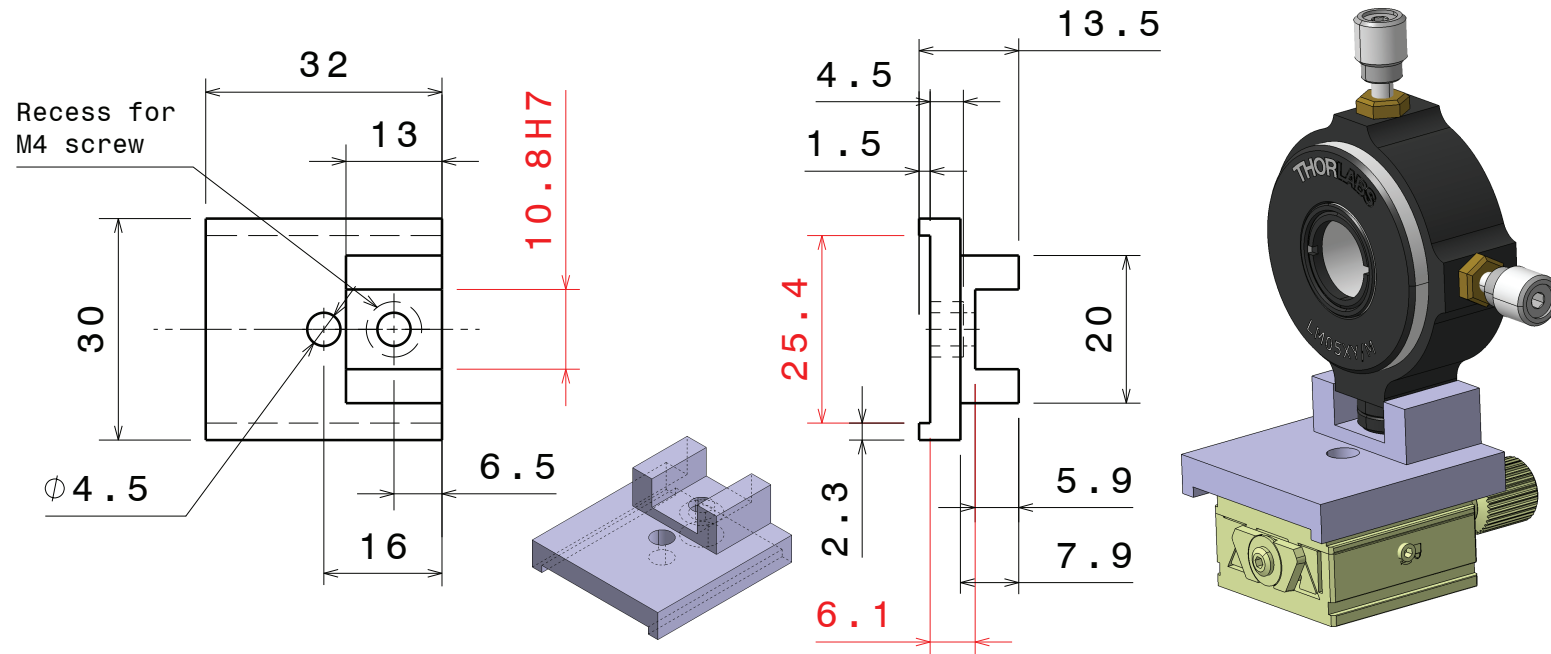


Figure C.3: Technical drawing of the DT12/M – LM05XY/M adapter. The LM05XY/M translation stage is connected through the designed piece with the z-translation stage DT12/M by two M4 screws. The assembly allows later on the precise translation of the mounted lens along all three degrees of freedom. The depicted setup is mounted on the side panel in fig. C.9. (Material: Duralumin)

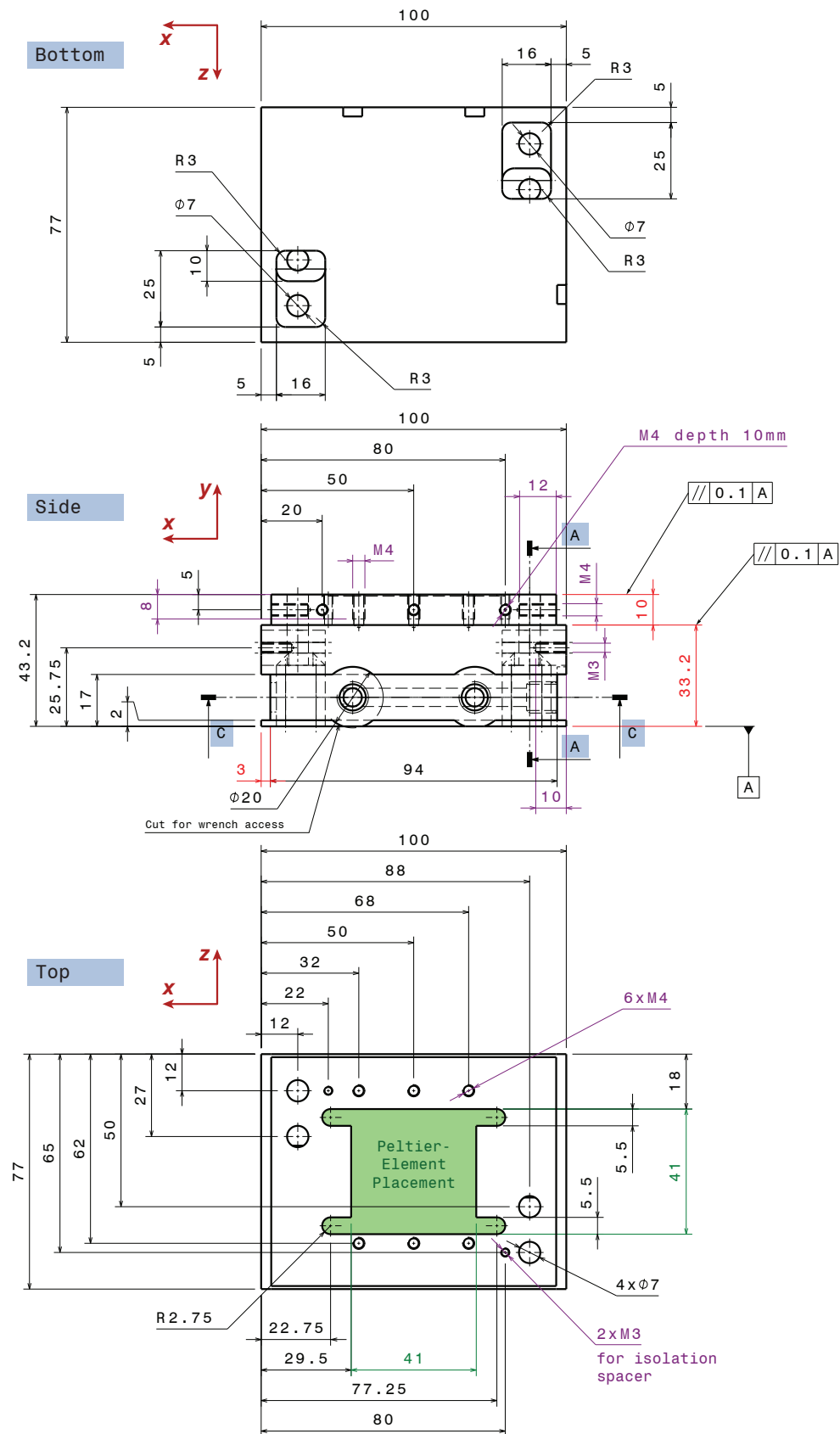


Figure C.4: TA support: base unit CAD part 1/3 – main views. (Material: Duralumin)

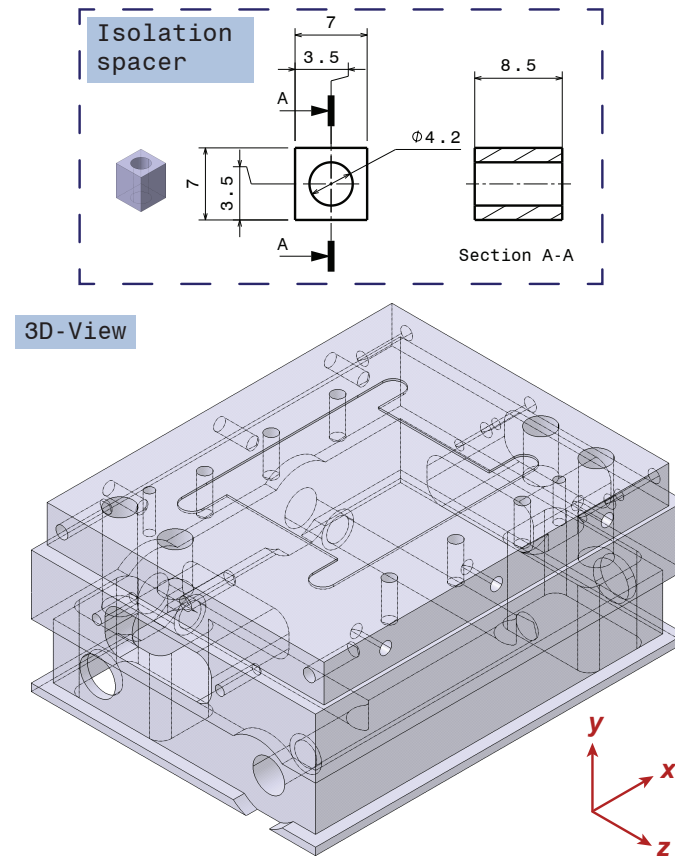
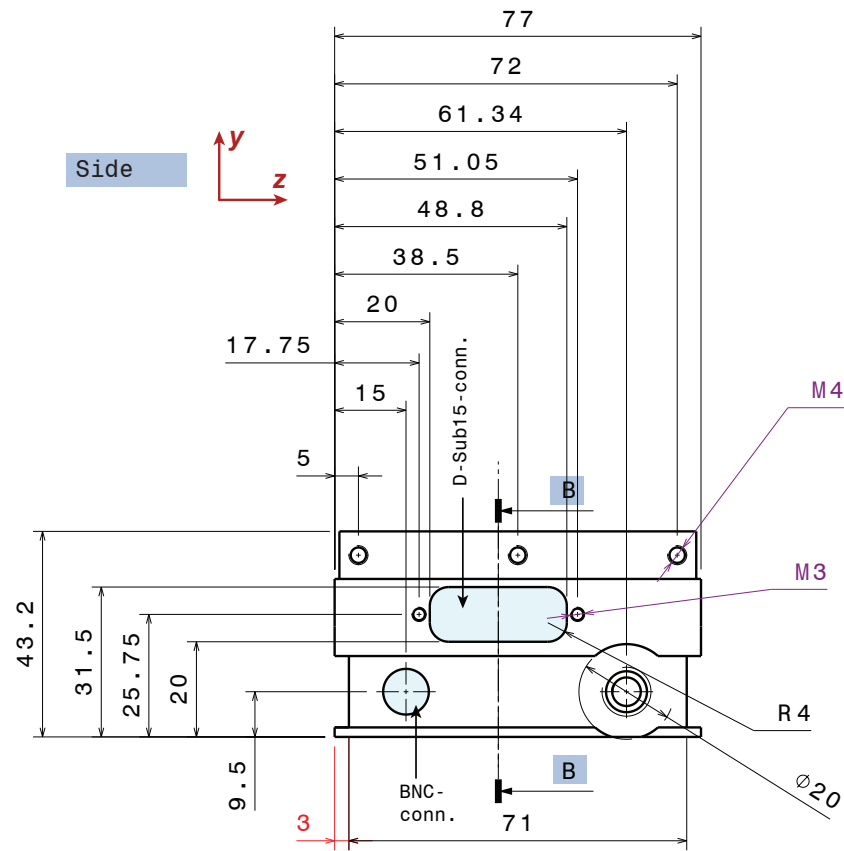


Figure C.5: TA support: base unit CAD part 2/3 – side view and 3D-model. The embedded CAD shows the isolation spacer, made from plastic.

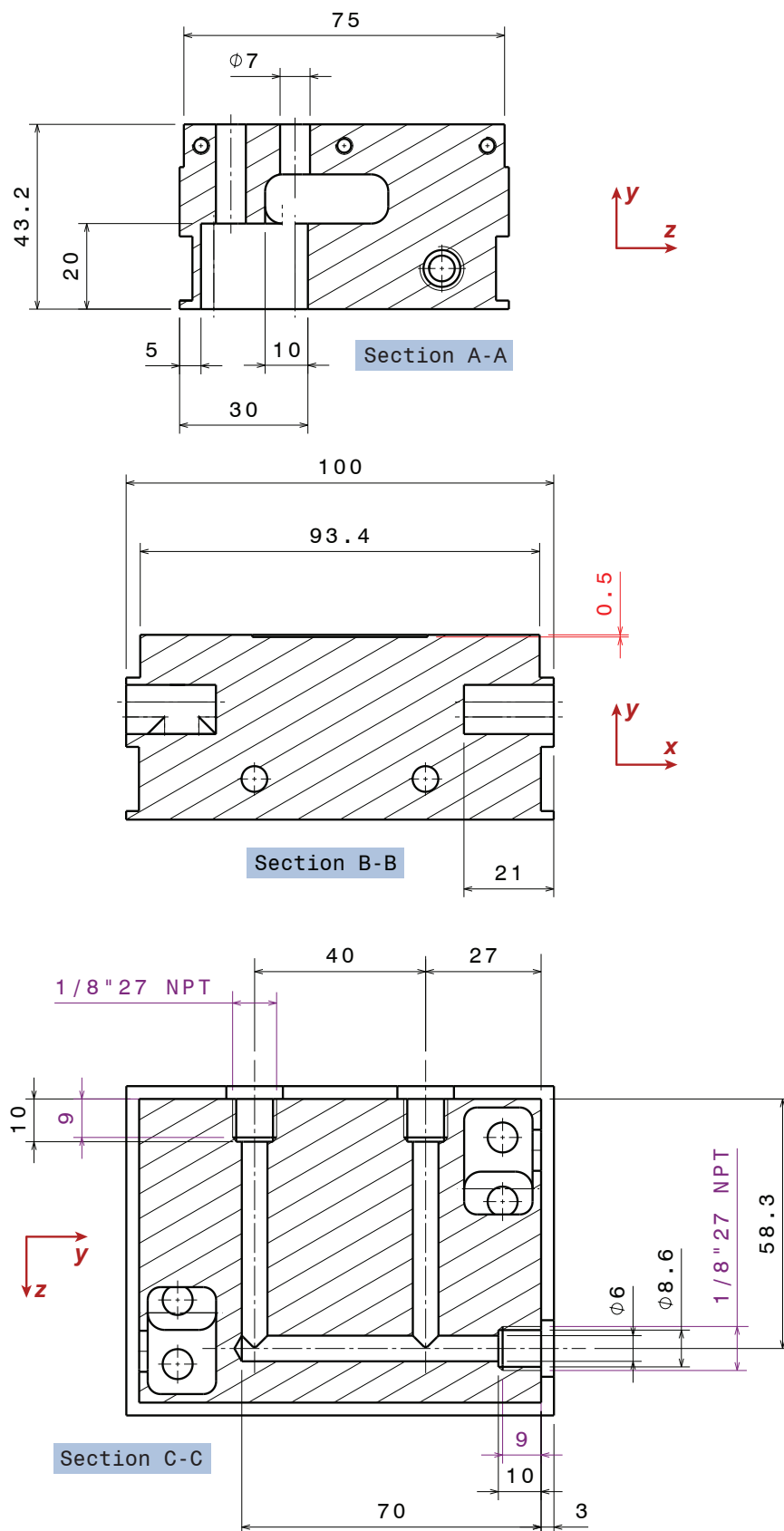


Figure C.6: TA support: base unit CAD part 3/3 – sections marked in the previous drawings in fig C.4 and fig. C.5.

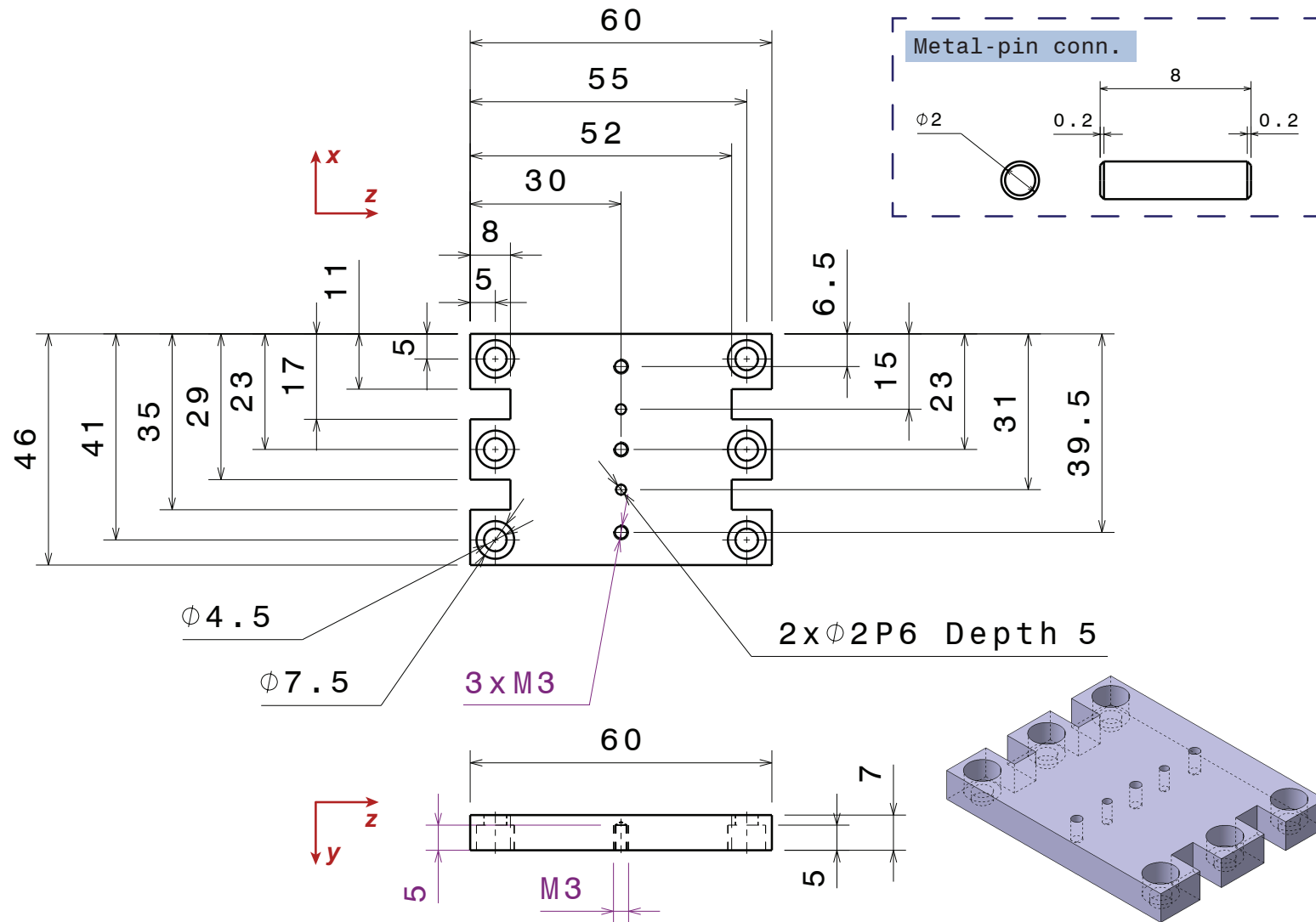


Figure C.7: TA support: chip holder base plate CAD. (Material: Brass)

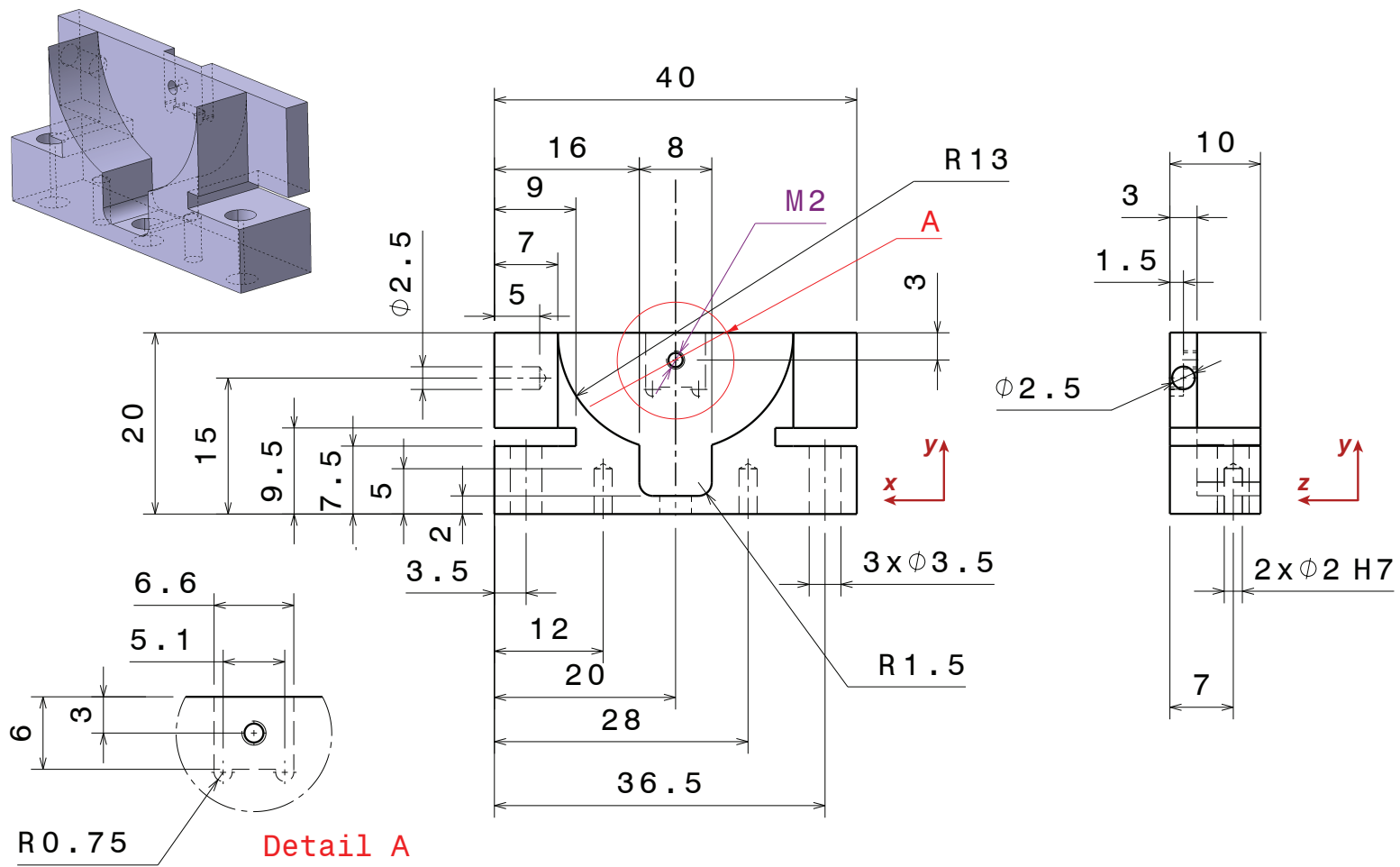


Figure C.8: *TA support: chip holder CAD. (Material: Brass)*

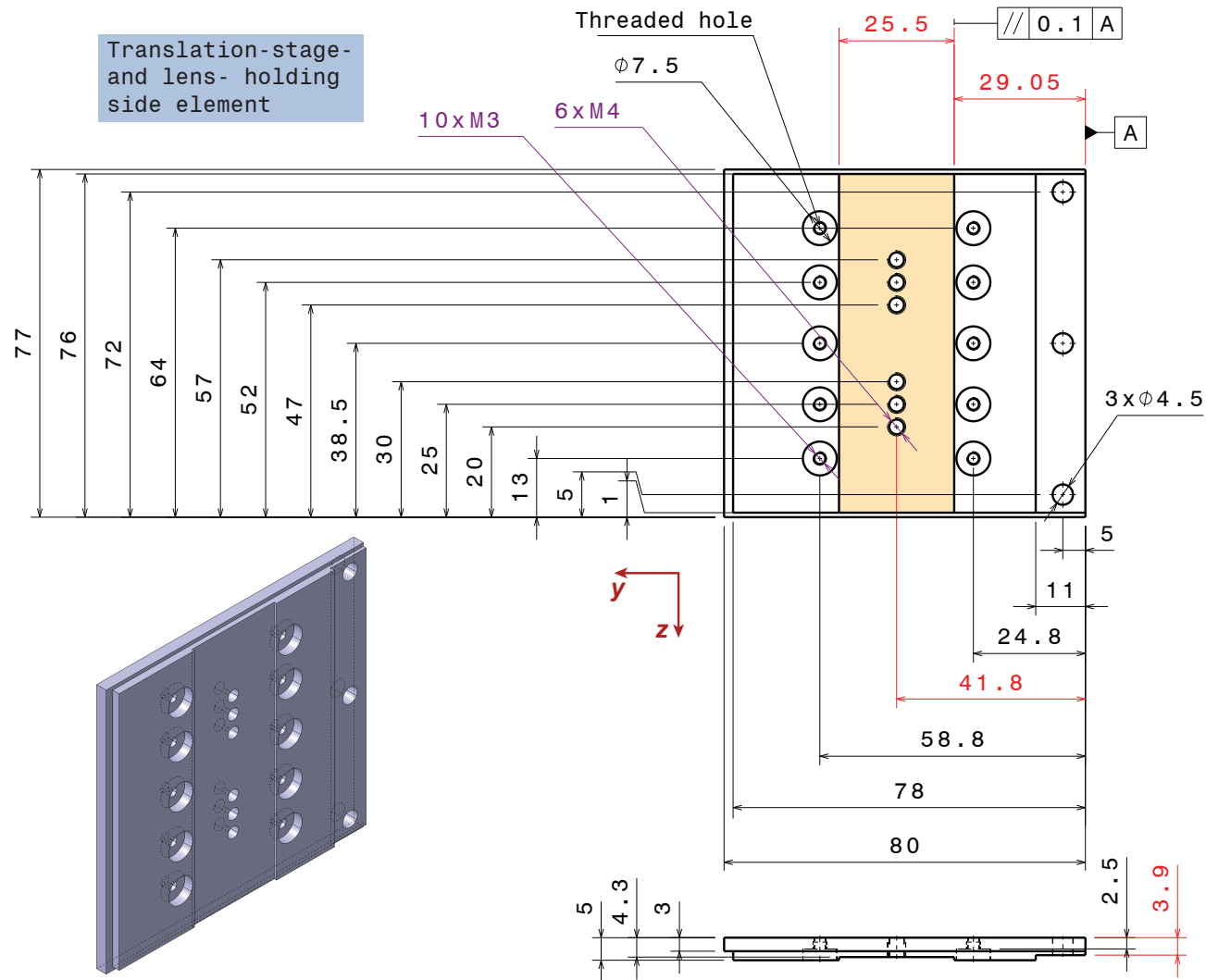


Figure C.9: TA support: Translation stage supporting side element. The lens translation stage assembly from fig. C.3 can be fixed through the DT12/M at various positions in the marked area. (Material: Duralumin)

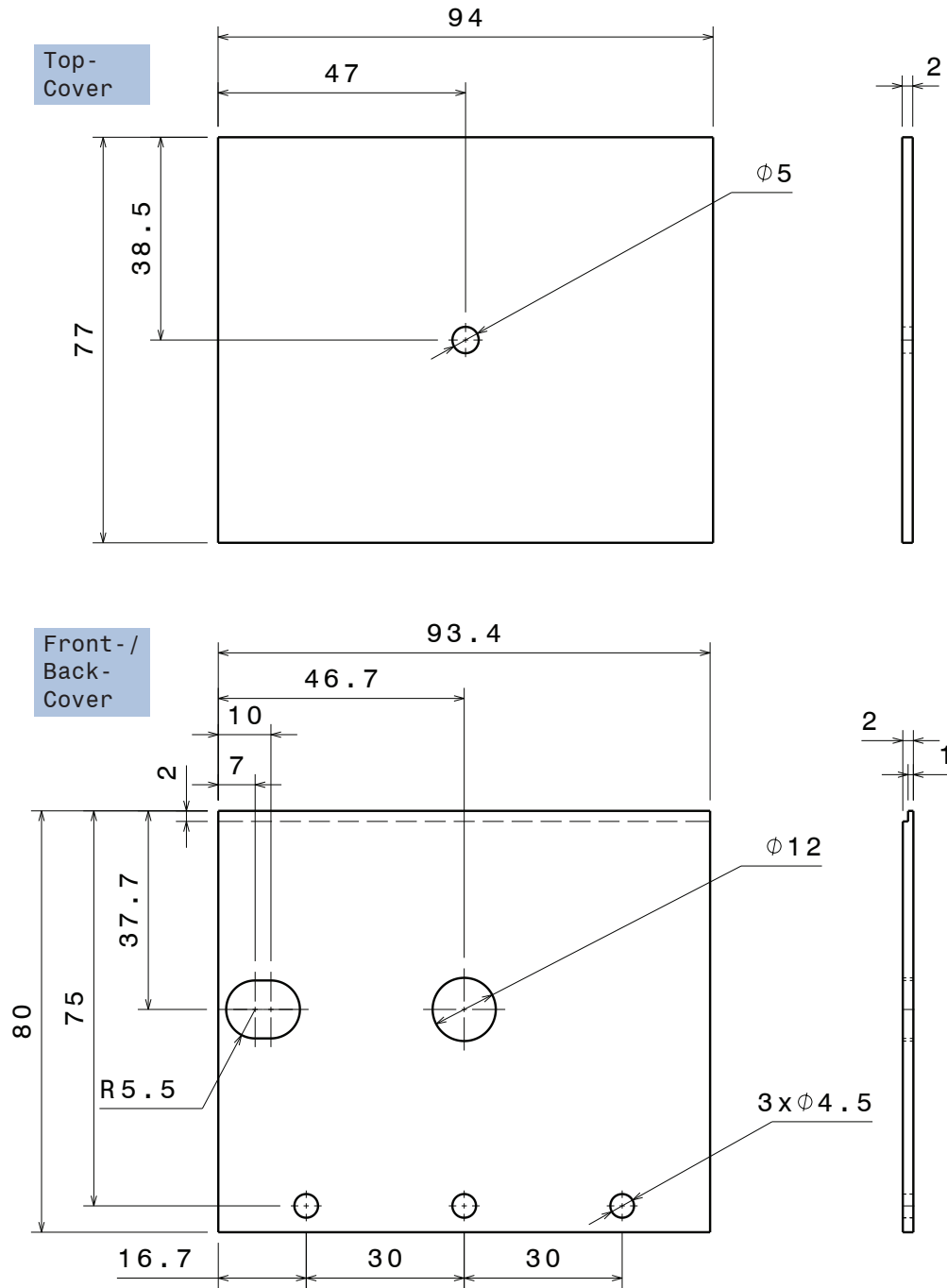


Figure C.10: TA support: front / back and top cover. (Material: Duralumin)

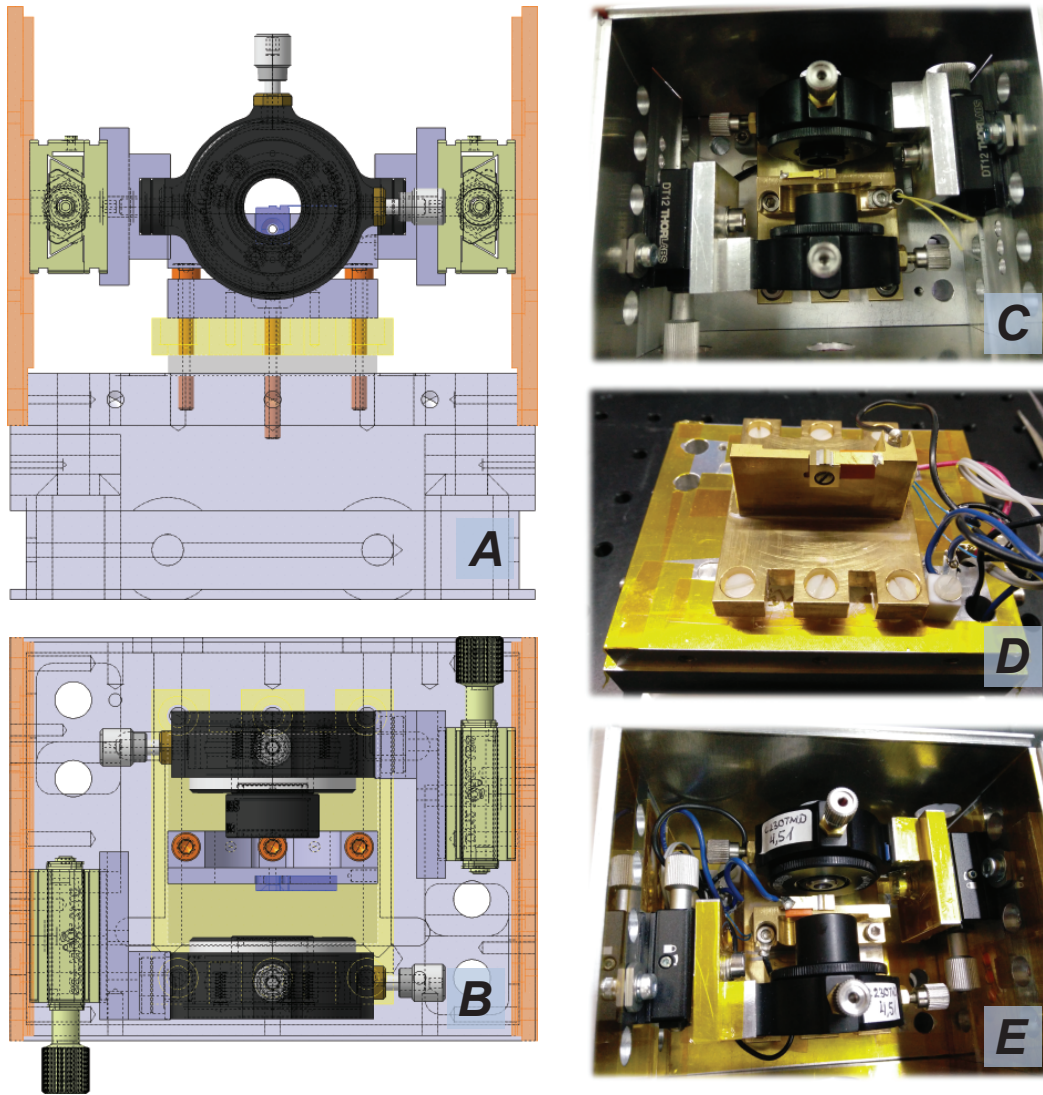


Figure C.11: *TA support: complete assembly. A and B show CAD assembly design, while C–E depict photos of the TA support at different setup stages.*

Optocoupling of Signals

Optocoupling (or opto-isolation) is a well known technique to galvanically isolate two communicating circuits. A high/low signal or even analog-signals can be transferred by means of a LED and a photo-diode (or photo-transistor).

On the consideration side, an optocoupler is similar to a relay (mechanical or solid-state) with the major improvements in switching times (tens of ns compared to few ms), the switching-power consumption (the LED in an optocoupler needs only few mA and less than 2 V to switch, compared to up to 50 mA for a similar voltage for relays) and higher duty cycles. Analog signal-transfer is not possible at all with mechanical relays. However, different to relays a common optocoupler can not switch directly high-voltage or high-current circuits. An additional wiring in this cases is necessary (usually using an additional external power source and a transistor operated in saturation).

Summing up the advantages and applications, optocouplers should be used to:

- Protect low-current / voltage (controlling) signals from high-current / voltage sources.
- Avoid ground loops for unconnected (not linked) devices, especially in the case of electrically noticeable mismatch in signal distances. In this case we avoid leakage current, which could damage the controlling electronics.
- Provide a stage for level-shifting of the controlling signals.

The only cases where optocoupler usage should be reconsidered, is if the required switching time is below the specifications of the optocoupling device and, in case of the analog circuit (see sec. D.2), if the introduced signal error is intolerable by the requested application.

D.1 TTL Signal Optocoupling

Figure D.1 shows the basic wiring of a TTL-logic optocoupler, which consist of a LED and a phototransistor. The usage of two different 5 V power sources, V_{CC1} and V_{CC2} , as well as two galvanically decoupled grounds (zero-reference potentials), $GND1$ and $GND2$, are indispensable. The first ground is marked as real *earth*, since in most applications the input side is connected to the main operating computer or FPGA, which controls the entire experiment. These devices in turn relate their zero-references to the mains-ground. Two galvanically decoupled power

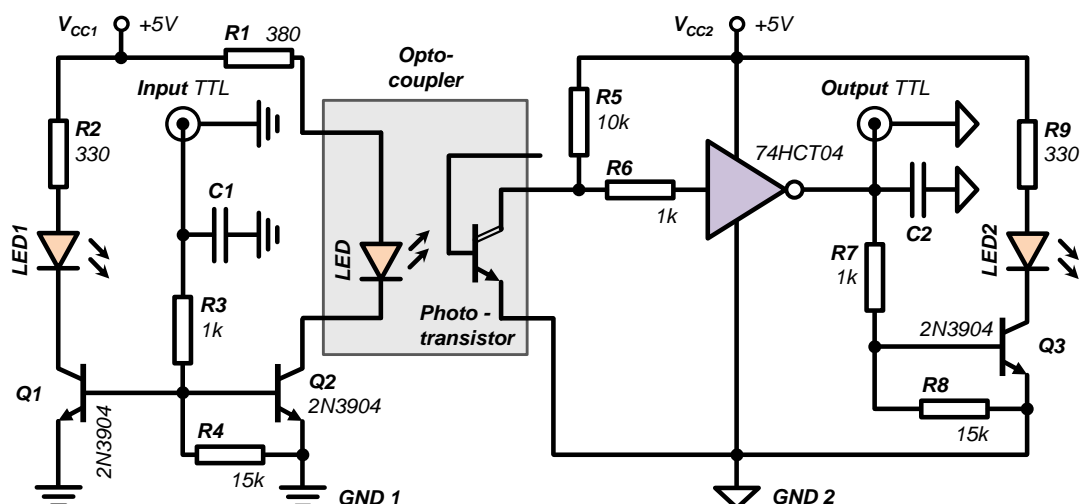


Figure D.1: Basic TTL optocoupling circuit, which can be used for example to wire the optocoupler models 6N137 or 4N25. (For different models the current limiting resistance $R1$ might need to be adapted.) LED1 and LED2 are used for monitoring high-level signals on the in- and output. The capacitors $C1$ and $C2$ are used to smooth out the signals and to avoid voltage overshoots. They also ultimately limit the switching time. Typical values range from 50 pF to 0.1 μ F.

supplies are easily obtained by using two separated step-down transformers to generate the necessary DC voltages from common AC mains. Of course the created DC 0-potential level should not be connected accidentally to earth.

The most preferred wiring solution in case of the application of a npn-like phototransistor within the optocoupler is the one with an inverted output (depicted in fig. D.1): Once a level-high (5 V) is applied to the *input*, the npn-transistor $Q2$ switches on the LED of the optocoupler. The signal is picked up by the phototransistor, which in turn switches the input of the hex-inverting buffer (74HCT04) from usually high (5 V) to low (0 V). Thus in turn, the inverted output of the optocoupler is again inverted by the buffer. The two external LEDs (LED1 and LED2) monitor the high-level of the signals at the input and output.

The switching time of the circuit is determined by the used optocoupler model and the smoothing capacitors at the input ($C1$) and output ($C2$). Typical values for the used average optocoupler models are ranging in between 50 pF and 0.1 μ F for the present circuit. This allows switching times up to 10 kHz, which corresponds to a maximally distinguished delay of 0.1 ms in between two consecutive TTL pulses.

Figure D.2 shows a faster optocoupling implementation by using the HCPL-2201 model. Actually, the delay time Δt_1 of the optocoupler reacting on the applied square signal (rising slope) already defines the maximum signal switching speed¹ allowed by the optocoupler. Figure D.3 illustrates the reaction dynamics of the faster HCPL-2201 optocoupling circuit. The delay time is $\Delta t_1 \approx 130$ ns on the rising slope and $\Delta t_2 \approx 180$ ns on the falling one. Hence, taking the larger delay, the maximum switching speed is about 5.5 MHz. The circuit from fig. D.2 showed even at 6 MHz a suitable response signal.

The use of hex-(inverted) buffers at the input side of the circuit poses the advantage to switch

¹The smallest time interval in between two consecutive TTL high-levels on the input, which are still distinguished by the optocoupler on the output, defines the switching speed.

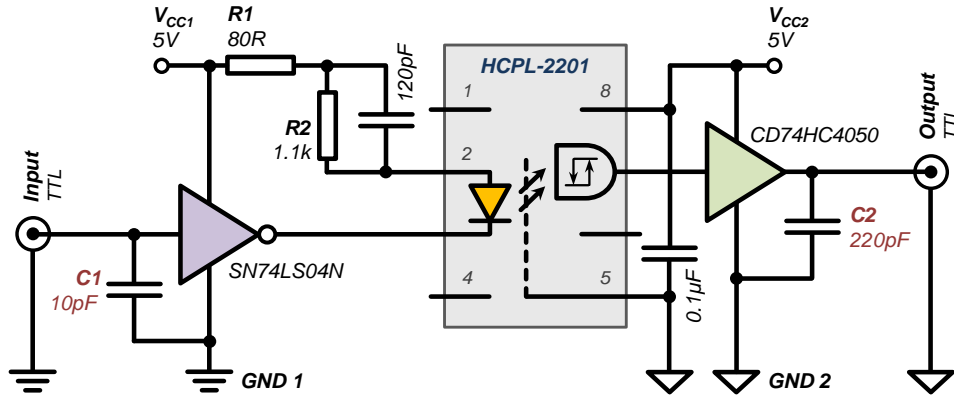


Figure D.2: Optocoupling circuit using HCPL-2201 (adapted from the datasheet [236]). The only modification are the capacities $C1$ and $C2$, which are used to smooth out voltage peaks on the input side and to avoid as much as possible voltage overshoots on the output. The marked values are found to be the optimal compromise for a switching speed up to 6 MHz. The involved buffers allow for automatic level-shifting from 3.3 V TTL-logic to 5 V on the output.

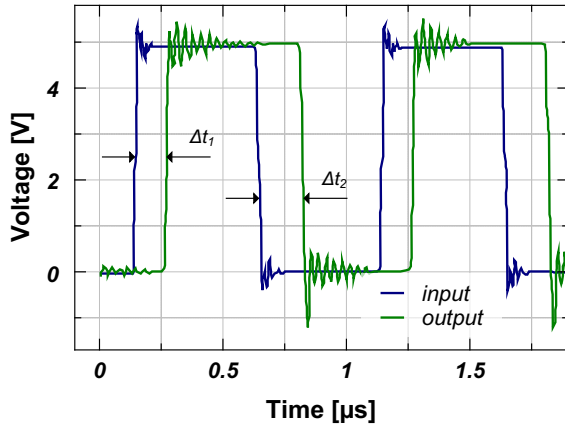


Figure D.3

Response of the HCPL-2201 circuit from fig. D.2 on a TTL input signal at 1 MHz speed. The blue line is the input signal from a frequency generator, while the green signal is the output of the optocoupler. The response delays are $\Delta t_1 \approx 130$ ns and $\Delta t_2 \approx 180$ ns for the rising and falling slope respectively.

from 3.3 V TTL-logic level to 5 V at the output without additional wiring.

A faster optocoupling is possible with the HCPL-7721 model. The realized circuit in fig. D.4 is according to [237]. Once again, only the capacitors $C1$ and $C2$ were added at the input and output. Their values are optimized to still allow a propagation velocity of 7.5 MHz, thereby minimizing voltage spikes and oscillations at the in- and output signals. Unfortunately, the promised delay time of only 40 ns and thus a possible speed of 25 MHz was not observed with the circuit in fig. D.4. It is possible that a basic wiring, as suggested in the datasheet [238] generates the promised delay time. However, this simplified realization showed in our setup high voltage overshoots at the in- and output.

All previously presented solutions are made for the optocoupling of a 5 V signal, providing the same output voltage level. For application with a higher voltage level at the output, a switching stage in form of a transistor and an additional higher voltage source might be used. However, some optocoupler models provide the possibility to directly handle or switch higher voltages on the output side. We will discuss one simple realization used in our experiment to switch insulated-gate bipolar transistors (IGBT).

The IGBT operation requires a 15 V for switching-on and a negative voltage (−12 V to −15 V) to compensate for switching losses due to the Miller-effect which appears as an emerging

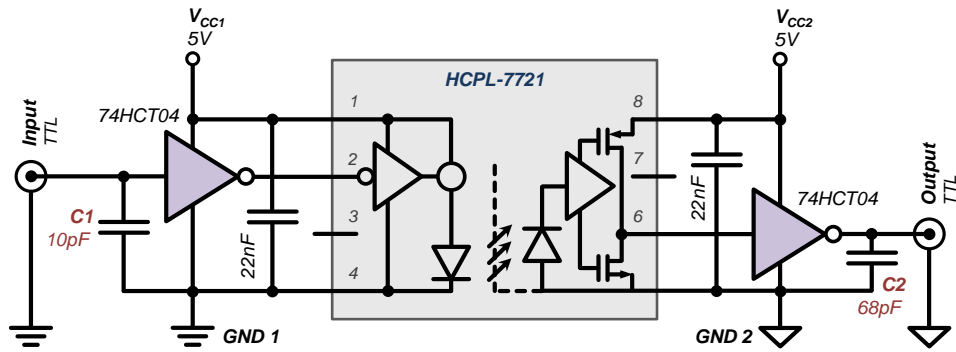


Figure D.4: Optocoupling circuit using the faster optocoupler HCPL-7721 (adapted from [237]). The only modification are the capacities $C1$ and $C2$, which avoid voltage peaks and oscillations at the in- and output. The maximally achieved switching speed is 7.5 MHz.

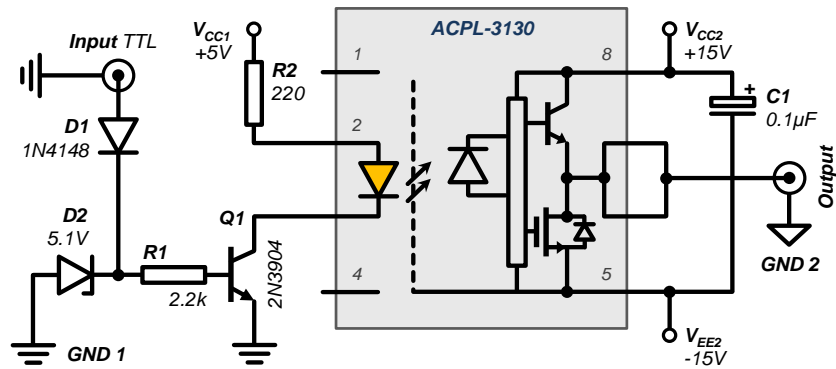


Figure D.5: Optocoupling circuit using the optocoupler ACPL-3130 to drive an IGBT-gate, providing 15 V for on-switching and -15 V for off-switching at the output.

collector-base capacity in the IGBT [239]. The applied negative voltage discharges the gate of the IGBT and therefore maintains the switching dynamics. We use the *ACPL-3130* as optocoupler model, which is predestinated to operate IGBTs and therefore to switch between the positive and negative voltage levels at the output [240]. The photodiode inside the optocoupler operates a npn-transistor and a n-JFET (n-channel junction gate field-effect transistor). If no voltage is applied to the gate of the n-JFET, it is conducting. By contrary, the resistance increases by applying voltage to the gate, up until the n-JFET becomes an insulator. In this case no current passes through the drain-source connection. According to this pure switching application, the n-JFET is similar but inverse in its action to a npn-transistor. Now, the operation of the *ACPL-3130* optocoupler in fig. D.5 becomes clear: If there is no voltage induced on the PD (LED off) the npn-transistor is off, while the n-JFET is conducting. Hence, the output is pulled to -15 V . In the opposite case, when the LED is on and the PD-voltage is applied simultaneously to the gates of the n-JFET and the npn-transistor. The first isolates while the latter one conducts, thus pulling the output to 15 V . Again, both possible voltage-levels are with respect to the common ground *GND2*, which is isolated from the input side *GND1*.

D.2 Analog Signal Optocoupler

Analog signal optocoupling is slightly more complicated than the transmission of pure digital signals, which distinguish only high and low voltage levels. Additionally, there are less devices on the market which are providing an "out-of-the-box" analog signal transmission. The main technical reason for this mismatch in product range is the way analog signals are created by a computer (or micro-controller, FPGA, etc.) in first place: Usually a digital-to-analog converter (*DAC*) is implemented and therefore generally the preceding digital signal is optocoupled.

We will present here the analog optocoupling circuit based on the *HCNR200*, which allows for the transmission of signals over the range of 0 V to 10 V . Figure D.6 depicts the realized circuit suggested in [241]. The circuit operation is well described in the cited datasheet and will not be repeated here. In [241] it is indicated that the capacitors *C1* and *C2*, which are used to smooth voltage overshoots at the in- and output, are the main response speed limitations of the circuit. We reduced the recommended values of 47 pF and 33 pF to $C1 = C2 = 3.3\text{ pF}$ to allow for higher frequency signals. Furthermore we use faster operational amplifiers than the suggested model *LT1097*. The *OPA37GP* provides the necessary speed and precision over the complete range of 0 V to 10 V . With the mentioned modifications we reach excellent performances already around 20 kHz for a 0 V to 10 V square signal (see fig. D.7), which is double of the speed proposed in [242] for the original components in the discussed circuit. The maximum reachable speed with still adequate signal transmission over the complete 10 V -range is 94 kHz . Using a faster operational amplifier, like the *AD845* [243], we even reached (with slight signal distortions) 110 kHz .

In cases where not the entire range of 0 V to 10 V of an analog channel (e.g. the NI-card) is required, it can be scaled down without precision losses by the simple operational amplifier circuit presented in fig. D.8. It contains first an inverting part (*OP1*), which re-scales the input voltage by $-(R2 - R1) \cdot V_{\text{in}}$. A second part provides a constant 10 V -reference [244], which is further on split by a voltage divider (*R6*). The previously scaled voltage from *OP1* and the adjusted part of the voltage reference are summed on a second operational amplifier stage *OP2*. The complete re-scaling of the input voltage is therefore set by the two variable resistances *R1*

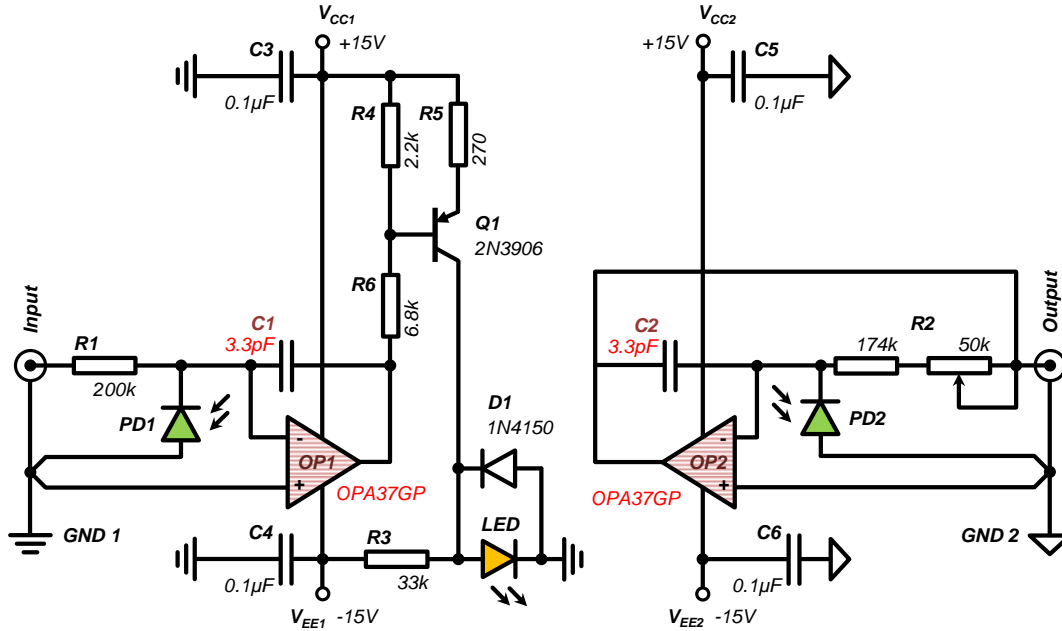


Figure D.6: Analog optocoupling circuit (from [241]). The particular modifications are marked in red: We implement faster operational amplifiers (OPA37GP and AD845JN were tested and showed a better behavior up to 100 kHz than the suggested model LT1097) and smaller capacitors for C1 and C2, compared to the technical datasheet [241].

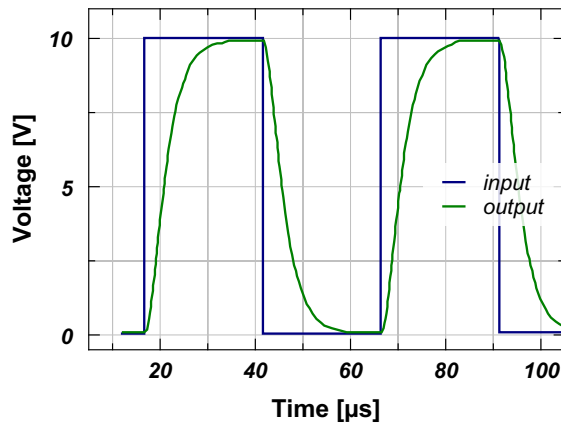
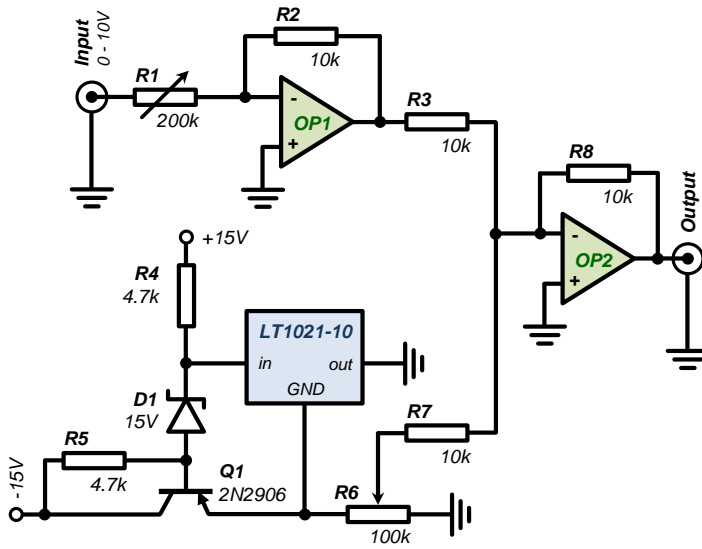


Figure D.7

Performance of the analog optocoupling circuit from fig. D.6 – response (green) on a 20 kHz / 10 V TTL input signal (blue).

**Figure D.8**

Rescaling circuit for voltages in the range of 0 V to 10 V. Alternatively for the implemented 10 V reference [244] it is possible to use [245] or [246].

and $R6$.

UV-LED Driver

In sec. 2.2.2 the influence of LIAD (*light-induced atomic desorption*) on the 2D-MOT vapor pressure and therefore the increased MOT-loading rate were presented. The light sources for the LIAD are powerful UV-LED arrays, which require a current driver. In this section the realization of such a high-power LED driver is discussed. The presented driver is used to power three LEDs of the type **LED395-66-60-110** of *Roithner LaserTechnik* [247].

The UV-LED is composed of an array of totally 60 LED's emitting light at a wavelength of 395 nm. Depending of the model, the UV-LEDs are emitting 250 mW or 600 mW of total power in a divergent beam. The characteristics of the UV-LED are determined by the forward voltage V_F and the forward current I_F . For the UV-LED models used the values are

$$V_F = 18 \text{ V} \quad I_F = 240 \text{ mA} / 500 \text{ mA} .$$

For supplying the UV-LED we use a constant current source (fig. E.1): A constant voltage source of 12 V (*Vigortronix VTX-214-015-124*¹) is powering a regulator (*LM317*), the output of which is reconnected to the adjust-pin. In this configuration the LM317 is supplying a constant current to the circuit determined by the resistances R_1 and R_2 [248]:

$$I[\text{A}] = 1.25 / (R_1 + R_2) .$$

The small resistance R_1 (2Ω - 3.3Ω) is a high power resistance (3 W) and limits the maximal current to $I_{\max} \sim 600 \text{ mA}$. Owing to this precaution the following potentiometer R_2 , which adjust the desired current value, is a low power model (1 W). The current through the UV-LED is switched, or might be further on adjusted by the Darlington-transistors T_1 and T_2 (*NPN epitaxial Darlington transistor TIP 122*). The shunt-resistance R_3 is used to measure the current in the circuit according to Ohm's law. Since the voltage drop on this 1Ω shunt-resistance is small (max. $\sim 600 \text{ mV}$), the signal is amplified by *OP2* (*quad-operational amplifier LM324N*) by a factor of [249]

$$V_{\text{out}}/V_{\text{in}} = 1 + (R_2/R_1) = 8.5 .$$

This stretches the voltage scale up to 5 V, which is the analog voltage-range of the used

¹We used the more powerful version of the AC-DC converter *Vigortronix VTX-214-020-124* to power two LEDs from one supply only.

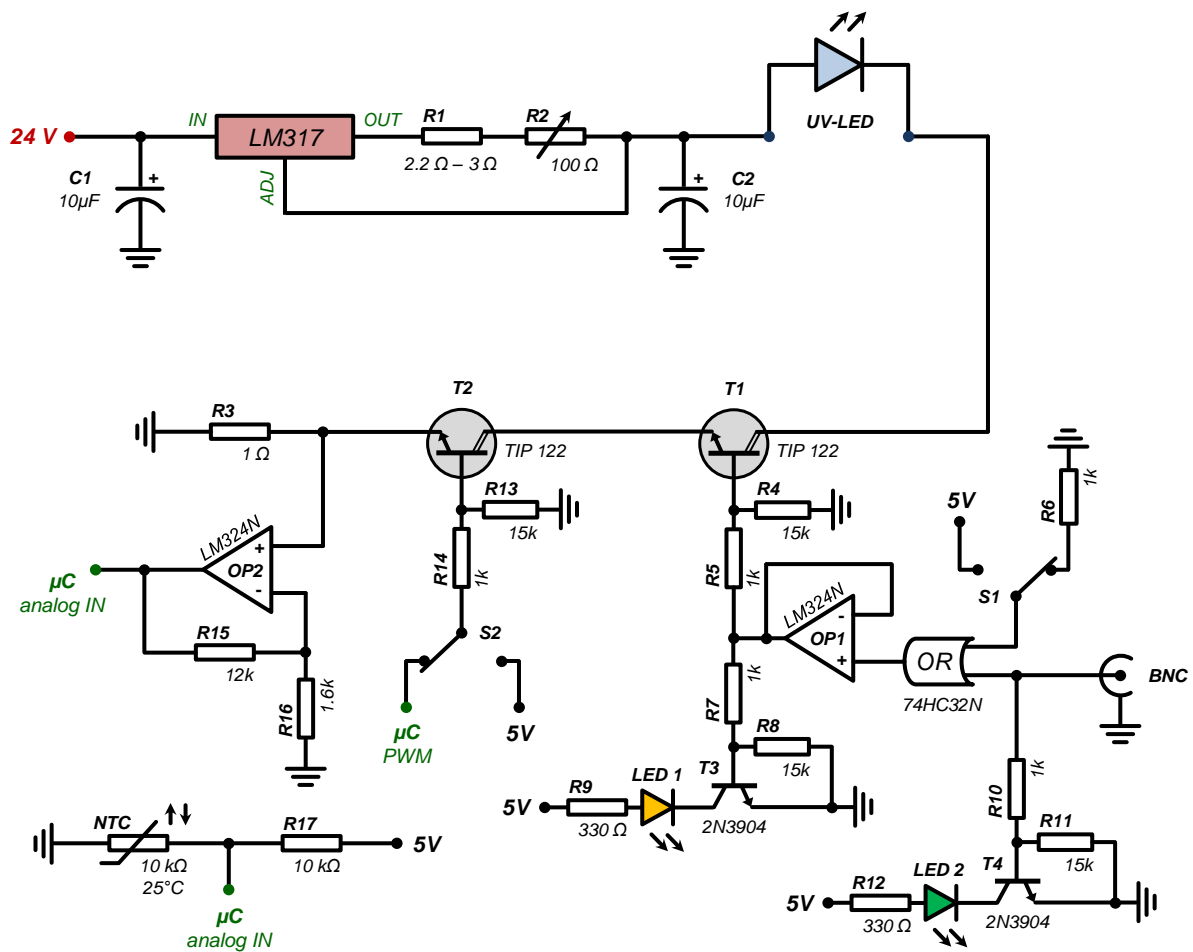


Figure E.1
The LED driver circuit for operating UV-LEDs of the type LED395-66-60-110 of Roithner LaserTechnik. The circuit provides a constant current source adjusted by R2. The two Darlington-type transistors T1 and T2 are used to switch on / off the UV-LED either externally (BNC or switch S1) or internally by a microcontroller (μC). The later also senses the current in the circuit by reading out the voltage drop over R3. Additionally the microcontroller monitors the temperature of the UV-LED with a NTC attached to the UV-LED (lower left part of the circuit).

microcontroller unit (MCU) *ATmega328*².

Both transistors, $T1$ and $T2$, were mainly used in saturation mode, acting as switches. The choice of Darlington-transistors is necessary due to their high gain (for TIP 122 the factor is $h_{FE} = 1000$, compared to $h_{FE} \sim 70$ of usual bipolar transistors), which allows to switch the desired LED currents with only few mA. The Transistor $T2$ is connected to a digital pin of the MCU ATmega328. Multiple tasks can be accomplished by the ATmega328:

- *Temperature monitoring*

Each UV-LED is equipped with a temperature sensor in form of a thermistor (*NTC* - resistance with *Negative Temperature Coefficient*, *EPCOS 10k Ω B57703M*-series type). The MCU measures the voltage drop on the NTC and deduces the temperature of the LED. The maximal operation temperature of the UV-LED is rated to 80 °C. In addition to the heat produced by the UV-LEDs themselves, they are placed in an approximate distance of 3 cm from the glass cell of the 2D-MOT which is heated up to 60 °C. Once the UV-LED reaches ~ 65 °C it is switched off by the MCU through $T2$ and switched on again, either after a given time passed by (10 min) or the temperature dropped below a given threshold (50 °C). This secure operation ensures a long life-time of the UV-LED.

- *Strobe the UV-LED*

It was observed, that the continuous operation of the UV-LEDs reduces the MOT capture efficiency. The MCU is used to flash the UV-LEDs through the transistor $T2$. The task is managed by a timer-interrupt function (generally *ISR* - *Interrupt Service Routine*): In fixed time-intervals the MCU processor gets interrupted to process a different short task. In the present case the digital state for switching $T2$ gets simply switched to the opposite state of the respective current state, once the interrupt is fired. Thus, flashing and other tasks (i.e. measuring the current in the circuit and the temperature of the UV-LED) can be performed as "quasi"-parallel tasks.

The fastest flash-time observed is ~ 10 ms ($\hat{=}$ 100 Hz), even though the rise time of the UV-LED is characterized by the manufacturer to be on the nano-second scale. The slower switching can be attributed to the rise-time / behavior of the Darlington-transistor.

- *Current adjustment*

Operating $T2$ in the not-saturated limit of the transistor would allow to adjust the current in the circuit. Therefore the MCU-pin controlling $T2$ is equipped with the possibility of pulse-width modulation (*PWM*): The MCU produces a periodic square-signal (of 5 V amplitude) with an asymmetric width. The time average of this signal simulates different voltage levels in between 0 V to 5 V, depending on the width of the 5 V-plateau inside the period of each square pulse. However, in the present circuit realization using Darlington-transistors, it would be necessary to drive the base on a very small scale (few hundred mV) with a high precision (up to 1 mV). Since a current stabilization / controlling is not necessary in the application of the UV-LEDs, this was not realized to keep the circuit simple.

- *Display the parameters*

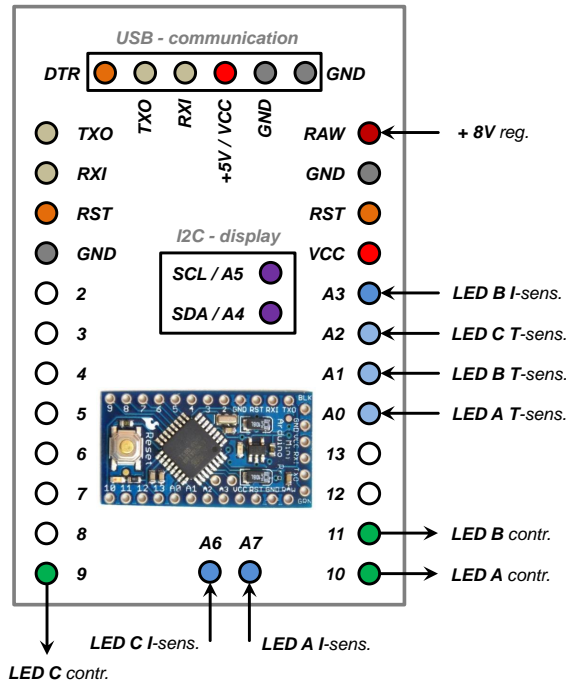
²Pins of the MCU are indicated by μC in fig. E.1

Additionally, a liquid crystal display module (*LCD*) is attached to the MCU, which displays alternately the temperature and current on the three UV-LEDs. The MCU uses the two-wire communication interface (*I2C* protocol) to control the display (by a remote 8-bit expander *PCF8574*).

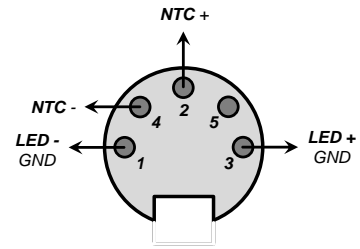
In case of malfunction of the MUC, its operation can be bridged by the switch *S2*, putting *T2* permanently on.

The other Darlington-transistor *T1* is used to switch the UV-LED externally: Either manually by switching *S1*, or by a TTL-signal through a *BNC* connector. Both signals are compared by an *OR-gate* (*74HC32N*), leading to a high-output either when the switch is operated, or a high TTL-signal is present. Since the output current of the OR-gate might be too low (max. 5 mA), it is amplified by an operational amplifier (*OP1*), which is connected as voltage follower. Two standard LEDs are built in for indication: *LED1* indicates when the UV-LED is switched on through *T1*, while *LED2* is on, as soon as a signal on the BNC input is present. In that way it is possible to identify if the LEDs are in "security-cooling-down" mode.

The realized driver included three times the circuit from fig. E.1, in order to drive simultaneously three UV-LEDs. All three UV-LEDs share one MCU which measures all three temperature sensors and three current sensors successively. The pinout of the MCU is given in fig. E.2a. Figure E.2b shows the "triple" driver and the pinout of the 5-pole DIN-connector (**NYS 325** series) used to connect the UV-LEDs. In section 2.2.2 the performance of the UV-LEDs on the vapor-pressure in the 2D-MOT is documented in great detail.



(a) MCU pinout



(b) The realized driver

Figure E.2: (a) MCU pinout in the UV-LED driver. In the current realization of the driver three circuits of the kind of fig E.1 are included. All three UV-LED are monitored and controlled by one MCU. For easier implementation we use an Arduino Mini-Pro, which includes a pre-compiled ATmega328. (b) Driver realization: Photo of the build driver and the DIN-connector pinout, used to connect the UV-LEDs. On the top of the photo the 16×2 LCD is visible, which indicates the temperature and current of each LED.

Microcontroller Based Security System

Modern cold gases experiments are technically complex machines, build, improved and modified over many years by different generations of researchers. Over a life-span of at least 10 years it can consume easily 0.5 to 1 M€ of material and construction costs.

Most experiments include high-power lasers and water-cooled high-bias field magnetic coils, supplied by few hundred amps. These constitute major heat sources, which need to be monitored permanently in order to assure a secure operation of the experimental system. Therefore most experiments today involve a security system.

While the so far easiest systems implemented similarly in our current experimental setup are entirely analog, based on comparators (e.g. *LM393*), which compare the resistance of a NTC-thermistor (*Negative Temperature Coefficient* thermistor) with a fixed resistance value, these systems are not very flexible in their operation. Neither a direct read-out of the temperature can be implemented (without major electronic effort), nor a variably customized switching-logic in case of multiple sensors is easily realizable.

Both, a menu based, adjustable switching- or "reaction"-logic as well as direct calculation of physical quantities (e.g. temperature or water flow) from electronic measures (e.g. resistance or voltage) are straightforward in their implementation in digitally programmable devices. In this chapter we will present a miniaturized realization of a security system.

Device selection

Three kind of programmable devices possessing digital (and analog) in- and outputs (*I/O*) are available on the market. The oldest and simplest member of this family are microcontrollers (μC), followed by FPGAs (**F**ield **P**rogrammable **G**ate **A**rray) and the SoCs (**S**ystem **o**n a **C**hip). The latter was technically introduced through the implementation in handheld devices and can be bought in form of e.g. the Raspberry Pi platform to realize custom projects. The boards have an operational system already installed and have multiple digital outputs. Depending on the level of the model, FPGAs represent similar systems but mostly without an operational system installed. Both systems can process parallel tasks, while FPGAs are more reliable in their timing. Therefore, FPGAs are used for the overall experimental control.

On the downside both platforms are comparably more difficult to program, compared to μC . Projects on μC can be written in C. Through the Arduino platform the compilation and communication with the boards allows for an easy implementation of the security projects.

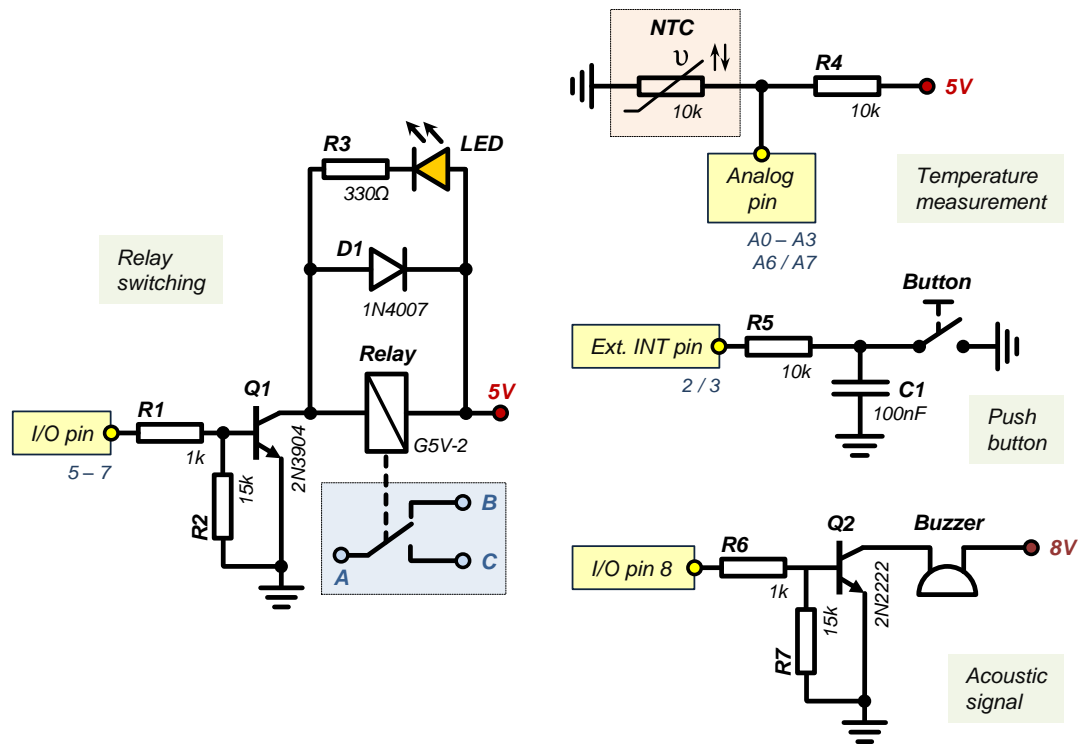


Figure F.1: Mini security system – circuit parts. The main parts of the security system circuit are the relay switching (left part), the temperature measurement through a NTC thermistor, the push-button detection at an external interrupt pin and the activation of an acoustic piezzo buzzer through a npn-transistor (all last three items are on the right part). In the realization within the "mini" security system we implemented three relay switches, six NTC sensors and two push buttons. Not depicted are the power supply circuit (8 V and 5 V from AC) and the I2C-connection for the LCD.

The Atmel μC installed on the boards already includes at least 8 analog inputs. Compared to FPGAs and SoC, μC are slower in their calculation power and allow only consecutive tasks within a logic-loop. However, parallel tasking can be implemented through interrupts of the main routine to some extend.

The mini security system

The first realized mini security system within this thesis is based on the *Arduino Mini-Pro*, the same board used for the LED-driver in appendix E, which includes the ATmega328 μC chip. As any project realized on a μC , it contains a wiring- and a coding- (or "logic") part.

Circuit

The Arduino-board pin assignment can be found in appendix E, fig. E.2a. Digital-I/O pins are just numbered, while analog inputs carry a capital *A* in front of their associated pin number. The relevant circuit parts are shown in fig. F.1. The entire system contains three relay switches and six voltage-measurement connections, designated to be applied with 10k Ω -NTC thermistors.

Each relay is switched by a digital I/O pin through a npn-transistor ($Q1$). Thereby the resistance $R1$ reduces the current-drain from the μC -pin, while $R2$ discharges the basis of the transistor for off-switching. The diode $D1$ allows for discharging of the relay coil in case the npn-transistor interrupts the supply of the relay. The switching of the power supplies or laser interlocks in case of an alarm through a mechanical relay allows for an absolute galvanic decoupling of the distinct systems. This becomes crucial in order to avoid ground-loops and voltage leaks in the experiment, which would be otherwise conducted through the security installation in this case. A similar npn-transistor circuit is used to activate a buzzer for acoustic signalization of an alarm.

The NTC thermistors are used to transform temperature into a corresponding resistance value. In turn, the resistance is detected through the voltage drop at the NTC through one of six possible analog connections of the μC . There are many kinds of NTCs on the market, but the current system was optimized for the usage of NTCs featuring a resistance of $10\text{ k}\Omega$ at room temperature. But it is possible to adapt the system for any kind of NTCs later-on, simply through the code of the μC , since the determination of the temperature in dependence of the measured resistance is calculated through a formula given in the data sheets. Yet, the usual operation resistance should be comparable to the additionally wired fixed resistance value of $R4$ near the 5 V supply. Otherwise the exploited voltage / temperature range of the sensor and hence the sensitivity of the circuit will decrease. In addition to NTCs we also detect the resistance of a water-flow sensor-switch, in our case a simple two state (open or closed) switch. Although this task could be accomplished by a digital pin, the system was originally designed to detect the real flow rate by a different sensor and hence the usage of the analog μC -input became more convenient.

The two analog inputs $A4$ and $A5$ are used to control a 16×2 LCD display through a two-wire communication ($I2C$).

For the navigation through the menu and settings of the security systems we implemented two push-buttons. Both are connected to the external interrupt (INT) pins of the μC . These pins are continuously monitored by the μC , independent of its actual task and thus a pressed button will neither be missed nor a special wait-and-check routine is later on necessary in order to obtain an user input. Additionally to a software implementation, we debounce the push button on the hardware side by the small capacitor $C1$.

Security loop and menu

In the principle operation, the μC measures consecutively the voltage drop on the NTC sensors and calculates the corresponding temperature. After comparing the temperature with the maximally allowed set-temperature, the system decides if an alarm has to be set. In case of an alarm the corresponding relays are switched. The user has to connect the corresponding interlock in that way, that the normal operation is provided only when the relay is switched actively by the security system. This ensures, that an operation is impossible in case the security system is accidentally not operational. Figure F.2 shows the main security loop. The diagram includes the task of the two buttons during the permanent μC main-loop operation.

If an alarm is detected the system remains in the switched relay-state, but monitors continuously all of the (active) sensors, including the one which previously caused the alarm. Even if the temperature drops below the set value, the alarm remains: The reset has to be accomplished

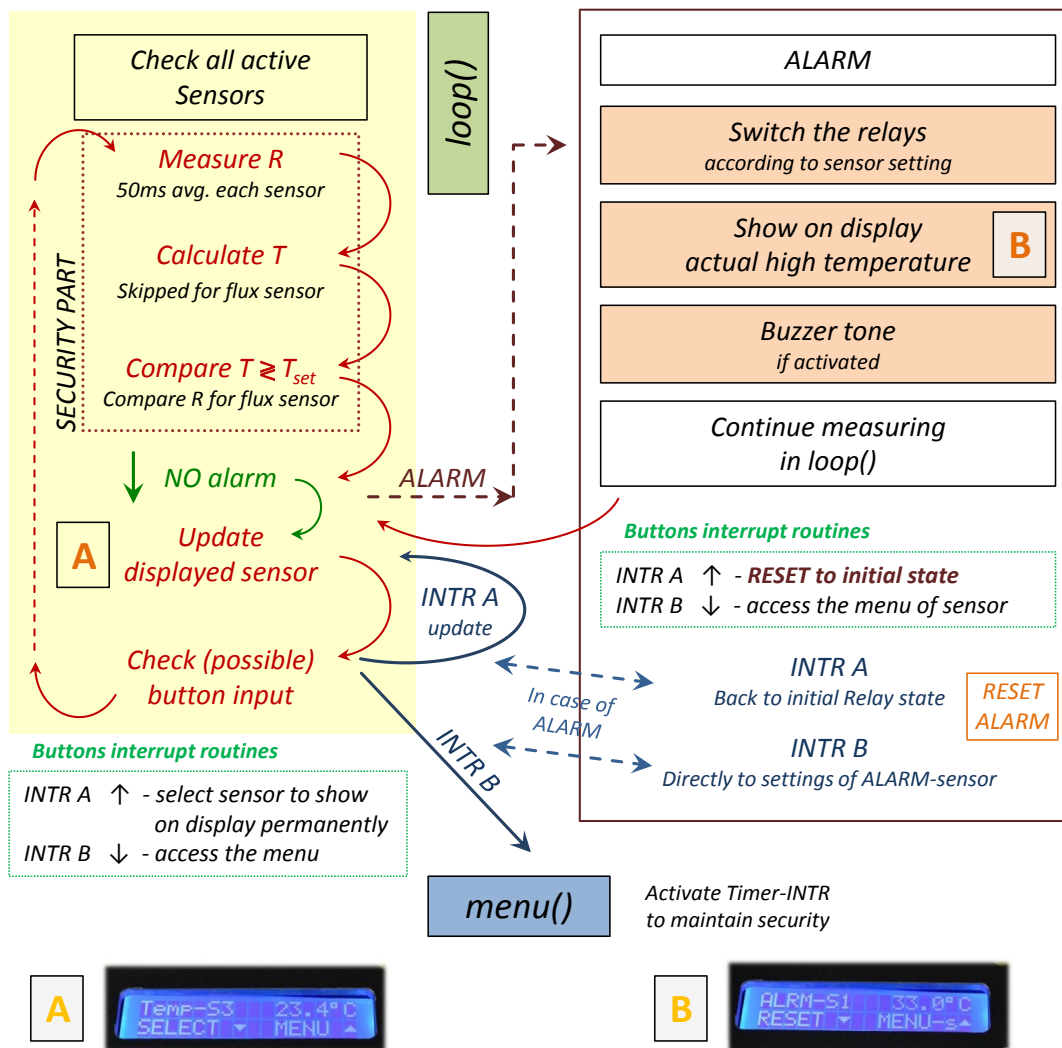


Figure F.2: Main security loop program. In the main loop the μC records in an array all active NTC thermistors or resistances (in case of the flow sensor) and compares after conversion the values to the set temperatures. One selected sensor is permanently displayed on the LCD. The second push button allows to access the menu. If a sensor causes an alarm the previously configured relays are switched and the LCD shows the last temperature which exceeded the set temperature. The main security loop continuous, while the alarm has to be reset manually. Alternatively it is possible to jump directly to the settings of the alarming sensor.

by the user in the current version of the program. If an additional sensor detects an alarm, the switched relay state is the one corresponding to the last detected alarm state.

Settings, like the maximal threshold temperature, the relay state at the start as well as the relay switching in case of an alarm can be done by accessing the menu function from the main-loop. At this point a timer interrupt function (*Timer-INTR*) is activated: During the navigation through the menu the internal timer stops each 3s the actual operation and overwrites a boolean variable. In each menu or input sub-loop this variable is continuously controlled and in case of being true, the actual function is left for performing a security check of the active sensors. In this way we ensure the security operation even during user-input tasks (quasi-parallel tasking).

The menu function is a rather complicated nesting of separate sub-loops (see diagram in fig. F.3). Each sub-menu has its own appearance on the two-line LCD and the corresponding button functions. The sub-menus are closed "while"-loops, which are running for a given time (8s) or as long as a button input from the user is detected. In case no input is detected through the buttons, the program jumps to the following sub-menu according to the diagram in fig. F.3. After each input the settings are stored in the μC internal storage (*EEPROM*) and available as initial settings even after powering off the μC .

A more versatile system would include two microcontrollers. One would measure and ensure the security in a continuous loop, while the other one would be used for the displaying of data and customer input.

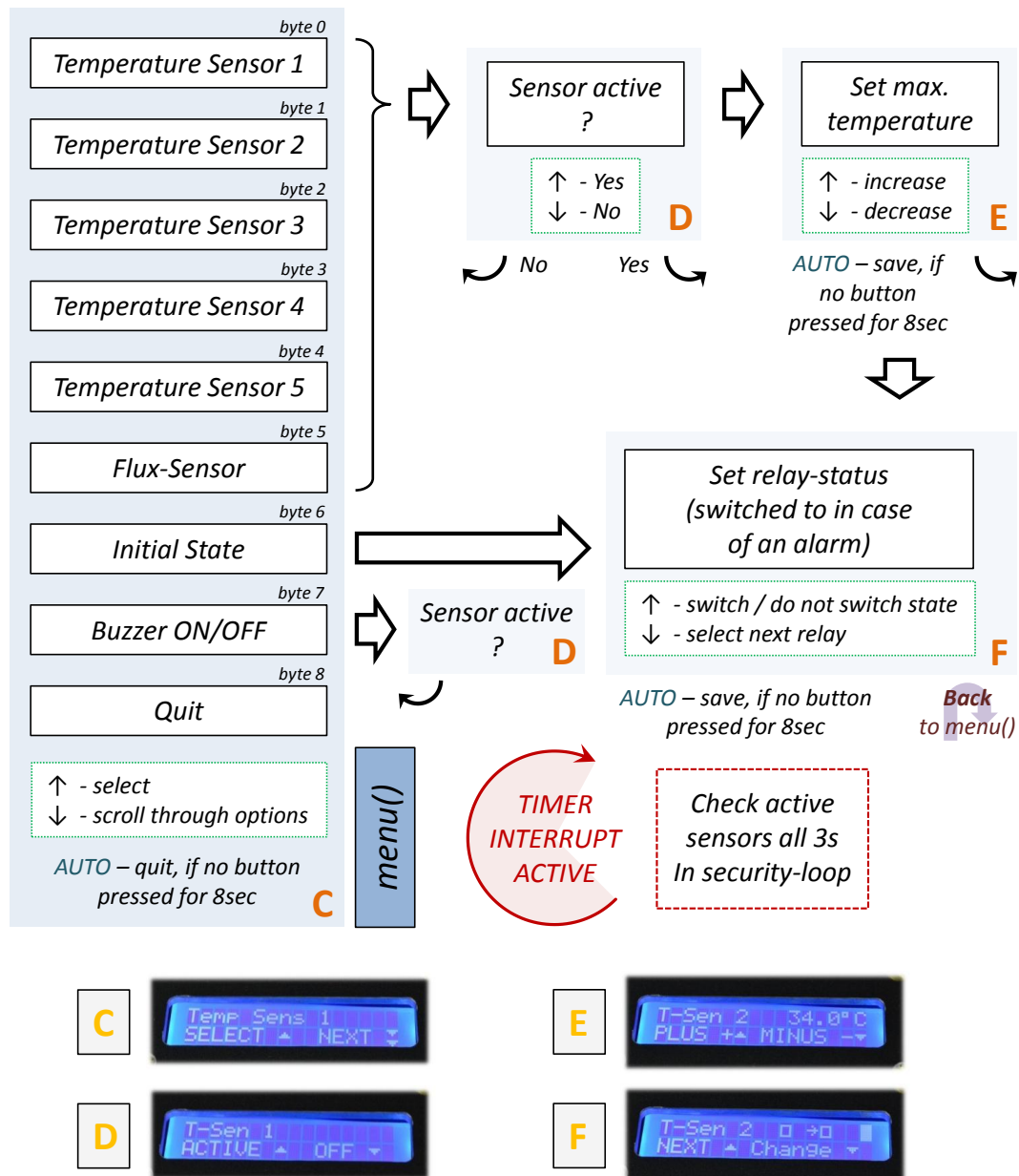


Figure F.3: Menu loop and sub-items. The menu itself and each sub-item is a while-loop with multiple arguments: Either time-bound or depending on the user input the while-loop will be left and the program proceeds to the next item. Depending on the main-menu item-number different sub-menus are called. A timer interrupt function stops the sub-loops each 3s and runs the main security loop. Once leaving the menu, the program continues in the main security loop (see fig. F.2).

50Hz Mains Synchronization Device

The 50 Hz-mains synchronization device was built to synchronize the start of an experimental sequence with the mains wave form, in order to avoid magnetic field fluctuations in cases where a high precision of the field is required. Additionally, the realized circuit allows for regulating the MOT loading for ${}^6\text{Li}$ and ${}^{40}\text{K}$ by two distinct digital PID-circuits. The regulation is achieved by monitoring the two fluorescence signals of the clouds (compare fig. 2.5) and adjusting the amplitudes of the light sources through AOMs in the 2D-MOT and the Zeeman slower. Since both tasks, the synchronization to a 50 Hz-signal and the MOT-loading dynamics in dependence of the pre-cooling sources, are comparably slow in their dynamics, the challenge can be accomplished in a flexible way by means of a microcontroller (μC). We use an Arduino UNO board, which includes the *ATmega328P* chip, which has the same specifications as the previously introduced ATmega328.

The 50 Hz-mains synchronization part of the circuit is depicted in fig. G.1: Part of the transformer circuit, which creates all the necessary DC-voltages for the remaining PID section, is used to monitor the AC-mains signal (*BNC – AC monitor*). For fitting the AC-signal into the analog input of the μC , we cut the negative part of the wave signal (diode *D1*) and turn down the voltage level by a simple divider circuit (resistances *R1* and *R2*). An additional Zener diode (*D2*) protects the analog input (*A0*) of the microcontroller against voltage overshoots.

The μC detects first the peak voltage of the AC-waveform (in average around 2.4 V for the circuit in fig. G.1). In a second step, given a fixed small margin (20 mV typically, reaching thereby the limit of the resolution), the μC routine searches for the re-appearance of half of the maximum voltage level. Additionally, we ensure during the search of the required voltage range that the values increase. In that way we trigger always on the rising slope (see embedded image in fig. G.1). Alternatively, an interrupt routine on a digital pin can be implemented for the triggering routine, detecting the rising (falling) voltage over (below) the TTL threshold of the μC . However, the present solution on an analog pin allows for sampling the entire (half-) waveform of the AC signal.

The PID-control part of the circuit for regulating the MOT-loading of ${}^6\text{Li}$ and ${}^{40}\text{K}$ is depicted in fig. G.2. In case the regulation is activated, the two relays (*Relay 1* and *Relay 2*) are switching the outputs (*BNC OUT 1* and *BNC OUT 2*) from an external AOM-driver source to the internal control. The fluorescence signals from both MOTs, ranging from 0 V to 3 V, are detected by two distinct 16-bit analog-to-digital converters (*ADC 1* and *ADC 2*) through the two inputs *BNC IN 1* and *BNC IN 2*. The detected voltage is transmitted by a two wire

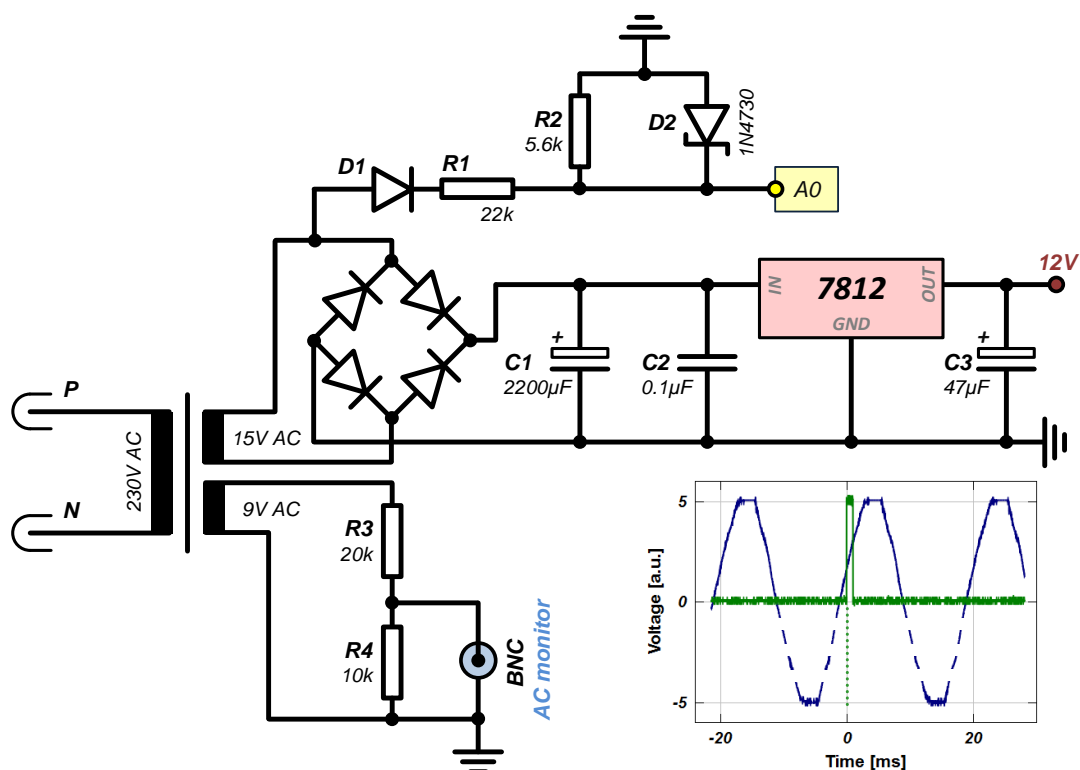


Figure G.1: 50Hz mains synchronization circuit. The 230 V AC voltage is stepped down by a transformer to either 15 V or 9 V AC. One output is used to directly monitor the AC-signal. For the detection through an analog input of the μC we cut the negative voltage part. The circuit also shows the realization of a DC-power source of 12 V from the 15 V AC input. In the entire system we use an additional transformer to create all the necessary voltages for the PID circuit in fig. G.2 and the μC itself. The embedded picture shows the monitored AC signal (the μC detects only the positive voltage part) and the trigger is fired at half of the detected maximal peak value.

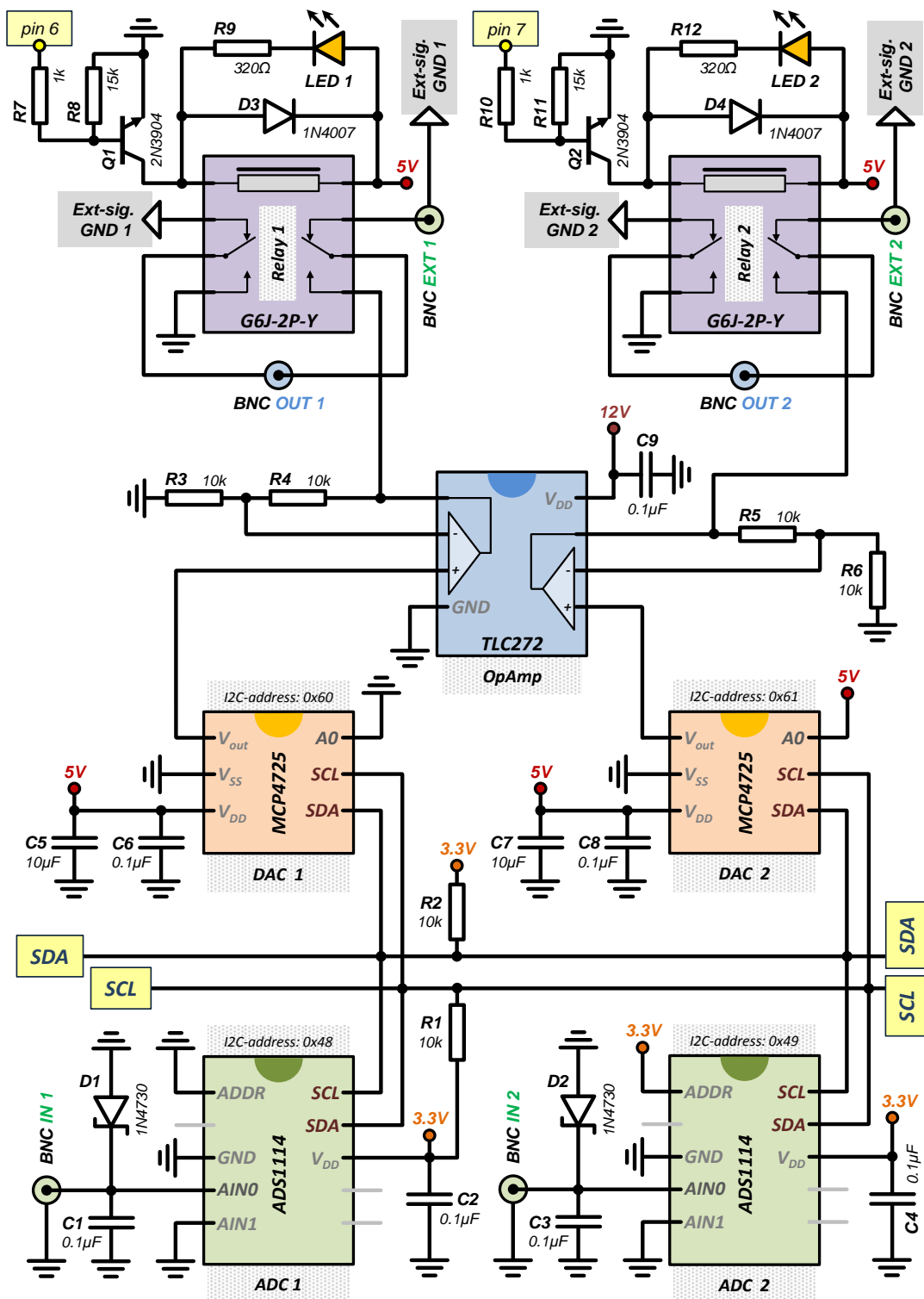


Figure G.2: 50Hz mains synchronization box - regulation part.

protocol (*I2C*) to the μC . Through the same communication line the μC sends the calculated PID response to the two 12-bit digital-to-analog converters (*DAC 1* and *DAC 2*). The output of each DAC is amplified by a factor two by an operational amplifier (*OpAmp*) in order to realize the entire voltage control scope up to 10 V. Finally this signal is conducted in the two output BNCs. Once a desired fluorescence level is reached for both MOTs, the μC fires a trigger.

Time-of-Flight Expansions

In this section we present some details on the derivation of the density evolution during time of flight (*TOF*) for different trapping potentials and different underlying statistical distributions, i.e. the Boltzmann and Fermi-Dirac distribution. In the experiment the gas expands either freely during TOF or under the influence of a bias curvature. The relevant cases, which are mentioned in the main text will be presented in this section.

H.1 Free Expansion during TOF

Once the cloud is released from the trap, it expands freely during TOF. The expansion velocity in direction x_i takes place with the acquired momentum p_i . After the time t the new position of an atom x'_i , previously being at x_i is given by:

$$x'_i(t) = x_i + \frac{p_i}{m} t. \quad (\text{H.1})$$

For the corresponding momentum we derive $p'_i = p_i$, again due to the free expansion. Now we have to substitute the position coordinate in the underlying phase space density distribution function and recalculate the momentum integrals, in order to obtain the changed density profile through time.

H.1.1 TOF evolution from a harmonic trapping potential

The Hamiltonian describing a particle of mass m in a harmonic trap with frequencies ω_i is well known to be

$$H_{\text{harm.}} = \frac{p^2}{2m} + \frac{m}{2} \sum_i \omega_i^2 x_i^2. \quad (\text{H.2})$$

After some free expansion the position coordinate transforms according to eq. (H.1):

$$\begin{aligned} H_{\text{harm.}}(t) &= \frac{p'^2}{2m} + \frac{m}{2} \sum_i \omega_i^2 x_i'^2 = \\ &= \frac{1}{2m} \sum_i \left\{ p_i \sqrt{1 + \omega_i^2 t^2} + m \omega_i^2 \frac{x_i t}{\sqrt{1 + \omega_i^2 t^2}} \right\}^2 + \frac{m}{2} \sum_i \frac{\omega_i^2 x_i^2}{1 + \omega_i^2 t^2}. \end{aligned} \quad (\text{H.3})$$

In case of a thermal cloud we will integrate the Boltzmann phase space distribution function,

$$f_B(\mathbf{r}, \mathbf{p}) = \frac{1}{Z} e^{-\beta H(\mathbf{r}, \mathbf{p})} \quad \text{with} \quad Z = e^{\beta \mu}, \quad \beta = 1/k_B T,$$

over the momentum coordinates to obtain the density distribution,

$$n(\mathbf{r}, t) = \frac{1}{(2\pi\hbar)^3} \int d^3\mathbf{p} \frac{1}{Z} \exp\left(-\beta H(\mathbf{r}, \mathbf{p}, t)\right). \quad (\text{H.4})$$

The integration is performed by substituting the first sum expression of $H_{\text{harm.}}(t)$ in eq. (H.3) by a new momentum coordinate. The simple gaussian integral over the absolute value of momentum releases

$$n(\mathbf{r}, t) = \frac{1}{2\pi^2\hbar^3} \frac{1}{Z} \sqrt{\frac{\pi}{2}} \left(\frac{\beta}{m}\right)^{-3/2} \prod_i \frac{\exp\left(-\beta m \omega_i^2 x_i^2 / 2 (1 + \omega_i^2 t^2)\right)}{\sqrt{1 + \omega_i^2 t^2}}. \quad (\text{H.5})$$

Integrating further over one or two spatial coordinates results in the 2D- and 1D-density distribution projections respectively:

$$2D: \quad n(x, y, t) = \int_{-\infty}^{\infty} n(\mathbf{r}, t) dz = \frac{1}{2\pi\hbar^3} \frac{1}{Z} \frac{m}{\beta^2 \omega_z} \prod_{x,y} \frac{1}{\sqrt{1 + \omega_i^2 t^2}} \exp\left(-\beta \frac{1}{1 + \omega_i^2 t^2} \frac{m \omega_i^2 x_i^2}{2}\right). \quad (\text{H.6})$$

$$1D: \quad n(x, t) = \int_{-\infty}^{\infty} n(x, y, t) dy = \frac{1}{\sqrt{2\pi}\hbar^3} \frac{1}{Z} \frac{m^{1/2}}{\beta^{5/2} \omega_y \omega_z} \frac{1}{\sqrt{1 + \omega_x^2 t^2}} \exp\left(-\beta \frac{1}{1 + \omega_x^2 t^2} \frac{m \omega_x^2 x^2}{2}\right). \quad (\text{H.7})$$

The fugacity Z is used to normalize the distributions to the total atom number N . The time dependency can be found as well in the amplitude as in the width of the time evolving density distributions. Having a Gaussian function of the form $A \cdot \exp(-x^2/2\sigma^2)$ we can deduce the evolution of the width σ from the equations above to

$$\sigma^2(t) = \sigma_0^2 \cdot (1 + \omega_i^2 t^2) \quad \text{with} \quad \sigma_0^2 = \frac{1}{\beta m \omega_i^2}, \quad (\text{H.8})$$

which was stated in a similar form in eq. (2.13).

Similar calculations can be performed for the Fermi-Dirac distribution,

$$f_{\text{FD}}(\mathbf{r}, \mathbf{p}) = \frac{1}{\frac{1}{Z} e^{\beta H(\mathbf{r}, \mathbf{p})} + 1},$$

which is valid in the quantum degenerate regime and used to describe the ultra cold sample of ^{40}K in sec. 5.5. The integration over the momentum coordinates in the case of the Fermi-Dirac distribution f_{FD} under the expanding Hamiltonian of eq. (H.3) yields

$$n(\mathbf{r}, t) = -\frac{1}{\hbar^3} \left(\frac{m}{2\pi} k_B T\right)^{3/2} \left(\prod_i \frac{1}{\sqrt{1 + \omega_i^2 t^2}}\right) \text{Li}_{3/2} \left[-Z \exp\left(-\frac{\beta m}{2} \sum_i \frac{\omega_i^2 x_i^2}{1 + \omega_i^2 t^2}\right)\right], \quad (\text{H.9})$$

where Li_n denotes the polylogarithmic function of order n introduced in the main text in

eq. (5.39). By further integrating the 3D-density profile above, we obtain the 2D and 1D profiles:

$$2D: \quad n(x, y, t) = -\frac{m}{2\pi} \frac{(k_B T)^2}{\hbar^3 \omega_x} \left(\prod_{x,y} \frac{1}{\sqrt{1 + \omega_i^2 t^2}} \right) \mathbf{Li}_2 \left[-Z \exp \left(-\frac{\beta m}{2} \sum_{x,y} \frac{\omega_i^2 x_i^2}{1 + \omega_i^2 t^2} \right) \right]. \quad (\text{H.10})$$

$$1D: \quad n(x, t) = -\sqrt{\frac{m}{2\pi}} \frac{(k_B T)^{5/2}}{\hbar^3 \omega_y \omega_z} \frac{1}{\sqrt{1 + \omega_x^2 t^2}} \mathbf{Li}_{5/2} \left[-Z \exp \left(-\beta \frac{1}{1 + \omega_x^2 t^2} \frac{m \omega_x^2 x^2}{2} \right) \right]. \quad (\text{H.11})$$

Comparing the resulting density distributions in the particular discussed case of the harmonic trapping potential with the corresponding distributions at $t = 0$ (in absence of TOF), we can formulate the following transformation

$$x_i \rightarrow x_i / \sqrt{1 + \omega_i^2 t^2} \quad \text{and} \quad n_0 \rightarrow n_0 / \prod_{i=\text{dim.}} \sqrt{1 + \omega_i^2 t^2}, \quad (\text{H.12})$$

which allows to obtain the TOF distributions from the in-situ ones. The number of factors included in the peak density n_0 transformation depends on the dimension of the considered density profile.

H.2 TOF Evolution in Presence of a Magnetic Curvature

If we apply a constant bias field, created by a pair of coils in Helmholtz configuration, for example to distinguish two different spin states during the imaging, we have to take into account that the coil-pair creates also terms of second order, known as magnetic curvature (see sec. 5.4.2). The corresponding potential is derived in eq. (5.24) to

$$U_{\text{mag-curv}} = \frac{m}{2} \left\{ \omega_c^2 r^2 - \left(\sqrt{2} \omega_c \right)^2 z^2 \right\}. \quad (\text{H.13})$$

According to Newton's equations a particle with initial ($t = 0$) position \mathbf{r} and momentum \mathbf{p} will follow the new trajectory described by

$$\begin{aligned} r'(t) &= r \cos(\omega_c t) + \frac{p_r}{m \omega_c} \sin(\omega_c t) \\ z'(t) &= z \cosh(\sqrt{2} \omega_c t) + \frac{p_z}{m \sqrt{2} \omega_c} \sinh(\sqrt{2} \omega_c t) \end{aligned} \quad (\text{H.14})$$

The corresponding momentum evolution $\mathbf{p}'(t)$ is simply derived by differentiation. Furthermore, it can be shown, that the infinitesimal phase space element remains unchanged through time, i.e. $dx'_i dp'_i = dx_i dp_i$.

The new position \mathbf{r}' and momentum \mathbf{p}' coordinates need to be inserted in the corresponding phase space distribution function, in order to integrate out the density distribution function $n(\mathbf{r}, t)$ through TOF and obtain the corresponding cloud profile evolution, similar to the cases of free expansion discussed before.

H.2.1 Case of Boltzmann distribution

In the first case the thermal cloud leaves a harmonic trap with frequencies ω_i to expand in the curvature potential from eq. (H.13), being described by a Boltzmann distribution function. Hence, we insert the expressions from eq. (H.14) and the corresponding momenta into the Hamiltonian of eq. (H.2),

$$\begin{aligned}
 H_{\text{harm.-curv.}}(t) = & \sum_{i=x,y} \frac{p_i^2}{2m} \left\{ \cos^2 \alpha_c + \frac{\omega_i^2}{\omega_c^2} \sin^2 \alpha_c \right\} + \frac{m\omega_i^2}{2} \left\{ \cos^2 \alpha_c + \frac{\omega_c^2}{\omega_i^2} \sin^2 \alpha_c \right\} x_i^2 \\
 & + \frac{\omega_c}{2} x_i p_i \left\{ \frac{\omega_i^2}{\omega_c^2} - 1 \right\} \sin 2\alpha_c \\
 & + \frac{p_z^2}{2m} \left\{ \cosh^2 \alpha_{2c} + \frac{\omega_z^2}{2\omega_c^2} \sinh^2 \alpha_{2c} \right\} + \frac{m\omega_z^2}{2} \left\{ \cosh^2 \alpha_{2c} + \frac{2\omega_c^2}{\omega_z^2} \sinh^2 \alpha_{2c} \right\} z^2 \\
 & + \frac{\omega_c}{\sqrt{2}} z p_z \left\{ \frac{\omega_z^2}{2\omega_c^2} + 1 \right\} \sinh 2\alpha_{2c} .
 \end{aligned} \tag{H.15}$$

We introduced the expressions $\alpha_c = \omega_c t$ and $\alpha_{2c} = \sqrt{2}\omega_c t$ to shorten the notation. The terms for the trapping curvature and the anti-trapping z-direction are quite similar - only the trigonometric functions has to be replaced by their hyperbolic counterparts and the curvature frequency ω_c by $\sqrt{2}\omega_c$.

We will skip the intermediate steps and mention directly the two possible 1D-density profiles, where we either integrated along both trapping direction, or one trapping and one anti-trapping direction. The corresponding integrals reveal

$$\begin{aligned}
 \text{Trapping dir.:} \quad n(x, t) = & \frac{1}{Z} \sqrt{\frac{m}{2\pi}} \frac{(k_B T)^{5/2}}{\hbar^3 \omega_y \omega_z \left\{ \cos^2 \alpha_c + \frac{\omega_x^2}{\omega_c^2} \sin^2 \alpha_c \right\}^{1/2}} \cdot \\
 & \cdot \exp \left(-\beta \frac{1}{\cos^2 \alpha_c + \frac{\omega_x^2}{\omega_c^2} \sin^2 \alpha_c} \frac{m\omega_x^2 x^2}{2} \right) ,
 \end{aligned} \tag{H.16}$$

and

$$\begin{aligned}
 \text{Anti-trapping dir.:} \quad n(z, t) = & \frac{1}{Z} \sqrt{\frac{m}{2\pi}} \frac{(k_B T)^{5/2}}{\hbar^3 \omega_x \omega_y \left\{ \cosh^2 \alpha_{2c} + \frac{\omega_z^2}{2\omega_c^2} \sinh^2 \alpha_{2c} \right\}^{1/2}} \cdot \\
 & \cdot \exp \left(-\beta \frac{1}{\cosh^2 \alpha_{2c} + \frac{\omega_z^2}{2\omega_c^2} \sinh^2 \alpha_{2c}} \frac{m\omega_z^2 z^2}{2} \right) .
 \end{aligned} \tag{H.17}$$

If we now fit a Gaussian function, $A \cdot \exp(-x^2/2\sigma^2)$, to the imaged distributions, we might observe two different expansions for the width $\sigma(t)$. Along the trapping axis x the width will oscillate,

$$\sigma_x^2(t) = \sigma_{0x}^2 \cdot \left\{ \cos^2(\omega_c t) + \frac{\omega_x^2}{\omega_c^2} \sin^2(\omega_c t) \right\} , \tag{H.18}$$

while along the anti-trapping direction z we will observe an expansion,

$$\sigma_z^2(t) = \sigma_{0z}^2 \cdot \left\{ \cosh^2(\sqrt{2}\omega_c t) + \frac{\omega_z^2}{2\omega_c^2} \sinh^2(\sqrt{2}\omega_c t) \right\}. \quad (\text{H.19})$$

In the limit of $\omega_c t \ll 1$, or equivalently for sufficient short TOF times t compared to the curvature frequency scale $1/\omega_c$, we find again the result of eq. (H.8), which would be independent of the curvature value in this particular case.

H.2.2 Case of Fermi distribution

The derivation of the density profile for a degenerate cloud obeying the Fermi-Dirac distribution follows similar steps as above. However, the results are expressed by rather longer formulas, so that we will just mention the relevant expressions of the 1D-profiles at this point. For the two possible curvature scenarios we find

$$\begin{aligned} \text{Trapping dir.:} \quad n(x, t) = & -\sqrt{\frac{m}{2\pi}} \frac{(k_B T)^{5/2}}{\hbar^3 \omega_y \omega_z \left\{ \cos^2 \alpha_c + \frac{\omega_x^2}{\omega_c^2} \sin^2 \alpha_c \right\}^{1/2}} \cdot \\ & \cdot \text{Li}_{5/2} \left[-Z \exp \left(-\beta \frac{1}{\cos^2 \alpha_c + \frac{\omega_x^2}{\omega_c^2} \sin^2 \alpha_c} \frac{m \omega_x^2 x^2}{2} \right) \right], \end{aligned} \quad (\text{H.20})$$

and

$$\begin{aligned} \text{Anti-trapping dir.:} \quad n(z, t) = & -\sqrt{\frac{m}{2\pi}} \frac{(k_B T)^{5/2}}{\hbar^3 \omega_x \omega_y \left\{ \cosh^2 \alpha_{2c} + \frac{\omega_z^2}{2\omega_c^2} \sinh^2 \alpha_{2c} \right\}^{1/2}} \cdot \\ & \cdot \text{Li}_{5/2} \left[-Z \exp \left(-\beta \frac{1}{\cosh^2 \alpha_{2c} + \frac{\omega_z^2}{2\omega_c^2} \sinh^2 \alpha_{2c}} \frac{m \omega_z^2 z^2}{2} \right) \right]. \end{aligned} \quad (\text{H.21})$$

The final expressions are very similar to the Boltzmann case. An expansion in curvature demands a precise knowledge of the curvature frequency ω_c . Otherwise, it adds up as a fit parameter in the analysis for the density distribution. Therefore, the determination of Z (see sec. 5.5.4) gets more complicated, leading to imprecise T/T_F estimations.

Supplemental Calculations for Chapter 3

I.1 Scalar Product from Eq. (3.11)

In sec. 3.3 we introduced the scalar product eq. (3.11):

$$\langle \alpha(\mathbf{r}, \mathbf{p}) | \beta(\mathbf{r}, \mathbf{p}) \rangle = \int d^3\mathbf{r} d^3\mathbf{p} f_0(\mathbf{r}, \mathbf{p}) \alpha(\mathbf{r}, \mathbf{p}) \beta(\mathbf{r}, \mathbf{p}) . \quad (\text{I.1})$$

Theorem. *The above expression satisfies the definition of a scalar product.*

Proof. The symmetry property,

$$\langle \alpha(\mathbf{r}, \mathbf{p}) | \beta(\mathbf{r}, \mathbf{p}) \rangle = \langle \beta(\mathbf{r}, \mathbf{p}) | \alpha(\mathbf{r}, \mathbf{p}) \rangle ,$$

is simply given by the integral properties¹. In the same way the linearity is easy to show:

$$\begin{aligned} \langle \alpha(\mathbf{r}, \mathbf{p}) | \beta(\mathbf{r}, \mathbf{p}) + \lambda \gamma(\mathbf{r}, \mathbf{p}) \rangle &= \int d^3\mathbf{r} d^3\mathbf{p} f_0(\mathbf{r}, \mathbf{p}) \alpha(\mathbf{r}, \mathbf{p}) (\beta(\mathbf{r}, \mathbf{p}) + \lambda \gamma(\mathbf{r}, \mathbf{p})) \\ &= \int d^3\mathbf{r} d^3\mathbf{p} f_0(\mathbf{r}, \mathbf{p}) \alpha(\mathbf{r}, \mathbf{p}) \beta(\mathbf{r}, \mathbf{p}) + \\ &\quad + \lambda \int d^3\mathbf{r} d^3\mathbf{p} f_0(\mathbf{r}, \mathbf{p}) \alpha(\mathbf{r}, \mathbf{p}) \gamma(\mathbf{r}, \mathbf{p}) \\ &= \langle \alpha(\mathbf{r}, \mathbf{p}) | \beta(\mathbf{r}, \mathbf{p}) \rangle + \lambda \langle \alpha(\mathbf{r}, \mathbf{p}) | \gamma(\mathbf{r}, \mathbf{p}) \rangle . \end{aligned}$$

The scalar product is positive definite, since for $\langle \alpha(\mathbf{r}, \mathbf{p}) | \alpha(\mathbf{r}, \mathbf{p}) \rangle$ we integrate over α^2 and the quantity $\alpha(\mathbf{r}, \mathbf{p})$ is real-valued. Similar argument hold for

$$\langle \alpha | \alpha \rangle = 0 \Leftrightarrow \alpha = 0 .$$

■

¹It should be reminded, that the quantities α and β are real-valued functions in all our calculations

1.2 Properties of the Liouville Operator

In sec. 3.3 we introduced the Liouville operator,

$$\hat{\mathbf{L}} = \frac{\mathbf{p}}{m} \cdot \partial_{\mathbf{r}} - \nabla U(\mathbf{r}) \cdot \partial_{\mathbf{p}}. \quad (\text{I.2})$$

Here we will prove some important properties of the operator which were used in the previously mentioned section.

Theorem. *The operator $\hat{\mathbf{L}}$ commutes with the parity operator $\hat{\Pi}_i$, applied on a pair of spatial and momentum coordinates at once,*

$$\hat{\Pi}_i f(p_i, x_i) = f(-p_i, -x_i). \quad (\text{I.3})$$

(point reflection at the origin in phase space).

Proof. We proof the statement by direct calculation:

$$\begin{aligned} \hat{\mathbf{L}} \hat{\Pi}_i f(p_i, x_i) &= \hat{\mathbf{L}} f(-p_i, -x_i) \\ &= \left\{ \frac{p_i}{m} \partial_{x_i} - \partial_{x_i} U(\mathbf{r}) \cdot \partial_{p_i} \right\} f(-p_i, -x_i) \\ &= \left\{ \frac{p'_i}{m} \partial_{x'_i} - \partial_{x'_i} U(\mathbf{r}') \cdot \partial_{p'_i} \right\} f(p'_i, x'_i) \\ &= \hat{\Pi}_i \hat{\mathbf{L}} f(p'_i, x'_i) = \hat{\mathbf{L}} f(p'_i, x'_i). \end{aligned}$$

From the second to the third line we replaced $p_i = -p'_i$ and $x_i = -x'_i$. The sign of the potential energy $U(\mathbf{r}')$ does not change under the assumption of a symmetric potential, which is the case for the quadrupole potential in eq. (2.3). Thus, the operator $\hat{\mathbf{L}}$ is invariant under the simultaneous sign change of the space and momentum coordinates. By renaming the coordinates the statement is shown. ■

Theorem. *If only the parity of all position or momentum coordinates is changed, the sign of the operator $\hat{\mathbf{L}}$ changes, e.g. for the momentum coordinates \mathbf{p} :*

$$\mathbf{p} \rightarrow -\mathbf{p} \quad \Rightarrow \quad \hat{\mathbf{L}} \rightarrow -\hat{\mathbf{L}}. \quad (\text{I.4})$$

Proof.

$$\begin{aligned} \hat{\mathbf{L}} \hat{\Pi}_{\mathbf{p}} f(\mathbf{p}, \mathbf{x}) &= \hat{\mathbf{L}} f(-\mathbf{p}, \mathbf{x}) \\ &= \left\{ \frac{\mathbf{p}}{m} \cdot \partial_{\mathbf{r}} - \nabla U(\mathbf{r}) \cdot \partial_{\mathbf{p}} \right\} f(-\mathbf{p}, \mathbf{x}) \\ &= \left\{ -\frac{\mathbf{p}'}{m} \cdot \partial_{\mathbf{r}} + \nabla U(\mathbf{r}) \cdot \partial_{\mathbf{p}'} \right\} f(\mathbf{p}', \mathbf{x}) \\ &= -\hat{\mathbf{L}} f(\mathbf{p}', \mathbf{x}). \end{aligned}$$

The theorem can be shown in the same way for $\mathbf{x} \rightarrow -\mathbf{x}$, supposing the spatial symmetry of the potential, $U(-x_i) = U(x_i)$. ■

Theorem. The operator $\hat{\mathbf{L}}$ is antisymmetric under the scalar product defined in eq. (I.1),

$$\langle \alpha(\mathbf{r}, \mathbf{p}) | \hat{\mathbf{L}} \beta(\mathbf{r}, \mathbf{p}) \rangle = - \langle \hat{\mathbf{L}} \alpha(\mathbf{r}, \mathbf{p}) | \beta(\mathbf{r}, \mathbf{p}) \rangle \quad (\text{I.5})$$

Proof. By usage of partial integration we proof the statement:

$$\begin{aligned} \langle \alpha | \hat{\mathbf{L}} \beta \rangle &= \int d^3\mathbf{r} d^3\mathbf{p} f_0(\mathbf{r}, \mathbf{p}) \alpha(\mathbf{r}, \mathbf{p}) \hat{\mathbf{L}} \beta(\mathbf{r}, \mathbf{p}) \\ &= \int d^3\mathbf{r} d^3\mathbf{p} f_0(\mathbf{r}, \mathbf{p}) \alpha(\mathbf{r}, \mathbf{p}) \left\{ \frac{\mathbf{p}}{m} \cdot \partial_{\mathbf{r}} \beta - \nabla U(\mathbf{r}) \cdot \partial_{\mathbf{p}} \beta \right\} \\ &= \int d^3\mathbf{r} d^3\mathbf{p} f_0(\mathbf{r}, \mathbf{p}) \alpha(\mathbf{r}, \mathbf{p}) \frac{\mathbf{p}}{m} \cdot \partial_{\mathbf{r}} \beta - \\ &\quad - \int d^3\mathbf{r} d^3\mathbf{p} f_0(\mathbf{r}, \mathbf{p}) \alpha(\mathbf{r}, \mathbf{p}) \nabla U(\mathbf{r}) \cdot \partial_{\mathbf{p}} \beta = \\ &= \left[f_0(\mathbf{r}, \mathbf{p}) \alpha(\mathbf{r}, \mathbf{p}) \frac{\mathbf{p}}{m} \beta \right] \Big|_{-\infty}^{\infty} - \int d^3\mathbf{r} d^3\mathbf{p} f_0(\mathbf{r}, \mathbf{p}) \frac{\mathbf{p}}{m} \beta \cdot \partial_{\mathbf{r}} \alpha - \\ &\quad - \left[f_0(\mathbf{r}, \mathbf{p}) \alpha(\mathbf{r}, \mathbf{p}) \nabla U(\mathbf{r}) \beta \right] \Big|_{-\infty}^{\infty} + \int d^3\mathbf{r} d^3\mathbf{p} f_0(\mathbf{r}, \mathbf{p}) \nabla U(\mathbf{r}) \beta \cdot \partial_{\mathbf{p}} \alpha = \\ &= - \int d^3\mathbf{r} d^3\mathbf{p} f_0(\mathbf{r}, \mathbf{p}) \beta(\mathbf{r}, \mathbf{p}) \left\{ \frac{\mathbf{p}}{m} \cdot \partial_{\mathbf{r}} \alpha - \nabla U(\mathbf{r}) \cdot \partial_{\mathbf{p}} \alpha \right\} \\ &= - \langle \hat{\mathbf{L}} \alpha | \beta \rangle . \end{aligned}$$

In the fourth step we assumed that the functions α and β , as well as the normalized distribution function f_0 vanish at least as $1/p^2$ at the infinite limits of the phase space.

A special case of the current theorem is the scalar product with 1, i.e.

$$\int d^3\mathbf{r} d^3\mathbf{p} f_0(\mathbf{r}, \mathbf{p}) \hat{\mathbf{L}} \alpha(\mathbf{r}, \mathbf{p}) = 0 , \quad (\text{I.6})$$

since $f_0(\mathbf{r}, \mathbf{p})$ is a stationary solution of the time independent Boltzmann equation ($\hat{\mathbf{L}} f_0(\mathbf{r}, \mathbf{p}) = 0$). ■

I.3 Vanishing Intergral Terms in Eq. (3.12)

In sec. 3.3 it was mentioned, that the second term in eq. (3.12) vanishes due to symmetry considerations,

$$\left\langle p_i^2 \left| e^{-t\hat{\mathbf{L}}} (\mathbf{p} \cdot \mathbf{q}) \right. \right\rangle = 0 .$$

We will perform at this point the calculation explicitly. The Taylor expansion of the exponential function and the rewriting of the definition of the scalar product (eq. (3.11)) unfolds the

expression to

$$\begin{aligned} \left\langle p_i^2 \left| e^{-t\hat{\mathbf{L}}} (\mathbf{p} \cdot \mathbf{q}) \right. \right\rangle &= \sum_{n=0}^{\infty} \frac{(-t)^n}{n!} \left\langle p_i^2 \left| \hat{\mathbf{L}}^n (\mathbf{p} \cdot \mathbf{q}) \right. \right\rangle \\ &= \sum_{n=0}^{\infty} \frac{(-t)^n}{n!} \int d^3\mathbf{r} d^3\mathbf{p} f_0(\mathbf{r}, \mathbf{p}) p_i^2 \hat{\mathbf{L}}^n (\mathbf{p} \cdot \mathbf{q}) . \end{aligned} \quad (\text{I.7})$$

We regard particularly the integration over p_j with $j \neq i$. The n -th integration term is calculated by

$$\begin{aligned} \int_{k \neq j} d^2 p_k \int_{k \neq j} d^2 r_k p_i^2 \left\{ \int_{-\infty}^{\infty} dr_j \int_{-\infty}^{\infty} dp_j f_0 \hat{\mathbf{L}}^n(p_j q_j) \right\} &= \\ = \int_{k \neq j} d^2 p_k d^2 r_k p_i^2 \left\{ \int_{-\infty}^{\infty} dr_j \int_0^{\infty} dp_j f_0 \hat{\mathbf{L}}^n(p_j q_j) - \int_{-\infty}^{\infty} dr_j \int_0^{-\infty} dp_j f_0 \hat{\mathbf{L}}^n(p_j q_j) \right\} \\ = \int_{k \neq j} d^2 p_k d^2 r_k p_i^2 \left\{ \int_{-\infty}^{\infty} dr_j \int_0^{\infty} dp_j f_0 \hat{\mathbf{L}}^n(p_j q_j) - \int_{\infty}^{-\infty} (-dr'_j) \int_0^{\infty} (-dp'_j) f_0 \hat{\mathbf{L}}^n(-p'_j q_j) \right\} \\ = \int_{k \neq j} d^2 p_k d^2 r_k p_i^2 \left\{ \int_{-\infty}^{\infty} dr_j \int_0^{\infty} dp_j f_0 \hat{\mathbf{L}}^n(p_j q_j) + \int_{-\infty}^{\infty} dr'_j \int_0^{\infty} dp'_j f_0 \hat{\mathbf{L}}^n(-p'_j q_j) \right\} = 0 . \end{aligned}$$

Using one of the properties of the operator $\hat{\mathbf{L}}$ shown in eq. (I.3), we can flip the signs of momentum and position simultaneously in the second integral in the third line, leading to $\hat{\mathbf{L}}[p_j, r_j] = \hat{\mathbf{L}}'[p'_j, r'_j]$. The linearity of $\hat{\mathbf{L}}$ leads to the annihilation of the two integrals in the last line. Similar calculations can be done for the term $j = i$, leading to the same result.

The same arguments can be used to show

$$\left\langle p_i^2 \left| e^{-t\hat{\mathbf{L}}} (p_j p_k) \right. \right\rangle = 0 , \quad \text{for } j \neq k .$$

Indeed, we would split out the integration over dr_j and dp_j and follow the argumentation similar to the integration presented above.

I.4 Properties of the Momentum Redistribution Matrix θ_{ij} from Eq. (3.16)

In this section we will show the symmetry property of the θ_{ij} matrix, which is defined in sec. 3.3 by

$$\theta_{ij}(t) = \left\langle \frac{\beta p_i^2}{m} \left| \left[e^{-t\hat{\mathbf{L}}} - 1 \right] \left(\frac{\beta p_j^2}{m} \right) \right. \right\rangle + 2\delta_{ij} .$$

First, we will proof the following statement:

Theorem. *The momentum redistribution matrix $\theta_{ij}(t)$ is an even function of time t .*

This will later on simplify the proof of the symmetry property of the matrix.

Proof. In order to deal with the simplified integral, we will expand the e function:

$$\theta_{ij}(t) = 2\delta_{ij} + \frac{\beta^2}{m^2} \sum_{n \geq 1} \frac{(-t)^n}{n!} \int d^3\mathbf{r} \int d^3\mathbf{p} f_0(\mathbf{r}, \mathbf{p}) p_i^2 \hat{\mathbf{L}}^n p_j^2 ,$$

where we will now further split-off the dp_j integration,

$$\begin{aligned} \int d^3\mathbf{p} f_0(\mathbf{r}, \mathbf{p}) p_i^2 \hat{\mathbf{L}}^n p_j^2 &= \\ &= \int_{k \neq j} d^2p_k \left\{ \int_0^\infty f_0(\mathbf{r}, \mathbf{p}) p_i^2 \hat{\mathbf{L}}^n p_j^2 dp_j - \int_0^{-\infty} f_0(\mathbf{r}, \mathbf{p}) p_i^2 \hat{\mathbf{L}}^n p_j^2 dp_j \right\} \quad (p'_j = -p_j) \Rightarrow \\ &= \int_{k \neq j} d^2p_k \left\{ \int_0^\infty f_0(\mathbf{r}, \mathbf{p}) p_i^2 \hat{\mathbf{L}}^n p_j^2 dp_j + \int_0^\infty f_0(\mathbf{r}, p_k, p'_j) p_i^2 (-1)^n \hat{\mathbf{L}}^n p_j'^2 dp'_j \right\} . \end{aligned}$$

We applied eq. (I.4) in the last step, since we exchanged the sign of p_j only (without flipping the spatial coordinate r_j). Taking into account the form of $f_0(\mathbf{r}, \mathbf{p})$ (i.e. f_0 depends only on the absolute value of the momentum p , which is invariant under the transformation in the integral above), all terms with odd n vanish. The result can be summarized to

$$\begin{aligned} \theta_{ij}(t) &= 2\delta_{ij} + \frac{\beta^2}{m^2} \sum_{n=1}^{\infty} \frac{(-t)^{2n}}{(2n)!} \int d^3\mathbf{r} d^3\mathbf{p} f_0(\mathbf{r}, \mathbf{p}) p_i^2 \hat{\mathbf{L}}^{2n} p_j^2 \\ &= \delta_{ij} + \frac{\beta^2}{m^2} \sum_{n=1}^{\infty} \frac{(-t)^{2n}}{(2n)!} \langle p_i^2 | \hat{\mathbf{L}}^{2n} p_j^2 \rangle . \end{aligned} \tag{I.8}$$

■

Theorem. The momentum redistribution matrix $\theta_{ij}(t)$ is symmetric,

$$\theta_{ij}(t) = \theta_{ji}(t) .$$

Proof. We will continue the discussion of the previous proof, using directly eq. (I.8). By applying successively eq. (I.5) we deduce

$$\langle p_i^2 | \hat{\mathbf{L}}^{2n} p_j^2 \rangle = - \langle \hat{\mathbf{L}} p_i^2 | \hat{\mathbf{L}}^{2n-1} p_j^2 \rangle = \dots = (-1)^{2n} \langle \hat{\mathbf{L}}^{2n} p_i^2 | p_j^2 \rangle = \langle \hat{\mathbf{L}}^{2n} p_i^2 | p_j^2 \rangle .$$

The scalar product itself is symmetric for real-valued functions. Furthermore, taking into account the symmetry of the Kronecker-delta δ_{ij} , the statement of the theorem is shown. ■

I.5 The Virial Theorem

We will study the expectation value of the quantity $C(t) \langle \mathbf{r} \cdot \mathbf{p} \rangle$, in order to derive the Virial theorem. For a steady state the time derivative vanishes, $\partial_t C(t) = 0$. Rewriting the expectation value as an integral over the distribution f yields:

$$\partial_t C(t) = \int d^3\mathbf{p} d^3\mathbf{r} \partial_t f (\mathbf{r} \cdot \mathbf{p}) = - \int d^3\mathbf{p} d^3\mathbf{r} (\mathbf{r} \cdot \mathbf{p}) \hat{\mathbf{L}} f = \int d^3\mathbf{p} d^3\mathbf{r} f \hat{\mathbf{L}} (\mathbf{r} \cdot \mathbf{p}) \stackrel{!}{=} 0 . \tag{I.9}$$

In the second step we used the Boltzmann equation, while in the last step we utilized the previously shown identity eq. (I.5). We can now apply directly $\hat{\mathbf{L}}$ from eq. (I.2),

$$\hat{\mathbf{L}}(\mathbf{r} \cdot \mathbf{p}) = \frac{p^2}{m} - \mathbf{r} \cdot \partial_{\mathbf{r}} U .$$

If we assume a potential of the form $U(r) = r^n$, the last identity inserted in eq. (I.9) reveals the Virial theorem,

$$2\langle E_{\text{kin}} \rangle - n\langle U \rangle = 0 . \quad (\text{I.10})$$

In the case of the quadrupole potential we have $n = 1$, and the Virial theorem is $2\langle E_{\text{kin}} \rangle = \langle U \rangle$, as stated in eq. (3.18).

I.6 Approximation of the Potential Energy in Eq. (3.45)

For the Taylor approximation of the potential energy $U(\mathbf{r}(\tau))$ we insert the developed spatial coordinate from eq. (3.44) in the argument:

$$\begin{aligned} U(\mathbf{r}(\tau)) &\approx U\left(\mathbf{r}_0 + \tau \frac{\mathbf{p}_0}{m} + \frac{\tau^2}{2} \frac{\mathbf{F}_\delta}{m}\right) \\ &= U(\mathbf{r}_0) + \left\{ \tau \frac{\mathbf{p}_0}{m} + \frac{\tau^2}{2} \frac{\mathbf{F}_\delta}{m} \right\} \partial_{\mathbf{r}} U(\mathbf{r}_0) + \\ &\quad + \frac{1}{2} \left\{ \sum_i \left(\frac{p_{0i}}{m} \tau + \frac{\tau^2}{2} \frac{F_{\delta i}}{m} \right)^2 \partial_{r_i}^2 U(\mathbf{r}_0) + \right. \\ &\quad \left. + 2 \sum_{i \neq j} \left(\frac{p_{0i}}{m} \tau + \frac{\tau^2}{2} \frac{F_{\delta i}}{m} \right) \left(\frac{p_{0j}}{m} \tau + \frac{\tau^2}{2} \frac{F_{\delta j}}{m} \right) \partial_{r_i} \partial_{r_j} U(\mathbf{r}_0) \right\} \\ &\approx U(\mathbf{r}_0) + \left\{ \tau \frac{\mathbf{p}_0}{m} + \frac{\tau^2}{2} \frac{\mathbf{F}_\delta}{m} \right\} \partial_{\mathbf{r}} U(\mathbf{r}_0) + \\ &\quad + \frac{\tau^2}{2m^2} \left\{ \sum_i p_{0i}^2 \partial_{r_i}^2 U(\mathbf{r}_0) + 2 \sum_{i \neq j} p_{0i} p_{0j} \partial_{r_i} \partial_{r_j} U(\mathbf{r}_0) \right\} . \end{aligned} \quad (\text{I.11})$$

In the last step we retained only terms up to second order in τ . Sorting the last expression yields eq. (3.45).

Fermi-Temperature of the SOC System in Sec. 4.3

In this appendix section we derive the Fermi-temperature in the modeled system of spin-orbit coupling which is presented in sec. 4.3. The designed Hamiltonian is given by eq. (4.18),

$$H_{\text{SOC}}(\mathbf{r}, \mathbf{p}) = \frac{p^2}{2m} + \frac{m\omega_r^2}{2}(x^2 + y^2) + \frac{m\omega_z^2}{2}z^2 - \mu b(x\hat{\sigma}_x - y\hat{\sigma}_y) = \frac{p^2}{2m} + U(\mathbf{r}), \quad (\text{J.1})$$

thereby we will continue using the harmonic approximation of the ODT potential within the entire present section.

We will follow the discussion in sec. 5.5.2 in order to derive the Fermi-temperature. Therefore, we use the step function $\Theta(x)$ to describe the density distribution at zero temperature,

$$f_{T=0} = \Theta(\mu_c - E). \quad (\text{J.2})$$

At $T = 0$ the fermions occupy the energy levels E from the lowest possible up to the Fermi-energy $E_F = \mu_c$, which is hence by definition the last occupied energy level.

The spatial density distribution $n(\mathbf{r})$ is obtained directly from the integration over a sphere of occupied momentum values,

$$n_{T=0}(\mathbf{r}) = \int_{p^2 < 2m(E_F - U(\mathbf{r}))} \frac{d^3\mathbf{p}}{(2\pi\hbar)^3} = \frac{1}{6\pi^2\hbar^3} \{2m(E_F - U(\mathbf{r}))\}^{3/2} \quad (\text{J.3})$$

Further integration along the imaging direction z , which is not affected by the SOC terms yields the 2D-density,

$$n_{T=0}(x, y) = \int_{\frac{m\omega_z^2}{2}z^2 \leq E_F - U(x, y)} n_{T=0}(\mathbf{r}) dz = \frac{1}{4\pi\hbar^3} \frac{m}{\omega_z} \{E_F - U(x, y)\}^2. \quad (\text{J.4})$$

In the following we will calculate the Fermi-temperature for the two eigen-energy branches, determined in eq. (4.23) for the Hamiltonian in eq. (J.1), separately by calculating the total atom number,

$$N_{\pm} = \int \mathbf{e}_{\pm}^{\dagger} n_{T=0}(x, y) \mathbf{e}_{\pm} dx dy = \int_{E_{F\pm} \geq E_{\pm}} n_{\pm(T=0)}(x, y) dx dy. \quad (\text{J.5})$$

This will allow us to calculate the dependency of the Fermi-temperature on the atom number in each energy branch.

We will shift both eigen-energy branches by the same constant energy amount $(\mu b)^2/2m\omega_r^2$ compared to eq. (4.22), in order to avoid sign changes of the energy ($E'_-(r) \geq 0$ for $r \in [0, \infty]$),

$$E'_\pm(r) = \frac{m\omega_r^2}{2}r^2 \pm \mu br + \frac{(\mu b)^2}{2m\omega_r^2}. \quad (\text{J.6})$$

At $T = 0$ the Fermi-energy $E_{F\pm}$ fixes the last populated level in the system. Thus, we fix the boundary at $E_{F\pm} \geq E'_\pm$ for the further integration in eq. (J.5) for the calculation of the total atom number,

$$\begin{aligned} E_{F\pm} \geq \frac{m\omega_r^2}{2}r^2 \pm \mu br + \frac{(\mu b)^2}{2m\omega_r^2}, \quad \Leftrightarrow \\ \left[r - \frac{\mp \mu b - \sqrt{2m\omega_r^2 E_{F\pm}}}{m\omega_r^2} \right] \cdot \left[r - \frac{\mp \mu b + \sqrt{2m\omega_r^2 E_{F\pm}}}{m\omega_r^2} \right] \leq 0. \end{aligned} \quad (\text{J.7})$$

The upper sign belongs to the upper branch E'_+ , the lower sign to the lower branch E'_- . We will integrate in the following the atom number for the two energy branches in two separated parts.

Fermi-energy of the upper branch E'_{F+}

For the upper branch the first zero-crossing of the r -axis (first term in eq. (J.7) in square brackets) ranges at $r < 0$. Hence, the integral in eq. (J.5) is calculated within the non-symmetric boundaries

$$0 \leq r \leq \frac{-\mu b + \sqrt{2m\omega_r^2 E_{F+}}}{m\omega_r^2}. \quad (\text{J.8})$$

This reveals the rather complicated expression for the total atom number N_+ as a function of the Fermi-energy E_{F+} ,

$$N_+ \hbar^3 \omega_r^2 \omega_z = \frac{1}{120 \zeta'^3} \left[\kappa'^6 - 10 \kappa'^4 \zeta' E_{F+} + 60 \kappa'^2 \zeta'^2 E_{F+}^2 + 40 \zeta'^3 E_{F+}^3 - 64 \sqrt{2} \kappa' (\zeta' E_{F+})^{5/2} \right], \quad (\text{J.9})$$

where we used similar definitions as in eq. (4.33) to shorten the notation,

$$\kappa' = \mu b, \quad \zeta' = m\omega_r^2. \quad (\text{J.10})$$

The eq. (J.9) can be only solved numerically for $E_{F+}(N_+, \kappa', \zeta')$.

Fermi-energy of the lower branch E'_{F-}

For the integration limits on the lower energy branch we have to consider two cases (see fig. J.1). In case of

$$E_{F-} \leq \frac{(\mu b)^2}{2m\omega_r^2} \Rightarrow \frac{\mu b - \sqrt{2m\omega_r^2 E_{F-}}}{m\omega_r^2} \leq r \leq \frac{\mu b + \sqrt{2m\omega_r^2 E_{F-}}}{m\omega_r^2} \quad \text{Case 1}, \quad (\text{J.11})$$

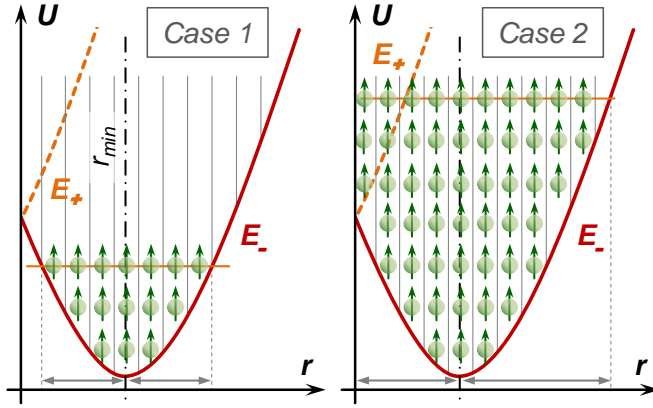


Figure J.1

Illustration of the two integration cases for calculating the total atom number at zero temperature in the lower energy branch. Depending on the atom number N_- for fixed potential parameters, the occupation is either symmetric with respect to the potential minimum r_{min} (Case 1) or not (Case 2). In the latter case the Fermi-temperature will be higher than the potential gap between the upper and lower branch, $k_B T_{F-} \geq E_+(0) - E_-(r_{min})$.

the integration boundaries in eq. (J.5) are symmetric and the atom number yields

$$N_- = 2\pi \int_{Case\ 1} n_-(r) r dr = \frac{1}{\hbar^3 \omega_r^2 \omega_z} \frac{8\sqrt{2}}{15} \frac{\mu b}{\sqrt{m \omega_r^2}} E_{F-}^{5/2} \quad \text{for } E_{F-} \leq \frac{(\mu b)^2}{2m \omega_r^2}. \quad (J.12)$$

Knowing the relation between the Fermi-energy and the atom number allows to translate the constraint "Case 1" in eq. (J.11) to an upper bound for the particle number N_- ,

$$E_{F-} = k_B T_{F-} = \left\{ \frac{15}{8\sqrt{2}} \frac{\sqrt{m \omega_r^2}}{\mu b} \hbar^3 \omega_r^2 \omega_z N_- \right\}^{2/5} \quad \text{for } N_- \leq \frac{16}{15 \hbar^3 \omega_r^2 \omega_z} \left(\frac{\mu b}{\sqrt{2m \omega_r^2}} \right)^6. \quad (J.13)$$

In the second case, we use similar considerations as we used to determine the integration boundaries in eq. (J.8) for the upper branch. Indeed, the integration goes in the second case over the following interval:

$$E_{F-} \geq \frac{(\mu b)^2}{2m \omega_r^2} \Rightarrow 0 \leq r \leq \frac{\mu b + \sqrt{2m \omega_r^2 E_{F-}}}{m \omega_r^2} \quad \text{Case 2}, \quad (J.14)$$

which leads to the atom number – Fermi-energy relation

$$\begin{aligned} N_- &= 2\pi \int_{Case\ 2} n_-(r) r dr \\ &= \frac{1}{120 \zeta'^3} \frac{1}{\hbar^3 \omega_r^2 \omega_z} \left[\kappa'^6 - 10 \kappa'^4 \zeta' E_{F-} + 60 \kappa'^2 \zeta'^2 E_{F-}^2 + 40 \zeta'^3 E_{F-}^3 + 64 \kappa' \sqrt{2} (\zeta' E_{F-})^{5/2} \right], \end{aligned} \quad (J.15)$$

where we used again the quantities from eq. (J.10) to shorten the notation. We note, that the only difference between the second case in eq. (J.15) and the expression eq. (J.9) for the upper branch is the sign of the last term. The only relevant case is *Case 1*, since we want to explore the lower band structure and therefore avoid the occupation of the higher band. Indeed (see fig. J.1), for the second case the Fermi-temperature is already larger than the energy branch-gap ΔU from eq. (4.27).

For the lower energy branch we evaluate the Fermi-temperature for the relevant experimental conditions, which were mentioned in sec. 4.4. Fig. J.2a presents the Fermi-temperature T_{F-}

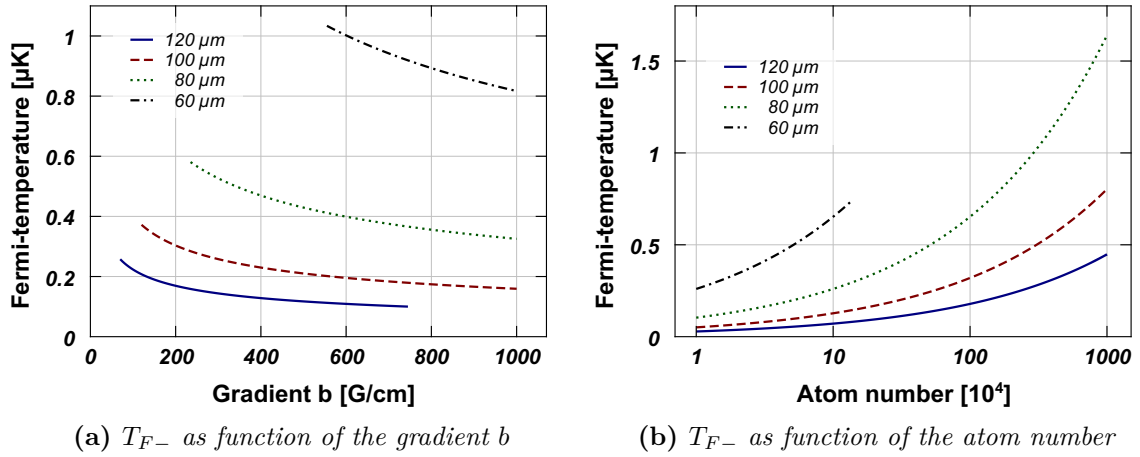


Figure J.2: Fermi-temperature T_{F-} characterization for an ODT potential of total power of 50 W and different waist sizes. In (a) we fix the atom number to $2 \cdot 10^5$ and calculate T_{F-} for different gradients b according to the presented analysis. The trapping frequencies ω_r and ω_z are obtained from eq. (4.14). For (b) we vary the atom number, fixing the gradient to $b = 380 \text{ G/cm}$.

as a function of the gradient b for different ODT potentials, but for a fixed atom number of $2 \cdot 10^5$ spin-polarized ^6Li atoms. On the other hand, fig. J.2b depicts the Fermi-temperature as a function of the atom number for a fixed gradient of 380 G/cm and same ODT parameters. For the relevant experimental scenarios we find $T_{F-} < 1 \mu\text{K}$ and therefore the Fermi-temperature is by far lower than the proposed temperature range $T < 11 \mu\text{K}$ in fig. 4.5. The latter one was determined as an upper bound for an optimal resolution of the ring structure of the density in the lower energy branch.

Bibliography

- [1] M. PLANCK: *Entropie und Temperatur strahlender Wärme*. In: *Annalen der Physik*, **vol. 306**, **no. 4** (1900), pp. 719–737. ISSN: 1521–3889 (cited on page 1).
- [2] A. EINSTEIN: *Über einen die Erzeugung und Verwandlung des Lichtes betreffenden heuristischen Gesichtspunkt*. In: *Annalen der Physik*, **vol. 322**, **no. 6** (1905), pp. 132–148. ISSN: 1521–3889 (cited on page 1).
- [3] N. BOHR: *The Structure of the Atom*. In: *Nature*, **no. 2801** (1923), pp. 29–44 (cited on page 1).
- [4] E. SCHRÖDINGER: *Quantisierung als Eigenwertproblem*. In: *Annalen der Physik*, **vol. 384**, **no. 4** (1926), pp. 361–376. ISSN: 1521–3889 (cited on page 1).
- [5] W. HEISENBERG and W. PAULI: *Zur Quantendynamik der Wellenfelder*. In: *Zeitschrift für Physik*, **vol. 56**, **no. 1** (1929), pp. 1–61. ISSN: 0044-3328 (cited on page 1).
- [6] P. A. M. DIRAC: *The Quantum Theory of the Electron*. In: *Proceedings of the Royal Society of London. Series A, Containing Papers of a Mathematical and Physical Character*, **vol. 117**, **no. 778** (1928), pp. 610–624 (cited on page 1).
- [7] P. A. M. DIRAC: *On the Annihilation of Electrons and Protons*. In: *Mathematical Proceedings of the Cambridge Philosophical Society*, **vol. 26**, **no. 3** (1930), pp. 361–375 (cited on page 1).
- [8] A. EINSTEIN: *Quantentheorie des einatomigen idealen Gases*. In: *Sitzungsberichte der Preussischen Akademie der Wissenschaften* (1924), pp. 261–267 (cited on page 1).
- [9] S. BOSE: *Plancks Gesetz und Lichtquantenhypothese*. In: *Zeitschrift für Physik*, **vol. 26**, **no. 1** (1924), pp. 178–181. ISSN: 0044-3328 (cited on page 1).
- [10] M. H. ANDERSON, J. R. ENSHER, M. R. MATTHEWS, C. E. WIEMAN, and E. A. CORNELL: *Observation of Bose-Einstein Condensation in a Dilute Atomic Vapor*. In: *Science*, **vol. 269**, **no. 5221** (1995), pp. 198–201. ISSN: 0036-8075 (cited on pages 1, 3, 4).
- [11] K. B. DAVIS, M.-O. MEWES, M. R. ANDREWS, N. J. VAN DRUTEN, D. S. DURFEE, D. M. KURN, and W. KETTERLE: *Bose-Einstein Condensation in a Gas of Sodium Atoms*. In: *Phys. Rev. Lett.*, **vol. 75** (22 Nov. 1995), pp. 3969–3973 (cited on pages 1, 3, 4).
- [12] C. C. BRADLEY, C. A. SACKETT, J. J. TOLLETT, and R. G. HULET: *Evidence of Bose-Einstein Condensation in an Atomic Gas with Attractive Interactions*. In: *Phys. Rev. Lett.*, **vol. 75** (9 Aug. 1995), pp. 1687–1690 (cited on pages 1, 4).
- [13] N. F. MOTT and L. FRIEDMAN: *Metal-insulator transitions in VO₂, Ti₂O₃ and Ti_{2-x}V_xO₃*. In: *Philosophical Magazine*, **vol. 30**, **no. 2** (1974), pp. 389–402 (cited on page 1).

- [14] J. HUBBARD: *Electron Correlations in Narrow Energy Bands*. In: *Proceedings of the Royal Society of London A: Mathematical, Physical and Engineering Sciences*, **vol.** 276, **no.** 1365 (1963), pp. 238–257. ISSN: 0080-4630 (cited on page 1).
- [15] R. P. FEYNMAN: *Simulating Physics with Computers*. In: *International Journal of Theoretical Physics*, **vol.** 21, **no.** 6 (1982), pp. 467–488. ISSN: 1572–9575 (cited on page 1).
- [16] M. GREINER, O. MANDEL, T. ESSLINGER, T. W. HÄNSCH, and I. BLOCH: *Quantum Phase Transition from a Superfluid to a Mott Insulator in a Gas of Ultracold Atoms*. In: *Nature*, **vol.** 415, **no.** 6867 (2002), pp. 39–44 (cited on page 1).
- [17] D. G. FRIED, T. C. KILLIAN, L. WILLMANN, D. LANDHUIS, S. C. MOSS, D. KLEPPNER, and T. J. GREYTAK: *Bose-Einstein Condensation of Atomic Hydrogen*. In: *Phys. Rev. Lett.*, **vol.** 81 (18 Nov. 1998), pp. 3811–3814 (cited on page 3).
- [18] F. SCHRECK, L. KHAYKOVICH, K. L. CORWIN, G. FERRARI, T. BOURDEL, J. CUBIZOLLES, and C. SALOMON: *Quasipure Bose-Einstein Condensate Immersed in a Fermi Sea*. In: *Phys. Rev. Lett.*, **vol.** 87 (8 Aug. 2001), p. 080403 (cited on page 3).
- [19] A. G. TRUSCOTT, K. E. STRECKER, W. I. McALEXANDER, G. B. PARTRIDGE, and R. G. HULET: *Observation of Fermi Pressure in a Gas of Trapped Atoms*. In: *Science*, **vol.** 291, **no.** 5513 (2001), pp. 2570–2572. ISSN: 0036-8075 (cited on page 3).
- [20] M. TAGLIEBER, A.-C. VOIGT, T. AOKI, T. W. HÄNSCH, and K. DIECKMANN: *Quantum Degenerate Two-Species Fermi-Fermi Mixture Coexisting with a Bose-Einstein Condensate*. In: *Phys. Rev. Lett.*, **vol.** 100 (1 Jan. 2008), p. 010401 (cited on pages 3, 6).
- [21] I. FERRIER-BARBUT, M. DELEHAYE, S. LAURENT, A. T. GRIER, M. PIERCE, B. S. REM, F. CHEVY, and C. SALOMON: *A Mixture of Bose and Fermi Superfluids*. In: *Science*, **vol.** 345, **no.** 6200 (2014), pp. 1035–1038. ISSN: 0036-8075 (cited on page 3).
- [22] J. W. PARK, C.-H. WU, I. SANTIAGO, T. G. TIECKE, S. WILL, P. AHMADI, and M. W. ZWIERLEIN: *Quantum degenerate Bose-Fermi mixture of chemically different atomic species with widely tunable interactions*. In: *Phys. Rev. A*, **vol.** 85 (5 May 2012), p. 051602 (cited on pages 3, 6).
- [23] B. DEMARCO and D. S. JIN: *Onset of Fermi Degeneracy in a Trapped Atomic Gas*. In: *Science*, **vol.** 285, **no.** 5434 (1999), pp. 1703–1706. ISSN: 0036-8075 (cited on pages 3, 4).
- [24] C.-H. WU, I. SANTIAGO, J. W. PARK, P. AHMADI, and M. W. ZWIERLEIN: *Strongly interacting isotopic Bose-Fermi mixture immersed in a Fermi sea*. In: *Phys. Rev. A*, **vol.** 84 (1 July 2011), p. 011601 (cited on pages 3, 6).
- [25] M. LANDINI, S. ROY, G. ROATI, A. SIMONI, M. INGUSCIO, G. MODUGNO, and M. FATTORI: *Direct evaporative cooling of ^{39}K atoms to Bose-Einstein condensation*. In: *Phys. Rev. A*, **vol.** 86 (3 Sept. 2012), p. 033421 (cited on page 3).
- [26] G. MODUGNO, G. FERRARI, G. ROATI, R. J. BRECHA, A. SIMONI, and M. INGUSCIO: *Bose-Einstein Condensation of Potassium Atoms by Sympathetic Cooling*. In: *Science*, **vol.** 294, **no.** 5545 (2001), pp. 1320–1322. ISSN: 0036-8075 (cited on page 3).

-
- [27] G. ROATI, F. RIBOLI, G. MODUGNO, and M. INGUSCIO: *Fermi-Bose Quantum Degenerate $^{40}\text{K} - ^{87}\text{Rb}$ Mixture with Attractive Interaction*. In: *Phys. Rev. Lett.*, **vol.** 89 (15 Sept. 2002), p. 150403 (cited on page 3).
 - [28] S. L. CORNISH, N. R. CLAUSSEN, J. L. ROBERTS, E. A. CORNELL, and C. E. WIEMAN: *Stable ^{85}Rb Bose-Einstein Condensates with Widely Tunable Interactions*. In: *Phys. Rev. Lett.*, **vol.** 85 (9 Aug. 2000), pp. 1795–1798 (cited on page 3).
 - [29] M. KÖHL, H. MORITZ, T. STÖFERLE, K. GÜNTER, and T. ESSLINGER: *Fermionic Atoms in a Three Dimensional Optical Lattice: Observing Fermi Surfaces, Dynamics, and Interactions*. In: *Phys. Rev. Lett.*, **vol.** 94 (8 Mar. 2005), p. 080403 (cited on page 3).
 - [30] C. SILBER, S. GÜNTHER, C. MARZOK, B. DEH, P. W. COURTEILLE, and C. ZIMMERMANN: *Quantum-Degenerate Mixture of Fermionic Lithium and Bosonic Rubidium Gases*. In: *Phys. Rev. Lett.*, **vol.** 95 (17 Oct. 2005), p. 170408 (cited on page 3).
 - [31] R. PIRES, J. ULMANIS, S. HÄFNER, M. REPP, A. ARIAS, E. D. KUHNLE, and M. WEIDEMÜLLER: *Observation of Efimov Resonances in a Mixture with Extreme Mass Imbalance*. In: *Phys. Rev. Lett.*, **vol.** 112 (25 June 2014), p. 250404 (cited on page 3).
 - [32] T. WEBER, J. HERBIG, M. MARK, H.-C. NÄGERL, and R. GRIMM: *Bose-Einstein Condensation of Cesium*. In: *Science* (2002). ISSN: 0036-8075 (cited on page 3).
 - [33] S.-K. TUNG, C. PARKER, J. JOHANSEN, C. CHIN, Y. WANG, and P. S. JULIENNE: *Ultracold mixtures of atomic ^6Li and ^{133}Cs with tunable interactions*. In: *Phys. Rev. A*, **vol.** 87 (1 Jan. 2013), p. 010702 (cited on page 3).
 - [34] J. E. SIMSARIAN, A. GHOSH, G. GWINNER, L. A. OROZCO, G. D. SPROUSE, and P. A. VOYTAS: *Magneto-Optic Trapping of ^{210}Fr* . In: *Phys. Rev. Lett.*, **vol.** 76 (19 May 1996), pp. 3522–3525 (cited on page 3).
 - [35] S. AUBIN, E. GOMEZ, L. A. OROZCO, and G. D. SPROUSE: *High efficiency magneto-optical trap for unstable isotopes*. In: *Review of Scientific Instruments*, **vol.** 74, **no.** 10 (2003), pp. 4342–4351 (cited on page 3).
 - [36] A. P. KULOSA, D. FIM, K. H. ZIPFEL, S. RÜHMANN, S. SAUER, N. JHA, K. GIBBLE, W. ERTMER, E. M. RASEL, M. S. SAFRONOVA, U. I. SAFRONOVA, and S. G. PORSEV: *Towards a Mg Lattice Clock: Observation of the $^1S_0 - ^3P_0$ Transition and Determination of the Magic Wavelength*. In: *Phys. Rev. Lett.*, **vol.** 115 (24 Dec. 2015), p. 240801 (cited on page 3).
 - [37] M. RIEDMANN, H. KELKAR, T. WÜBBENA, A. PAPE, A. KULOSA, K. ZIPFEL, D. FIM, S. RÜHMANN, J. FRIEBE, W. ERTMER, and E. RASEL: *Beating the density limit by continuously loading a dipole trap from millikelvin-hot magnesium atoms*. In: *Phys. Rev. A*, **vol.** 86 (4 Oct. 2012), p. 043416 (cited on page 3).
 - [38] T. KUROSU and F. SHIMIZU: *Laser Cooling and Trapping of Calcium and Strontium*. In: *Japanese Journal of Applied Physics*, **vol.** 29, **no.** 11A (1990), p. L2127 (cited on page 3).
 - [39] P. HALDER, C.-Y. YANG, and A. HEMMERICH: *Alternative route to Bose-Einstein condensation of two-electron atoms*. In: *Phys. Rev. A*, **vol.** 85 (3 Mar. 2012), p. 031603 (cited on page 3).

- [40] S. KRAFT, F. VOGT, O. APPEL, F. RIEHLE, and U. STERR: *Bose-Einstein Condensation of Alkaline Earth Atoms: ^{40}Ca* . In: *Phys. Rev. Lett.*, **vol. 103** (13 Sept. 2009), p. 130401 (cited on page 3).
- [41] M. K. TEY, S. STELLMER, R. GRIMM, and F. SCHRECK: *Double-degenerate Bose-Fermi mixture of strontium*. In: *Phys. Rev. A*, **vol. 82** (1 July 2010), p. 011608 (cited on page 3).
- [42] S. STELLMER, M. K. TEY, R. GRIMM, and F. SCHRECK: *Bose-Einstein condensation of ^{86}Sr* . In: *Phys. Rev. A*, **vol. 82** (4 Oct. 2010), p. 041602 (cited on page 3).
- [43] X. XU, T. H. LOFTUS, J. L. HALL, A. GALLAGHER, and J. YE: *Cooling and trapping of atomic strontium*. In: *J. Opt. Soc. Am. B*, **vol. 20**, **no. 5** (May 2003), pp. 968–976 (cited on page 3).
- [44] S. DE, U. DAMMALAPATI, K. JUNGSMANN, and L. WILLMANN: *Magneto-optical trapping of barium*. In: *Phys. Rev. A*, **vol. 79** (4 Apr. 2009), p. 041402 (cited on page 3).
- [45] J. R. GUEST, N. D. SCIELZO, I. AHMAD, K. BAILEY, J. P. GREENE, R. J. HOLT, Z.-T. LU, T. P. O’CONNOR, and D. H. POTTERVELD: *Laser Trapping of ^{225}Ra and ^{226}Ra with Repumping by Room-Temperature Blackbody Radiation*. In: *Phys. Rev. Lett.*, **vol. 98** (9 Feb. 2007), p. 093001 (cited on page 3).
- [46] M. LU, N. Q. BURDICK, and B. L. LEV: *Quantum Degenerate Dipolar Fermi Gas*. In: *Phys. Rev. Lett.*, **vol. 108** (21 May 2012), p. 215301 (cited on page 3).
- [47] M. LU, N. Q. BURDICK, S. H. YOUN, and B. L. LEV: *Strongly Dipolar Bose-Einstein Condensate of Dysprosium*. In: *Phys. Rev. Lett.*, **vol. 107** (19 Oct. 2011), p. 190401 (cited on page 3).
- [48] H. KADAU, M. SCHMITT, M. WENZEL, C. WINK, T. MAIER, I. FERRIER-BARBUT, and T. PFAU: *Observing the Rosensweig Instability of a Quantum Ferrofluid*. In: *Nature*, **vol. 530**, **no. 7589** (2016), pp. 194–197 (cited on pages 3, 4).
- [49] Y. TANG, N. Q. BURDICK, K. BAUMANN, and B. L. LEV: *Bose-Einstein condensation of ^{162}Dy and ^{160}Dy* . In: *New Journal of Physics*, **vol. 17**, **no. 4** (2015), p. 045006 (cited on page 3).
- [50] J. MIAO, J. HOSTETTER, G. STRATIS, and M. SAFFMAN: *Magneto-optical trapping of holmium atoms*. In: *Phys. Rev. A*, **vol. 89** (4 Apr. 2014), p. 041401 (cited on page 3).
- [51] K. AIKAWA, A. FRISCH, M. MARK, S. BAIER, R. GRIMM, and F. FERLAINO: *Reaching Fermi Degeneracy via Universal Dipolar Scattering*. In: *Phys. Rev. Lett.*, **vol. 112** (1 Jan. 2014), p. 010404 (cited on pages 3, 4).
- [52] K. AIKAWA, A. FRISCH, M. MARK, S. BAIER, A. RIETZLER, R. GRIMM, and F. FERLAINO: *Bose-Einstein Condensation of Erbium*. In: *Phys. Rev. Lett.*, **vol. 108** (21 May 2012), p. 210401 (cited on page 3).
- [53] B. HEMMERLING, G. K. DRAYNA, E. CHAE, A. RAVI, and J. M. DOYLE: *Buffer gas loaded magneto-optical traps for Yb, Tm, Er and Ho*. In: *New Journal of Physics*, **vol. 16**, **no. 6** (2014), p. 063070 (cited on page 3).
- [54] D. SUKACHEV, A. SOKOLOV, K. CHEBAKOV, A. AKIMOV, S. KANORSKY, N. KOLACHEVSKY, and V. SOROKIN: *Magneto-optical trap for thulium atoms*. In: *Phys. Rev. A*, **vol. 82** (1 July 2010), p. 011405 (cited on page 3).

-
- [55] T. FUKUHARA, Y. TAKASU, M. KUMAKURA, and Y. TAKAHASHI: *Degenerate Fermi Gases of Ytterbium*. In: *Phys. Rev. Lett.*, **vol.** 98 (3 Jan. 2007), p. 030401 (cited on pages 3, 4).
 - [56] S. DÖRSCHER, A. THOBE, B. HUNDT, A. KOCHANKE, R. L. TARGAT, P. WINDPASSINGER, C. BECKER, and K. SENGSTOCK: *Creation of quantum-degenerate gases of ytterbium in a compact 2D-/3D-magneto-optical trap setup*. In: *Review of Scientific Instruments*, **vol.** 84, **no.** 4 (2013), p. 043109 (cited on page 3).
 - [57] V. D. VAIDYA, J. TIAMSUPHAT, S. L. ROLSTON, and J. V. PORTO: *Degenerate Bose-Fermi mixtures of rubidium and ytterbium*. In: *Phys. Rev. A*, **vol.** 92 (4 Oct. 2015), p. 043604 (cited on page 3).
 - [58] V. V. IVANOV, A. KHRAMOV, A. H. HANSEN, W. H. DOWD, F. MÜNCHOW, A. O. JAMISON, and S. GUPTA: *Sympathetic Cooling in an Optically Trapped Mixture of Alkali and Spin-Singlet Atoms*. In: *Phys. Rev. Lett.*, **vol.** 106 (15 Apr. 2011), p. 153201 (cited on page 3).
 - [59] Y. TAKASU, K. MAKI, K. KOMORI, T. TAKANO, K. HONDA, M. KUMAKURA, T. YABUZAKI, and Y. TAKAHASHI: *Spin-Singlet Bose-Einstein Condensation of Two-Electron Atoms*. In: *Phys. Rev. Lett.*, **vol.** 91 (4 July 2003), p. 040404 (cited on page 3).
 - [60] T. FUKUHARA, S. SUGAWA, and Y. TAKAHASHI: *Bose-Einstein condensation of an ytterbium isotope*. In: *Phys. Rev. A*, **vol.** 76 (5 Nov. 2007), p. 051604 (cited on page 3).
 - [61] H. HACHISU, K. MIYAGISHI, S. G. PORSEV, A. DEREVIANKO, V. D. OVSIANNIKOV, V. G. PAL'CHIKOV, M. TAKAMOTO, and H. KATORI: *Trapping of Neutral Mercury Atoms and Prospects for Optical Lattice Clocks*. In: *Phys. Rev. Lett.*, **vol.** 100 (5 Feb. 2008), p. 053001 (cited on page 3).
 - [62] K.-A. BRICKMAN, M.-S. CHANG, M. ACTON, A. CHEW, D. MATSUKEVICH, P. C. HALJAN, V. S. BAGNATO, and C. MONROE: *Magneto-optical trapping of cadmium*. In: *Phys. Rev. A*, **vol.** 76 (4 Oct. 2007), p. 043411 (cited on page 3).
 - [63] G. UHLENBERG, J. DIRSCHERL, and H. WALTHER: *Magneto-optical trapping of silver atoms*. In: *Phys. Rev. A*, **vol.** 62 (6 Nov. 2000), p. 063404 (cited on page 3).
 - [64] B. NAYLOR, A. REIGUE, E. MARÉCHAL, O. GORCEIX, B. LABURTHE-TOLRA, and L. VERNAC: *Chromium dipolar Fermi sea*. In: *Phys. Rev. A*, **vol.** 91 (1 Jan. 2015), p. 011603 (cited on page 3).
 - [65] B. NAYLOR, E. MARÉCHAL, J. HUCKANS, O. GORCEIX, P. PEDRI, L. VERNAC, and B. LABURTHE-TOLRA: *Cooling of a Bose-Einstein Condensate by Spin Distillation*. In: *Phys. Rev. Lett.*, **vol.** 115 (24 Dec. 2015), p. 243002 (cited on page 3).
 - [66] A. GRIESMAIER, J. WERNER, S. HENSLER, J. STUHLER, and T. PFAU: *Bose-Einstein Condensation of Chromium*. In: *Phys. Rev. Lett.*, **vol.** 94 (16 Apr. 2005), p. 160401 (cited on page 3).
 - [67] F. PEREIRA DOS SANTOS, J. LÉONARD, J. WANG, C. J. BARRELET, F. PERALES, E. RASEL, C. S. UNNIKRISSNAN, M. LEDUC, and C. COHEN-TANNOUDJI: *Bose-Einstein Condensation of Metastable Helium*. In: *Phys. Rev. Lett.*, **vol.** 86 (16 Apr. 2001), pp. 3459–3462 (cited on page 3).

- [68] A. ROBERT, O. SIRJEAN, A. BROWAEYS, J. POUPARD, S. NOWAK, D. BOIRON, C. I. WESTBROOK, and A. ASPECT: *A Bose-Einstein Condensate of Metastable Atoms*. In: *Science*, **vol.** 292, **no.** 5516 (2001), pp. 461–464. ISSN: 0036-8075 (cited on page 3).
- [69] J. M. MCNAMARA, T. JELTES, A. S. TYCHKOV, W. HOGERVORST, and W. VASSEN: *Degenerate Bose-Fermi Mixture of Metastable Atoms*. In: *Phys. Rev. Lett.*, **vol.** 97 (8 Aug. 2006), p. 080404 (cited on page 3).
- [70] T. HÄNSCH and A. L. SCHAWLOW: *Cooling of gases by laser radiation*. In: *Optics Communications*, **vol.** 13, **no.** 1 (1975), pp. 68–69. ISSN: 0030-4018 (cited on page 2).
- [71] H. J. METCALF and P. VAN DER STRATEN: *Laser Cooling and Trapping*. Springer-Verlag New York, 1999. ISBN: 978-0-387-98728-6 (cited on pages 2, 13, 15, 21).
- [72] S. CHU, L. HOLLBERG, J. E. BJORKHOLM, A. CABLE, and A. ASHKIN: *Three-dimensional viscous confinement and cooling of atoms by resonance radiation pressure*. In: *Phys. Rev. Lett.*, **vol.** 55 (1 July 1985), pp. 48–51 (cited on page 2).
- [73] E. L. RAAB, M. PRENTISS, A. CABLE, S. CHU, and D. E. PRITCHARD: *Trapping of Neutral Sodium Atoms with Radiation Pressure*. In: *Phys. Rev. Lett.*, **vol.** 59 (23 Dec. 1987), pp. 2631–2634 (cited on page 2).
- [74] J. DALIBARD and C. COHEN-TANNOUDJI: *Laser Cooling below the Doppler Limit by Polarization Gradients: Simple Theoretical Models*. In: *J. Opt. Soc. Am. B*, **vol.** 6, **no.** 11 (Nov. 1989), pp. 2023–2045 (cited on pages 2, 21).
- [75] J. WALRAVEN: *Atomic Hydrogen in Magnetostatic Traps*. In: *Quantum Dynamics of Simple Systems*. Ed. by G.-L. OPPO, S. M. BARNETT, E. RIIS, and M. WILKINSON. Vol. 44. SUSSP Proceedings. IOP: Bristol, 1996 (cited on pages 4, 105).
- [76] W. KETTERLE and N. J. VAN DRUTEN: *Evaporative Cooling of Trapped Atoms*. In: *Advances in Atomic, Molecular and Optical Physics*, **vol.** 37 (1996), pp. 181–236 (cited on pages 4, 87, 90).
- [77] W. KETTERLE, D. S. DURFEE, and D. M. STAMPER-KURN: *Making, probing and understanding Bose-Einstein condensates*. In: *arXiv preprint cond-mat/9904034* (Apr. 1999), pp. 67–176 (cited on page 4).
- [78] L. TARRUELL, D. GREIF, T. UEHLINGER, G. JOTZU, and T. ESSLINGER: *Creating, moving and merging Dirac points with a Fermi gas in a tunable honeycomb lattice*. In: *Nature*, **vol.** 483, **no.** 7389 (2012), pp. 302–305 (cited on page 4).
- [79] M. LEWENSTEIN, A. SANPERA, V. AHUFINGER, B. DAMSKI, A. SEN(DE), and U. SEN: *Ultracold atomic gases in optical lattices: mimicking condensed matter physics and beyond*. In: *Advances in Physics*, **vol.** 56, **no.** 2 (2007), pp. 243–379 (cited on page 4).
- [80] N. GOLDMAN, J. BUDICH, and P. ZOLLER: *Topological quantum matter with ultracold gases in optical lattices*. In: *Nature Physics*, **vol.** 12, **no.** 7 (2016), pp. 639–645 (cited on page 4).
- [81] T. LAHAYE, C. MENOTTI, L. SANTOS, M. LEWENSTEIN, and T. PFAU: *The physics of dipolar bosonic quantum gases*. In: *Reports on Progress in Physics*, **vol.** 72, **no.** 12 (2009), p. 126401 (cited on page 4).

-
- [82] S. R. GRANADE, M. E. GEHM, K. M. O'HARA, and J. E. THOMAS: *All-Optical Production of a Degenerate Fermi Gas*. In: *Phys. Rev. Lett.*, **vol.** 88 (12 Mar. 2002), p. 120405 (cited on page 4).
 - [83] B. SHUVE and J. H. THYWISSEN: *Enhanced Pauli blocking of light scattering in a trapped Fermi gas*. In: *Journal of Physics B: Atomic, Molecular and Optical Physics*, **vol.** 43, **no.** 1 (2010), p. 015301 (cited on page 5).
 - [84] A. GÖRLITZ, A. P. CHIKKATUR, and W. KETTERLE: *Enhancement and suppression of spontaneous emission and light scattering by quantum degeneracy*. In: *Phys. Rev. A*, **vol.** 63 (4 Mar. 2001), p. 041601 (cited on page 5).
 - [85] C. CHIN, R. GRIMM, P. JULIENNE, and E. TIESINGA: *Feshbach resonances in ultracold gases*. In: *Rev. Mod. Phys.*, **vol.** 82 (2 Apr. 2010), pp. 1225–1286 (cited on pages 5, 90, 103).
 - [86] M. W. ZWIERLEIN, J. R. ABO-SHAER, A. SCHIROTZEK, C. H. SCHUNCK, and W. KETTERLE: *Vortices and superfluidity in a strongly interacting Fermi gas*. In: *Nature*, **vol.** 435, **no.** 7045 (2005), pp. 1047–1051 (cited on pages 5, 6).
 - [87] D. S. PETROV, C. SALOMON, and G. V. SHLYAPNIKOV: *Weakly Bound Dimers of Fermionic Atoms*. In: *Phys. Rev. Lett.*, **vol.** 93 (9 Aug. 2004), p. 090404 (cited on page 5).
 - [88] J. BARDEEN, L. N. COOPER, and J. R. SCHRIEFFER: *Theory of Superconductivity*. In: *Phys. Rev.*, **vol.** 108 (5 Dec. 1957), pp. 1175–1204 (cited on page 5).
 - [89] W. KETTERLE and M. W. ZWIERLEIN: *Making, probing and understanding ultracold Fermi gases*. In: *Riviste Societa Italiana di Fisica* (5–6 July 2008), pp. 247–422 (cited on pages 6, 116).
 - [90] Q. CHEN, J. STAJIC, S. TAN, and K. LEVIN: *BCS–BEC crossover: From high temperature superconductors to ultracold superfluids*. In: *Physics Reports*, **vol.** 412, **no.** 1 (2005), pp. 1–88. ISSN: 0370-1573 (cited on page 6).
 - [91] E. HALLER, J. HUDSON, A. KELLY, D. A. COTTA, B. PEAUDECERF, G. D. BRUCE, and S. KUHR: *Single-atom imaging of fermions in a quantum-gas microscope*. In: *Nature Physics*, **vol.** 11, **no.** 9 (2015), pp. 738–742 (cited on page 6).
 - [92] P. M. PREISS, R. MA, M. E. TAI, J. SIMON, and M. GREINER: *Quantum gas microscopy with spin, atom-number, and multilayer readout*. In: *Phys. Rev. A*, **vol.** 91 (4 Apr. 2015), p. 041602 (cited on page 6).
 - [93] L. W. CHEUK, M. A. NICHOLS, M. OKAN, T. GERSDORF, V. V. RAMASESH, W. S. BAKR, T. LOMPE, and M. W. ZWIERLEIN: *Quantum-Gas Microscope for Fermionic Atoms*. In: *Phys. Rev. Lett.*, **vol.** 114 (19 May 2015), p. 193001 (cited on page 6).
 - [94] A. OMRAN, M. BOLL, T. A. HILKER, K. KLEINLEIN, G. SALOMON, I. BLOCH, and C. GROSS: *Microscopic Observation of Pauli Blocking in Degenerate Fermionic Lattice Gases*. In: *Phys. Rev. Lett.*, **vol.** 115 (26 Dec. 2015), p. 263001 (cited on page 6).
 - [95] W. S. BAKR, A. PENG, M. E. TAI, R. MA, J. SIMON, J. I. GILLEN, S. FÖLLING, L. POLLET, and M. GREINER: *Probing the Superfluid-to-Mott Insulator Transition at the Single-Atom Level*. In: *Science*, **vol.** 329, **no.** 5991 (2010), pp. 547–550. ISSN: 0036-8075 (cited on page 6).

- [96] J. LEVINSSEN, T. G. TIECKE, J. T. M. WALRAVEN, and D. S. PETROV: *Atom-Dimer Scattering and Long-Lived Trimers in Fermionic Mixtures*. In: *Phys. Rev. Lett.*, **vol.** 103 (15 Oct. 2009), p. 153202 (cited on page 6).
- [97] A.-C. VOIGT, M. TAGLIEBER, L. COSTA, T. AOKI, W. WIESER, T. W. HÄNSCH, and K. DIECKMANN: *Ultracold Heteronuclear Fermi-Fermi Molecules*. In: *Phys. Rev. Lett.*, **vol.** 102 (2 Jan. 2009), p. 020405 (cited on page 6).
- [98] T. G. TIECKE, M. R. GOOSEN, A. LUDEWIG, S. D. GENSEMER, S. KRAFT, S. J. J. M. F. KOKKELMANS, and J. T. M. WALRAVEN: *Broad Feshbach Resonance in the $^6\text{Li} - ^{40}\text{K}$ Mixture*. In: *Phys. Rev. Lett.*, **vol.** 104 (5 Feb. 2010), p. 053202 (cited on page 6).
- [99] E. WILLE, F. M. SPIEGELHALDER, G. KERNER, D. NAIK, A. TRENKWALDER, G. HENDL, F. SCHRECK, R. GRIMM, T. G. TIECKE, J. T. M. WALRAVEN, S. J. J. M. F. KOKKELMANS, E. TIESINGA, and P. S. JULIENNE: *Exploring an Ultracold Fermi-Fermi Mixture: Interspecies Feshbach Resonances and Scattering Properties of ^6Li and ^{40}K* . In: *Phys. Rev. Lett.*, **vol.** 100 (5 Feb. 2008), p. 053201 (cited on pages 6, 37).
- [100] F. M. SPIEGELHALDER, A. TRENKWALDER, D. NAIK, G. KERNER, E. WILLE, G. HENDL, F. SCHRECK, and R. GRIMM: *All-optical production of a degenerate mixture of ^6Li and ^{40}K and creation of heteronuclear molecules*. In: *Phys. Rev. A*, **vol.** 81 (4 Apr. 2010), p. 043637 (cited on page 7).
- [101] A. TRENKWALDER, C. KOHSTALL, M. ZACCANTI, D. NAIK, A. I. SIDOROV, F. SCHRECK, and R. GRIMM: *Hydrodynamic Expansion of a Strongly Interacting Fermi-Fermi Mixture*. In: *Phys. Rev. Lett.*, **vol.** 106 (11 Mar. 2011), p. 115304 (cited on page 7).
- [102] M. JAG, M. ZACCANTI, M. CETINA, R. S. LOUS, F. SCHRECK, R. GRIMM, D. S. PETROV, and J. LEVINSSEN: *Observation of a Strong Atom-Dimer Attraction in a Mass-Imbalanced Fermi-Fermi Mixture*. In: *Phys. Rev. Lett.*, **vol.** 112 (7 Feb. 2014), p. 075302 (cited on page 7).
- [103] X.-C. YAO, H.-Z. CHEN, P. WU, X.-P. LIU, X.-Q. WANG, X. JIANG, Y. DENG, A. CHEN, and J.-W. PAN: *Observation of Coupled Vortex Lattices in a Mass-Imbalance Bose and Fermi Superfluid Mixture*. In: *Phys. Rev. Lett.*, **vol.** 117 (14 Sept. 2016), p. 145301 (cited on page 7).
- [104] U. GAVISH and Y. CASTIN: *Matter-Wave Localization in Disordered Cold Atom Lattices*. In: *Phys. Rev. Lett.*, **vol.** 95 (2 July 2005), p. 020401 (cited on page 7).
- [105] G. ROATI, C. D'ERRICO, L. FALLANI, M. FATTORI, C. FORT, M. ZACCANTI, G. MODUGNO, M. MODUGNO, and M. INGUSCIO: *Anderson localization of a non-interacting Bose-Einstein condensate*. In: *Nature*, **vol.** 453, **no.** 7197 (2008), pp. 895–898 (cited on page 7).
- [106] Y. NISHIDA and S. TAN: *Universal Fermi Gases in Mixed Dimensions*. In: *Phys. Rev. Lett.*, **vol.** 101 (17 Oct. 2008), p. 170401 (cited on pages 7, 12).
- [107] A. RIDINGER, S. CHAUDHURI, T. SALEZ, U. EISMANN, D. R. FERNANDES, K. MAGALHÃES, D. WILKOWSKI, C. SALOMON, and F. CHEVY: *Large atom number dual-species magneto-optical trap for fermionic ^6Li and ^{40}K atoms*. In: *The European Physical Journal D*, **vol.** 65, **no.** 1 (2011), pp. 223–242. ISSN: 1434-6079 (cited on page 7).

-
- [108] A. RIDINGER: *Towards quantum degenerate Fermi mixtures: Photoassociation of weakly bound ${}^6\text{Li} - {}^{40}\text{K}$ molecules*. Thesis. Ecole Normale Supérieure de Paris - ENS Paris, Apr. 2011 (cited on pages 9, 12, 14, 17, 32, 36, 128).
 - [109] T. SALEZ: *Towards quantum degenerate atomic Fermi mixtures*. Thesis. Ecole Normale Supérieure de Paris - ENS Paris, Sept. 2011 (cited on page 9).
 - [110] D. R. FERNANDES: *Trapping and cooling of fermionic alkali atoms to quantum degeneracy. Sub-Doppler cooling of Potassium-40 and Lithium-6 in gray molasses*. Thesis. Université Pierre et Marie Curie, Sept. 2014 (cited on pages 9, 12, 20, 25, 83, 93, 94).
 - [111] F. SIEVERS: *Ultracold Fermi mixtures and simultaneous sub-Doppler laser cooling of fermionic ${}^6\text{Li}$ and ${}^{40}\text{K}$* . Thesis. Université Pierre et Marie Curie - Paris VI, July 2014 (cited on pages 9, 10, 13, 17, 20, 23, 31, 44, 100).
 - [112] N. KRETZSCHMAR: *Experiments with Ultracold Fermi Gases: Quantum Degeneracy of Potassium-40 and All-solid-state Laser Sources for Lithium*. Thesis. ENS Paris - Ecole Normale Supérieure de Paris, June 2015 (cited on page 9).
 - [113] A. RIDINGER, S. CHAUDHURI, T. SALEZ, D. R. FERNANDES, N. BOULOUPA, O. DULIEU, C. SALOMON, and F. CHEVY: *Photoassociative creation of ultracold heteronuclear ${}^6\text{Li} {}^{40}\text{K}^*$ molecules*. In: *EPL (Europhysics Letters)*, **vol. 96**, **no. 3** (2011), p. 33001 (cited on page 9).
 - [114] D. R. FERNANDES, F. SIEVERS, N. KRETZSCHMAR, S. WU, C. SALOMON, and F. CHEVY: *Sub-Doppler laser cooling of fermionic 40 K atoms in three-dimensional gray optical molasses*. In: *EPL (Europhysics Letters)*, **vol. 100**, **no. 6** (2012), p. 63001 (cited on pages 9, 20, 22, 23).
 - [115] W. D. PHILLIPS and H. METCALF: *Laser Deceleration of an Atomic Beam*. In: *Phys. Rev. Lett.*, **vol. 48** (9 Mar. 1982), pp. 596–599 (cited on page 10).
 - [116] K. DIECKMANN, R. J. C. SPREEUW, M. WEIDEMÜLLER, and J. T. M. WALRAVEN: *Two-dimensional magneto-optical trap as a source of slow atoms*. In: *Phys. Rev. A*, **vol. 58** (5 Nov. 1998), pp. 3891–3895 (cited on page 10).
 - [117] Y. NISHIDA: *Phases of a bilayer Fermi gas*. In: *Phys. Rev. A*, **vol. 82** (1 July 2010), p. 011605 (cited on pages 12, 116, 117).
 - [118] D. SUCHET: *Simulating the dynamics of harmonically trapped Weyl particles with cold atoms*. Thesis. Université Pierre et Marie Curie, July 2016 (cited on pages 12, 46, 51, 59, 115, 117).
 - [119] G. LAMPORESI, J. CATANI, G. BARONTINI, Y. NISHIDA, M. INGUSCIO, and F. MINARDI: *Scattering in Mixed Dimensions with Ultracold Gases*. In: *Phys. Rev. Lett.*, **vol. 104** (15 Apr. 2010), p. 153202 (cited on page 12).
 - [120] K. A. YAKIMOVICH and A. G. MOZGOVOI: *Experimental Investigation of the Density and Surface Tension of Molten Lithium at Temperatures up to 1300 K*. In: *High Temperature*, **vol. 38**, **no. 4** (2000), pp. 657–659. ISSN: 1608-3156 (cited on page 13).
 - [121] J. TAYLOR: *XCVIII. The surface energies of the alkali metals*. In: *The London, Edinburgh, and Dublin Philosophical Magazine and Journal of Science*, **vol. 46**, **no. 379** (1955), pp. 867–876 (cited on page 13).

- [122] B. DeMARCO, H. ROHNER, and D. S. JIN: *An enriched 40K source for fermionic atom studies*. In: *Review of Scientific Instruments*, **vol.** 70, **no.** 4 (1999), pp. 1967–1969 (cited on page 14).
- [123] C. KLEMP, T. VAN ZOEST, T. HENNINGER, O. TOPIC, E. RASEL, W. ERTMER, and J. ARLT: *Ultraviolet light-induced atom desorption for large rubidium and potassium magneto-optical traps*. In: *Phys. Rev. A*, **vol.** 73 (1 Jan. 2006), p. 013410 (cited on page 15).
- [124] B. P. ANDERSON and M. A. KASEVICH: *Loading a vapor-cell magneto-optic trap using light-induced atom desorption*. In: *Phys. Rev. A*, **vol.** 63 (2 Jan. 2001), p. 023404 (cited on page 15).
- [125] E. MIMOUN, L. D. SARLO, D. JACOB, J. DALIBARD, and F. GERBIER: *Fast production of ultracold sodium gases using light-induced desorption and optical trapping*. In: *Phys. Rev. A*, **vol.** 81 (2 Feb. 2010), p. 023631 (cited on page 15).
- [126] G. FERRARI, M.-O. MEWES, F. SCHRECK, and C. SALOMON: *High-power multiple-frequency narrow-linewidth laser source based on a semiconductor tapered amplifier*. In: *Opt. Lett.*, **vol.** 24, **no.** 3 (Feb. 1999), pp. 151–153 (cited on page 17).
- [127] T. TIECKE: *Properties of Potassium*. May 2011 (cited on pages 20, 28).
- [128] M. E. GEHM: *Properties of 6Li*. Feb. 2003 (cited on pages 20, 28).
- [129] F. SIEVERS, N. KRETZSCHMAR, D. R. FERNANDES, D. SUCHET, M. RABINOVIC, S. WU, C. V. PARKER, L. KHAYKOVICH, C. SALOMON, and F. CHEVY: *Simultaneous sub-Doppler laser cooling of fermionic ^6Li and ^{40}K on the D_1 line: Theory and experiment*. In: *Phys. Rev. A*, **vol.** 91 (2 Feb. 2015), p. 023426 (cited on pages 20, 23).
- [130] G. MODUGNO, C. BENK Ö, P. HANNAFORD, G. ROATI, and M. INGUSCIO: *Sub-Doppler laser cooling of fermionic ^{40}K atoms*. In: *Phys. Rev. A*, **vol.** 60 (5 Nov. 1999), R3373–R3376 (cited on page 21).
- [131] V. GOKHROO, G. RAJALAKSHMI, R. K. EASWARAN, and C. S. UNNIKRISHNAN: *Sub-Doppler deep-cooled bosonic and fermionic isotopes of potassium in a compact 2D + -3D MOT set-up*. In: *Journal of Physics B: Atomic, Molecular and Optical Physics*, **vol.** 44, **no.** 11 (2011), p. 115307 (cited on page 21).
- [132] E. BRION, L. H. PEDERSEN, and K. MOLMER: *Adiabatic elimination in a lambda system*. In: *Journal of Physics A: Mathematical and Theoretical*, **vol.** 40, **no.** 5 (2007), p. 1033 (cited on page 21).
- [133] R. HAN, H. K. NG, and B.-G. ENGLERT: *Raman transitions without adiabatic elimination: a simple and accurate treatment*. In: *Journal of Modern Optics*, **vol.** 60, **no.** 4 (2013), pp. 255–265 (cited on page 21).
- [134] M. OL'SHANÏ and V. MINOGIN: *Three-dimensional velocity-selective coherent population trapping of a (3+3)-level atom*. In: *Optics Communications*, **vol.** 89, **no.** 5 (1992), pp. 393–398. ISSN: 0030-4018 (cited on page 21).
- [135] S. KULIN: *Préparation et manipulation de paquets d'ondes atomiques ultrafroids*. Thesis. Université Pierre et Marie Curie - Paris VI, Sept. 1997 (cited on page 21).
- [136] A. NAGEL: *Precision Spectroscopy of Coherent Dark States in Thermal Cesium Vapour*. Thesis. Rheinische Friedrich-Wilhelms-Universität Bonn, Apr. 1999 (cited on page 21).

-
- [137] M. WEIDEMÜLLER, T. ESSLINGER, M. A. OL'SHANII, A. HEMMERICH, and T. W. HÄNSCH: *A Novel Scheme for Efficient Cooling below the Photon Recoil Limit*. In: *EPL (Europhysics Letters)*, **vol.** 27, **no.** 2 (1994), p. 109 (cited on page 22).
 - [138] M. S. SHAHRIAR, P. R. HEMMER, M. G. PRENTISS, P. MARTE, J. MERVIS, D. P. KATZ, N. P. BIGELOW, and T. CAI: *Continuous polarization-gradient precooling-assisted velocity-selective coherent population trapping*. In: *Phys. Rev. A*, **vol.** 48 (6 Dec. 1993), R4035–R4038 (cited on page 22).
 - [139] P. M. DUARTE, R. A. HART, J. M. HITCHCOCK, T. A. CORCOVILOS, T.-L. YANG, A. REED, and R. G. HULET: *All-optical production of a lithium quantum gas using narrow-line laser cooling*. In: *Phys. Rev. A*, **vol.** 84 (6 Dec. 2011), p. 061406 (cited on page 25).
 - [140] J. SEBASTIAN, C. GROSS, K. LI, H. C. J. GAN, W. LI, and K. DIECKMANN: *Two-stage magneto-optical trapping and narrow-line cooling of ^6Li atoms to high phase-space density*. In: *Phys. Rev. A*, **vol.** 90 (3 Sept. 2014), p. 033417 (cited on page 25).
 - [141] D. C. MCKAY, D. JERVIS, D. J. FINE, J. W. SIMPSON-PORCO, G. J. A. EDGE, and J. H. THYWISSEN: *Low-temperature high-density magneto-optical trapping of potassium using the open $4S \rightarrow 5P$ transition at 405 nm*. In: *Phys. Rev. A*, **vol.** 84 (6 Dec. 2011), p. 063420 (cited on page 25).
 - [142] A. T. GRIER, I. FERRIER-BARBUT, B. S. REM, M. DELEHAYE, L. KHAYKOVICH, F. CHEVY, and C. SALOMON: *Λ -enhanced sub-Doppler cooling of lithium atoms in D_1 gray molasses*. In: *Phys. Rev. A*, **vol.** 87 (6 June 2013), p. 063411 (cited on page 25).
 - [143] G. SALOMON, L. FOUCHÉ, P. WANG, A. ASPECT, P. BOUYER, and T. BOURDEL: *Gray-molasses cooling of 39K to a high phase-space density*. In: *EPL (Europhysics Letters)*, **vol.** 104, **no.** 6 (2013), p. 63002 (cited on page 25).
 - [144] G. COLZI, G. DURASTANTE, E. FAVA, S. SERAFINI, G. LAMPORESI, and G. FERRARI: *Sub-Doppler cooling of sodium atoms in gray molasses*. In: *Phys. Rev. A*, **vol.** 93 (2 Feb. 2016), p. 023421 (cited on page 25).
 - [145] H.-Z. CHEN, X.-C. YAO, P. WU, X.-P. LIU, X.-Q. WANG, X. WANG, A. CHEN, and J.-W. PAN: *Production of large ^{41}K Bose-Einstein condensates using D_1 gray molasses*. In: *Phys. Rev. A*, **vol.** 94 (3 Sept. 2016), p. 033408 (cited on page 25).
 - [146] D. NATH, R. K. EASWARAN, G. RAJALAKSHMI, and C. S. UNNIKRISHNAN: *Quantum-interference-enhanced deep sub-Doppler cooling of ^{39}K atoms in gray molasses*. In: *Phys. Rev. A*, **vol.** 88 (5 Nov. 2013), p. 053407 (cited on page 25).
 - [147] A. BURCHIANI, G. VALTOLINA, J. A. SEMAN, E. PACE, M. DE PAS, M. INGUSCIO, M. ZACCANTI, and G. ROATI: *Efficient all-optical production of large ^6Li quantum gases using D_1 gray-molasses cooling*. In: *Phys. Rev. A*, **vol.** 90 (4 Oct. 2014), p. 043408 (cited on page 25).
 - [148] A. L. MIGDALL, J. V. PRODAN, W. D. PHILLIPS, T. H. BERGEMAN, and H. J. METCALF: *First Observation of Magnetically Trapped Neutral Atoms*. In: *Phys. Rev. Lett.*, **vol.** 54 (24 June 1985), pp. 2596–2599 (cited on page 25).
 - [149] B. DEMARCO: *Quantum Behavior of an Atomic Fermi Gas*. Thesis. University of Colorado, 2001 (cited on pages 25, 27).

- [150] J. PÉREZ-RÍOS and A. S. SANZ: *How does a magnetic trap work?* In: *American Journal of Physics*, **vol. 81**, **no. 11** (2013), pp. 836–843 (cited on page 25).
- [151] T. MAYER-KUCKUK: *Atomphysik*. B. G. Teubner Stuttgart, 1997. ISBN: 3-519-43042-8 (cited on page 27).
- [152] B. DEMARCO and D. S. JIN: *Exploring a quantum degenerate gas of fermionic atoms*. In: *Phys. Rev. A*, **vol. 58** (6 Dec. 1998), R4267–R4270 (cited on page 27).
- [153] T. L. GUSTAVSON, A. P. CHIKKATUR, A. E. LEANHARDT, A. GÖRLITZ, S. GUPTA, D. E. PRITCHARD, and W. KETTERLE: *Transport of Bose-Einstein Condensates with Optical Tweezers*. In: *Phys. Rev. Lett.*, **vol. 88** (2 Dec. 2001), p. 020401 (cited on page 30).
- [154] C. GROSS, H. C. J. GAN, and K. DIECKMANN: *All-optical production and transport of a large ^6Li quantum gas in a crossed optical dipole trap*. In: *Phys. Rev. A*, **vol. 93** (5 May 2016), p. 053424 (cited on page 30).
- [155] M. GREINER, I. BLOCH, T. W. HÄNSCH, and T. ESSLINGER: *Magnetic transport of trapped cold atoms over a large distance*. In: *Phys. Rev. A*, **vol. 63** (3 Feb. 2001), p. 031401 (cited on page 30).
- [156] W. WOHLLEBEN, F. CHEVY, K. MADISON, and J. DALIBARD: *An atom faucet*. In: *The European Physical Journal D - Atomic, Molecular, Optical and Plasma Physics*, **vol. 15**, **no. 2** (2001), pp. 237–244. ISSN: 1434-6079 (cited on page 30).
- [157] H. J. LEWANDOWSKI, D. M. HARBER, D. L. WHITAKER, and E. A. CORNELL: *Simplified System for Creating a Bose-Einstein Condensate*. In: *Journal of Low Temperature Physics*, **vol. 132**, **no. 5** (2003), pp. 309–367. ISSN: 1573-7357 (cited on page 31).
- [158] K. NAKAGAWA, Y. SUZUKI, M. HORIKOSHI, and J. KIM: *Simple and efficient magnetic transport of cold atoms using moving coils for the production of Bose-Einstein condensation*. In: *Applied Physics B*, **vol. 81**, **no. 6** (2005), pp. 791–794. ISSN: 1432-0649 (cited on page 31).
- [159] J. LÉONARD, M. LEE, A. MORALES, T. M. KARG, T. ESSLINGER, and T. DONNER: *Optical transport and manipulation of an ultracold atomic cloud using focus-tunable lenses*. In: *New Journal of Physics*, **vol. 16**, **no. 9** (2014), p. 093028 (cited on page 31).
- [160] *PCO PixelFly QE 270XS - User's Manual*. PCO AG. 2006 (cited on page 33).
- [161] A. KESHET and W. KETTERLE: *A distributed, graphical user interface based, computer control system for atomic physics experiments*. In: *Review of Scientific Instruments*, **vol. 84**, **no. 1** (2013), p. 015105 (cited on page 37).
- [162] W. KOHN: *Cyclotron Resonance and de Haas-van Alphen Oscillations of an Interacting Electron Gas*. In: *Phys. Rev.*, **vol. 123** (4 Aug. 1961), pp. 1242–1244 (cited on page 43).
- [163] S. BRAUN, J. P. RONZHEIMER, M. SCHREIBER, S. S. HODGMAN, T. ROM, I. BLOCH, and U. SCHNEIDER: *Negative Absolute Temperature for Motional Degrees of Freedom*. In: *Science*, **vol. 339**, **no. 6115** (2013), pp. 52–55. ISSN: 0036-8075 (cited on page 43).
- [164] K. B. DAVIS, M.-O. MEWES, M. A. JOFFE, M. R. ANDREWS, and W. KETTERLE: *Evaporative Cooling of Sodium Atoms*. In: *Phys. Rev. Lett.*, **vol. 74** (26 June 1995), pp. 5202–5205 (cited on page 43).

-
- [165] P. CHOMAZ, F. GULMINELLI, and O. JUILLET: *Generalized Gibbs ensembles for time-dependent processes*. In: *Annals of Physics*, **vol. 320**, **no. 1** (2005), pp. 135–163. ISSN: 0003–4916 (cited on page 65).
 - [166] D. SUCHET, M. RABINOVIC, T. REIMANN, N. KRETSCHMAR, F. SIEVERS, C. SALOMON, J. LAU, O. GOULKO, C. LOBO, and F. CHEVY: *Analog simulation of Weyl particles with cold atoms*. In: *EPL (Europhysics Letters)*, **vol. 114**, **no. 2** (2016), p. 26005 (cited on page 65).
 - [167] P. G. SILVESTROV and K. B. EFETOV: *Quantum Dots in Graphene*. In: *Phys. Rev. Lett.*, **vol. 98** (1 Jan. 2007), p. 016802 (cited on page 68).
 - [168] S. M. YOUNG, S. ZAHEER, J. C. Y. TEO, C. L. KANE, E. J. MELE, and A. M. RAPPE: *Dirac Semimetal in Three Dimensions*. In: *Phys. Rev. Lett.*, **vol. 108** (14 Apr. 2012), p. 140405 (cited on page 69).
 - [169] H. WEYL: *Elektron und Gravitation. I*. In: *Zeitschrift für Physik*, **vol. 56**, **no. 5** (1929), pp. 330–352. ISSN: 0044–3328 (cited on page 69).
 - [170] A. BANSIL, H. LIN, and T. DAS: *Colloquium*. In: *Rev. Mod. Phys.*, **vol. 88** (2 June 2016), p. 021004 (cited on page 69).
 - [171] Y. XU, I. BELOPOLSKI, N. ALIDoust, M. NEUPANE, G. BIAN, C. ZHANG, R. SANKAR, G. CHANG, Z. YUAN, C.-C. LEE, S.-M. HUANG, H. ZHENG, J. MA, D. S. SANCHEZ, B. WANG, A. BANSIL, F. CHOU, P. P. SHIBAYEV, H. LIN, S. JIA, and M. Z. HASAN: *Discovery of a Weyl Fermion semimetal and topological Fermi arcs*. In: *Science* (2015). ISSN: 0036–8075 (cited on page 69).
 - [172] B. Q. LV, H. M. WENG, B. B. FU, X. P. WANG, H. MIAO, J. MA, P. RICHARD, X. C. HUANG, L. X. ZHAO, G. F. CHEN, Z. FANG, X. DAI, T. QIAN, and H. DING: *Experimental Discovery of Weyl Semimetal TaAs*. In: *Phys. Rev. X*, **vol. 5** (3 July 2015), p. 031013 (cited on page 69).
 - [173] L. LU, Z. WANG, D. YE, L. RAN, L. FU, J. D. JOANNOPOULOS, and M. SOLJAČIĆ: *Experimental observation of Weyl points*. In: *Science*, **vol. 349**, **no. 6248** (2015), pp. 622–624. ISSN: 0036–8075 (cited on page 69).
 - [174] O. KLEIN: *Die Reflexion von Elektronen an einem Potentialsprung nach der relativistischen Dynamik von Dirac*. In: *Zeitschrift für Physik*, **vol. 53**, **no. 3** (1929), pp. 157–165. ISSN: 0044–3328 (cited on page 69).
 - [175] R. GERRITSMA, B. P. LANYON, G. KIRCHMAIR, F. ZÄHRINGER, C. HEMPEL, J. CASANOVA, J. J. GARCÍA-RIPOLL, E. SOLANO, R. BLATT, and C. F. ROOS: *Quantum Simulation of the Klein Paradox with Trapped Ions*. In: *Phys. Rev. Lett.*, **vol. 106** (6 Feb. 2011), p. 060503 (cited on page 69).
 - [176] M. KATSNELSON, K. NOVOSELOV, and A. GEIM: *Chiral tunnelling and the Klein paradox in graphene*. In: *Nature physics*, **vol. 2**, **no. 9** (2006), pp. 620–625 (cited on page 69).
 - [177] D. C. TSUI, H. L. STORMER, and A. C. GOSSARD: *Two-Dimensional Magnetotransport in the Extreme Quantum Limit*. In: *Phys. Rev. Lett.*, **vol. 48** (22 May 1982), pp. 1559–1562 (cited on page 70).
 - [178] H. L. STORMER, D. C. TSUI, and A. C. GOSSARD: *The fractional quantum Hall effect*. In: *Rev. Mod. Phys.*, **vol. 71** (2 Mar. 1999), S298–S305 (cited on page 70).

- [179] J. R. ABO-SHAER, C. RAMAN, J. M. VOGELS, and W. KETTERLE: *Observation of Vortex Lattices in Bose-Einstein Condensates*. In: *Science*, **vol.** 292, **no.** 5516 (2001), pp. 476–479. ISSN: 0036-8075 (cited on page 70).
- [180] Y.-J. LIN, R. L. COMPTON, K. JIMÉNEZ-GARCÍA, J. V. PORTO, and I. B. SPIELMAN: *Synthetic magnetic fields for ultracold neutral atoms*. In: *Nature*, **vol.** 462, **no.** 7273 (2009), pp. 628–632 (cited on page 70).
- [181] K. W. MADISON, F. CHEVY, V. BRETIN, and J. DALIBARD: *Stationary States of a Rotating Bose-Einstein Condensate: Routes to Vortex Nucleation*. In: *Phys. Rev. Lett.*, **vol.** 86 (20 May 2001), pp. 4443–4446 (cited on page 70).
- [182] Y.-J. LIN, K. JIMÉNEZ-GARCÍA, and I. SPIELMAN: *Spin-orbit-coupled Bose-Einstein condensates*. In: *Nature*, **vol.** 471, **no.** 7336 (2011), pp. 83–86 (cited on page 70).
- [183] Y. AHARONOV and D. BOHM: *Significance of Electromagnetic Potentials in the Quantum Theory*. In: *Phys. Rev.*, **vol.** 115 (3 Aug. 1959), pp. 485–491 (cited on pages 70, 71).
- [184] G. DRESSELHAUS: *Spin-Orbit Coupling Effects in Zinc Blende Structures*. In: *Phys. Rev.*, **vol.** 100 (2 Oct. 1955), pp. 580–586 (cited on page 70).
- [185] A. YU, V. I. MELNIKOV, and E. I. RASHBA: *Effect of spin-orbit coupling on the energy spectrum of a 2D electron system in a tilted magnetic field*. In: *Sov. Phys. JETP*, **vol.** 71, **no.** 2 (1990), pp. 401–405 (cited on page 70).
- [186] M. Z. HASAN and C. L. KANE: *Colloquium: Topological insulators*. In: *Rev. Mod. Phys.*, **vol.** 82 (4 Nov. 2010), pp. 3045–3067 (cited on page 70).
- [187] A. MANCHON, H. KOO, J. NITTA, S. FROLOV, and R. DUINE: *New perspectives for Rashba spin-orbit coupling*. In: *Nature materials*, **vol.** 14, **no.** 9 (2015), pp. 871–882 (cited on page 70).
- [188] I. ŽUTIĆ, J. FABIAN, and S. DAS SARMA: *Spintronics: Fundamentals and applications*. In: *Rev. Mod. Phys.*, **vol.** 76 (2 Apr. 2004), pp. 323–410 (cited on page 70).
- [189] L. MEIER, G. SALIS, I. SHORUBALKO, E. GINI, S. SCHÖN, and K. ENSSLIN: *Measurement of Rashba and Dresselhaus spin-orbit magnetic fields*. In: *Nature Physics*, **vol.** 3, **no.** 9 (2007), pp. 650–654 (cited on page 70).
- [190] G. JUZELIŪNAS, J. RUSECKAS, and J. DALIBARD: *Generalized Rashba-Dresselhaus spin-orbit coupling for cold atoms*. In: *Phys. Rev. A*, **vol.** 81 (5 May 2010), p. 053403 (cited on page 70).
- [191] G. HOOFT: *Magnetic monopoles in unified gauge theories*. In: *Nuclear Physics: B*, **vol.** 79, **no.** 2 (1974), pp. 276–284 (cited on page 71).
- [192] F. A. BAIS and R. J. RUSSELL: *Magnetic-monopole solution of non-Abelian gauge theory in curved spacetime*. In: *Phys. Rev. D*, **vol.** 11 (10 May 1975), pp. 2692–2695 (cited on page 71).
- [193] J. DALIBARD, F. GERBIER, G. JUZELIŪNAS, and P. ÖHBERG: *Colloquium: Artificial gauge potentials for neutral atoms*. In: *Rev. Mod. Phys.*, **vol.** 83 (4 Nov. 2011), pp. 1523–1543 (cited on page 71).
- [194] J. RUSECKAS, G. JUZELIŪNAS, P. ÖHBERG, and M. FLEISCHHAUER: *Non-Abelian Gauge Potentials for Ultracold Atoms with Degenerate Dark States*. In: *Phys. Rev. Lett.*, **vol.** 95 (1 June 2005), p. 010404 (cited on page 71).

-
- [195] T. D. STANESCU, C. ZHANG, and V. GALITSKI: *Nonequilibrium Spin Dynamics in a Trapped Fermi Gas with Effective Spin-Orbit Interactions*. In: *Phys. Rev. Lett.*, **vol.** 99 (11 Sept. 2007), p. 110403 (cited on page 71).
 - [196] G. JUZELIŪNAS, J. RUSECKAS, M. LINDBERG, L. SANTOS, and P. ÖHBERG: *Quasirelativistic behavior of cold atoms in light fields*. In: *Phys. Rev. A*, **vol.** 77 (1 Jan. 2008), p. 011802 (cited on page 71).
 - [197] F. GERBIER and J. DALIBARD: *Gauge fields for ultracold atoms in optical superlattices*. In: *New Journal of Physics*, **vol.** 12, **no.** 3 (2010), p. 033007 (cited on page 71).
 - [198] S. SINHA, R. NATH, and L. SANTOS: *Trapped Two-Dimensional Condensates with Synthetic Spin-Orbit Coupling*. In: *Phys. Rev. Lett.*, **vol.** 107 (27 Dec. 2011), p. 270401 (cited on page 71).
 - [199] X. CHEN, M. RABINOVIC, B. M. ANDERSON, and L. SANTOS: *Ring model for trapped condensates with synthetic spin-orbit coupling*. In: *Phys. Rev. A*, **vol.** 90 (4 Oct. 2014), p. 043632 (cited on page 71).
 - [200] R. GRIMM, M. WEIDEMÜLLER, and Y. B. OVCHINNIKOV: *Optical Dipole Traps for Neutral Atoms*. In: *Advances In Atomic, Molecular, and Optical Physics*, **vol.** 42 (2000). Ed. by B. BEDERSON and H. WALTHER, pp. 95–170. ISSN: 1049–250X (cited on pages 71, 118).
 - [201] W. PETRICH, M. H. ANDERSON, J. R. ENSHER, and E. A. CORNELL: *Stable, Tightly Confining Magnetic Trap for Evaporative Cooling of Neutral Atoms*. In: *Phys. Rev. Lett.*, **vol.** 74 (17 Apr. 1995), pp. 3352–3355 (cited on page 84).
 - [202] M.-S. HEO, J.-Y. CHOI, and Y.-I. SHIN: *Fast production of large ^{23}Na Bose-Einstein condensates in an optically plugged magnetic quadrupole trap*. In: *Phys. Rev. A*, **vol.** 83 (1 Jan. 2011), p. 013622 (cited on page 84).
 - [203] R. DUBESSY, K. MERLOTI, L. LONGCHAMON, P.-E. POTTIE, T. LIENNARD, A. PERRIN, V. LORENT, and H. PERRIN: *Rubidium-87 Bose-Einstein condensate in an optically plugged quadrupole trap*. In: *Phys. Rev. A*, **vol.** 85 (1 Jan. 2012), p. 013643 (cited on page 84).
 - [204] B. DEMARCO, J. L. BOHN, J. P. BURKE, M. HOLLAND, and D. S. JIN: *Measurement of p-Wave Threshold Law Using Evaporatively Cooled Fermionic Atoms*. In: *Phys. Rev. Lett.*, **vol.** 82 (21 May 1999), pp. 4208–4211 (cited on pages 88, 91).
 - [205] C. COHEN-TANNOUDJI: *Atomes ultrafroids - Piègeage non dissipatif et refroidissement évaporatif*. University Lecture. 1996 (cited on pages 88–90, 105).
 - [206] O. J. LUITEN, M. W. REYNOLDS, and J. T. M. WALRAVEN: *Kinetic theory of the evaporative cooling of a trapped gas*. In: *Phys. Rev. A*, **vol.** 53 (1 Jan. 1996), pp. 381–389 (cited on pages 89, 90, 105).
 - [207] B. S. REM: *The Road to the Unitary Bose Gas*. Thesis. Université Pierre et Marie Curie - Paris VI, Dec. 2013 (cited on pages 89, 105).
 - [208] J. WALRAVEN: *Elements of Quantum Gases: Thermodynamic and Collisional Properties of Trapped Atomic Gases*. University Lecture. Feb. 2010 (cited on page 89).
 - [209] H. F. HESS: *Evaporative cooling of magnetically trapped and compressed spin-polarized hydrogen*. In: *Phys. Rev. B*, **vol.** 34 (5 Sept. 1986), pp. 3476–3479 (cited on page 90).

- [210] S. FALKE, H. KNÖCKEL, J. FRIEBE, M. RIEDMANN, E. TIEMANN, and C. LISDAT: *Potassium ground-state scattering parameters and Born-Oppenheimer potentials from molecular spectroscopy*. In: *Phys. Rev. A*, **vol.** 78 (1 July 2008), p. 012503 (cited on page 91).
- [211] Y.-J. LIN, A. R. PERRY, R. L. COMPTON, I. B. SPIELMAN, and J. V. PORTO: *Rapid production of ^{87}Rb Bose-Einstein condensates in a combined magnetic and optical potential*. In: *Phys. Rev. A*, **vol.** 79 (6 June 2009), p. 063631 (cited on page 94).
- [212] A. LUDEWIG: *Feshbach Resonances in 40K*. Thesis. University of Amsterdam, Mar. 2012 (cited on pages 95, 98, 104).
- [213] K. M. O'HARA, M. E. GEHM, S. R. GRANADE, and J. E. THOMAS: *Scaling laws for evaporative cooling in time-dependent optical traps*. In: *Phys. Rev. A*, **vol.** 64 (5 Oct. 2001), p. 051403 (cited on page 95).
- [214] D. A. S. MEYRATH: *Quantum and Atom Optics*. Feb. 2017 (cited on page 97).
- [215] T. P. MEYRATH: *Electromagnet Design Basics for Cold Atom Experiments*. Aug. 2004 (cited on page 101).
- [216] E. TIMMERMANS, P. TOMMASINI, M. HUSSEIN, and A. KERMAN: *Feshbach resonances in atomic Bose-Einstein condensates*. In: *Physics Reports*, **vol.** 315, **no.** 1 (1999), pp. 199–230 (cited on page 103).
- [217] C. REGAL: *Experimental realization of BCS-BEC crossover physics with a Fermi gas of atoms*. Thesis. University of Colorado - Department of Physics, 2006 (cited on pages 104, 106).
- [218] R. M. CORLESS, G. H. GONNET, D. E. HARE, D. J. JEFFREY, and D. E. KNUTH: *On the Lambert W Function*. 1996 (cited on page 105).
- [219] T. LOFTUS, C. A. REGAL, C. TICKNOR, J. L. BOHN, and D. S. JIN: *Resonant Control of Elastic Collisions in an Optically Trapped Fermi Gas of Atoms*. In: *Phys. Rev. Lett.*, **vol.** 88 (17 Apr. 2002), p. 173201 (cited on page 106).
- [220] C. A. REGAL, M. GREINER, and D. S. JIN: *Observation of Resonance Condensation of Fermionic Atom Pairs*. In: *Phys. Rev. Lett.*, **vol.** 92 (4 Jan. 2004), p. 040403 (cited on page 106).
- [221] C. A. REGAL, C. TICKNOR, J. L. BOHN, and D. S. JIN: *Tuning p-Wave Interactions in an Ultracold Fermi Gas of Atoms*. In: *Phys. Rev. Lett.*, **vol.** 90 (5 Feb. 2003), p. 053201 (cited on page 106).
- [222] J. S. KRAUSER, J. HEINZE, S. GÖTZE, M. LANGBECKER, N. FLÄSCHNER, L. COOK, T. M. HANNA, E. TIESINGA, K. SENGSTOCK, and C. BECKER: *Investigation of Feshbach Resonances in ultra-cold 40K spin mixtures*. In: *arXiv - Condensed Matter, Quantum Gases* (Jan. 2017) (cited on page 106).
- [223] Q. BEAUFILS, A. CRUBELLIER, T. ZANON, B. LABURTHE-TOLRA, E. MARÉCHAL, L. VERNAC, and O. GORCEIX: *Feshbach resonance in d-wave collisions*. In: *Phys. Rev. A*, **vol.** 79 (3 Mar. 2009), p. 032706 (cited on page 106).

-
- [224] T. BOURDEL, L. KHAYKOVICH, J. CUBIZOLLES, J. ZHANG, F. CHEVY, M. TEICHMANN, L. TARRUELL, S. J. J. M. F. KOKKELMANS, and C. SALOMON: *Experimental Study of the BEC-BCS Crossover Region in Lithium 6*. In: *Phys. Rev. Lett.*, **vol. 93** (5 July 2004), p. 050401 (cited on page 107).
 - [225] C. H. SCHUNCK, M. W. ZWIERLEIN, C. A. STAN, S. M. F. RAUPACH, W. KETTERLE, A. SIMONI, E. TIESINGA, C. J. WILLIAMS, and P. S. JULIENNE: *Feshbach resonances in fermionic ^6Li* . In: *Phys. Rev. A*, **vol. 71** (4 Apr. 2005), p. 045601 (cited on page 107).
 - [226] M. BARTENSTEIN, A. ALTMAYER, S. RIEDL, S. JOCHIM, C. CHIN, J. H. DENSCHLAG, and R. GRIMM: *Crossover from a Molecular Bose-Einstein Condensate to a Degenerate Fermi Gas*. In: *Phys. Rev. Lett.*, **vol. 92** (12 Mar. 2004), p. 120401 (cited on page 107).
 - [227] M. W. ZWIERLEIN, C. A. STAN, C. H. SCHUNCK, S. M. F. RAUPACH, A. J. KERMAN, and W. KETTERLE: *Condensation of Pairs of Fermionic Atoms near a Feshbach Resonance*. In: *Phys. Rev. Lett.*, **vol. 92** (12 Mar. 2004), p. 120403 (cited on page 107).
 - [228] J. KINAST, S. L. HEMMER, M. E. GEHM, A. TURLAPOV, and J. E. THOMAS: *Evidence for Superfluidity in a Resonantly Interacting Fermi Gas*. In: *Phys. Rev. Lett.*, **vol. 92** (15 Apr. 2004), p. 150402 (cited on page 114).
 - [229] C. A. REGAL, C. TICKNOR, J. L. BOHN, and D. S. JIN: *Creation of ultracold molecules from a Fermi gas of atoms*. In: *Nature*, **vol. 424**, **no. 6944** (2003), pp. 47–50 (cited on page 114).
 - [230] N. NAVON, S. NASCIMBÈNE, F. CHEVY, and C. SALOMON: *The Equation of State of a Low-Temperature Fermi Gas with Tunable Interactions*. In: *Science*, **vol. 328**, **no. 5979** (2010), pp. 729–732. ISSN: 0036-8075 (cited on page 114).
 - [231] T. PAIVA, R. SCALETTAR, M. RANDERIA, and N. TRIVEDI: *Fermions in 2D Optical Lattices: Temperature and Entropy Scales for Observing Antiferromagnetism and Superfluidity*. In: *Phys. Rev. Lett.*, **vol. 104** (6 Feb. 2010), p. 066406 (cited on page 117).
 - [232] I. BLOCH, J. DALIBARD, and W. ZWERGER: *Many-body physics with ultracold gases*. In: *Rev. Mod. Phys.*, **vol. 80** (3 July 2008), pp. 885–964 (cited on page 118).
 - [233] C. J. HAWTHORN, K. P. WEBER, and R. E. SCHOLTEN: *Littrow configuration tunable external cavity diode laser with fixed direction output beam*. In: *Review of Scientific Instruments*, **vol. 72**, **no. 12** (2001), pp. 4477–4479 (cited on page 119).
 - [234] *Tapered Amplifier - GaAs Semiconductor Laser Diode*. Eagleyard photonics. Sept. 2008 (cited on page 127).
 - [235] J. C. B. KANGARA, A. J. HACHTEL, M. C. GILLETTE, J. T. BARKELOO, E. R. CLEMENTS, S. BALI, B. E. UNKS, N. A. PROITE, D. D. YAVUZ, P. J. MARTIN, J. J. THORN, and D. A. STECK: *Design and construction of cost-effective tapered amplifier systems for laser cooling and trapping experiments*. In: *American Journal of Physics*, **vol. 82**, **no. 8** (2014), pp. 805–817 (cited on page 128).
 - [236] *Very High CMR Logic Gate Optocouplers*. Avago Technologies. Sept. 2016 (cited on page 143).
 - [237] *Optocoupler Designer's Guide*. Agilent Technologies. June 2002 (cited on pages 143, 144).
 - [238] *40ns Propagation Delay, CMOS Optocoupler*. Avago Technologies. Apr. 2013 (cited on page 143).

- [239] *IGBT (Insulated Gate Bipolar Transistor)*. Siemens - Infineon (cited on page 145).
- [240] *ACPL-3130 Very High CMR 2.5 Amp Output Current IGBT Gate Driver Optocoupler*. Avago Technologies. Oct. 2013 (cited on page 145).
- [241] *HCNR200 and HCNR201 - High-Linearity Analog Optocouplers*. Avago Technologies. July 2014 (cited on pages 145, 146).
- [242] *SPICE Circuit Simulations for the HCNR200 and HCNR210 Analog Optocouplers*. Avago Technologies. Jan. 2012 (cited on page 145).
- [243] *AD845 - Precision, 16 MHz CBFET Op Amp*. Analog Devices. 2003 (cited on page 145).
- [244] *LT1021 - Precision Reference*. Linear Technology. 1995 (cited on pages 145, 147).
- [245] *LT1031/LK0070 - Precision 10V Reference*. Linear Technology. 2005 (cited on page 147).
- [246] *REF102 - 10V Precision Voltage Reference*. Texas Instruments. June 2009 (cited on page 147).
- [247] *LED 395-66-60-110 - High Power LED Array, 60 chips, Glass Window*. Roithner LaserTechnik GmbH. Feb. 2012 (cited on page 149).
- [248] *LM317 - 3-Terminal Adjustable Regulator*. Texas Instruments. Sept. 2016 (cited on page 149).
- [249] P. HOROWITZ and W. HILL: *The Art of Electronics*. New York, NY, USA: Cambridge University Press, 1989. ISBN: 0-521-37095-7 (cited on page 149).

Acknowledgements

A modern quantum gas experiment is a huge technological challenge on multiple levels in distinct fields, for example electronics, optics and mechanical design. It is a great team effort to build, maintain or modify an experimental setup and to keep the machine running in order to obtain the presented experimental data. I would like to take this opportunity to acknowledge the contributions to the presented work of all the people who helped me during the period of my PhD.

- First, I want to express my gratitude to my thesis supervisors, Frédéric Chevy and Christophe Salomon, for providing me the opportunity to work for four years in their laboratory and for organizing a more than adequate financial basis for the experiment so that we never had any privation in instrumentation. Christophe has incredible experience working with technological tools and an incomparable intuition for finding the small bugs, which would from time to time paralyze our machine. His ability to estimate within seconds the magnitude of observable quantities is astonishing and therefore he was able to provide us each time with very good ranges for the necessary tuning parameters, which guided our search for technological solutions or relevant data. Frédéric has an outstanding theoretical understanding of a vast variety of subjects in physics. It is undoubtful that without his help, a major part of the presented work would not be possible. Both, Frédéric and Christophe, always gave our team the right portion of liberty over the years, so that we could discover the quantum world of atoms and the corresponding techniques at our own pace!
- Second, I would like to thank my lab-mates and friends, from the previous and current FerMix generations, who accompanied me every day in the lab. From the older generation, I would like to thank Franz Sievers and Norman Kretzschmar, who introduced me to the experiment and helped me a lot during my first year in the lab. The small electronics projects Norman gave me during this time introduced me, step by step, to the subject of analogue circuits and motivated me later to continue on into the digital world of microcontrollers. Norman was the major drive during my first years, shaping the experimentalist and "technician" I have become. I also want to thank Diogo Fernandes for introducing me into the controls of the experiment and Daniel Suchet for his nice and clear mathematica library, which is still used to analyze the experimental TOF or lifetime data. I am also very grateful to our youngest members, Thomas Reimann, Cedric Enesa and Markus Bohlen, who accompanied me during my last years working on the experiment and proof-read the manuscript with great patience. I wish them all the best for their future scientific endeavors with the K-Li machine.

- Similarly, I want to mention all of my colleagues from the neighboring labs belonging to our group, who contributed on a daily basis by sharing useful advice and lending equipment, whenever it was necessary. On that note, I would like to thank Benno Rem, Igor Ferrier-Barbut, Andrew Grier and Marion Delehayé from the old Lithium experiment. I owe especially my deepest gratitude to Sébastien Laurent, with whom I became close friends over the course of my PhD. Sébastien introduced me to the french culture and lifestyle, always provided a good advise also outside the laboratory life and shared very interesting, extended discussions about literature and music. Thanks to Sébastien, I have been integrated into the french society, which is, without any doubt, one of the key points of a PhD-program abroad. I would also like to thank the youngest members of our large group, Matthieu Pierce and Shuwei Jin and all the numerous "stagiaires", who worked in our group over different periods – they all supported greatly our experiments and contributed their spirit to the friendly and stimulating research atmosphere. Through our discussions, I realized that I need to continue to contemplate several questions, which I had assumed that I understood or that I had not considered in the first place. Special thanks goes to Darby Bates for proofreading parts of the thesis. Last but not least, I want to thank Tarik Yefsah, who joined our team as a permanent researcher during my last year, for his inexhaustible energy to push forward the experiment, even when difficult problems arose.
- It would be wrong to neglect the other PhD students and researchers of the cold gases community in the LKB, with whom I have spent time in the lab and elsewhere. Representatively, I would like to thank Konstantin Ott, Davide Dreon, Torben Pöpplau, Felix Werner and my conference-"travel buddy" Chayma Bouazza. I would also like to thank Fabrice Gerbier, Jakob Reichel, Pierre-Jean Nacher and Geneviève Tastevin for their fruitful and motivating discussions and advice.
- We would be unable to travel to any conference or to buy our equipment without the secretariat of our department. I want to thank Christophe Bernard, Monique Granon, Dominique Giafferi, Nora Aissous, Audrey Gohlke and Thierry Tardieu for their work and apologize for making it more difficult by losing sometimes the delivery slips and missing from time to time some deadlines. Speaking of missed deadlines, I would like to acknowledge the help of the école doctorale, especially Stéphane Emery and Laura Ledez, in filling out forms and handling all the necessary bureaucracy, after I had almost passed the deadlines for the submissions of my manuscript and thesis defense.
- During my PhD, part of the LKB building underwent a major renovation. Throughout this process, the entire facility management team of the LKB did an amazing job protecting the experiment and maintaining the electrical and water circuits in our underground laboratory. Therefore, I want to express my gratitude to the team of Didier Courtiade, Catherine Gripe and Célia Ruschinzik, and the electric workshop team of Jean-Marc Jussear, Franck Bouchereau and Philippe Rousseau. Without your permanent engagement, the experiment would not have survived.
- I acquired a lot of technological knowledge about mechanical and electronic design during my four years at the LKB. From a mere hobby, it has developed into a passion. Therefore, I wish to thank the engineers Jean-Michel Isac and Arnaud Leclercq, for introducing

me to the basics of mechanical design considerations and for correcting my amateurish design drawings. I owe my deepest gratitude to the workers of the mechanical workshop, particularly to Jules Aimé Silembo, Mathieu Sardin, Allan Hourdry, Aboubakar Lassana and the retired members Richard Pescari and Michel Quidu, as well as to the welding team of Jose Romer and Georges Cornudet, who taught me to realize different mechanical pieces on my own in the machine shop. During the aforementioned renovation period, I spent a lot of time on several electronic projects, of which a few are discussed in the appendix of this manuscript. All these projects would not have been possible without the help of Toufik El Atmani and Lionel Perennes. Thank you very much for always finding time to answer my questions whenever I suddenly appeared in your workshop. I owe you most of the electronic skills I have acquired so far.

Without the technical staff, the high-tech experiment FerMix could never have achieved today's form. This manuscript is dedicated to the workers of the LKB who invested hours, days, and often entire weeks to support and realize our technological requirements!

- My thanks also go to the jury members Jook T. M. Walraven, Isabelle Bouchoule, Stefan Kuhr, Patricia Vignolo and Carlos Lobo for joining my thesis committee and reading, commenting, and reporting on my thesis manuscript.
- I would like to thank few friends who accompanied me through the last years outside of the lab and provided a contrast to the daily scientific work, notably Isabel Espinosa, Gerbold Menard and Emilien Nory. Also, I wish to acknowledge the long lasting friendships with Jonathan Vorndamme and Volker Voss. It was also a pleasure to be introduced to organ playing by Matteo Parenti – thank you very much for this unique opportunity!
- Finally, I would like to express my deepest gratitude to my family, particularly to my brother, Alexander, my mother, and especially my father for the enduring, unlimited, and invaluable support. I apologize for sometimes taking for granted, without acknowledging sufficiently, the sacrifices they made.

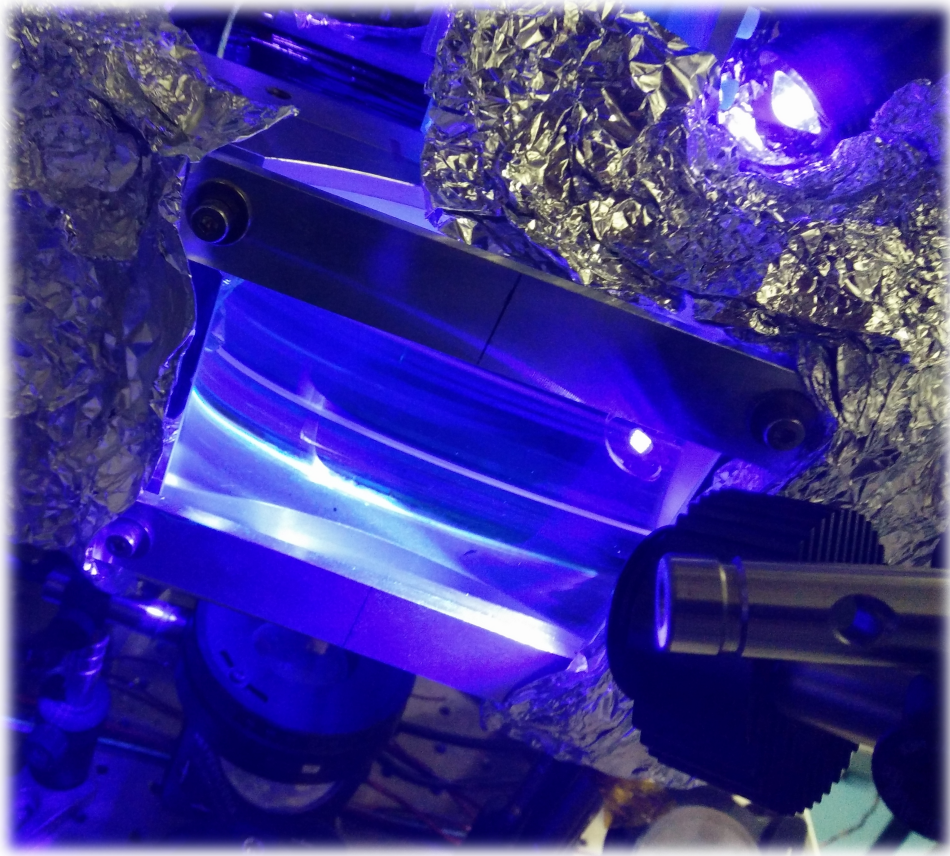


Photo of the blue UV-LEDs shining on the heated 2D-MOT glass cell for the application of LIAD (see section 2.2.2).

Résumé

Dans cette thèse, nous avons étudié expérimentalement les propriétés physiques des fermions ultra-froids grâce à une machine conçue pour refroidir un mélange fermionique de ^6Li et ^{40}K . Après une courte description concernant la construction de l'expérience et quelques améliorations que j'ai implémentées pendant ma thèse (telles que la désorption atomique par lumière ultraviolette dans le 2D-MOT), l'exposé se concentre sur deux observations principales de l'origine fermionique des gaz de potassium et de lithium.

La première partie présente la quasithermalization du ^6Li dans un potentiel quadrupolaire, créé par un piège magnétique. Malgré l'absence de collisions dans un gaz fermionique polarisé en dessous d'une température donnée, nous observons une redistribution d'énergie dans l'ensemble statistique après une excitation dans le piège linéaire. Une étude expérimentale détaillée ainsi qu'une analyse théorique du phénomène sont présentées. De plus, une transformation canonique de l'hamiltonien du système permet la description de particules sans masses dans un piège harmonique. Les résultats expérimentaux du système réel (gaz ^6Li dans un potentiel quadrupolaire) sont donc réinterprétés pour décrire ces particules non massiques, difficiles à observer. Un développement supplémentaire de notre système expérimental permet également la réalisation d'un couplage spin-orbite non-abélien dans le gaz fermionique sans interactions.

Dans la deuxième partie, on décrit la réalisation d'un gaz dégénéré de ^{40}K à l'aide du refroidissement évaporatif. Une succession d'étapes d'évaporation, utilisant différentes technologies de piégeage, nous permet d'obtenir $1.5 \cdot 10^5$ atomes dans l'état fondamental à une température de 62 nK, température équivalente à 17 % de la température de Fermi.

Mots Clés

Atomes froids, gaz de fermions dégénéré, refroidissement par évaporation, quasithermalization, particules de Weyl, couplage spin-orbite

Abstract

In this thesis we investigate experimentally the physics of ultra-cold fermions on an apparatus designed to create a cold fermionic mixture consisting of ^6Li and ^{40}K . After a short description of the experimental apparatus and of a few technical particularities implemented during my PhD, for example the light-induced atomic desorption in the 2D-MOT by UV-light, we focus on two main observations of the fermionic nature of the gas.

The first part describes the quasithermalization of ^6Li in a magnetic quadrupole potential. Even though collisions are absent in a spin-polarized fermionic gas below a given temperature, the statistical ensemble undergoes energy redistribution after an excitation within the linear potential. We present an extensive experimental study as well as a comprehensive theoretical analysis of this phenomenon. Moreover, the studied Hamiltonian can be canonically mapped onto a system of massless, harmonically trapped particles and the previously developed results are re-interpreted in order to describe this experimentally inaccessible system. A further development of the realized experiment allows even for the implementation of non-Abelian spin-orbit coupling in a gas of non-interacting fermions.

In the second part, we describe the evaporative cooling of ^{40}K to quantum degeneracy. Through different evaporative cooling stages we reach with a final number of $1.5 \cdot 10^5$ atoms in the ground-state a temperature of 62 nK, which corresponds to 17 % of the Fermi temperature.

Keywords

Cold atoms, degenerate Fermi gas, evaporative cooling, quasithermalization, Weyl particles, spin-orbit coupling